University College Cork, Ireland
Coláiste na hOllscoile Corcaigh

Nonlinear Vibration Energy Harvesters for Powering the Internet of Things

A dissertation undertaken at the

Tyndall National Institute

and presented to the

Department of Electrical and Electronic Engineering

at the

National University of Ireland, University College Cork

in partial fulfilment of the requirements for the degree of

Doctor of Philosophy (PhD)

in

Electrical and Electronic Engineering

by

Pranay Podder, M.Tech.

Supervisor: **Dr. Saibal Roy**

2017

Copyright Information:

ABSTRACT

The ever decreasing power consumption in electronic devices and sensors have facilitated the development of autonomous wireless sensor nodes (WSNs), which ushered in the era of the Internet of Things (IoT). However, the problem of long-term power supply to the numerous WSNs pervasively dispersed to enable the IoT is yet to be resolved. This work focuses on the development of novel vibration energy harvesting (VEH) devices and technologies for effective transduction of mostly wide-band and noisy ambient mechanical vibrations to power WSNs. In this thesis meso-scale and MEMS-scale nonlinear and frequency tunable VEH devices have been designed, fabricated and characterized. The first meso-scale VEH prototype developed in this thesis combines a nonlinear bistable oscillator with mechanical impact induced nonlinearity, which exhibits upto 118% broadening in the frequency response over a standalone bistable system. The second meso-scale prototype combines magnetic repulsion induced bistable nonlinearity with stretching induced monostable cubic nonlinearity in a single device structure. The device effectively merged the beneficial features of the individual nonlinear bistable and monostable systems, and demonstrates upto 85% enhanced spectral performance compared to the bistable device. The third prototype is a MEMS-scale device fabricated using spiral silicon spring structure and double-layer planar micro-coils. A magnetic repulsion induced frequency tuning mechanism was incorporated in the prototype, and it was demonstrated that both linear and nonlinear hysteretic frequency responses could be tuned (by upto 18.6%) to match various ambient vibration frequencies. In order to enhance the power generating capability of MEMS-scale electromagnetic devices, an ultra-dense multi-layer micro-coil architecture has been developed. The proposed ultra-dense micro-coil is designed to incorporate double number of turns within the same volume as a conventional micro-coil, and significantly enhance the magnetic flux linkage gradient resulting in higher power output (~4 times). However, attempts to fabricate the ultra-dense coil have not been successful due to lack of proper insulation between the successive coil layers. Finally, a power management system combining diode equivalent low voltage drop (DELVD) circuit and a boost regulator module was developed. It was demonstrated that energy harvested from harmonic and bandlimited random vibrations using linear, nonlinear bistable, and combined nonlinear VEH devices could be conditioned into usable electricity by the power management system with 60% - 75% efficiency. In addition to developing new prototypes and techniques, this thesis recommends directions towards future research for further improvement in vibration energy harvesting devices and technologies.

ACKNOWLEDGEMENTS

Throughout the course of this research I have had the opportunity to collaborate, work, and interact with a diverse group of people. For me, these interactions have been the most rewarding part of this research work. I would like thank my thesis advisor, Prof. Saibal Roy, for giving me the opportunity to pursue research in the interesting topic of energy harvesting. He helped me find direction during my thesis work, and offered encouragement and advice, and provided the necessary resources. I am also deeply grateful to Dr. Andreas Amann, who is an insightful researcher and a fantastic teacher. Our fruitful collaboration, and specifically the numerous weekly meetings enriched my research experience tremendously and helped shape my research mind-set. I am thankful to Dr. Ray Duffy for serving as my mentor in this research work, and for his valuable comments in the review meetings.

I gratefully acknowledge the help with device fabrication and characterization from the people in the Specialty Products & Services (SP&S): Joe O'Brien, Richard Murphy, Jim Scully, Elias Haddad, Paul Tassie, Tony Compagno, Ken Rodgers, Vince Lodge, Michael Schmidt, Brendan Sheehan, Eoin Sheehan and many others. I want to thank Donal O'Sullivan and Dermot Houston for their help, and William Knott for the access to the MakerSpace whenever needed. I owe thanks to the people in the Electrochemical Materials and Energy (EME) Lab, especially Declan Casey, Fiona Barry and Tomas Clancy, and to Dr. James Rohan for granting access to the lab.

A huge thank you to my group members: Tuhin Maity, Peter Constantinou, Dhiman Mallick for those lively discussions, the endless supply of enthusiasm, and the friendship above all. A special thanks to my colleagues in the office A.6.3.31 for maintaining a warm and friendly atmosphere. My time in Cork was made enjoyable by the amazing friends I met here: Ricky, Santosh, Gangotri, Anushka, Sneha, Shatabdi, Swatchith, Saroj, Subha da, Tandra di and many others. This journey would not have been the same without you. Also, thank you to the people in the UCC Indians Society for organizing those vivacious events and day-trips.

I owe a very important thank you to Dr. Anirban Bhattacharyya for introducing me to the MEMS technology and processes during my graduate studies, for the inspiration to pursue research and for his insightful advice.

I am deeply grateful to my family, especially my parents, and my sister and brother, for the unconditional love and support throughout my life. Finally, a heartfelt thank you to my wife, who made great sacrifices to help me pursue my goals.

LIST OF ABBREVIATIONS

AFM	Atomic Force Microscopy
BJT	Bipolar Junction Transistor
BQD	Bistable Quadratic
BQT	Bistable Quartic
CMOS	Complementary Metal Oxide Semiconductor
CRDC	Current Reversal Detection Circuit
DAE	Differential and Algebraic Equation
DELVD	Diode Equivalent Low Voltage Drop
DRIE	Deep Reactive Ion Etching
EDX	Energy Dispersive X-ray
EMVEH	Electromagnetic Vibration Energy Harvester
FBR	Full Bridge Rectifier
FEA	Finite Element Analysis
FEM	Finite Element Method
FIB	Focused Ion Beam
FMEA	Failure Modes and Effects Analysis
EHFOM	Energy Harvester Figure of Merit
ICP	Inductively Coupled Plasma
IoT/E	Internet of Things/ Everything
MEMS	Micro-Electro-Mechanical Systems
MOSFET	Metal Oxide Semiconductor Field Effect Transistor
MPPT	Maximum Power Point Tracking
MQT	Monostable Quartic
NPD	Normalized Power Density
NPI	Normalized Power Integral
ODE	Ordinary Differential Equation

PDE	Partial Differential Equation
PDMS	Polydimethylsiloxane
PECVD	Plasma Enhanced Chemical Vapour Deposition
PERIE	Plasma Enhanced Reactive Ion Etching
PMMA	Polymethyl Methacrylate
PMN-PT	Lead Magnesium Niobate – Lead Titanate
PSD	Power Spectral Density
PTFE	Polytetrafluoroethylene
PVD	Physical Vapour Deposition
PVDF	Polyvinylidene fluoride
PZN-PT	Lead Zinc Niobate – Lead Titanate
PZT	Lead Zirconate Titanate
SEM	Scanning Electron Microscope
SOI	Silicon on Insulator
SSHI	Synchronized Switch Harvesting on Inductor
TEG	Thermoelectric Generator
TENG	Tribo-Electric Nano-Generator
VEH	Vibration Energy Harvester
WSN	Wireless Sensor Nodes

PUBLICATIONS

Refereed Journal Articles

1. **P Podder**, D Mallick, A Amann, S Roy, Influence of combined fundamental potentials in a nonlinear vibration energy harvester, Nature Scientific Reports 6, 37292, 2016.
2. **P Podder**, A Amann, S Roy, Combined effect of bistability and mechanical impact on the performance of a nonlinear electromagnetic vibration energy harvester, IEEE/ASME Trans. on Mechatronics 21 (2),2016.
3. S Roy, **P Podder**, D Mallick, Nonlinear energy harvesting using electromagnetic transduction for wide bandwidth, IEEE Magnetics Letters 7, 1-4, 2016.
4. **P Podder**, A Amann, S Roy, A bistable electromagnetic micro-power generator using FR4-based folded arm cantilever, Sensors and Actuators A: Physical 227 2015.
5. **P Podder**, P Constantinou, D Mallick, A Amann, S Roy, Magnetic tuning of nonlinear electromagnetic vibration energy harvester, IEEE Journal of MEMS, 2017.
6. D. Mallick, **P. Podder**, P. Constantinou, S. Roy, Dual Degrees-of-freedom MEMS Electromagnetic Energy Harvester, Sensors and Actuators A.: Physical, (Under review).

Refereed International Conference Proceedings

1. **P Podder**, P Constantinou, A Amann, S Roy, Frequency adjustable MEMS vibration energy harvester, 27th MME Conference, Cork, Ireland, 2016.
2. **P Podder**, P Constantinou, D Mallick, S Roy, Silicon MEMS bistable electromagnetic vibration energy harvester using double layer micro-coils, 15th PowerMEMS Conference, Boston, USA, 2015.
3. **P Podder**, D Mallick, S Roy, Bandwidth widening in nonlinear electromagnetic vibrational generator by combined effect of bistability and stretching, 14th PowerMEMS Conference, Awaji Island, Japan, 2014.
4. D Mallick, **P Podder**, S. Roy, Wideband electromagnetic energy harvesting from ambient vibrations, AIP Conf. Proceedings, 59th DAE Solid State Physics Symposium, Vellore, India, 2015.
5. S Roy, D Mallick, **P Podder**, Nonlinear energy harvesting using electromagnetic transduction for wider bandwidth, ICMAT 2015 and IUMRS-ICA 2015, Singapore, 2015.

6. **P Podder**, A Amann, S Roy, FR4 based bistable electromagnetic vibration energy harvester, 28th EuroSensors Conference, Brescia, Italy, 2014.

Book Chapter

1. Vibrational Energy Harvesting, Beyond CMOS Nano Devices, by Larcher, L., Roy, S., Mallick, D., **Podder, P.**, de Vittorio, M., Todaro, T., Guido, F., Bertacchini, A., Hinchet, R., Keraudy, J. and Ardila, G., in the book titled "Beyond-CMOS Nanodevices 1 (ed F. Balestra)", John Wiley & Sons, Inc., Hoboken, NJ, USA. (2014); doi: 10.1002/9781118984772.ch6; ISBN: 9781848216549.

Filed Patent and Invention Disclosure

1. 'Vibrational energy harvesting device combining multiple nonlinearity' – S. Roy, **P. Podder**, D. Mallick, A. Amann- Patent application: PCT filing 16th June 2016, PCT/EP2016/063940.

TABLE OF CONTENTS

1 INTRODUCTION - ENERGY HARVESTING FOR THE INTERNET OF THINGS

This chapter gives an overview on the motivation and need of vibration energy harvesting technologies for powering the internet-of-things. It starts with the advancement in low power electronics, driven by the Moore's law, which ushered in the development of low-power wireless sensor nodes (WSNs). Then the present day approach of powering the WSNs, including energy storage (battery, super capacitor) and energy harvesting systems are discussed. This is followed by identification of issues and scopes of improvement in present-day vibration energy harvesting systems. Finally, the chapter is concluded with a synopsis of the thesis.

1.1 Background

Over the last few decades, the size of active device (or MOSFET channel length) has been decreasing, which led to the decreasing power dissipation of individual MOSFETs and increasing switching speed. These developments contributed to the general trend of decreasing power consumption in electronic devices, and helped the development of low power wireless sensor nodes (WSNs). It is envisaged that in the coming decades the WSNs will become ubiquitous, and usher in to the era of the Internet of Things/ Everything (IoT/E), which would enable seamless interaction between the physical and the digital world.

1.1.1 The Moore's law: smaller, faster, cheaper

Intel's Gordon Moore famously predicted more than a half century ago that the minimum achievable feature size of semiconductor devices (which determines the channel length of MOSFETs) will be decreasing by a factor of 2 every couple of years. This prediction has

been proven to be quite accurate in general, despite some recent slowdown. As the semiconductor industry enters the sub 10nm domain, the laws of physics are making it increasingly difficult to shrink the MOSFET channel length further.
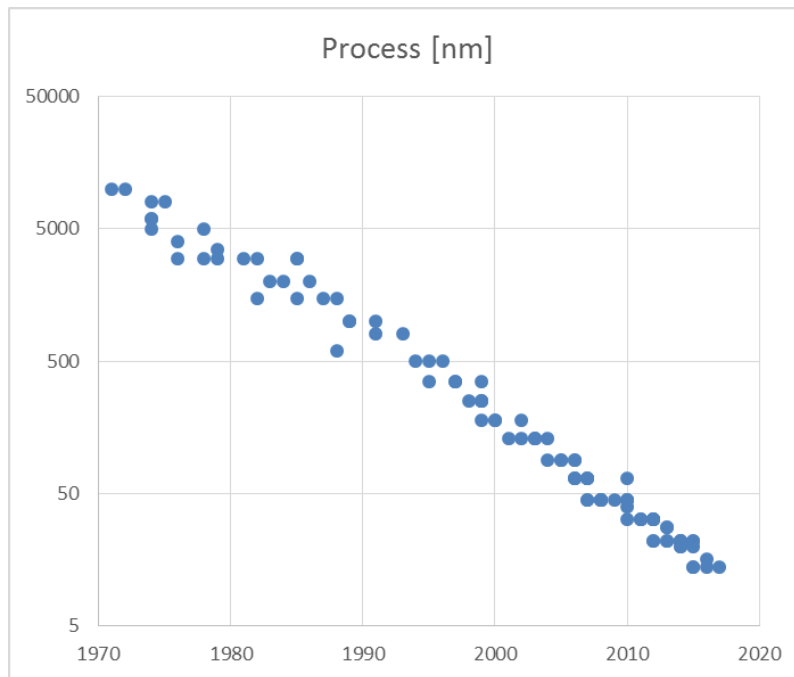
Figure 1.1: Shrinking feature size in CMOS integrated circuit fabrication process [1]

One of the important implications of the Moore's law is that with shorter channel length in each successive generation, the speed of the MOSFETs has been increasing, while the power dissipated in each individual MOSFET has been decreasing. The reduction in switching energy of individual logic devices has been shown in Figure 1.2 [Theis and Wong [2]]. The switching energy dissipation of individual logic devices have been scaled down to < 1 fJ, and isprojected to be reduced further with successive generations. However, scaling down of energy dissipation in recent years are facing tremendous engineering challenge due to increased gate leakage current (quantum tunnelling) and OFF state leakage current through nanoscale MOSFET channels. These challenges are partly responsible for the deviation of recent power reduction trends from that projected by Rolf Landauer in 1988 [Landauer [3]].
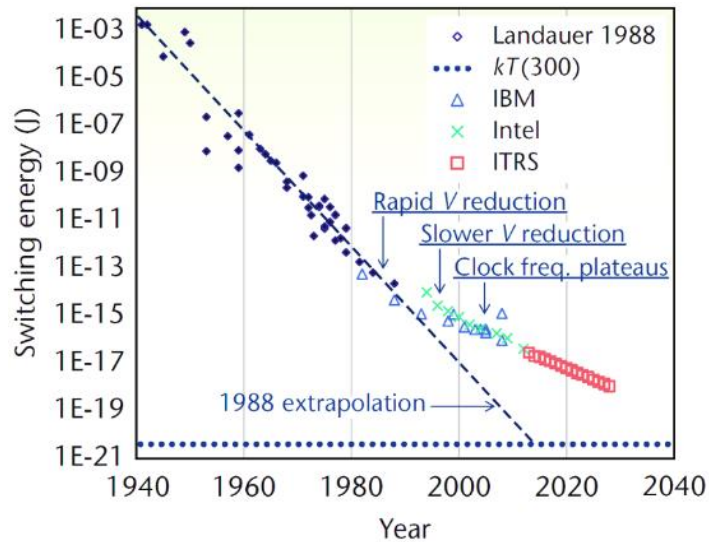
Figure 1.2: Minimum switching energy dissipation in logic devices used in computing systems as a function of time [Theis and Wong [2]].

Lesser known than the Moore's law is the Gene's law, proposed by Gene Frantz in 2000 [4], which states that the power dissipation in embedded digital signal processors (DSPs) would be halved every 18 months. Similar reductions in power dissipation of DSPs and sensors was also predicted by Amirtharajah and Chandrakasan [5] in 1998. In general, the microelectronic techniques used to scale down device size have also contributed greatly towards the gradual decrease in power dissipation of DSPs and micro-processors.
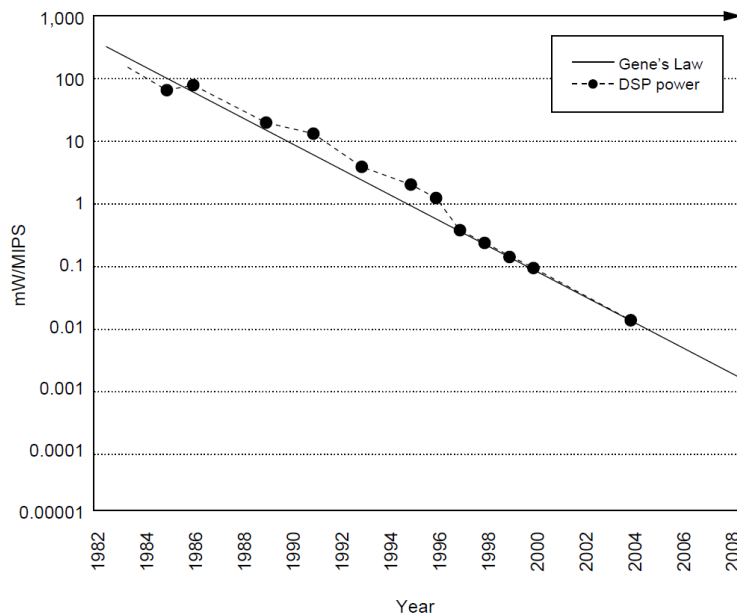
Figure 1.3: Gene's law: Power dissipation in embedded DSP processors decreasing by a factor of 2 every 18 months [Frantz [4]].

The reduction in power dissipation and gain in efficiency of individual MOSFETs or CMOS switches might not be immediately apparent from the consumer point of view, as system designers and manufacturers tend to include more advanced features and functionalities into DSPs and other microelectronic circuits with each successive generation of devices. Nevertheless, the combined effect of reduction in size and power dissipation has resulted phenomenal gain in terms of efficiency and cost, and heralded the possibility of realization of the Internet of Things/ Everything (IoT/E).

1.1.2 The Internet of Things/ Everything (IoT/E)

The proponents of the Internet of Things/ Everything (IoT/E) envisage a world where everything is connected to the internet. In such a world, the sensors embedded in objects or things would collect data and transmit them over to data centres through wireless networks.
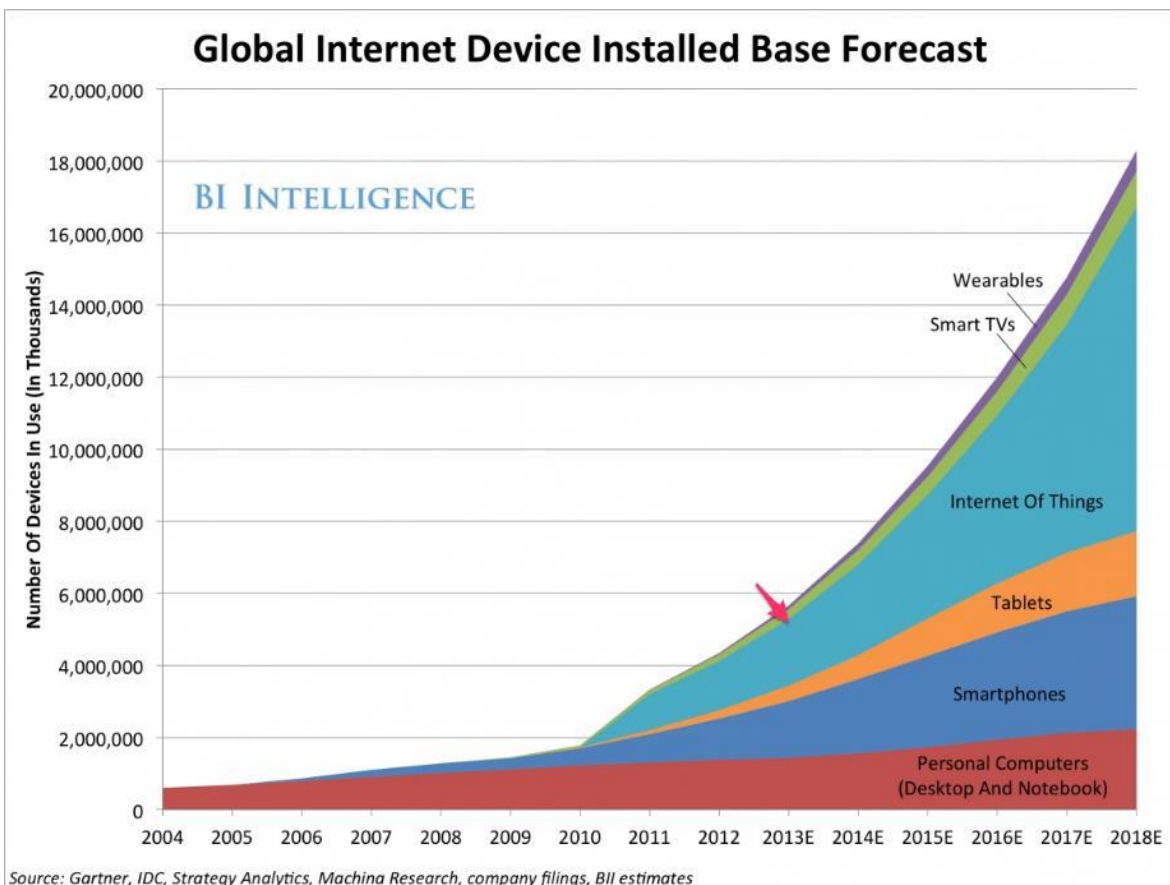
Figure 1.4: Growth of internet connected devices. The number of IoT devices are expected to surpass all others in the decade 2020 – 2030. [6]

Analytics powered by machine learning and AI would generate actionable intelligence from the enormous amount of collected data that would enable visualization and

optimization of processes at unprecedented scale and accuracy, which would realize the paradigm of "Ubiquitous Computing". Ubiquitous computing is defined as a smart environment where "the physical world that is richly and invisibly interwoven with sensors, actuators, displays, and computational elements, embedded seamlessly in the everyday objects of our lives, and connected through a continuous network." [Weiser, et al. [7]]. It has been estimated by various research and analysis agencies that over 50 billion devices will be connected to the internet over the next few years. The rapid growth and advancement in the microelectronics and MEMS (micro-electromechanical systems) technology and digital wireless communication has enabled the development of miniaturized devices and systems capable of sensing, computing and communicating, which has been collectively termed as wireless sensor nodes (WSNs). A dispersed network of such WSNs form the wireless sensor networks, which form the backbone of the IoT/E.
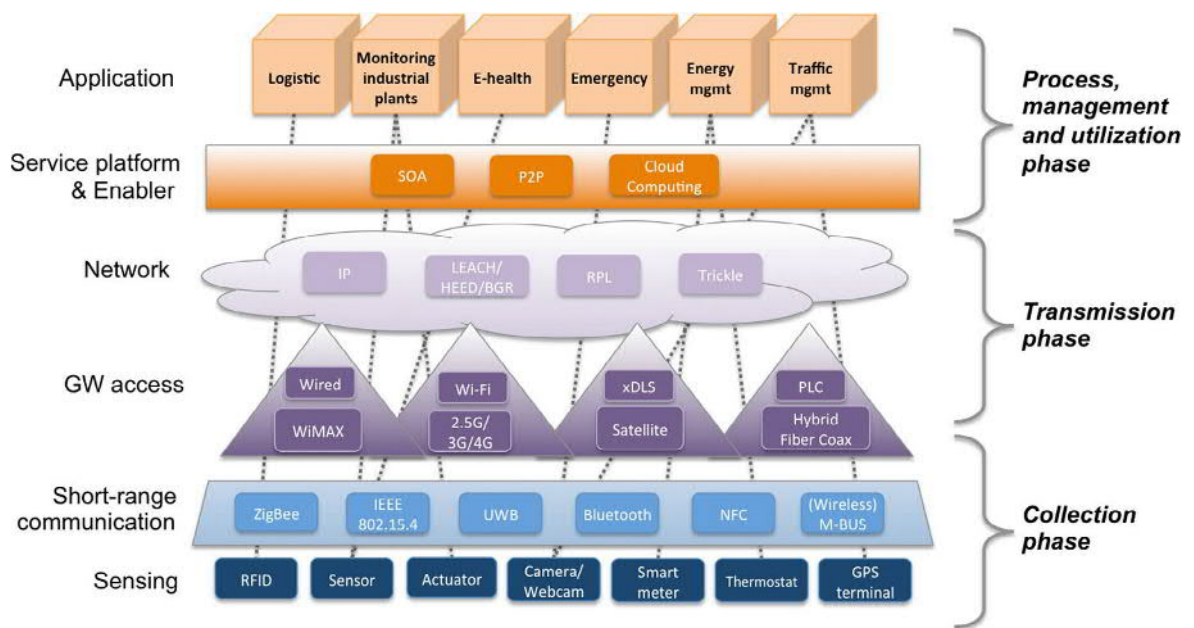
Figure 1.5: The IoT architecture [Borgia [8]].

The WSNs (the so-called 'edge nodes' or 'edge devices') will be responsible for sensing and collecting the data, which is transferred to the gateway (GW) devices through different low power short range wireless communication protocol. The gateway devices process the data, and transmit them over to the cloud computing servers for further analysis and development of intelligence. The insights gathered from the intelligence can benefit a plethora of applications ranging from monitoring of industrial plants and processes to management of logistics, traffic, healthcare, emergency situations etc.

1.1.3 The wireless sensor node (WSNs)
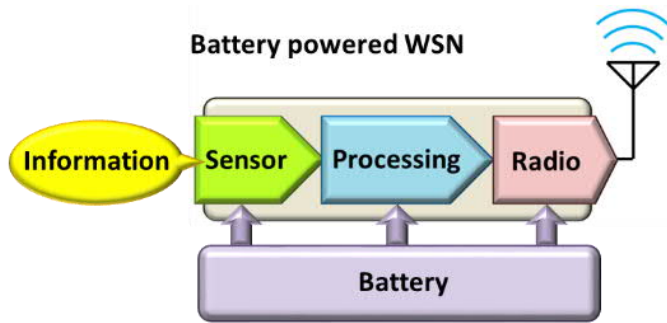
Figure 1.6: The wireless sensor nodes comprise of sensor, processor/ microcontroller, transciever and power source battery.

The generic composition of wireless sensor nodes (WSNs) include the sensor, micro-controller, wireless transceiver, and the power supply unit. The power supply unit typically comprise an energy storage module (e.g. battery) and power management module. The problem with such battery powered WSN modules is the limited lifetime of the batteries, which may last from a few weeks to a couple of years, depending on the duty cycle, computational loads, transmission distance and other factors. In the context of a dispersed network of thousands of WSNs, it is impracticable and uneconomical to deploy battery health monitoring system and battery replacement at regular intervals.
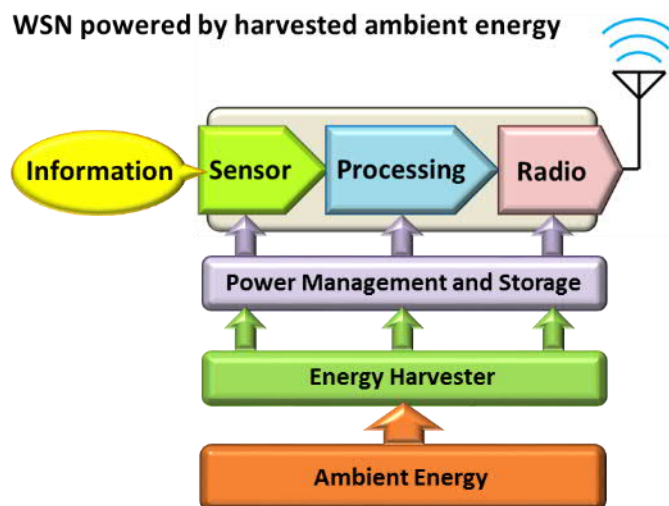
Figure 1.7: The energy harvester transduces ambient energy into electricity, which is processed and transferred to the sensing, processing and radio modules.

Therefore, harnessing the ambient energy sources through various transduction mechanisms are proposed as one of the potential solutions to provide perpetual autonomy to the WSNs.

1.2 Powering the WSNs by harvesting ambient energy

The environment is full of energy sources that can be harnessed via appropriate transducing systems to power WSNs. The major ambient energy sources can be classified as light, wind flow, thermal gradient, mechanical vibrations and tidal water flow. Each of these energy sources has been investigated and transduced into electricity at different scales.

1.2.1 Solar photovoltaic energy harvesting

The photovoltaic transduction method which transforms ambient light into usable electricity has been in use for several decades. The basic unit of a solar photovoltaic transduction system is the photovoltaic cell, which comprises semiconductor materials doped with p-type and n-type dopants to form a p-n junction. The p and n-type regions are separated by an internal potential barrier at the junction, which is depleted of charge carriers such as electrons and holes. As incident light (or photons) is absorbed in the p-n junction, hole and electron separation occurs. Under the influence of the internal potential barrier, the holes and electrons migrate to the two separate electrodes, and cause a flow of current through an external electric load.
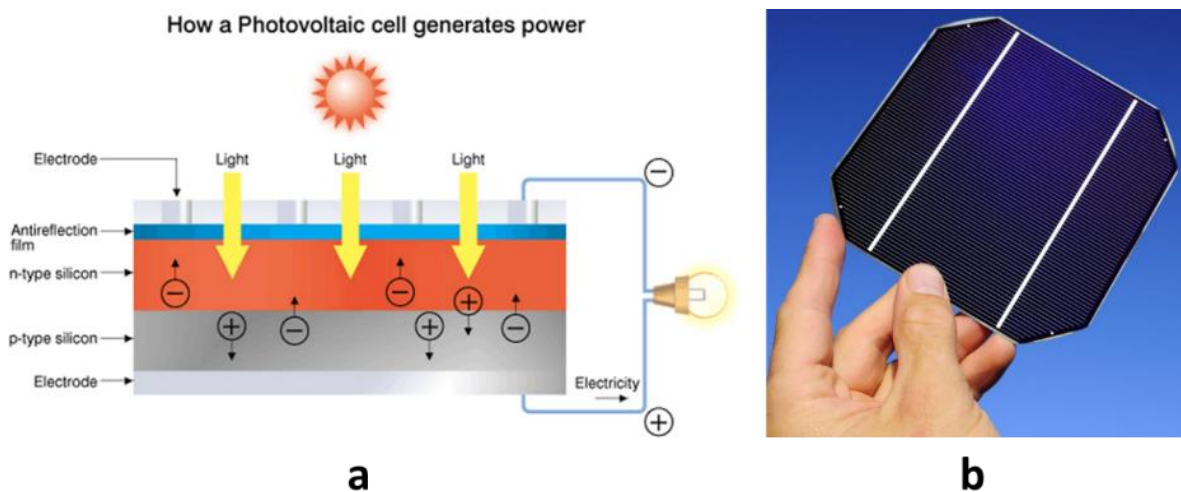
Figure 1.8: (a) Working principle of photovoltaic cell [9]. (b) Fabricated cell [10].

The photovoltaic transduction mechanism is highly scalable, and photovoltaic cells generating a few microwatts (for watch and calculators) to solar power plants generating hundreds of megawatts (for powering factories or thousands of households) has been developed. The power harvested in photovoltaic transduction can be expressed as,

$$P_{PV} = \eta E A_{cell}$$

Where η denotes the cell efficiency, E is the intensity of incident light, and A_{cell} is the active surface area of the photovoltaic cell. The abundance of light from the sun and other terrestrial sources combined with the predictable availability and ease of scalability have driven research in the field of photovoltaics, resulting continued steady increase in efficiency and decrease in cost per unit energy.
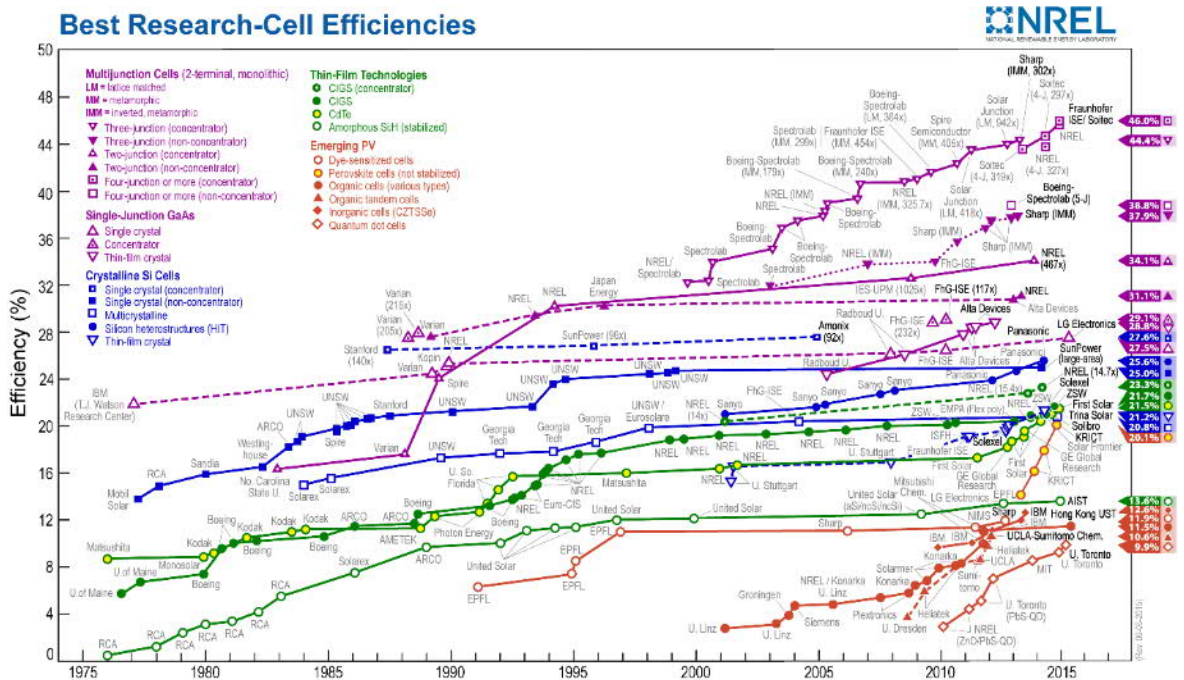
Figure 1.9: Improvement in photovoltaic cell efficiency over the years [11].

While the initial developments in photovoltaic energy harvesting was based on crystalline silicon cells, more exotic materials such as GaAs, CIGS, CdTe, polymers etc. has been successfully utilized to develop more efficient photovoltaic cells.

Small scale photovoltaic energy harvesting systems have been deployed to power wireless sensor nodes by several groups. A battery-free solar powered transmit-only temperature sensing module was demonstrated by Roundy, et al. [12]. Similar photovoltaic powered WSN modules for sensing environmental parameters have been developed by Jiang, et al. [13] and Dutta, et al. [14] among others. While most of the photovoltaic-powered WSNs used silicon based cells, high efficiency advanced materials and topologies are particularly interesting for such applications due to the limited exposed surface area. The multi-junction solar cells are designed with multiple excitation states that are capable of more

efficient usage of the solar or ambient light spectrum [Barnett, et al. [15]] and demonstrate efficiencies approaching ~ 50%. Both the outdoor and indoor installation of photovoltaic powered WSNs require a supplementary battery or supercapacitor in the corresponding power management module to sustain operation during night or low light conditions.

1.2.2 Thermoelectric energy harvesting

The thermoelectric energy harvesting mechanism exploits the Seebeck effect, where the thermal gradient between the junction of two different materials can trigger flow of charge carriers and thereby, an electric current. Although the Seebeck effect was discovered in 1821, the potential benefits of this effect to harvest waste heat is being explored lately.
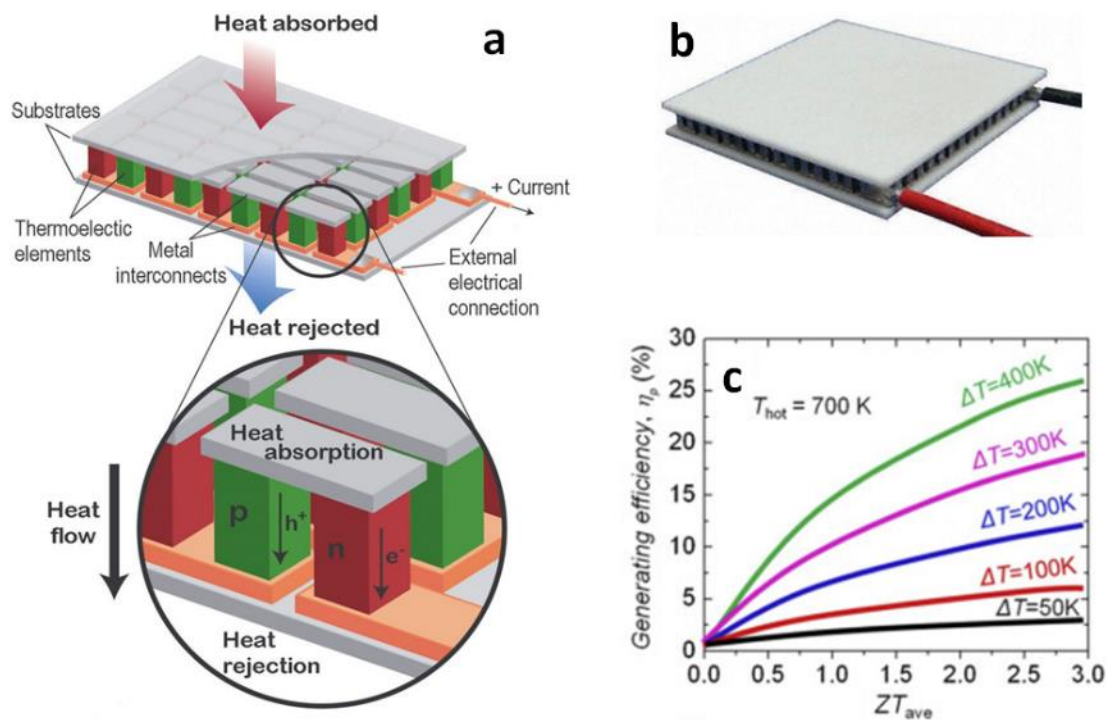
Figure 1.10: (a) working principle of thermoelectric generator [Snyder and Toberer [16]]. (b) Fabricated thermoelectric generator [17]. (c) Increasing efficiency of thermoelectric generator with increasing *ZT* [Zhang and Zhao [18]].

The modern thermoelectric generators use p-n junctions made from lanthanide compounds, and thermal gradient is maintained between the junctions to facilitate generation and flow of charge carriers (electrons and holes). The flow of charge carriers in their respective directions are driven by the potential difference between the junctions, which results from the different shift in electron energy levels in the p and n-type materials under a thermal gradient. The growing interest in both small scale and large scale thermoelectric generation

has resulted continued rise in the efficiency of thermoelectric generators over the last few decades. The power harvested by thermoelectric generators (TEGs) can be expressed as,

$$P_{TEG} = P_H \eta_{Carnot}$$

1.2

Where P_H is the maximum power attainable from heat flux, and is given by,

$$P_H = k \frac{\Delta T}{L}$$

1.3

Where k is the thermal conductivity, ΔT is the temperature gradient and L denotes the distance between the hot and cold surfaces. The maximum possible efficiency of heat engines such as TEGs is defined by the Carnot efficiency (η_{Carnot}) given by,

$$\eta_{Carnot} = \frac{T_{High} - T_{Low}}{T_{High}}$$

1.4

Where T_{High} and T_{Low} denote the temperatures of the hot and cold surfaces respectively.
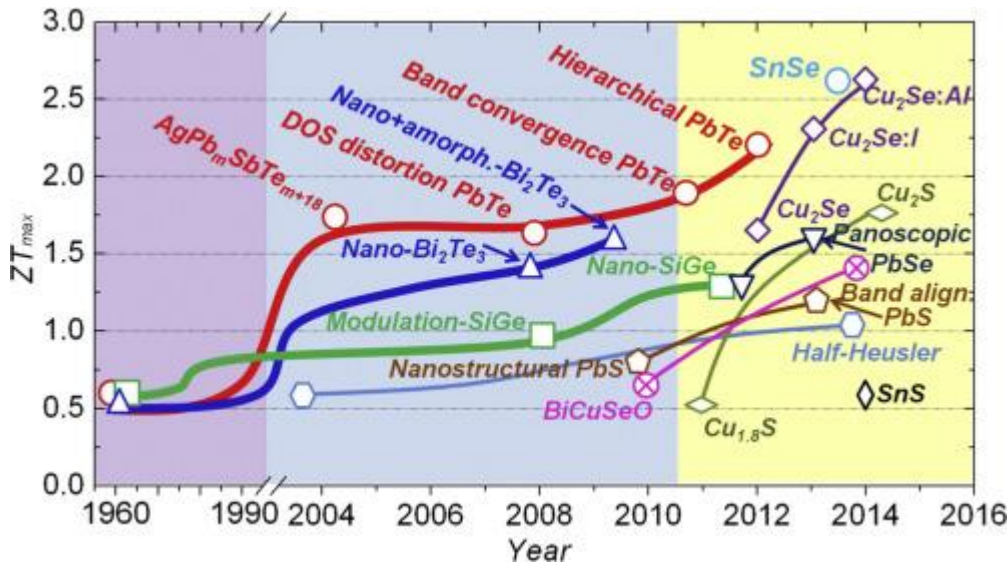
Figure 1.11: Development in *ZT* values of thermoelectric materials over the years [Zhang and Zhao [18]].

However, the actual efficiency of state-of-the-art TEGs is far less than the ideal Carnot efficiency, and can be expressed as,

$$\eta_{TEG} = \left[\frac{T_{High} - T_{Low}}{T_{High}} \right] \frac{\sqrt{1 + ZT} - 1}{\sqrt{1 + ZT} + (T_{Low}/T_{High})}$$

1.5

Where *ZT* is a dimensionless figure of merit given by,

$$ZT = \frac{\sigma S^2 T}{\kappa}$$

1.6

Where σ is the electrical conductivity, S is the Seebeck coefficient, κ is the thermal conductivity, and T is the temperature. As indicated in Figure 1.10 (c), the efficiency of TEGs increases with increasing ZT values for a given temperature gradient. Therefore, development of thermoelectric materials with higher ZT values is a thriving research area. In the recent years, the highest ZT value of 2.6 have been demonstrated for SnSe (tin selenide) and Cu_2Se (copper selenide) systems [Zhang and Zhao [18]].

The high operating temperature of conventional combustion engines (300º C - 1000º C) make an attractive case for generation of electricity from waste heat for recharging on board batteries of vehicles [Crane, et al. [19]]. While such high temperature gradients are uncommon in conventional environments (except for factories), TEGs capable of operating at a temperature difference of 3º C or lower has been demonstrated, specifically targeting body area network [Leonov, et al. [20]] and wearable device applications. More than 10% efficiency has been demonstrated in recent years [Minnich, et al. [21], Zhao, et al. [22]] by using advanced thermoelectric materials.

1.2.3 Radio frequency (RF) energy harvesting

Wireless transmission of electricity was first conceived by Nikola Tesla and Heinrich Hertz [Brown [23], Lumpkins [24]], who proposed to radiate power into the free space and then capture and convert the wireless power into usable DC power at a target location. However, the growth of interest in wireless RF energy harvesting is a relatively recent phenomenon, which has been driven by the exponentially growing number of RF energy radiating sources, such as radio, TV, satellite, cellular, WiFi signals etc. [Kim, et al. [25]]. RF energy harvesters are designed to capture the energy radiated by these sources through antennas, and convert the harvested energy into usable DC through proper power management circuitry. The energy incident on the antenna of such devices from the source can be expressed as,

$$P_{RF} = \frac{P_0 \eta \lambda^2}{4\pi R^2}$$

1.7

Where P_0 is the power radiated by the transmission antenna, η is the efficiency, λ is the wavelength and R denotes the distance between the receiver and the source. The strong dependence of the received power on the distance between the source and the harvester

imply that in many real life scenarios, the energy available from ambient RF signal can be very low.
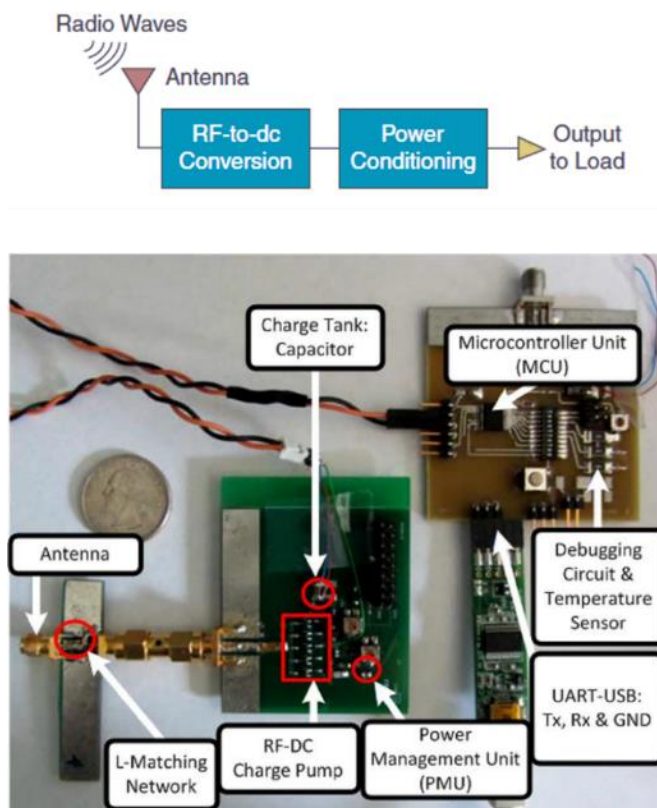
Figure 1.12: The general structure of RF energy harvester, and a fabricated prototype consisting of embedded sensor, microcontroller and power management circuit. [Kim, et al. [25]]

RF energy harvesting systems to scavenge energy from ambient radio, TV, cellular and WiFi signals has been developed by Dolgov, et al. [26], Piñuela, et al. [27], Masotti, et al. [28], Ajmal, et al. [29] and several other researchers. The RF energy transfer and harvesting technologies could be useful in charging batteries wirelessly in situations where it is difficult or even impossible to access the installed wireless network devices (such as, buildings, bridges, chemical plants etc.). Also, this technology offers the benefit of flexibility in terms of installation and integration, and on-demand operation regardless of the time of the day. However, a major limitation of the RF energy scavenging systems is the inverse-square dependence of the harvested energy on the distance from transmitting sources, which makes very low power level (< 10 µW) available from background RF radiation.

1.2.4 Vibration energy harvesting

Mechanical vibrations are generated in numerous sources (such as vehicles, machinery, aircraft, human motion etc.) which can be harnessed to power WSNs. Vibration energy harvesting systems work by transducing the ambient vibration via electromagnetic, piezoelectric or electrostatic mechanisms, often through a spring-mass-damper based oscillator.
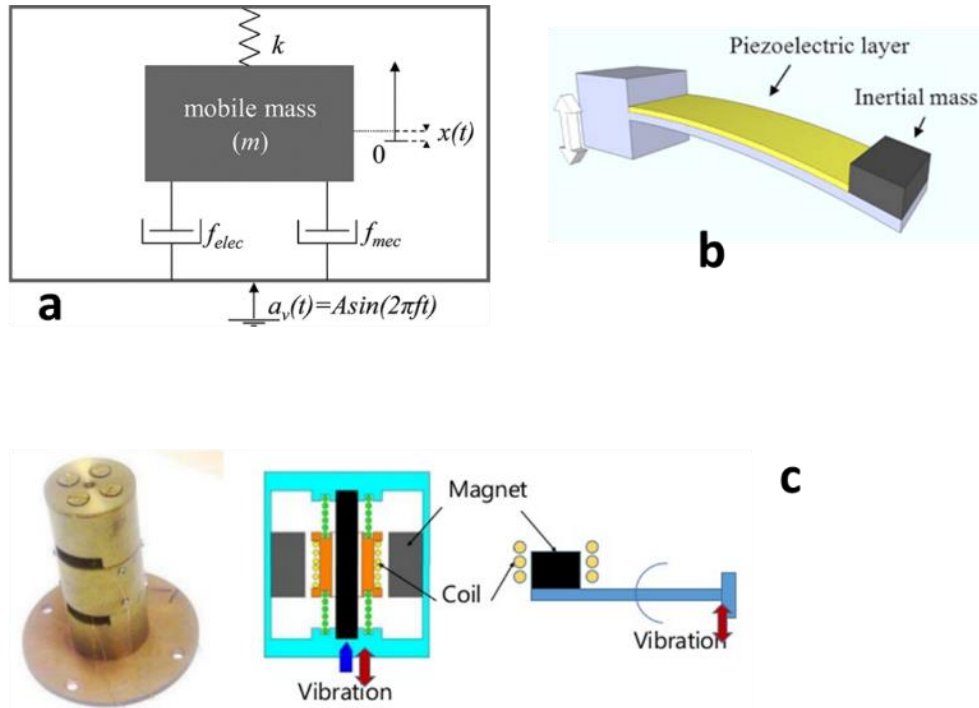
Figure 1.13: (a) Generic vibration energy harvesting topology [Boisseau, et al. [30]], (b) Piezoelectric transduction [31], (c) Electromagnetic transduction [32].

The idea of harvesting electricity for low power devices was first proposed by Williams and Yates [33], who developed the expression for theoretical maximum power available from a vibration source,

$$P_{Vib} = \frac{M\zeta_e a^2}{4\omega(\zeta_e + \zeta_m)^2} \qquad 1.8$$

Where M is the proof mass of the energy harvesting oscillator, a is the acceleration, ω is the angular frequency of oscillation, ζ_e and ζ_m are the electrical and mechanical damping coefficients respectively.

However, this expression does not take into account the restrictions on maximum oscillation amplitude imposed by the limited internal volume of energy harvesters. A more

practical estimation of the maximum energy harvestable by a device with limited dimensions was introduced by Mitcheson, et al. [34] as,

$$P_{Vib} = \frac{1}{2} Y_0 Z_l \omega^3 M$$

1.9

where Y_0 is the amplitude of the source vibration, Z_l denotes the maximum allowable displacement of the proof mass M, and $\omega = 2\pi f$ is the angular frequency, assuming harmonic source vibration.

Following the initial work by Williams and Yates [33], several linear [Roundy and Wright [35], Torah, et al. [36] and others]and nonlinear [Cottone, et al. [37], Basset, et al. [38] and others] oscillator based vibration energy harvesters have been developed.

1.2.5 Energy harvester power management

The energy transduced from ambient sources need to be converted into usable form by appropriate power conditioning/ management circuitry, which is very often a critical part of the energy harvesting system. The design philosophy of energy harvester power management circuits is to efficiently convert the incoming unregulated variable flow of energy into an outgoing regulated usable power source with load matched to the driven circuitry, while consuming as little energy as possible. The architecture of available power conditioning circuits are as diverse as the ambient energy sources, and the associated transduction mechanisms themselves. The solar photovoltaic and thermoelectric transducers generate DC electricity, which eliminates the need for a rectifier module in the power management circuit. However, wide range of variability of incident light intensity and thermal gradient, coupled with the nonlinear dependence in the voltage-current relationship, necessitates the incorporation of a maximum power point tracking (MPPT) mechanism in the power management circuits of photovoltaic and thermoelectric energy harvesters. On the other hand, the electricity generated by RF energy harvesters and the vibration energy harvesters is AC in nature, and must be converted into DC through efficient rectification circuit prior to further processing. The next processing steps may involve DC-DC converter circuits for efficient voltage level shifting to suite the requirements of energy storage (such as rechargeable batteries and supercapacitors) and load elements. Depending on the ambient energy source and available power level, other modules such as cold start, charge pump, micro-controller based control circuits etc. can be included in power conditioning circuits. Figure 1.14 shows a commercially available TI

BQ25504 ultra low power conditioning module including cold start, MPPT, boost converter and control circuits.
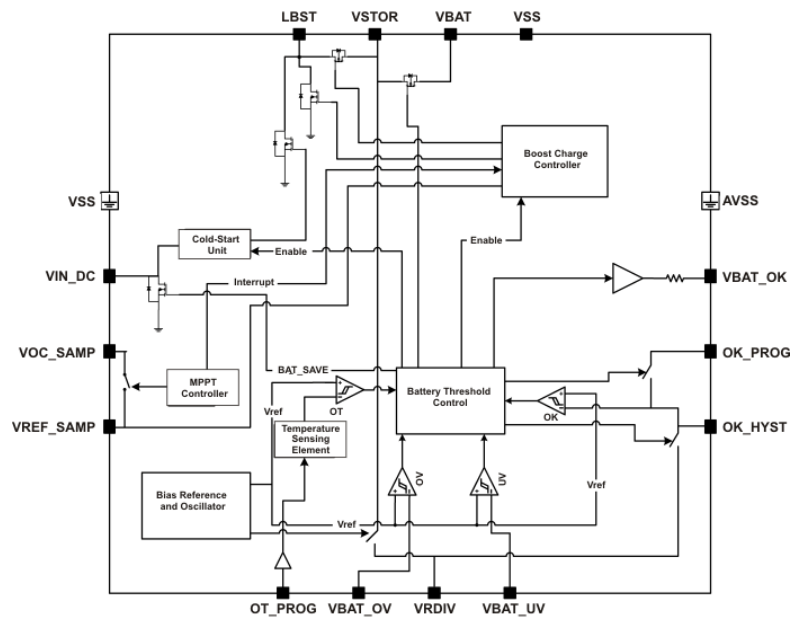
Figure 1.14: Texas Instruments BQ25504 ultra low-power high-efficiency DC-DC boost converter for solar cell power management.

1.3 Research motivation

This section discuss the motivation behind the research pursued in this thesis. First, various sources of ambient vibration and their nature is described, and the opportunities for application of vibration energy harvesting are defined. Finally, the some of the challenges in the field of vibration energy harvesting are discussed.

1.3.1 Vibration sources

The ambient vibration sources can be broadly categorized as vehicles, machinery, infrastructure (e.g. bridges, buildings), human and animal motions. Each of these sources produce vibrations that range from resonant single frequency to broadband random. The automobiles, machinery and appliances tend to produce vibrations at resonant single or multiple dominant frequencies. On the other hand, moving human beings produce broadband vibrations with dominant frequencies in the lower end of the spectrum.

Vibration Source	Acceleration (g)	Frequency (Hz)	Type/ Characteristics
Vehicles			
Ford Fiesta - Front Suspension Arm	0.5 - 5	10 - 60	Broadband with peaks near 20 Hz and 50 Hz
Ford Focus - Engine	1 - 2	35	Resonant with peaks at 35 Hz
VW Transporter Van - Battery Holder	0.1 - 0.3	276	Resonant with peak at 276 Hz
VW Transporter Van - Dashboard	0.15 - 0.35	30 - 100	Dominant resonant peaks at 33, 65, 92Hz
VW Transporter Van - Engine Block	0.2 - 1.6	40 - 500	Several dominant peaks, highest at 236 – 264 Hz
VW Transporter Van - Front Wheel Hub	0.1 - 1	30 - 100	Dominant resonant peaks at 35, 92, 310
Tourist bus - Floor	0.03 – 0.06	2 - 20	Broadband with peaks at 10.5, 12 Hz
Train - Floor	0.03 – 0.05	12 - 160	Broadband with peaks at 12, 102, 118 Hz
Aircraft – Boeing 737	0.4 – 0.8	100 - 1200	Broadband
Domestic appliances			
Chest Freezer	0.004 - 0.006	50 - 200	Random with several dominant peaks
Combination Boiler	0.02	100	Resonant
Microwave	0.1 - 0.3	100, 150, 200	Resonant
Tumble Drier	0.03 - 0.06	44	Random with dominant peak at 12, 44 Hz
Washing Machine	0.05 - 0.25	22, 65, 100	Random with dominant peaks
Human motion			
Chest	0.025 - 0.15	19 - 24	Dominant low frequency with 21 Hz peak
Head	0.016 - 0.08	19 - 27	Dominant low frequency with 21 Hz peak
Hip	0.05 - 0.08	19 - 35	Dominant low frequency with 20 Hz peak
Lower Leg	0.7 - 1.1	19 - 50	Dominant low frequency with 21.5 Hz peak
Wrist	0.036 - 0.08	19 - 40	Dominant low frequency with 22 Hz peak
Machinery			
Ward-Leonard Generator	0.4 to 1.6	200, 300, 400	Resonant with dominant peaks
Water Pump Motor	0.2 to 0.6	50 to 220	Resonant with multiple dominant peaks
Bridge			
Clifton suspension bridge (Bristol)	0.005 – 0.024	25 - 300	Broadband with peaks at 28, 105, 170, 292 Hz frequencies, depending upon the measurement location.
Chicago North bridge	0.02 – 0.9	2 - 20	Broadband with dominant low frequency
Tower bridge (London)	0.01 – 0.04	4 - 20	Broadband with dominant frequencies at 5, 11, 15, 20 Hz

Source of vibration data: *http://eh-network.org/data*; *http://realvibrations.nipslab.org/*

Vibrations generated by moving trains, aircrafts, bridges and domestic appliances demonstrate broadband response, often with multiple dominant frequencies. While the dominant vibration frequencies for most of sources are within the $10 - 500$ Hz range, some sources may generate substantially high frequency (> 1000 Hz) vibrations. The vibrational acceleration of sources also tend to vary over a quite broad range (a few milli-g to several g's). Therefore, detailed vibration data of the relevant source or host structure is necessary to design and optimize vibration energy harvesters for practical applications.

1.3.2 Opportunities in vibration energy harvesting

The ubiquity of vibrations generated by myriad sources in the modern urban landscapes imply huge opportunity for powering WSNs by using electricity transduced from mechanical vibrations. Despite the ubiquity of vibration energy, it is not feasible at this time to power all of the modern energy intensive devices and gadgets from ambient mechanical vibrations. An analytical expression for the upper limit of attainable energy using inertial energy harvesters was developed by Mitcheson, et al. [39]. Considering harmonic oscillation of the vibration source with angular frequency ω and amplitude Y_0, the maximum source acceleration a_{max} is given as,

$$a_{max} = Y_0\omega^2$$

<div align="right">1.10</div>

For extraction of maximum possible energy from the system, the magnitude of maximum electromechanical damping force cannot exceed the inertial force on the proof mass, Ma_{max}. By imposing the limit on the maximum allowable displacement of the proof mass as Z_l, and assuming a symmetric harmonic motion where energy can be extracted from motion in both directions, the total energy harvested per cycle can be obtained as,

$$E_{max} = 4Z_lMa_{max} = 4Z_lM\omega^2Y_0$$

<div align="right">1.11</div>

Then the maximum available power can be derived by dividing eq. 1.11 by the excitation time period as,

$$P_{max} = \frac{E_{max}}{2\pi/\omega} = \frac{2}{\pi}Y_0Z_l\omega^3M$$

<div align="right">1.12</div>

This expression yields the realization that the power requirements for modern personal electronics and mobile computing devices (such as laptop computers, smart phones, smart watches etc.) are very close to the fundamental limits, and therefore unfeasible [Figure

1.15]. On the other hand, the power requirements of the emerging IoT devices (WSNs, fitness trackers etc.) are well within the maximum harvestable range of power.

The equation shown in the figure:

$$P_{max} = \frac{2}{\pi} Y_0 Z_l \omega^3 m$$
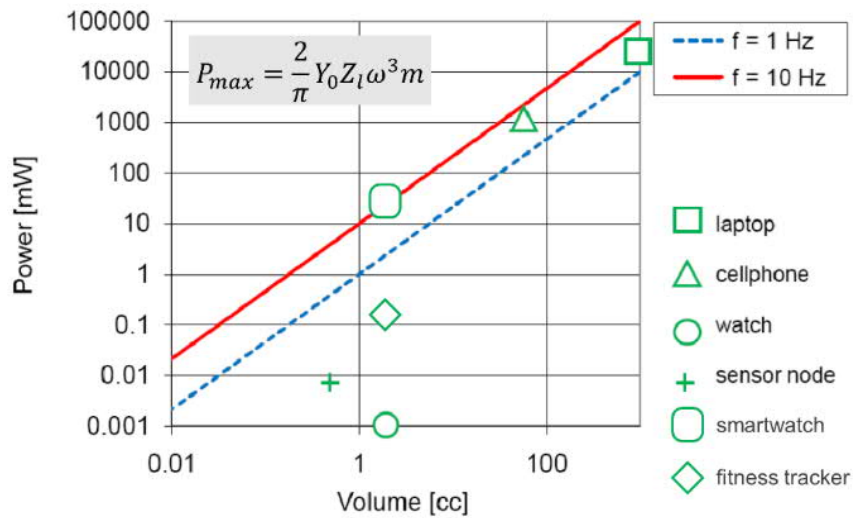
Figure 1.15: Harvestable maximum power for vibration driven generators as a function of device volume, for frequencies as shown [Mitcheson, et al. [39]].

The feasibility of application of vibration energy harvesting in the IoT sensor node scenarios is emerging as a realizable one. This is being driven by the gradually increasing efficiency and diminishing power requirements of some of the key WSN components (e.g. micro-controllers, processors, ADCs, radio modules etc.) over the years [Boyle, et al. [40]]. However, as more features and functionalities are integrated into each successive generation of devices, the benefits of increased efficiency might not directly translate into reduced power consumption. Nevertheless, the operational duty cycles of such devices could be manipulated to suite the responsive requirements and the availability of harvestable energy in a wide array of application scenarios. With the ongoing trend of diminishing power requirement, more and more IoT devices enabled with sensors and wireless communication are expected to be deployed to facilitate process automation, predictive maintenance, smart logistics, tracking and monitoring. Many of these IoT sensor nodes need to be completely autonomous in terms of power, which can potentially be harvested from ambient mechanical vibrations.
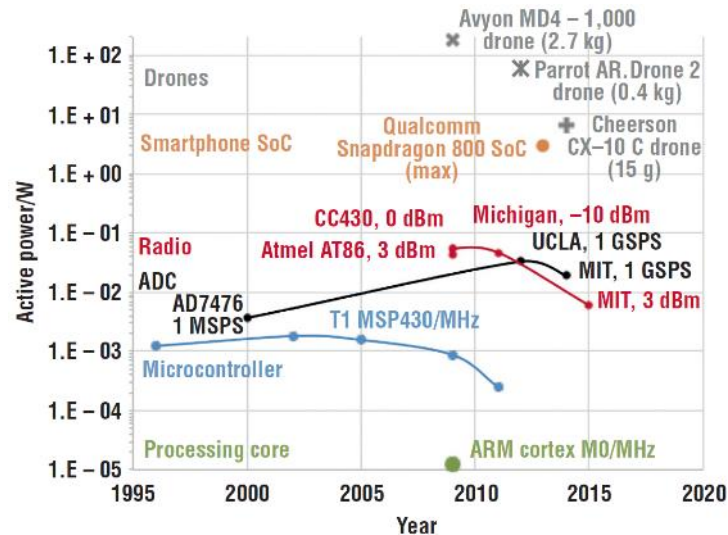
Figure 1.16: Indicative power consumption of various components and systems. The power requirements for most of the devices and and systems have been gradually decreasing over the years [Boyle, et al. [40]].

Further application opportunities of vibration energy harvesters include health monitoring devices and biomedical implants, which would benefit patients by avoiding expensive and risky surgical procedures for battery replacement. In summary, the myriad opportunities for vibration energy harvesting are only emerging and it can be envisaged to grow substantially in the era of the IoT/E.

1.3.3 Challenges in vibration energy harvesting

Despite the exciting opportunities for vibration energy harvesting, there are significant engineering challenges to overcome before widespread adoption of this technique, as discussed below.

- One of the major issues is the wide variability of the nature and frequency range of ambient vibrations. While it is relatively uncomplicated to design energy harvesters for resonant sources with a single dominant frequency, it is extremely difficult to develop devices capable of operating over multiple dominant frequencies or in broadband vibrations. The situation is even more complicated in scenarios where the dominant frequencies may shift with time, ambient temperature and other external conditions. However, it is critical to design and optimize devices for specific applications for efficient and reliable performance.

- Another issue is the lack of integrated batch fabrication processes for most of the reported devices, which is crucial for commercial viability and widespread

adoption of vibration energy harvesting systems. The miniaturization of the energy harvesting devices down to MEMS and micro-scales offer potential solutions to this problem, nevertheless, most of the reported MEMS-scale devices are only semi-integrated to date.

- The miniaturization of the energy harvesting devices introduces the third major challenge – the increase of operational frequency with shrinking dimensions, while most of the ambient energy is available in the lower end of the frequency spectrum. This miniaturization of the state-of-the-art vibration energy harvesters is necessary for effective integration with micro-fabricated sensors and power conditioning modules. Furthermore, reduction in power density is another important issue associated with miniaturization of vibration energy harvesting devices.

1.4 Thesis outline

This thesis is aimed at proposing solutions to some of these issues outlined in the previous section. Chapter 2 provides a detailed overview of the state-of-the-art in vibration energy harvesting using different transduction mechanisms, the incorporation of various mechanical nonlinearities to broaden the operational bandwidth, frequency tuning mechanisms and power management circuitry. The research methodology and techniques used in this thesis are discussed in Chapter 3, which include numerical modelling and simulation techniques, device fabrication and characterization techniques. Chapter 4 introduces a low frequency nonlinear bistable energy harvester, which combines the mechanical impact nonlinearity to broaden the bandwidth even further. Chapter 5 discuss the combined effect of the monostable and bistable nonlinear mechanisms in a single device, and demonstrate the potential to harvest the unique benefits of both over a broad frequency range. A nonlinear silicon MEMS micro-power generator is described in Chapter 6, which also incorporate a magnetic repulsion induced frequency tuning mechanism for post-fabrication frequency adjustability. The Chapter 7 discuss the development of a ultra-dense planar micro-coil for application in micro-power generators, which can potentially increase the harvester power density. A power management module is developed in Chapter 8, which aims to reduce the rectifier loss and improve efficiency of power conditioning. Finally, concluding remarks are presented in Chapter 9, including key contributions and directions for future research.

References

[1]   [Online]. Available: https://www.wikiwand.com/en/Transistor_count

[2]   T. N. Theis and H. S. P. Wong, "The End of Moore's Law: A New Beginning for Information Technology," *Computing in Science & Engineering,* vol. 19, pp. 41-50, 2017.

[3]   R. Landauer, "Dissipation and noise immunity in computation and communication," *Nature,* vol. 335, pp. 779-784, 1988.

[4]   G. Frantz, "Digital signal processor trends," *IEEE Micro,* vol. 20, pp. 52-59, 2000.

[5]   R. Amirtharajah and A. P. Chandrakasan, "Self-powered signal processing using vibration-based power generation," *IEEE Journal of Solid-State Circuits,* vol. 33, pp. 687-695, 1998.

[6]   T. Danova. (2014). *The Internet Of Everything: 2014*   [Online]. Available: http://uk.businessinsider.com/the-internet-of-everything-2014-slide-deck-sai-2014-2?op=1/#

[7]   M. Weiser, R. Gold, and J. S. Brown, "The origins of ubiquitous computing research at PARC in the late 1980s," *IBM Systems Journal,* vol. 38, pp. 693-696, 1999.

[8]   E. Borgia, "The Internet of Things vision: Key features, applications and open issues," *Computer Communications,* vol. 54, pp. 1-31, 12/1/ 2014.

[9]   *Solar   Boat   Regatta*   [Online].   Available: https://cockroach-boat.weebly.com/energy.html

[10]   S. Walker. (2014). *Understanding photovoltaic cells in solar power*   [Online]. Available: http://gbtimes.com/life/understanding-photovoltaic-cells-solar-power

[11]   N. R. E. L. (NREL). (2017). *Best Research-Cell Efficiency*   [Online Chart]. Available: http://www.nrel.gov/pv/assets/images/efficiency-chart.png

[12]   S. Roundy, B. P. Otis, Y.-H. Chee, J. M. Rabaey, and P. Wright, "A 1.9 GHz RF transmit beacon using environmentally scavenged energy," *optimization,* vol. 4, p. 4, 2003.

[13]   X. Jiang, J. Polastre, and D. Culler, "Perpetual environmentally powered sensor networks," presented at the Proceedings of the 4th international symposium on Information processing in sensor networks, Los Angeles, California, 2005.

[14]   P. Dutta, J. Hui, J. Jeong, S. Kim, C. Sharp, J. Taneja*, et al.*, "Trio: enabling sustainable and scalable outdoor wireless sensor network deployments," in *2006 5th International Conference on Information Processing in Sensor Networks*, 2006, pp. 407-415.

[15]   A. Barnett, D. Kirkpatrick, C. Honsberg, D. Moore, M. Wanlass, K. Emergy*, et al.*, "Milestones toward 50% efficient solar cell modules," DTIC Document 2007.

[16]   G. J. Snyder and E. S. Toberer, "Complex thermoelectric materials," *Nat Mater,* vol. 7, pp. 105-114, 2008.

[17]   S. Bush. *Thermoelectric generators and interface PCBs*   [Online]. Available: https://www.electronicsweekly.com/news/products/power-supplies/thermoelectric-generators-interface-pcbs-2017-04/

[18]   X. Zhang and L.-D. Zhao, "Thermoelectric materials: Energy conversion between heat and electricity," *Journal of Materiomics,* vol. 1, pp. 92-105, 6// 2015.

[19]   D. Crane, J. LaGrandeur, V. Jovovic, M. Ranalli, M. Adldinger, E. Poliquin*, et al.*, "TEG On-Vehicle Performance and Model Validation and What It Means for Further TEG Development," *Journal of Electronic Materials,* vol. 42, pp. 1582-1591, 2013.

[20]   V. Leonov, P. Fiorini, S. Sedky, T. Torfs, and C. V. Hoof, "Thermoelectric MEMS generators as a power supply for a body area network," in *The 13th International Conference on Solid-State Sensors, Actuators and Microsystems, 2005. Digest of Technical Papers. TRANSDUCERS '05.*, 2005, pp. 291-294 Vol. 1.

[21]   A. J. Minnich, M. S. Dresselhaus, Z. F. Ren, and G. Chen, "Bulk nanostructured thermoelectric materials: current research and future prospects," *Energy & Environmental Science,* vol. 2, pp. 466-479, 2009.

[22]   Y. Zhao, J. S. Dyck, B. M. Hernandez, and C. Burda, "Enhancing Thermoelectric Performance of Ternary Nanocrystals through Adjusting Carrier Concentration," *Journal of the American Chemical Society,* vol. 132, pp. 4982-4983, 2010/04/14 2010.

[23]   W. C. Brown, "The History of Power Transmission by Radio Waves," *IEEE Transactions on Microwave Theory and Techniques,* vol. 32, pp. 1230-1242, 1984.

[24]   W. Lumpkins, "Nikola Tesla's Dream Realized: Wireless power energy harvesting," *IEEE Consumer Electronics Magazine,* vol. 3, pp. 39-42, 2014.

[25]   S. Kim, R. Vyas, J. Bito, K. Niotaki, A. Collado, A. Georgiadis*, et al.*, "Ambient RF Energy-Harvesting Technologies for Self-Sustainable Standalone Wireless Sensor Platforms," *Proceedings of the IEEE,* vol. 102, pp. 1649-1666, 2014.

[26]   A. Dolgov, R. Zane, and Z. Popovic, "Power Management System for Online Low Power RF Energy Harvesting Optimization," *IEEE Transactions on Circuits and Systems I: Regular Papers,* vol. 57, pp. 1802-1811, 2010.

[27]   M. Piñuela, P. D. Mitcheson, and S. Lucyszyn, "Ambient RF Energy Harvesting in Urban and Semi-Urban Environments," *IEEE Transactions on Microwave Theory and Techniques,* vol. 61, pp. 2715-2726, 2013.

[28]   D. Masotti, A. Costanzo, M. D. Prete, and V. Rizzoli, "Genetic-based design of a tetra-band high-efficiency radio-frequency energy harvesting system," *IET Microwaves, Antennas & Propagation,* vol. 7, pp. 1254-1263, 2013.

[29]   T. Ajmal, V. Dyo, B. Allen, D. Jazani, and I. Ivanov, "Design and optimisation of compact RF energy harvesting device for smart applications," *Electronics Letters,* vol. 50, pp. 111-113, 2014.

[30]   S. Boisseau, G. Despesse, and B. A. Seddik, "Nonlinear H-Shaped Springs to Improve Efficiency of Vibration Energy Harvesters," *Journal of Applied Mechanics,* vol. 80, pp. 061013-061013-9, 2013.

[31]   M. Stewart. Vibrational energy harvesting. Available: http://www.npl.co.uk/science-technology/functional-materials/research/vibrational-energy-harvesting.

[32]   R. R. Gatti, "Spatially Varying Multi Degree of Freedom Electromagnetic Energy Harvesting," PhD Dissertation, School of Civil and Mechanical Engineering, Curtin University, 2013.

[33]   C. B. Williams and R. B. Yates, "Analysis of a micro-electric generator for microsystems," *Sensors and Actuators a-Physical,* vol. 52, pp. 8 - 11, 1996.

[34]   P. D. Mitcheson, T. C. Green, E. M. Yeatman, and A. S. Holmes, "Architectures for vibration-driven micropower generators," *Journal of Microelectromechanical Systems,* vol. 13, pp. 429-440, 2004.

[35]   S. Roundy and P. K. Wright, "A piezoelectric vibration based generator for wireless electronics," *Smart Materials and Structures,* vol. 13, p. 1131, 2004.

[36]   R. Torah, P. Glynne-Jones, M. Tudor, T. O. Donnell, S. Roy, and S. Beeby, "Self-powered autonomous wireless sensor node using vibration energy harvesting," *Measurement Science and Technology,* vol. 19, p. 125202, 2008.

[37]   F. Cottone, H. Vocca, and L. Gammaitoni, "Nonlinear energy harvesting," *Physical Review Letters,* vol. 102, p. 080601, 2009.

[38]   P. Basset, D. Galayko, F. Cottone, R. Guillemet, E. Blokhina, F. Marty*, et al.*, "Electrostatic vibration energy harvester with combined effect of electrical nonlinearities and mechanical impact," *Journal of Micromechanics and Microengineering,* vol. 24, p. 035001, 2014.

[39]   P. D. Mitcheson, E. M. Yeatman, G. K. Rao, A. S. Holmes, and T. C. Green, "Energy Harvesting From Human and Machine Motion for Wireless Electronic Devices," *Proceedings of the IEEE,* vol. 96, pp. 1457-1486, 2008.

[40]   D. E. Boyle, M. E. Kiziroglou, P. D. Mitcheson, and E. M. Yeatman, "Energy Provision and Storage for Pervasive Computing," *IEEE Pervasive Computing,* vol. 15, pp. 28-35, 2016.

2 LITERATURE REVIEW ON VIBRATION ENERGY HARVESTING

This chapter gives an overview on the research in the area of vibration energy harvesting. Over the last few years, a great deal of research work has been accomplished by various research groups. The field of vibration energy harvesting encompasses research on transduction mechanisms, device topologies, materials development, power management systems and applications. Initially the most of the developed prototypes were based on linear oscillators coupled with electromechanical transduction systems, which were capable of harvesting energy within a narrow frequency bandwidth. In order to broaden the operational frequency range, some researchers then incorporated different frequency tuning mechanisms into the vibration energy harvesting systems. However, the most of the tuning mechanisms had to be powered externally, and/or affected the energy density of the device adversely. Therefore, the idea of incorporating mechanical nonlinearity was proposed by some research groups, which enabled relatively broadband hysteretic frequency response. The different types of nonlinear mechanisms were investigated and combined with different transduction mechanisms to produce electrical energy from diverse vibration sources. The developments in VEH devices eventually led to research in power management systems and potential applications of such systems were explored.

2.1 Principle of vibration energy harvesting

The working principle of vibration energy harvesting devices is based on the transduction of mechanical vibrations into usable electrical energy. The existing electromechanical transduction mechanism can be broadly classified as electromagnetic, piezoelectric, electrostatic and triboelectric transductions. There are certain benefits and drawbacks

associated with the use of each of these transduction methods for vibration energy harvesting. This section describes the significant works done in implementing each of the transduction methods to vibration energy harvesting, and provides a comparative study.
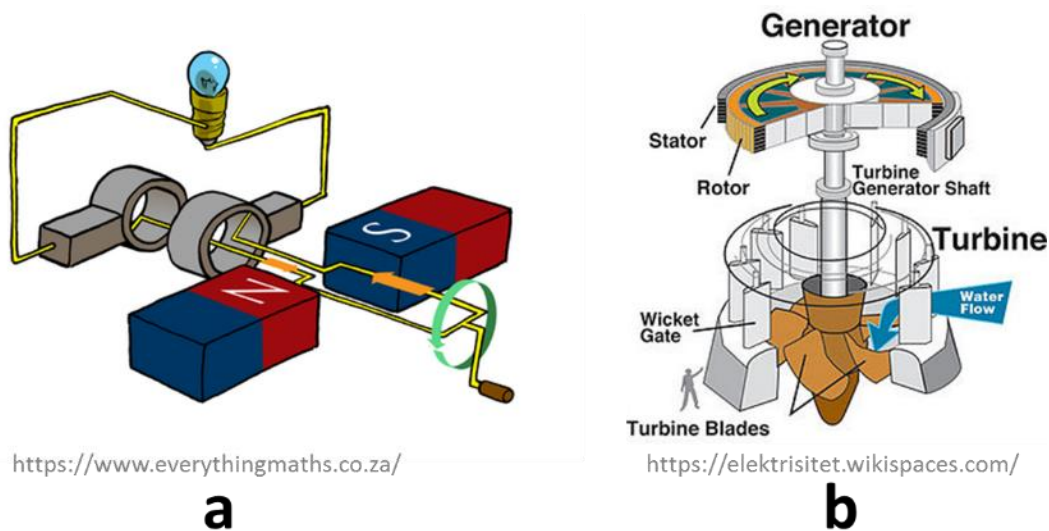
Figure 2.1: (a) Schematic diagram of a simple generator based on Faraday's law. (b) Mechanism of a hydroelectric generator.

2.1.1 Electromagnetic transduction

The principle of electromagnetic transduction emerges from the Faraday's law of electromagnetic transduction, which states that the electromotive force around a closed path is equal to the negative of the time rate of change of magnetic flux enclosed by the path. In essence, the electric current induced in a particular closed conducting loop (e.g. a coil) due to relative motion between the closed conducting loop (a coil) and a magnet is proportional to the gradient of the magnetic flux linkage between the coil and the magnet [Figure 2.1(a)]. This principle has been widely exploited in electric dynamos which can be scaled from very small (such as the ones used in bikes) to very large (such as industrial dynamo used in hydro and thermal power plants) sizes [Figure 2.1(b)]. However, with scaling down further to the MEMS or micro-scale, the operational efficiency of such dynamos drops drastically. This is due to the fact that the magnetic field strength scales with the volume of the permanent magnet, and the number of turns in planar spiral micro-coils scales with the available surface area [Beeby and O'Donnell [1]]. The most widely implemented electromagnetic transduction based generators often use the rotational mechanisms between a rotor and a stator to establish relative motion between magnets and coils [Cardwell [2]].
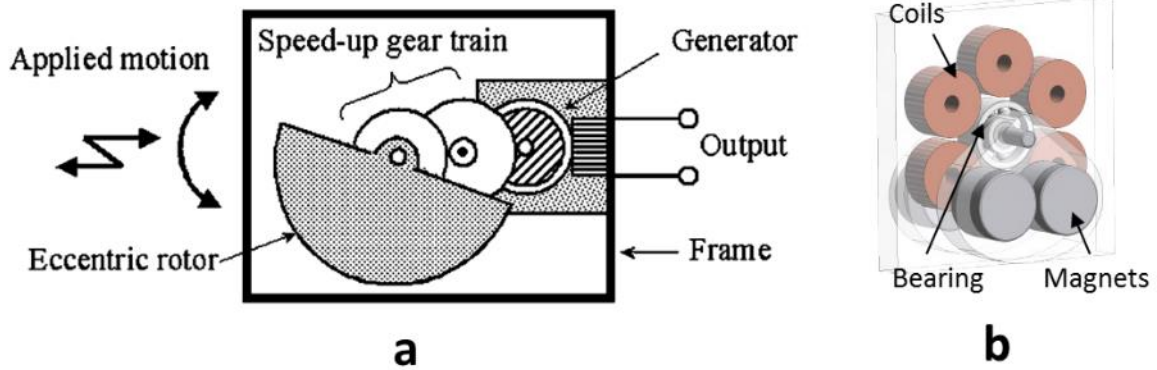
Figure 2.2: Electromagnetic energy harvester after (a) Seiko Instruments Inc. and (b) Spreemann, et al. [3].

The attempts towards miniaturization of rotational electromagnetic generators have been driven by the ever increasing efficiency of electronic devices and circuits and their applications, which ushered in the possibility of the devices being powered by energy harvested from the ambient sources. One of the notable pioneers in the field of commercial application of rotational electromagnetic micro-generators is the SEIKO Watch Corporation, who exploited such mechanisms in a wristwatch powered by harvesting the kinetic energy from the movements of the wearer [Hayakawa [4]]. Further investigations involving rotational or cylindrical motion in micro-energy harvesting using electromagnetic transductions includes the works of Sasaki, et al. [5] and Spreemann, et al. [3] [Figure 2.2]. One of the major benefits of incorporating rotational motion in energy harvesters is the ability to harness electricity from low frequency non-resonant vibration [3]. The device reported in [3] is capable of generating 0.4 – 3 mW power under a 100 μm amplitude vibration.

While the rotary motion based electromagnetic generators has been in use for over a century, linear motion based electromagnetic generators only became a focus of research in the 1990s. The earliest vibration energy harvesters incorporating electromagnetic transduction in a translational oscillatory motion were reported by Williams and Yates [6]. Following their pioneering work, several variations of the electromagnetic transducer for harvesting mechanical vibration energy have been reported. The basic construction of electromagnetic vibration energy harvesters can be broadly classified based on the electromagnetic coupling architecture, which is determined by the specific arrangements of the magnets and coils.
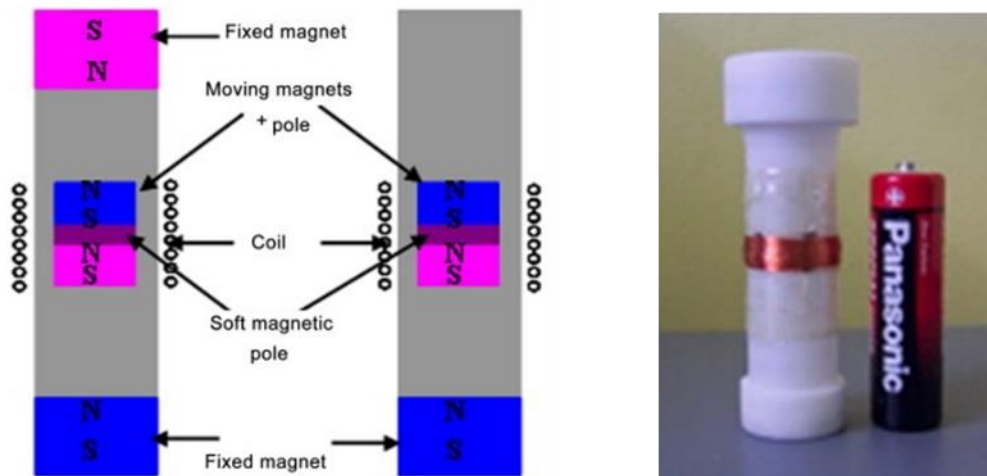
Figure 2.3: Magnet through coil arrangement of electromagnetic vibration energy harvester [Saha, et al. [7]]

One of the most widely exploited coupling architecture is based on cylindrical shaped magnets and coils, where either the magnet or the coil is allowed to oscillate under vibration. Energy harvesting devices based on such architecture were developed by Saha, et al. [7]. One of the prototypes comprised a transducing magnet suspended within a wire-wound coil by the repulsive interaction with a pair of fixed magnets [Figure 2.3]. The device produced an average load power of 950 μW during walking and 2.5 mW during slow running, while the device was placed inside a rucksack carried by a person [Figure 2.3]. In a more advanced version of this architecture, von Büren and Tröster [8] used a cylindrical array of permanent magnets and soft magnetic spacers such that alternating magnetic flux lines passed through an array of concentric cylindrical coils [Figure 2.4]. Depending on its location on the human body, the device generated 2 – 25 μW power from walking movements.

Another very common magnet-coil coupling architecture involves a suspended magnet (or a suspended coil) oscillating towards the static coil (or a static magnet), without travelling through. This architecture is often used in MEMS or micro-fabricated devices due to the inherently simpler geometry. Wang, et al. [9] applied this topology in a device with electroplated copper planar spring, planar micro-coil and discrete NdFeB magnet. The device generated 0.61 μW at a peak to peak voltage of 18 mV for an excitation of 1.5g at a frequency of 55 Hz.
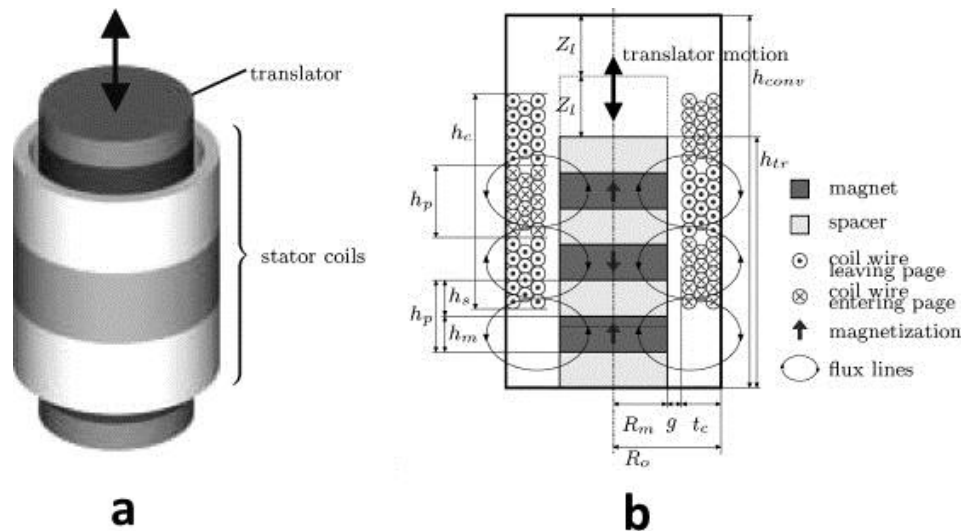
Figure 2.4: (a) Concentric cylindrical magnets-in-coil architecture by von Büren and Tröster [8], (b) The magnet assembly consists of alternating permanent magnet-soft magnetic spacer arrangement to propagate magnetic fluxlines through the stator coil.

A modified version of this architecture was used by Yang, et al. [10] where an array of 3 magnets was suspended from a beam above an array of 3 spiral planar coils [Figure 2.5]. The device produced multi-frequency response and generated 0.58 µW average powers at 14 µm vibrational amplitude. Yuan, et al. [11] took an integrated approach to realize this architecture where they used electrodeposited CoNiMnP magnet arrays and copper coils with a copper spring structure. The entire fabrication process is CMOS compatible and does not require manual assembly. However, the device generated 0.01 mV (< 1 nW power), which is too small to realistically power any electronic device.
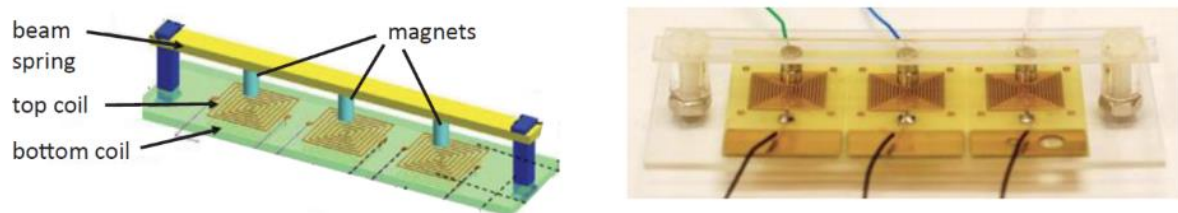
Figure 2.5: Multiple frequency vibration energy harvester [Yang, et al. [10]].

Another variation of this architecture was developed by Hoffmann, et al. [12] using flexible polyimide film as the resonator structure. At an applied vibrational excitation of ~10g, the device generated peak power up to 5 µW at 70 mV. Further micro-scale iterations of this architecture has been developed and investigated by Pan, et al. [13] [Figure 2.6], Roundy and Takahashi [14], and Han, et al. [15].
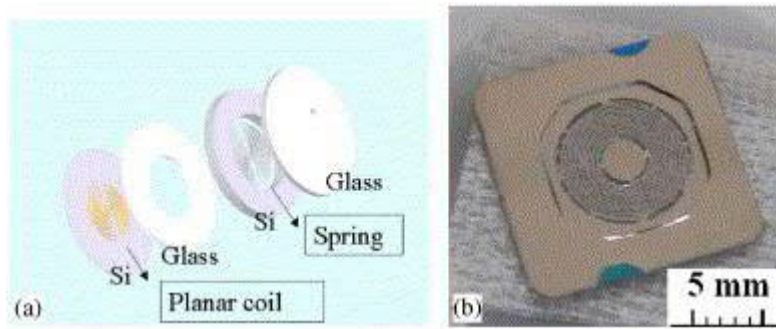
Figure 2.6: Micro-fabricated silicon energy harvester using sputtered FePt micro-magnet [Pan, et al. [13]].

The magnet and coil arrangements presented so far were such that the direction of oscillation is along the symmetry axis of the coil. On the other hand, architectures with the oscillation direction orthogonal to the coil symmetry axis have also been extensively studied by various research groups. Kulkarni, et al. [16] developed such an architecture based on silicon spring and moving coil, which produced 104 nW at an excitation of 3.9 m/s^2 [Figure 2.7(a)]. A different device based on the same architecture was developed by the same group using discrete components such as wire-wound copper micro-coil, bulk NdFeB magnets and beryllium-copper cantilever [Beeby, et al. [17]]. The device produced 46 μW power with a vibrational excitation of 0.6 m/s^2 at 52 Hz frequency [Figure 2.7(b)]. Galchev, et al. [18] improved upon this design with a multiple oscillating mass architecture that was capable of harvesting non-harmonic and low frequency vibrations. The device generated 5.9 μW power at 1g acceleration over a 20 Hz frequency range. A larger and significantly modified version of this architecture using a rotary suspension mechanism was developed by Hadas, et al. [19], which produced 0.26 mW power at 0.5g excitation. An useful and interesting extension of this architecture has been developed by Zhu, et al. [20], where the magnets are assembled in a Halbach array. Such arrangements have been shown to be able to significantly enhance the magnetic flux gradient in the desired direction, and increase the harvested energy.
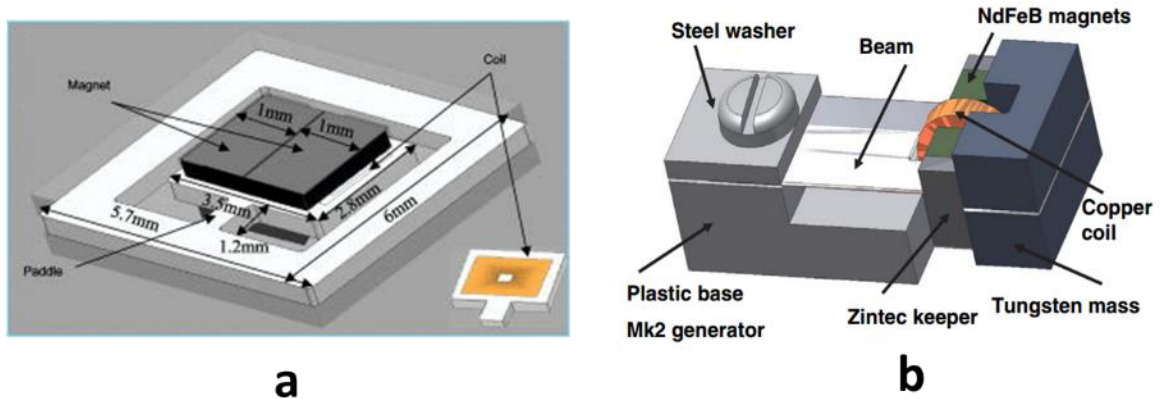
Figure 2.7: Micro-power harvesters after (a) Kulkarni, et al. [16] and (b) Beeby, et al. [17]

2.1.2 Piezoelectric transduction

Piezoelectricity represents the particular property of certain crystalline materials (such as Rochelle salt, quartz, barium titanate etc.), which produce electricity under applied mechanical stress, or vice versa. This effect was first demonstrated by brothers Pierre Curie and Jacques Curie as early as 1880. The conversion from mechanically induced stress to electrical energy occurs because of the existence of local charge separation or molecular dipoles in piezoelectric materials. On application of external mechanical force to the material, it results in a deformation in the dipole structure and imbalance in local charge, which can be harvested in the form of electricity. In order to convert mechanical vibration into electrical energy, piezoelectric materials are either deposited or bonded to a structural body (such as metal or polymer cantilever or diaphragm) or directly used as the transducer and structural body simultaneously (e.g. PVDF diaphragm). One of the reported advantages of using piezoelectricity in vibration energy harvesting is that it has higher energy density for most practical applications [Roundy and Wright [21]; Roundy, et al. [22]]. Another major advantage of the piezoelectric materials is the inherent capability to directly convert mechanical energy into electrical energy without any further external input, which allows for much simpler device architecture compared to other transduction mechanisms. This benefit become more obvious with scaling down to micro-scale, as it has been shown by Anthony, et al. [23]. Under normal circumstances, the charge produced in most piezoelectric materials is proportional to the applied stress, which necessitates the design optimization in the energy harvester such that stress is maximized under a certain mechanical load.
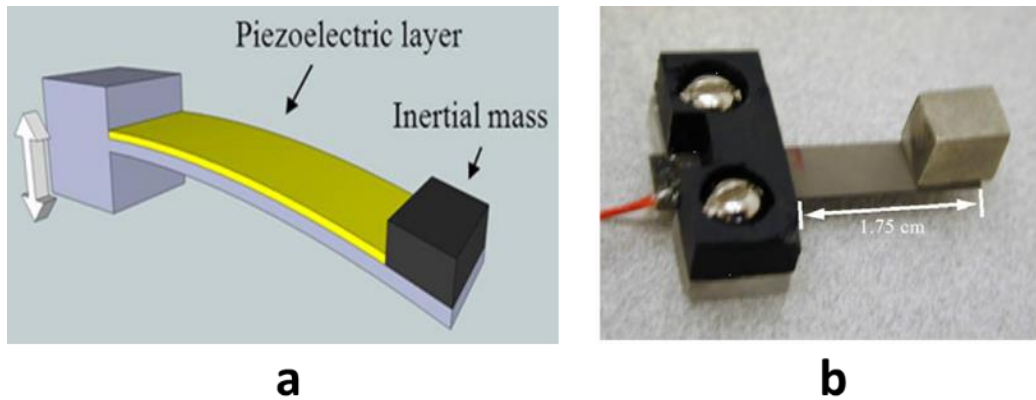
Figure 2.8: (a) Generic structure of piezoelectric vibration energy harvester, (b) Piezoelectric micro-power generator by Roundy and Wright [21]

Since the simple cantilever-shaped architecture creates the highest average strain for a given input force, it is one of the most common structures used in vibration energy harvesting [Roundy and Wright [21]]. Figure 2.8(b) shows a prototype piezoelectric energy harvester (PEH) where the authors bonded two lead zirconate titanate (PZT) layers on either sides of a rectangular steel beam and attached a proof mass at the tip. The proof mass assists in coupling the mechanical energy from external vibration to the piezoelectric patches and converts the alternating bending strains into electrical energy. Roundy and Wright [21] harvested 375 µW from a vibrational acceleration of 0.25g, and used that to power a 1.9 GHz radio transmitter [Figure 2.8(b)]. The idea of using the piezoelectric transduction to power implantable medical devices goes back to at least the 1960s, when Lewin, et al. [24] proposed to power pacemakers by harvesting the expansion and contraction of the aorta during systole/ diastole cycles. Further investigation on this concept was carried out by Häsler, et al. [25], where they developed an implantable energy harvester to produce electricity from the relative motion of ribs during respiratory cycles. A different approach of powering implanted medical devices or portable electronics was proposed by Shenck and Paradiso [26], where they used piezoelectric bimorphs and PVDF stave in soles of shoes [Figure 2.9]. Combined to a power management circuit, the device produced 1.3 mW average power continuously from a walking stride frequency of 0.8 Hz.
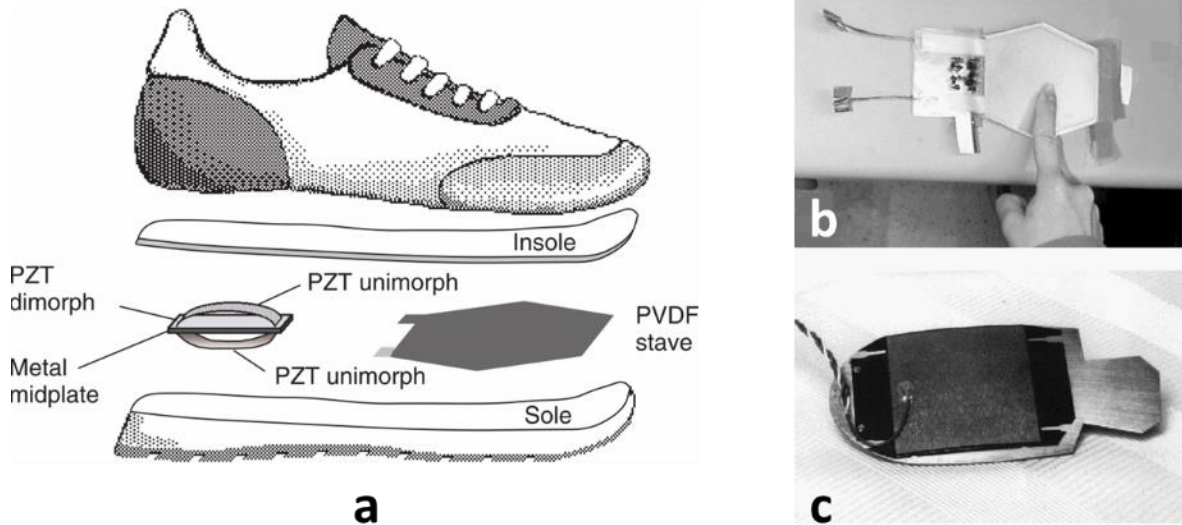
Figure 2.9: (a) Piezoelectric energy harvester mounted in a shoe [Shenck and Paradiso [26]], (b) the PVDF in-sole stave and (c) the PZT bimorph heel insert.

Some variations of the simple cantilever based piezoelectric energy harvester, intended for increased stress and thereby increased power output, have been developed. Glynne-Jones, et al. [27] designed and characterized a device consisting of a tapered steel beam with trapezoidal-shaped PZT layer on both sides. The tapered shape of the cantilever (wider at the fixed end, narrow at the free end) allows for more piezoelectric material at the fixed end, which is also the region with higher flexural stress, and results in higher power output. At a tip displacement of 0.8 mm and vibrational frequency of 80 Hz, the device produced 3 μW. A similar trapezoidal cantilever beam structure was developed by Reilly, et al. [28], which operated a wireless sensor node (WSN) and radio transmitter with 0.2% duty cycle. Mehraeen, et al. [29] also used a tapered cantilever structure with PZT transducer and coupled it to a high voltage based compensation scheme (SSHI or Synchronized Switch Harvesting on Inductor) to harvest 1.4 mW power at a vibration amplitude of 4 mm [Figure 2.10(a)]. Various iterations of the piezoelectric cantilever based energy harvester has been extensively investigated by several groups such as, Adhikari, et al. [30], Cao, et al. [31] and Becker, et al. [32].

While cantilever based designs are the most popular choice due to the relatively simple implementation, they are not optimal for direct force or pressure mode operations. Kim, et al. [33] proposed and investigated a diaphragm structure to harvest energy from pressure. Their study revealed the stress distribution in a clamped diaphragm and also proposed a scheme based on re-polling to maximize the harvested energy. Detailed analytical models

and experimental verification of such clamped circular diaphragm architecture was presented in later studies by Kim, et al. [34], Mo, et al. [35] and [36]. While these piezoelectric diaphragm based structures have shown promising results for implementation in pressure mode harvesting, they have also been successfully tested in regular vibrations as well [Minazara, et al. [37], Chen, et al. [38]]. However, the diaphragm based devices are also reported to have significantly higher resonance frequency in comparison to their cantilever based counterpart [37].
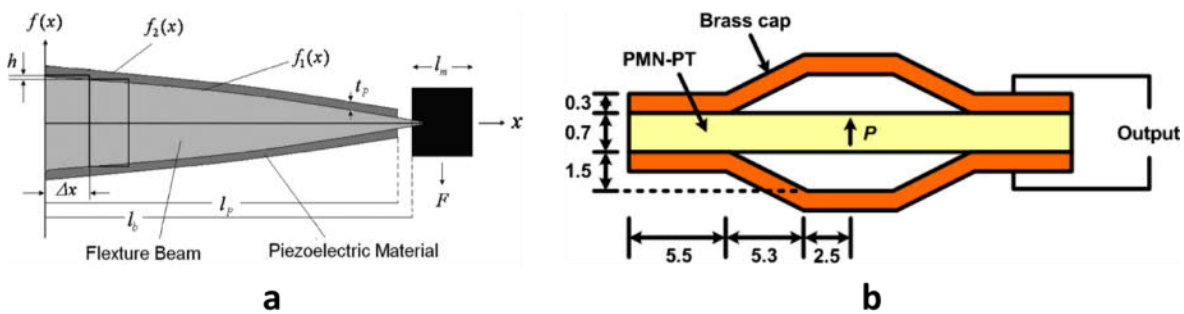
Figure 2.10: Tapered cantilever PZT harvester [Mehraeen, et al. [29]], (b) Piezoelectric cymbal energy harvester [Kim, et al. [39]]

Another interesting variation of the diaphragm based piezoelectric harvesters has been developed by using stack type architecture, which is often coupled to a cymbal mechanical transducer [Kim, et al. [39]]. The cymbal energy harvester in [39] used a PZT disc and reported 39 mW output power at 7.8 N sinusoidal excitation [Figure 2.10(b)]. In a rectangular cymbal type architecture, Ren, et al. [40] used piezoelectric PMN-PT material for harvesting 14 mW power at 500 Hz frequency with a 17 g proof mass. A mechanical force amplifier coupled to a 130 layer PZT stack in the shape of an energy harvester was developed by Feenstra, et al. [41]. Mounted onto a backpack with 220 N load, each of the piezoelectric stacks produced 0.4 mW power. In a similar 300-layer PZT stack used for energy harvesting, Xu, et al. [42] generated 15 mW at 1767 Hz frequency in resonance mode.

The successful implementation of piezoelectric energy harvesting principles in several meso-scale prototypes encouraged researchers to scale the devices down to micro or MEMS scale, which is also considered to make the integration with self-powered monolithic sensor systems plausible. Similar to most of the reported meso-scale devices, PZT and aluminium nitride (AlN) are some of the most commonly used piezoelectric materials in MEMS scale devices. However, scaling down adversely affects the oscillating

inertial mass, area of the piezoelectric material and overall device volume, which ultimately result in reduced output power level. Another notable feature of scaled down MEMS-sized devices is that the piezoelectric layer is usually deposited or bonded on one side of the vibrating cantilever or diaphragm, which emerges from the requirement of reduced complexity. This constraint often leads designers to an interesting choice in terms of coupling mode, electrode configuration and poling direction of the piezoelectric material. There are two practical piezoelectric coupling modes: the d_{31} mode and the d_{33} mode [Figure 2.11(a)]. In the d_{31} mode the applied stress is perpendicular to the piezoelectric poling direction. On the other hand, the applied stress is in the same direction as the piezoelectric poling direction in the d_{33} coupling mode. In a comparative study involving the two coupling modes and three different piezoelectric materials, PZT, PVDF and PZN-PT (lead zinc niobate – lead titanate), Baker, et al. [43] have shown that the d_{33} mode has higher coupling coefficient than the d_{31} mode. It has also been shown that in order to effectively use the d_{33} coupling mode for energy harvesting, the electrodes should be arranged in interdigitated fashion. In addition the utilization of interdigitated electrodes in d_{33} mode allows the output voltage to be determined by the finger spacing, as opposed to the piezoelectric material thickness [Kwon, et al. [44]].
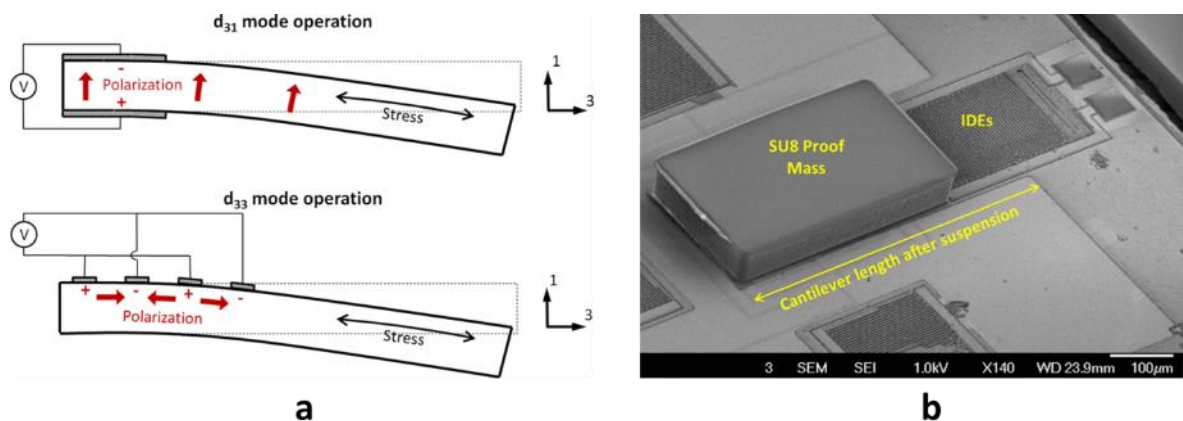
Figure 2.11: (a) The d_{31} and d_{33} coupling modes of piezoelectric energy harvester. The dual electrode arrangement is suitable to implement the d_{31} mode, while the interdigitated electrodes (IDEs) are appropriate for the d_{33} mode. (b) MEMS piezoelectric energy harvester using IDEs [Jeon, et al. [45]].

The d_{33} coupling mode was utilized by Jeon, et al. [45] in a MEMS scale PZT based cantilever device that produced 1 μW power under 1.1g acceleration at a frequency of 13.9 kHz [Figure 2.11(b)]. In most of the micro-scale PZT energy harvester devices, the PZT layer is deposited by the sol-gel method. This method involves the spin coating of a

precursor solution on a substrate, which is followed by evaporation of solvent and thermal annealing for crystallization. Typical thickness of sol-gel PZT layers is ~ 0.1 μm per coating [Fang, et al. [46]], which makes deposition of PZT layers thicker than a few microns difficult. Additionally, the thin film PZT developed by sol-gel process have been shown to demonstrate significantly lower electromechanical coupling coefficients compared to the bulk ceramic material. These limitations provoked Aktakka, et al. [47] to investigate the process of bonding bulk PZT on SOI substrate, followed by mechanical thinning of the PZT to achieve MEMS scale energy harvester [Figure 2.12]. The device produced 205 μW power at a vibrational acceleration of 1.5g over a half power bandwidth of 14.1 Hz.
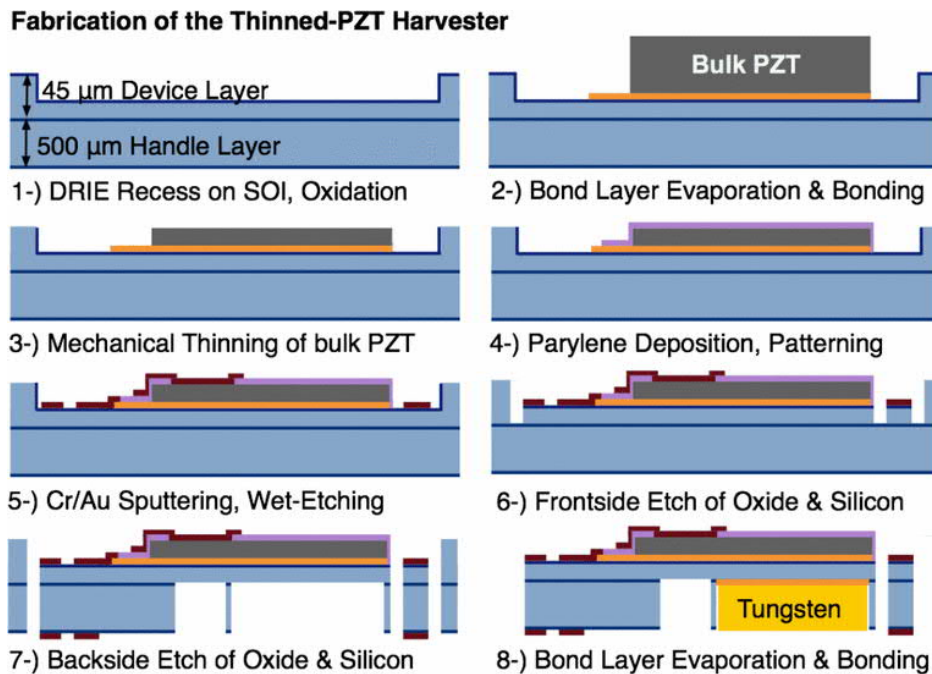
Figure 2.12: Process steps for thinned PZT harvester [Aktakka, et al. [47]]

As mentioned before, aluminium nitride (AlN) is another piezoelectric material used in MEMS energy harvesters, which offers some distinct advantages over PZT. In the context of compatibility to the well-established CMOS process flow, the most useful feature of AlN is that it can be easily deposited by sputtering and grown in the [0001] direction, which exhibit piezoelectricity [Defosseux, et al. [48]]. Therefore, the need for post-deposition external poling is eliminated in sputter-deposited AlN films. Furthermore, because of its lower dielectric constant compared to PZT, AlN has a higher piezoelectric voltage constant, which is an important advantage for coupling with diode rectified power processing circuits. Marzencki, et al. [49] used a AlN deposited cantilever type energy

harvester to couple with a CMOS power management circuit in the form of a system on a package (SoP) [Figure 2.13(a)]. The device produced 0.8 µW load power at an acceleration of 2g. The effect of packaging on the thin film based MEMS scale piezoelectric energy harvesters has been investigated by Elfrink, et al. [50]. They demonstrated that with vacuum packaging the air damping of vibrating cantilevers can be significantly mitigated, and the harvested power can be enhanced by more than 100 times [Figure 2.13(b) and (c)].
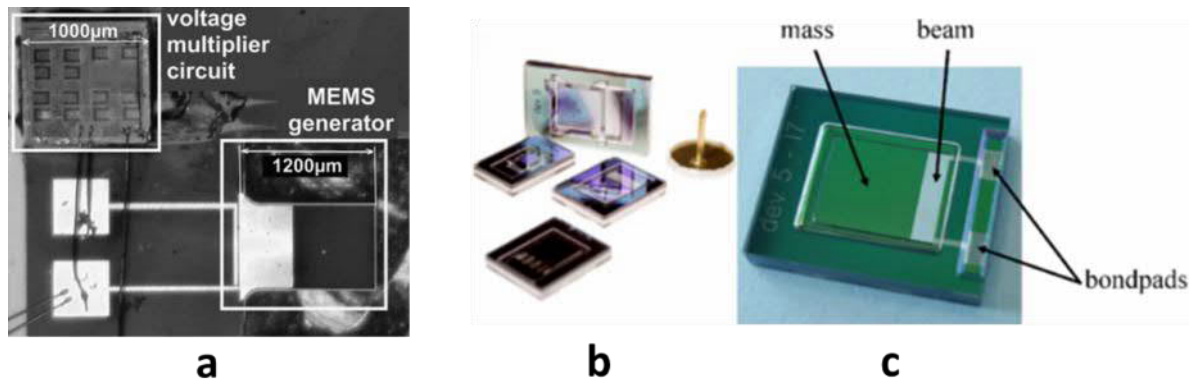
Figure 2.13: (a) System on package (SoP) combining MEMS generator and power management circuit [Marzencki, et al. [49]], (b) vacuum packaged vibration energy harvester and (c) close-up view of the packaged device [Elfrink, et al. [50]]

The quest to develop miniaturized piezoelectric energy harvesting devices also motivated research into piezoelectric nanowire based energy harvesters recently. In 2006, Wang and Song [51] and Song, et al. [52] reported the first energy harvesting devices based on piezoelectric ZnO nanowires [Figure 2.14]. They used an AFM (atomic force microscope) probe to apply force on a ZnO nanowire through contact mode scan. In a later work [Gao, et al. [53]], the same group demonstrated that the ZnO nanowires can also be grown on flexible plastic substrates, and when coupled to conductive polymer films, can result in a flexible energy harvester. In order to excite the nanowires using ultrasound wave, Wang, et al. [54] replaced the conductive AFM probe with a zig-zag shaped top electrode, and generated a DC power output of 1 pW from 2 mm^2 active area. Taking the piezoelectric nanowire based micro-power generators to the application regime Hu, et al. [55] demonstrated that the harvested electrical energy could be used to power sensor nodes with wireless transmission. Further investigation on application of such ZnO nanowire based devices have been successfully used in rotating tires for self-powered pressure or speed sensor [Hu, et al. [56], Lin, et al. [57]]. Due to these recent developments in terms of scientific breakthrough and potential applications, nanowire based piezoelectric energy

harvesters have seen a surge in research interest lately.
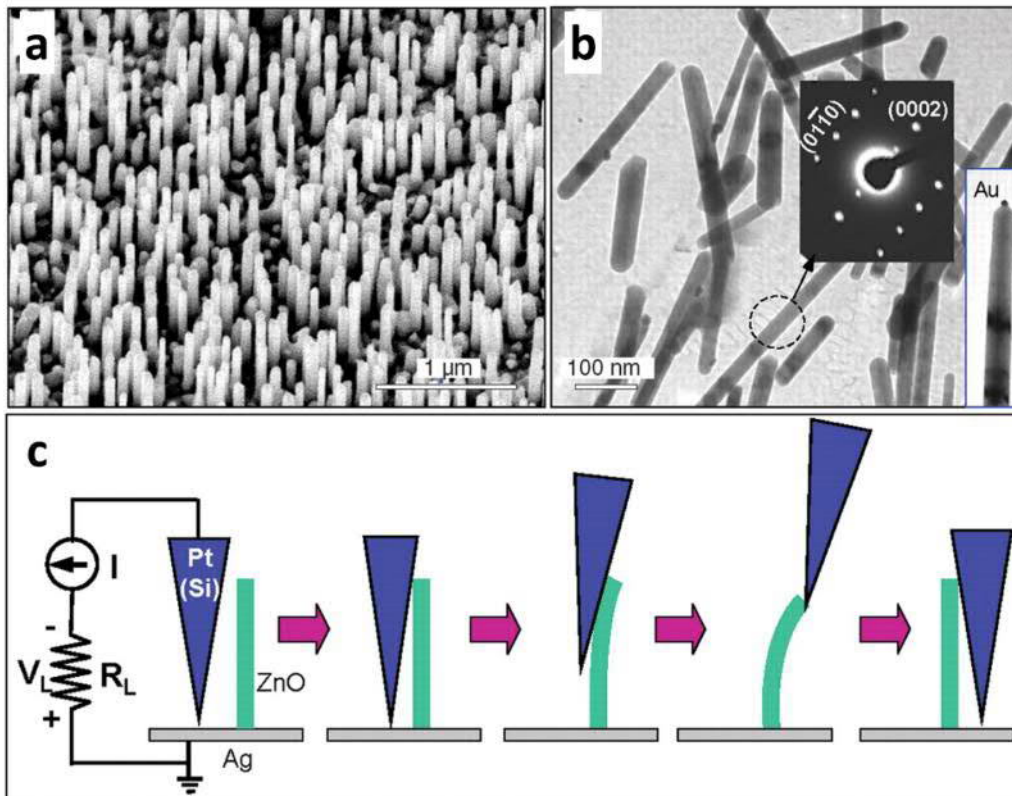
Figure 2.14: (a) SEM image of ZnO nanowires grown on Al_2O_3 substrate. (b) TEM images of ZnO nanowires, showing the typical structure of the nanowire. (c) Experimental setup and procedures for generating electricity by deforming a piezoelectric ZnO nanowire with a conductive AFM probe [Wang and Song [51]].

2.1.3 Electrostatic transduction

The electrostatic transduction works on the principle of exchange of electric charge between two conducting plates separated by a gap (filled with vacuum, air or any other dielectric material). Effectively, the relative movement between the conductive plates creates a variation in the capacitance between the plates, leading to exchange of charge through an external circuit or device [Figure 2.15(a)]. The electrostatic energy harvesting systems developed so far can be broadly classified into (i) electret-free electrostatic harvesters and (ii) electret-based electrostatic harvesters.

Electret-free electrostatic converters use an active electronic circuit to replenish the charge cycle, whereas electret-based harvesters are capable of directly converting mechanical energy into electricity. The advantage of electrostatic energy harvesters over electromagnetic or piezoelectric transduction is the potential to easily integrate into the

CMOS process flow, as opposed to electromagnetic (requires magnet, coil; complex architecture) and piezoelectric (requires deposition of exotic materials) transductions. Extensive review of electrostatic transduction based energy harvesters has been published by Boisseau, et al. [58] and more recently, by Khan and Qadir [59]. A low frequency meso-scale electret-free energy harvester was proposed by Mitcheson, et al. [60]. The device was fabricated on a quartz base plate with a polyimide membrane, which supported a gold proof mass suspended between the silicon top plate and the quartz base plate [Figure 2.15(b)]. The device was pre-charged to 26 V, which generated 24 µW power at a frequency of 10 Hz.
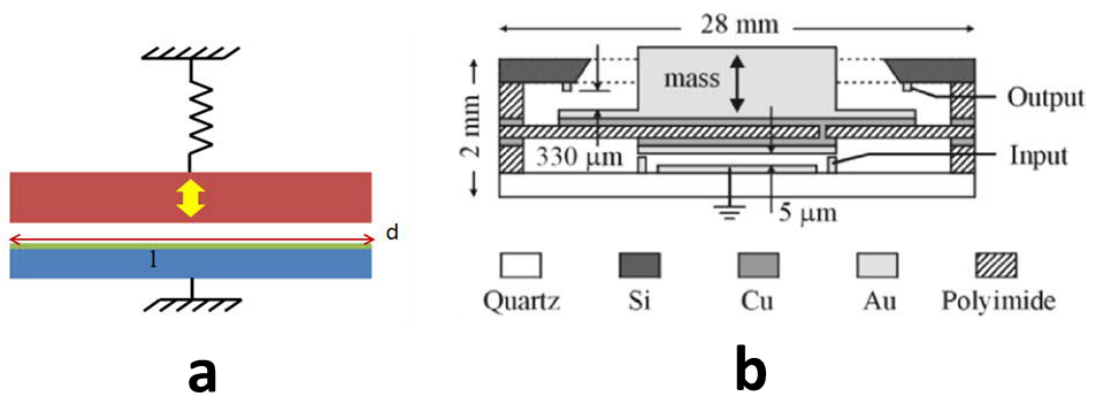
Figure 2.15: (a) Electrostatic transduction method, (b) electret-free generator by Mitcheson, et al. [60].

An electret-free low frequency (< 100 Hz) vibration energy harvester fabricated using silicon MEMS process was developed by Basrour, et al. [61]. At a vibrational acceleration of 9.4g, the device generated 70 µW power with a resonant frequency of 50 Hz. Another iteration of the electret-free electrostatic energy harvester has been reported by Basset, et al. [62], where the authors attempted to harvest energy from broadband vibrations. They developed a device with a movable mass supported by four serpentine beams. Mechanical stoppers were used between the frame and the oscillating mass to prevent short circuit between gap-closing interdigitated comb electrodes. With a continuously supplied pre-charge voltage of 30 V, the device generated 2.2 µW at 1g acceleration. Hoffmann, et al. [63] developed an electret-free generator with electrodes of triangular cross-section, and they reported that the tip angle of the isosceles triangular shaped electrodes was an important design parameter which affected the performance of the device to great extent. The triangular shaped electrodes allowed for larger change in capacitance in comparison to conventional area-overlap and gap-closing type architecture. For a device with an optimal

angle of 5.71°, 0.45 μW power was generated under a constant bias voltage of 15 V at an acceleration of 2g. A novel concept of liquid based electret-free electrostatic generator was proposed by Choi, et al. [64], who developed the generator to harvest low frequency human motion. A conducting liquid was enclosed between two electrodes, and the top electrode was insulated from the conducting liquid to prevent direct contact. In response to human motion, the conducting liquid moved inside the enclosure, which resulted variation in capacitance and produced electrical energy. The device generated 35 μW power as it was excited by vibration produced during a human running at a speed of 8 km h^{-1}. However, the electret-free electrostatic harvesters usually require to be connected to a source to provide the polarization. Therefore, electret based electrostatic generators have received significant attention recently, as they eliminate the need to be constantly connected to a polarizing voltage source.
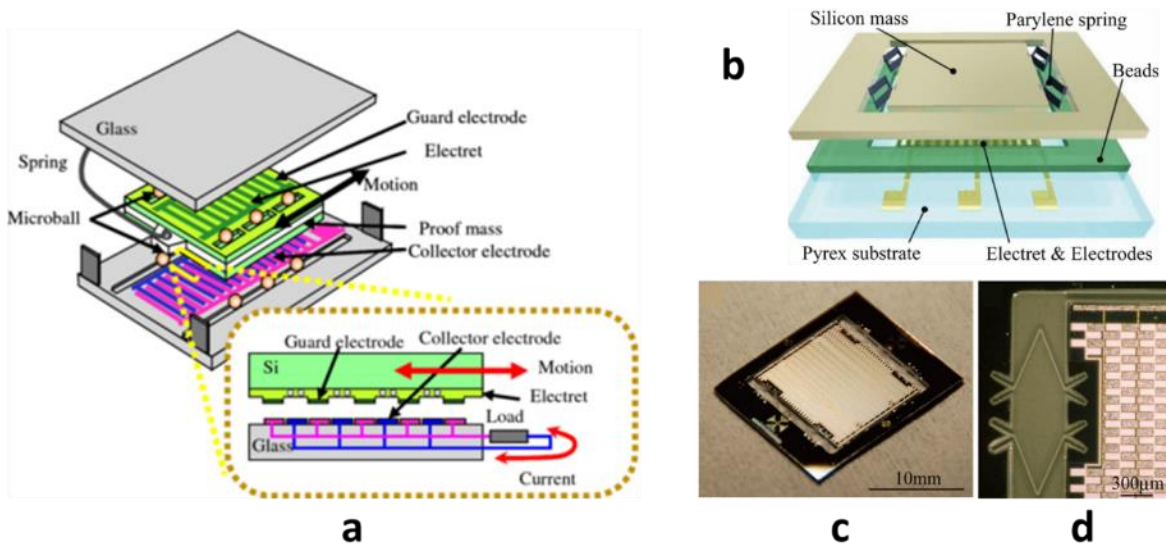
Figure 2.16: (a) Electrostatic micro power generator supported on micro-ball bearings. The use of micro-bearings for suspension yields low frequency operation [Naruse, et al. [65]]. (b) Schematic of electret based electrostatic generator [Edamoto, et al. [66]], (b) Backside of Si substrate, (c) Parylene high-aspect-ratio spring and patterned electret.

Electrets are dielectric materials with stable polarization, which can be induced by uncompensated space charges and/or ordering structural dipoles. Electret materials pre-charged with corona-discharge method exhibit quasi-permanent electric charge or dipole polarization. Therefore pre-charged electrets produce internal and external electric fields (similar to magnetic fields in the vicinity of magnets), which make them the electric equivalent of permanent magnets. Several material classes such as nonpolar/polar semi-

crystalline and amorphous synthetic polymers, biopolymers, electro-ceramics, and ferroelectric ceramic/polymer composites exhibit electret properties, and are extensively used for diverse sensor and actuator applications [Kestelman, et al. [67]]. Some of the prevalent applications of electrets are in electro-acoustic devices, microphones and photocopying machines. Recently, the use of electrets for application in novel bio-medical devices and high energy charge storage applications are also being investigated [Bauer [68]]. An electret based electrostatic energy harvesting device architecture suitable for low frequency vibration was developed by Naruse, et al. [65]. They proposed a suspension mechanism comprising a proof mass, beams, electret, electrodes and micro-ball bearings [Figure 2.16(b)]. The use of the micro-bearings allow for low operational frequency, long range of motion and precise maintenance of gap between electrodes. The device generated a power of 40 µW when subjected to a 0.4g vibrational acceleration at 2 Hz frequency.
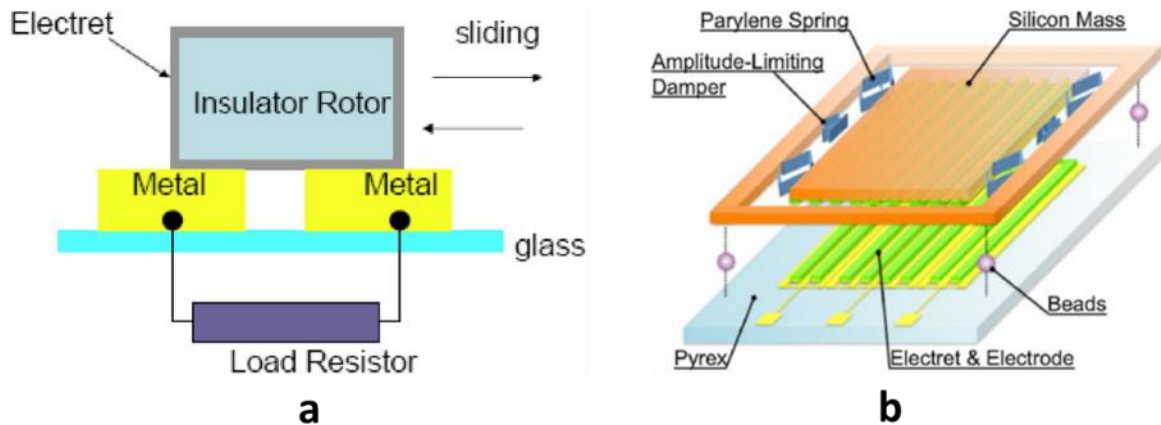
Figure 2.17: (a) Electrostatic harvester with Parylene-HT electret [69], (b) Levitated multiphase electret generator by Suzuki, et al. [70].

Edamoto, et al. [66] developed a low frequency electret based energy harvester, which they coupled to a novel energy management circuit [Figure 2.16(b)]. High aspect ratio parylene springs were used to support a silicon proof mass. Both the silicon proof mass and the Pyrex substrate were patterned with electret and electrodes respectively. CYTOP^{TM} (a commercially available amorphous fluoropolymer) was used as the electret material and was pre-charged via corona discharge during fabrication. The device produced a maximum power of 12.5 µW when subject to a 21 Hz vibration with 1 mm base amplitude. Lo and Tai [69] developed an harvester consisting of a stator with pre-defined metal electrodes and an insulated slider coated with Parylene-HT electret [Figure 2.17(a)]. This arrangement eliminated the necessity of precise control of airgap between electrodes in stator-slider based electrostatic generator. At a vibrational frequency of 20 Hz, the device

generated 18 μW power across a 80 MΩ load. A MEMS electret generator which also used electret-based levitation for passive control of gap-spacing was developed by Suzuki, et al. [70]. The authors used a high-performance perfluoro polymer material for patterned electret to induce a repulsive electrostatic force, which helped the slider stay levitated [Figure 2.17(b)]. A total power output of 1 μW was reported at 2g acceleration.

2.1.4 Triboelectric transduction

The triboelectric effect, which refers the generation of electric charge by friction between different materials, has been a familiar phenomenon for thousands of years. Although the origin of triboelectrification or triboelectric charge separation is often debatable [Henniker [71], Davies [72]], it is generally understood that this effect is initiated through 'adhesion', a non-chemical bond between the contact surfaces of two different materials. In order to establish electrochemical equilibrium between the surfaces of two different materials, charges (ions or electrons) move from one material to other through the bond of adhesion. On separation of the contact, the bond of adhesion is disrupted, and some of the bonded molecules often acquire excess electrons, while others tend to relinquish extra electron, ultimately resulting triboelectric charges on the surface.
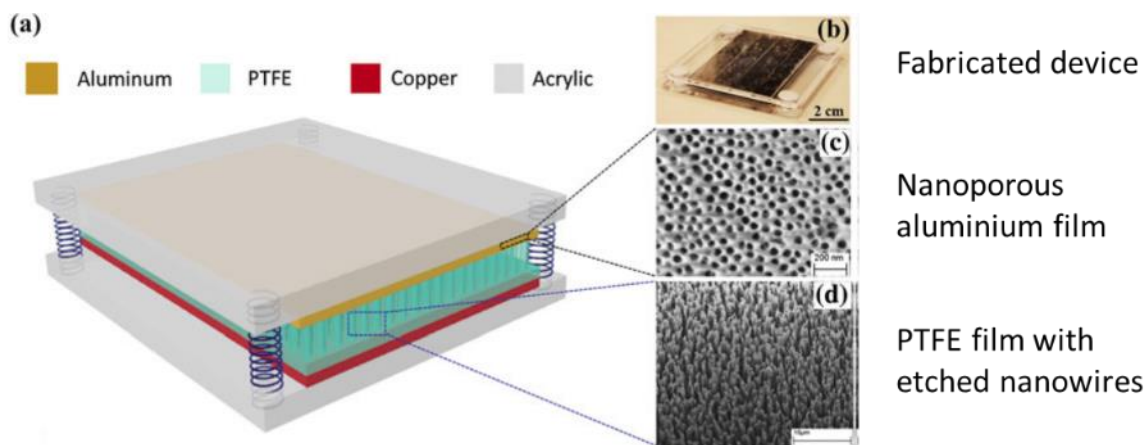
Figure 2.18: Triboelectric nanogenerator (TENG) developed by Chen, et al. [73].

A comprehensive review of energy harvesting based on triboelectric transduction has been published by Wang [74]. The use of triboelectric charge separation to power electronic devices by harvesting mechanical vibrations is a relatively new concept, and was first demonstrated by Chen, et al. [73] in 2013 [Figure 2.18]. The device effectively responded to vibrations of a frequency range from 2 to 200 Hz and generated a peak power of 2.2 mW, which was sufficient to light up a series of LEDs without perceivable delay. The

research group continued their prolific work in a number of prototypes and coined the acronym 'TENG' for 'Tribo-Electric Nano-Generator'. Wen, et al. [75] developed a TENG to harvest vibration energy from water wave. They used a corrugated Cu-Kapton-Cu sheet sandwiched between two flat nanostructured PTFE (Polytetrafluoroethylene) films to generate a peak power of 2 mW from vibrations within a frequency range 5 – 500 Hz [Figure 2.19]. In order to enhance contact electrification by increasing the effective surface area, they produced nanostructured PTFE by ICP (Inductively coupled plasma) etching technique.
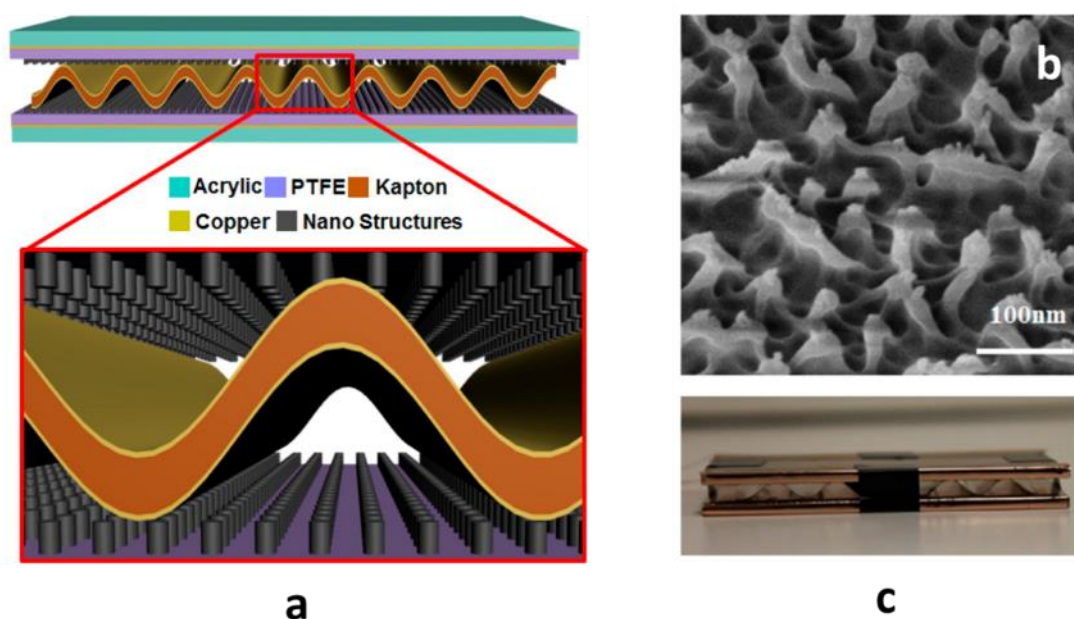
Figure 2.19: (a) Schematic of the device structure [Wen, et al. [75]]. The corrugated Kapton film is in periodical contact with the nanostructured PTFE films. (b) SEM image of the ICP-processed PTFE film surface. (c) The fabricated nanogenerator.

In addition to using triboelectric effect to generate electricity, a vibration sensor based on this principle was developed by Wang, et al. [76], with the capability of self-powered sensing of vibration frequency and amplitude over a broad frequency range. Noting that most of the real-life vibrations are not confined to a single dimension, the group developed a 3D-TENG capable of harvesting multi-directional vibration Yang, et al. [77]. They used nanoporous aluminium film and patterned PTFE film as the contact surfaces, suspended an iron mass using three springs to use as a proof mass [Figure 2.20]. The device worked by combining the vertical contact-separation mode and the in-plane sliding mode, and produced peak power of 4 mW with a wide operational frequency range of 75 Hz. It was demonstrated that in addition to multidirectional vibration harvesting capability, the device

was suitable for harvesting energy from rotational motion, human activity and vehicles. However, one of the known drawbacks of the triboelectric transduction has been the low current output (10s of µA) and Yang, et al. [78] attempted to remedy this problem by multiplying the active surface by using a 3D multi-layered stacked TENG. With synchronized motion of the multiple nanoporous Al – PTFE nanowire layers, they produced short-circuit current as high as 1.14 mA and peak power density of 104.6 Wm^{-2} over a 36 Hz frequency bandwidth. They demonstrated that the 3D-TENG was capable of lighting up 32 commercial LEDs when mounted inside a 3-inch diameter ball which is shaken by hand.
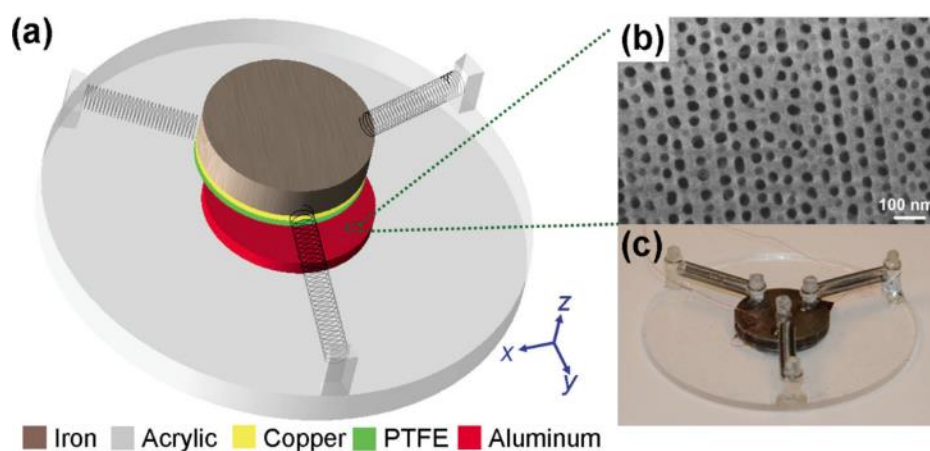
Figure 2.20: (a) Schematic of a TENG for harvesting multi-dimensional vibration [Yang, et al. [77]], (b) SEM image of nanoporous aluminum electrode, (c) fabricated prototype

The maximum achievable contact surface area is limited in solid material based triboelectric generators by the surface roughness of the materials. Therefore, in order to maximize the active surface contact area and increase the total transferable surface charge density, Tang, et al. [79] developed a liquid metal electrode based TENG. In addition to enhanced effective surface area, the liquid metal electrode provided other benefits such as low friction coefficient with solid and shape adaptability. By using nano-patterned Kapton film and mercury-based liquid metal, they achieved an output charge density of 430 μCm^{-2}, about four to five times higher than TENGs with solid materials. Remarkably, the liquid metal based TENG achieved an efficiency of 70.6% (in terms of instantaneous peak power), which is among the highest demonstrated by any waste energy scavenging device. Another interesting application of TENG was investigated by Yang, et al. [80], where the authors harvested vibrations generated by acoustic wave. The prototype generated 60.2 mW m^{-2} power density in an acoustic pressure range of 70-110 dB. In addition, the

generator was demonstrated to be performing as a self-powered sensor capable of automatically detecting the location of acoustic sources with reasonable accuracy. Furthermore, an array of these generators could also be used as self-powered microphones for recording sound. Fan, et al. [81] developed a paper based TENG to generate electricity from acoustic vibrations. They used nanoporous copper film and nanostructured PTFE as the triboelectric surfaces, and bonded them on the surface of a micro-holed (ϕ 400 μm) paper, which enhanced the broadband acoustic response [Figure 2.21]. The device produced a power density of 121 mW m^{-2} under a sound pressure level of 117 dB. It was demonstrated that in addition to generating electricity to power wearable and flexible electronics, the device could be used as a self-powered microphone.
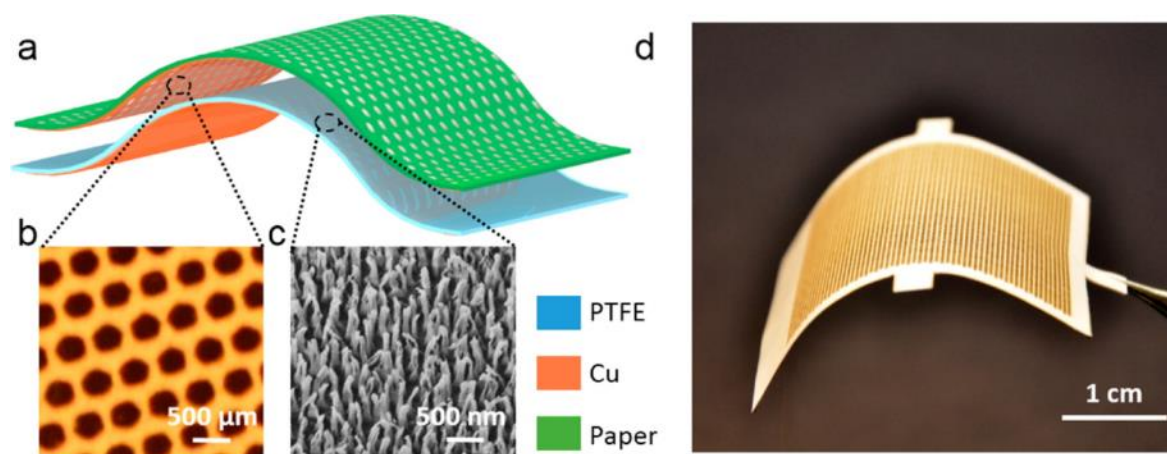
Figure 2.21: (a) Schematic diagram of the paper-based TENG [Fan, et al. [81]]. (b) The micro-holed paper electrode. (c) Nanostructuted PTFE film. (d) Fabricated prototype.

2.1.5 Comparison of transduction mechanisms

Each of the transduction mechanisms discussed in this section has their distinct application scenarios, and associated advantage or disadvantage when various performance and usability metrics are taken into account. Comparative studies of these transduction mechanisms based on qualitative/ quantitative analysis are presented in this subsection. The performance metrics considered here include the power density, output voltage and current. The most important compatibility or applicability metrics considered include the cost of device fabrication, compatibility with standard CMOS process, compatibility with existing power management systems and long term reliability.

Cost of device fabrication and CMOS process compatibility

The cost to fabricate an energy harvesting system and the compatibility of the fabrication process steps are important parameter to consider when potential commercial applications of integrated vibration energy harvesters are concerned. The cost of device fabrication includes the cost of materials and also depends on the complexity of the fabrication process, which may involve process steps that may or may not be compatible with the existing commercial CMOS process flow.

Each of the transduction techniques discussed so far involve a very diverse range of materials, and the fabrication process flows may include standard CMOS processes as well as advanced nanofabrication methods and exotic non-standard ones. The electromagnetic transducers use different hard and soft magnetic materials (e.g. NdFeB, electroplated CoPtP, NiFe etc.) and micro-coils. Some of these materials can be deposited by standard processes such as electrodeposition and sputtering, but others may require non-standard processes such as sintering, powder bonding etc. In addition, electromagnetic harvesters usually implement complicated device structure for accurate positioning of micro-magnets and micro-coils, which may lead to significantly large number of process steps and higher cost of device fabrication. In comparison to electromagnetic transduction, piezoelectric transduction can be implemented in relatively simple device structures, such as a cantilever or diaphragm. The most popular piezoelectric materials (e.g. PZT, PMN-PT etc.), however, are not cheap and may require non-standard processes (e.g. sol-gel) for deposition. Some piezoelectric materials such AlN, on the other hand, may be deposited using standard processes such as sputtering. In addition, relatively simple device structure for piezoelectric transductions translates to relatively fewer number of process steps. Therefore, the cost of device fabrication for piezoelectric transduction usually tend to be lower than the electromagnetic one. The electrostatic transducers are often implemented in the form of a capacitor, with two electrodes separated from each other by a small gap filled with dielectric fluid (most commonly air). Therefore, the electret-free electrostatic energy harvesters are generally fabricated in the form of vibrating silicon diaphragms acting as electrodes, or in the form of silicon inter-digitated comb structures to maximize the capacitive surface area between the electrodes. Both of these device structures are relatively simple to fabricate using the standard CMOS processes. On the other hand, electret-based electrostatic harvesters utilize deposited or coated electret materials such as

PTFE, SiO$_2$, Parylene, CYTOP etc. and charge them by electron or ion guns and corona discharge. Therefore, most of the materials and processes involved in the fabrication of electret-free or electret-based energy harvesters are compatible with the CMOS process flow. The promising technology of triboelectric energy harvesting employ inorganic and organic materials (e.g. PTFE, Kapton, PDMS etc.) and metals (Cu, Al etc.) which are inexpensive and generally compatible with CMOS process. However, the materials and films often require nano-patterned surfaces or the development of nano-wires and nano-structures for maximizing contact area and surface charge density, leading to high energy output. The processes required for development of the nano-structured surfaces are often non-standard and incompatible with the CMOS process flow, and may lead to significant cost in fabrication.

Power density and output voltage/ current consideration

Although the power required to operate individual devices, switches and sensors have been drastically reduced over the past, the complexity of the entire systems (which often involve large number of devices, switches and sensors on a single platform) have grown substantially. Therefore, a considerable amount of energy (100s of µW to 100s of mW, depending on various factors) needs to be harvested from the ambience to perform the different tasks (e.g. sensing, data processing, transmission) an autonomous WSN is required to perform. The power output of typical vibration energy harvesters generally depend on the volume (for electromagnetic and piezoelectric) or active surface area (for piezoelectric and triboelectric) and the oscillatory mass of the device. Therefore, one of the major concerns regarding miniaturization of energy harvesting devices down to MEMS or micro-scales is the reduced harvested energy, which might be too small for powering any device or for processing via power management circuits.

The electromagnetic energy harvesters produce quite low voltage (~ 10 mV – 5 V), but fairly high current (10µA – 1 mA), since the pick-up coils used in electromagnetic transducers represent relatively low electrical impedance. Depending on the device size, the power output of electromagnetic energy harvesters range between a few nanowatts (for micro-scale devices) to a few miliwatts (for macro-scale commercial devices). On the other hand, piezoelectric energy harvesters generate quite high voltage (10 V – 100 V) and lower current (10 nA – 100 µA). The low current output is due to the inherently high resistivity (~ 10s of MΩ) of the piezoelectric materials, which result in very high input impedance.

The output power level of macro and meso-scale piezoelectric energy harvesters are generally on par with the electromagnetic harvesters of similar size. However, at micro-scale, the piezoelectric devices tend to out-perform electromagnetic ones [Kim, et al. [82]]. This is a result of the fact that the electromagnetic flux linkage between the magnet and coil decreases with the third power of device dimension (i.e. with device volume) [O'Donnell, et al. [83]], while the piezoelectric electromechanical coefficient decreases with square of device dimension (i.e. with device surface area). The electrostatic energy harvester output voltages depend on the active supply voltage (in electret-free devices) or the charge in the electret material (in electret-based devices), and are typically in the range of 5 V – 50 V. Since the dielectric materials (air, or electrets) used between electrodes in electrostatic harvesters possess very high resistivity, the current produced by such devices is quite low (< 100 µA). The power output from electret-based harvesters tend to be higher than the electret-free harvesters, although the electrostatic harvesters generally produce lower power in comparison to the electromagnetic and piezoelectric devices. The triboelectric generators operate by separation of charge due to adhesion between different material surfaces, and can produce very high voltage (~ 100s of volts). However, the rate of flow of the separated charge from the material (insulators such as PTFE, Kapton etc.) surfaces through external circuits are often quite low, resulting in small output current. However, by increasing the interacting surface area, the output current can be proportionally enhanced in both triboelectric and electrostatic harvesters. In general, the instantaneous output power density of triboelectric generators tends to be the highest (~10s of mW) among the vibration to electricity transducers. However, most of the reported triboelectric energy harvester architectures operate under directly applied force or impact, and are not applicable in most of the vibration scenarios [Zhu, et al. [84]]. Moreover, the average power density, which is important for real device application, is generally not reported in the triboelectric energy harvesting literatures [Wang, et al. [85]].

Long-term reliability and operational lifetime

One of the important considerations in replacing conventional batteries with energy harvesters to power autonomous sensor nodes is the operational lifetime and long-term reliability of the energy harvesting devices. The factors that have a significant effect on the reliability of energy harvesting devices are the materials, the mechanism of operation and resilience towards the environment. The electromagnetic transducers offer excellent long

term reliability, as the degradation of rare-earth permanent magnets and copper coils over time is negligible, provided they are environmentally shielded. Otherwise, oxidation of iron in the magnet and copper in the coils may lead to gradual degradation in performance over the years. In addition, the ambient temperature must be sufficiently lower than the Curie temperature (~ 300º C for NdFeB, ~ 700º C for SmCo) of the magnetic material. The piezoelectric material films that offer the highest electromechanical coefficients (PZT, PMN-PT, AlN etc.) are in general brittle, which raises serious concerns over long-term reliability in mechanical vibrations. This issue can be addressed to some extent by using composite nanowire-based materials and piezoelectric polymers (i.e. PVDF), although the performance is greatly diminished. In addition the ambient temperature must be significantly lower than the Curie temperature (~ 300º C for PZT, ~ 400º C for AlN, ~ 120º C for PVDF). Furthermore, the polarization of piezoelectric films tend to depreciate over time, reducing power output. The electret-free electrostatic harvesters require the supply voltage for biasing the electrodes, which is not suitable for long-term (> 10 years) autonomous operation. Although the electret-based harvesters are capable of autonomous operation without external supply voltage, the charge implanted in the electrets may gradually degrade over a long period of time. The triboelectric energy harvesters are composed of materials in the form of specialized surfaces, which repeatedly come into contact (often collide) with each other throughout operational lifetime. This repeated contact may degrade the nanostructured surfaces over time and result in reduced power output. Since the triboelectric transduction technology is relatively new, there is not sufficient information available regarding the long-term reliability of triboelectric energy harvesters.

Research interest over the last decade

Vibrational energy harvesters utilizing the four principal transducing mechanisms have enjoyed increasing attention from researchers over the last few years, which have significantly bolstered the research output and publications. Historically, piezoelectric transduction have been investigated the most, primarily due to its relatively simple topologies and the possibility of on-chip integration with electronics. In comparison, electromagnetic transduction has been less popular in the same period due to complicated fabrication process and low output voltage at micro-scale, which is unsuitable for commercially available power management systems. Although the electrostatic

transduction lends itself directly to the standard CMOS fabrication process, it has not been as popular as the piezoelectric and electromagnetic devices, primarily due to external bias voltage requirement and lower power density. The latest development in transduction technology is the triboelectric transducer, which first appeared in vibration or kinetic energy harvesting devices in 2012 [Figure 2.22]. Driven by the unprecedented level of output voltage and instantaneous power density, triboelectric transducers are rapidly gaining popularity within the vibration energy harvesting community. Overall, given the advancement of IoT and wireless sensor technology, the scope of research and application of vibration energy harvesting is anticipated to increase in the years ahead.
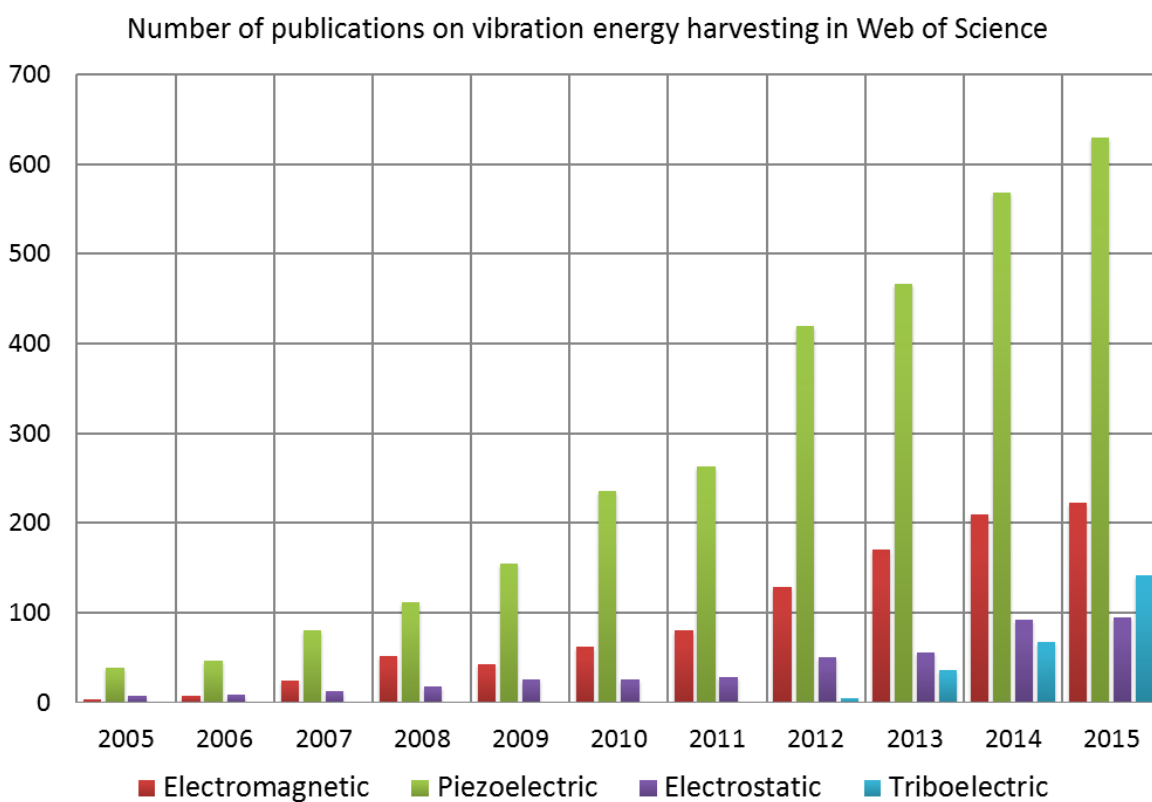
Figure 2.22: Number of publications on vibration energy harvesting over the past decade using different transduction mechanisms.

2.2 Linear vibration energy harvester

This section describes the theoretical background related to linear electromagnetic vibration energy harvesting systems, and its practical implementation reported in literature.

2.2.1 Theoretical background

In the most basic form, a vibration energy harvester can be considered to be a transducer (electromagnetic, piezoelectric, electrostatic, triboelectric etc.) coupled to an oscillator,

comprising mass-spring-damper system. Schematically, the vibration energy harvesters is often illustrated as shown in Figure 2.23, where the transduction can be represented as an electromechanical damping source.
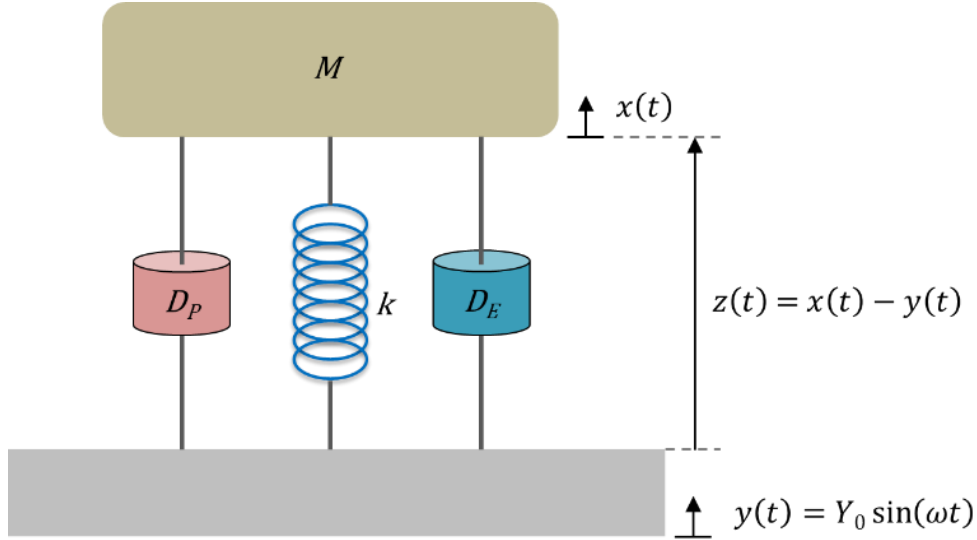
Figure 2.23: Schematic representation of the generic spring-mass-damper based vibration energy harvesting system.

Considering the relative motion of mass M with respect to the supporting base, a relative coordinate can be defined as,

$$z = x - y \qquad \text{2.1}$$

where x is the displacement of the equivalent mass, y is the displacement of the base, and z represents the relative displacement of the mass M. The external vibration $y(t)$ is assumed to be a harmonic function with amplitude Y_0 and angular frequency ω.

The dynamical equation of the system can be represented by the following mono-dimensional equation,

$$M\ddot{z} + kz + (D_P + D_E)\dot{z} = -M\ddot{y} \qquad \text{2.2}$$

where D_P is the parasitic damping and D_E represents the electromechanical damping factor. Combining D_P and D_E, the total damping factor D can be defined as,

$$D = D_P + D_E \qquad \text{2.3}$$

Using Laplace transformation, the eq. 2.2 can be expressed in the frequency domain as,

$$(Ms^2 + Ds + k)Z(s) = -Ms^2 Y(s) \qquad \text{2.4}$$

where $Z(s) = \int_0^\infty z(t) e^{-st} dt$, and $Y(s) = \int_0^\infty y(t) e^{-st} dt$, and $s = j\omega$ is the complex frequency. Rearranging eq. 2.4 yields the transfer function as,

$$H(s) = \frac{Z(s)}{Y(s)} = \frac{-Ms^2}{Ms^2 + Ds + k} \tag{2.5}$$

Dividing the numerator and denominator on the right hand side by M, eq. 2.5 can be rearranged as,

$$H(s) = \frac{-s^2}{s^2 + \dfrac{D}{M}s + \dfrac{k}{M}} \tag{2.6}$$

The natural frequency of undamped oscillation can be determined as $\omega_n = \sqrt{k/M}$, the normalized damping coefficient is given by $\xi = D/2M\omega_n$. Substituting $s = j\omega$ in eq. 2.6, the transfer function can be expressed as,

$$H(\omega) = \frac{\omega^2}{-\omega^2 + 2\xi\omega_n\omega j + \omega_n^2} \tag{2.7}$$

Dividing the numerator and denominator by ω_n^2 on the right hand side,

$$H(\omega) = \frac{\left(\dfrac{\omega}{\omega_n}\right)^2}{-\left(\dfrac{\omega}{\omega_n}\right)^2 + 2\xi\dfrac{j\omega}{\omega_n} + 1} \tag{2.8}$$

or,

$$Z(\omega) = \frac{\left(\dfrac{\omega}{\omega_n}\right)^2}{-\left(\dfrac{\omega}{\omega_n}\right)^2 + 2\xi\dfrac{j\omega}{\omega_n} + 1} Y(\omega) \tag{2.9}$$

By reverse Laplace transform, the eq. 2.9 can be expressed as,

$$z(t) = \frac{\left(\dfrac{\omega}{\omega_n}\right)^2}{-\left(\dfrac{\omega}{\omega_n}\right)^2 + 2\xi\dfrac{j\omega}{\omega_n} + 1} y(t) \tag{2.10}$$

The time domain steady state solution for eq. 2.2 can be assumed to be,

$$z(t) = Z_0 e^{j\omega t} \tag{2.11}$$

Differentiating eq. 2.11,

$$\dot{z}(t) = j\omega Z_0 e^{j\omega t} = j\omega z(t)$$

Substituting eq. 2.12 into 2.10,

$$\dot{z}(t) = \frac{j\omega \left(\frac{\omega}{\omega_n}\right)^2}{-\left(\frac{\omega}{\omega_n}\right)^2 + 2\xi\frac{j\omega}{\omega_n} + 1} y(t)$$

Or,

$$|\dot{z}(t)| = \frac{\frac{\omega^3}{\omega_n^2}}{\sqrt{\left(1 - \left(\frac{\omega}{\omega_n}\right)^2\right)^2 + \left(2\xi\frac{\omega}{\omega_n}\right)^2}} |y(t)|$$

If the magnetic field across the coil due to the magnet in an electromagnetic energy harvester is denoted by Φ_m, then the voltage induced in the coil is given by,

$$v(t) = -\frac{d\Phi_m}{dt} = -\frac{d\Phi_m}{dz}\frac{dz}{dt} = -k_m\dot{z}$$

Where k_m is the magnetic flux gradient or the electromechanical transduction factor, and is assumed to be constant.
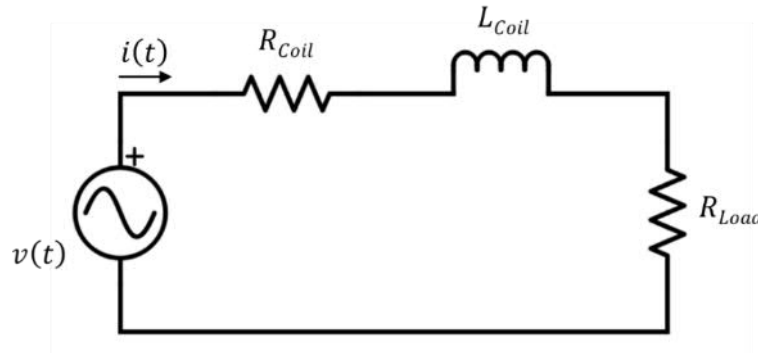
Figure 2.24: Generic electrical subsystem of electromagnetic vibration energy harvester connected to a resistive load.

The electrical subsystem electromagnetic energy harvester combining the coil and external load can be represented as shown in Figure 2.24, where $v(t)$ is the induced voltage, $i(t)$ is the current in the circuit, R_{Coil} is the coil resistance, L_{Coil} is the coil inductance and R_{Load} is the load resistance. The governing equation for the electrical subsystem can be determined by the Kirchhoff's voltage law as,

$$L_{Coil}\frac{di}{dt} + (R_{Coil} + R_{Load})i = -v(t) = k_m\dot{z} \qquad 2.16$$

The mechanical domain and the electrical domain are related through the electromechanical transduction factor k_m, which yields the current $i(t)$ to flow in the circuit. The current generates a magnetic field in the coil, which opposes the cause of the current (i.e. the relative motion between the magnet and coil) according to Lenz's law. This opposing force is fed back to the mechanical subsystem and is given by,

$$F_{EM} = k_m i \qquad 2.17$$

Applying Laplace transform to eq. 2.16 yields,

$$sL_{Coil}I(s) + (R_{Coil} + R_{Load})I(s) = k_m sZ(s) \qquad 2.18$$

where $I(s) = \int_0^\infty i(t)\,e^{-st}\,dt$, $Z(s) = \int_0^\infty z(t)\,e^{-st}\,dt$, and s represents the complex frequency. Rearranging eq. 2.18 gives,

$$I(s) = \frac{k_m}{sL_{Coil} + (R_{Coil} + R_{Load})}sZ(s) \qquad 2.19$$

The ambient vibration frequencies are usually in the lower end of the spectrum (< 5 kHz). In a typical electromagnetic energy harvester, the reactance due to the coil (sL_{Coil}) is negligibly small compared to the combined resistive load ($R_{Coil} + R_{Load}$) in such low frequencies. Therefore, the inverse Laplace transform of eq. 2.19 yields,

$$i(t) = \frac{k_m}{(R_{Coil} + R_{Load})}\dot{z}(t) \qquad 2.20$$

Now, substituting eq. 2.20 into eq. 2.17 gives,

$$F_{EM} = \frac{k_m^2}{(R_{Coil} + R_{Load})}\dot{z}(t) \qquad 2.21$$

Therefore, the transducer exerts a dissipative electromechanical feedback force which can be expressed as a viscous damping effect proportional to velocity with a damping coefficient D_E given by,

$$D_E = \frac{F_{EM}}{\dot{z}(t)} = \frac{k_m^2}{(R_{Coil} + R_{Load})} = 2M\xi_E\omega_n \qquad 2.22$$

where ξ_E denotes the electromechanical damping coefficient.

The maximum electrical power that can be extracted from the transducer is given by the following instantaneous power equation,

$$P(t) = \frac{d}{dt}\int_0^z F_{EM}(t)dz = \frac{d}{dt}\int_0^z D_E\dot{z}(t)dz = \int_0^{\dot{z}} D_E\dot{z}(t)d\dot{z} = \frac{1}{2}D_E[\dot{z}(t)]^2 \qquad \text{2.23}$$

Substituting eq. 2.23 in eq. 2.14,

$$P(t) = \frac{1}{2} \cdot 2M\xi_E\omega_n \left[\frac{\frac{\omega^3}{\omega_n^2}}{\sqrt{\left(1-\left(\frac{\omega}{\omega_n}\right)^2\right)^2 + \left(2\xi\frac{\omega}{\omega_n}\right)^2}}|y(t)|\right]^2 \qquad \text{2.24}$$

The total damping coefficient ξ can be split into the electromechanical and parasitic damping as,

$$\xi = \xi_E + \xi_P \qquad \text{2.25}$$

Where $D_P = 2M\xi_P\omega_n$ is the parasitic damping factor. Then eq. 2.24 can be re-written as,

$$P(t) = \frac{M\xi_E\left(\frac{\omega}{\omega_n}\right)^3\omega^3}{\left(1-\left(\frac{\omega}{\omega_n}\right)^2\right)^2 + \left(2(\xi_E+\xi_P)\frac{\omega}{\omega_n}\right)^2}|y(t)|^2 \qquad \text{2.26}$$

The eq. 2.26 is formally similar to that derived by Williams and Yates [6]. In case of resonant operation ($\omega = \omega_n$), eq. 2.26 can be simplified as,

$$P = \frac{M\xi_E\omega_n^3}{4(\xi_E+\xi_P)^2}|y(t)|^2 = \frac{M^2 D_E\omega_n^4}{4(D_E+D_P)^2}Y_0^2 \qquad \text{2.27}$$

by substituting, $\xi_E = D_E/2M\omega_n$, and $\xi_P = D_P/2M\omega_n$. Since the applied excitation is a pure sinusoid ($y(t) = Y_0\sin(\omega t)$), the input acceleration can be obtained as, $\ddot{y}(t) = -\omega^2 Y_0\sin(\omega t)$, or, $|\ddot{y}(t)| = \omega^2 Y_0$. The eq. 2.27 can be modified by this substitution as,

$$P = \frac{M\xi_E|\ddot{y}(t)|^2}{4\omega_n(\xi_E+\xi_P)^2} = \frac{M^2 D_E|\ddot{y}(t)|^2}{4(D_E+D_P)^2} \qquad \text{2.28}$$

The eq. 2.28 indicates that for small parasitic damping, the oscillating mass should be maximized and the electromechanical damping should be minimized in an electromagnetic energy harvester in order to generate maximum power from a given harmonic vibration excitation.

2.2.2 Linear oscillator and its application in vibration energy harvesting

The spring restoration force of the generic vibration energy harvester outlined in Figure 2.23 is given by,

$$F_{Lin} = -kz$$

2.29

Where the force F_{Lin} is a linear function of the relative displacement of the oscillating mass M. The resulting potential energy stored in the spring during oscillation is given by,

$$U_{Lin} = -\int_0^z F_{Lin}(z)\, dz = \frac{1}{2}kz^2$$

2.30

The resulting restoring force and potential energy profiles are plotted in Figure 2.25. It can be observed that the linear spring restoring force contributes to parabolic potential energy profile, which become steeper with increasing spring stiffness (i.e. increasing k).
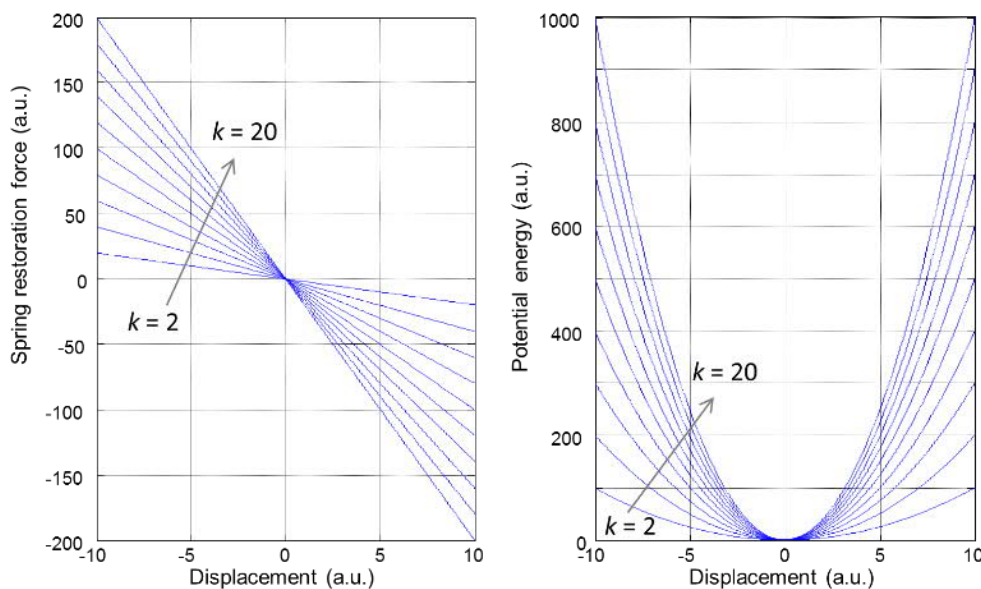
Figure 2.25: Variation of spring restoration force and potential energy profile with the linear spring coefficient.

The linear spring based oscillators usually produce frequency responses with sharp and narrow resonance peaks, or narrow-band responses. The earliest vibration energy harvesters employed this spring mechanism due to its relatively high quality factor, which resulted in high output energy at vibrational excitations with reasonably stable frequency. Roundy and Wright [21] developed a piezoelectric energy harvester within a volume of 1 cm^3 which powered a custom designed wireless sensor module (12 mW) with a duty cycle of 1.6%. A micro-scale cantilever (length 50 µm) based piezoelectric VEH was developed

by Jeon, et al. [45] which exhibited sharp resonance at a rather high frequency of 13.9 kHz. Similar linear frequency response was also observed by Ericka, et al. [86] in a piezoelectric diaphragm based device with a peak power frequency of 2.58 kHz. James, et al. [87] developed an electromagnetic generator with linear frequency response and power output of 2.5 mW [Figure 2.26(a)], which was used to power an LCD monitor and operate an infra-red data transfer link. A cylindrical topology based on discrete magnets and wire-wound coils was developed by Cao and Lee [88], which produced 35 mW to power a network of micro-accelerometers [Figure 2.26(b)].
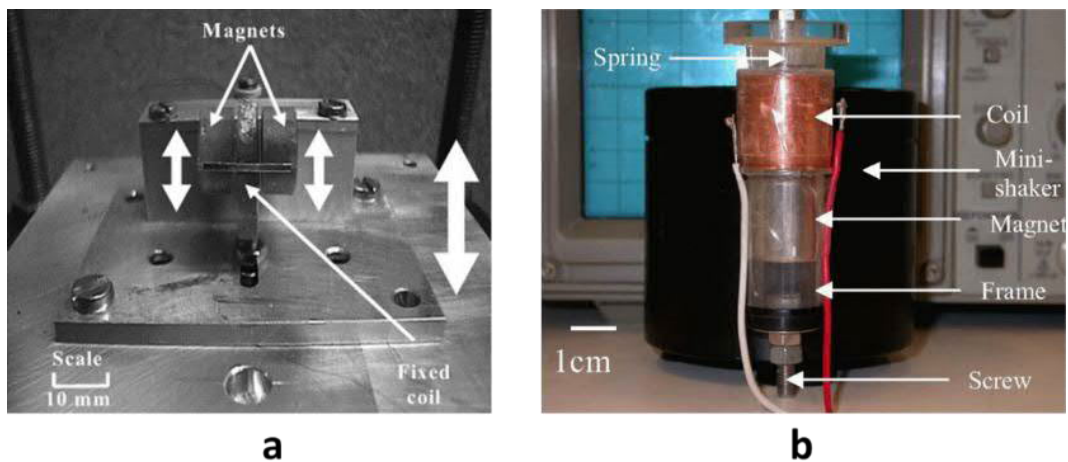
Figure 2.26: Linear electromagnetic vibration energy harvester after (a) James, et al. [87], and (b) Cao and Lee [88].

The high power density electromagnetic energy harvester developed by Beeby, et al. [17] was based on a cantilever structure and produced linear response in low accelerations, and moderately nonlinear response at higher accelerations.

Despite the initial success in demonstrating the capability of vibration energy harvesting, linear oscillator based devices suffer from severe limitations in terms of bandwidth. While the narrow bandwidth and high Q-factor typical of a linear vibration energy harvester is suitable for applications in stable fixed frequency vibrations, most of the natural vibration sources have broadband or random frequency spectrum.

2.3 Nonlinear vibration energy harvester

This section discuss the incorporation of mechanical nonlinearity in vibration energy harvesters and their impact on the frequency response and overall performance of the

devices under different excitation conditions. In addition to the monostable and bistable stiffness nonlinearities, the mechanical impact induced nonlinearities have been discussed.

2.3.1 Theoretical background

In the context of vibration energy harvesting, nonlinearities in oscillator are usually discussed in the formalism of nonlinear Duffing oscillators [Nayfeh and Mook [89]]. The generic nonlinear spring restoration force (F_{NonLin}) can be expressed as a combination of linear and nonlinear force terms as,

$$F_{NonLin} = -kz - k_3 z^3$$

2.31

where, z denotes the displacement of the equivalent inertial mass, k and k_3 represent the linear and nonlinear spring coefficients, respectively. The corresponding potential energy of a nonlinear oscillator can be expressed as,

$$U_{NonLin} = -\int_0^z F_{NonLin}(z)\, dz = \frac{1}{2}kz^2 + \frac{1}{4}k_3 z^4$$

2.32

Depending upon the values of k and k_3, the eq. 2.32 and eq. 2.31 can represent the potential energy functions and spring restoration forces corresponding to either a linear ($k > 0$, $k_3 = 0$), or a nonlinear ($k \neq 0$, $k_3 > 0$) oscillator [Daqaq, et al. [90]]. Specifically, for the condition $k > 0$, $k_3 > 0$, the potential energy profile become a nonlinear monostable system with cubic force-displacement relationship in the spring. On the other hand, the condition $k < 0$, $k_3 > 0$ produces a bistable potential energy profile with two stable states on either sides of the initial equilibrium. Each of these nonlinear oscillator configurations exhibit their characteristic frequency responses when incorporated in vibration energy harvesting systems.

2.3.2 Nonlinear Duffing monostable harvester

The motivation for use of nonlinearities in vibration energy harvesting devices stem from the need to broaden the frequency response to comply with the spectrum of ambient vibration sources. One of the earliest nonlinear energy harvesters deploying the monostable Duffing nonlinearity was developed by Mann and Sims [91], where the authors used magnetic levitation to emulate nonlinear spring restoration force [Figure 2.27(a)]. A magnet was suspended within a cylindrical structure by two oppositely oriented magnets, and the voltage induced in coils wrapped around the suspended magnet exhibited hysteretic frequency response under harmonic excitation. This work demonstrated that nonlinear

energy harvesters could be successfully used to harvest energy from vibrational frequencies that were significantly higher than the natural resonance frequency of a comparable linear device. Nonlinear harvesters based on similar architecture where magnetic repulsion force were also investigated by Saha, et al. [7] and Constantinou, et al. [92]. A different approach of incorporating the cubic stiffness nonlinearity in spring design was proposed by Marinkovic and Koser [93]. They exploited the stretching of fixed-fixed thin cantilever structures at large deflections, which produced cubic Duffing nonlinear spring restoration force [Figure 2.27(b)].
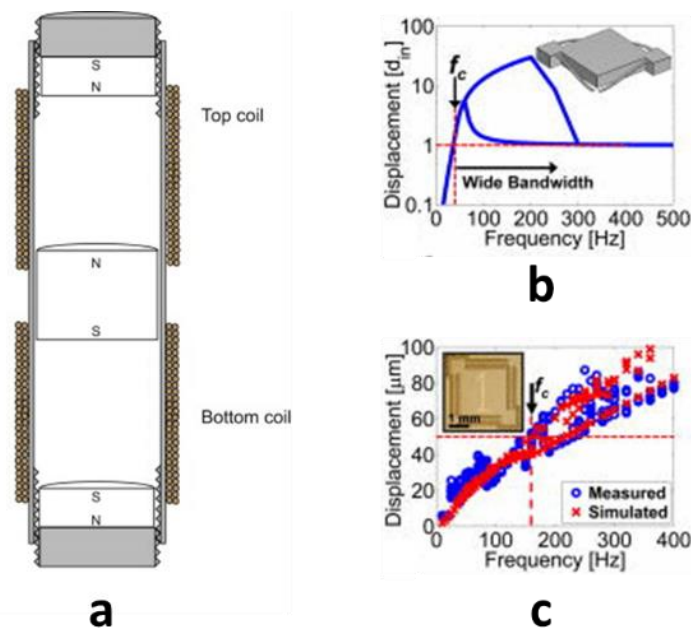
Figure 2.27: (a) Magnetic levitation-based nonlinear Duffing monostable harvester [Mann and Sims [91]]. (b) Stretching-based nonlinear Duffing monostable harvester [Marinkovic and Koser [93]], the device operates off-resonance, resulting in a wide operational bandwidth. (c) Experimental and simulated response under constant amplitude vibrations (50 μm).

A MEMS-scale prototype was fabricated in silicon-on-insulator substrate, and piezoelectric transduction was incorporated by sol-gel deposited PZT. The device produced a broad hysteretic frequency response (160 – 400 Hz). This device architecture was also implemented in meso-scale prototype based on FR4 (PCB) material and electromagnetic transduction by Mallick, et al. [94]. It was established through detailed theoretical analysis and experimental validation that broadening of frequency response in monostable Duffing oscillators are dependent on the strength of nonlinearity, excitation amplitude and effective parasitic damping.

While the monostable Duffing oscillator based vibration energy harvesters performed reasonably in harmonic excitations, most of the ambient vibrations are non-harmonic and broadband in nature, often with randomly varying frequency and amplitude. It was demonstrated by Daqaq [95] that the monostable nonlinear harvesters are not suitable for such random vibrational excitations. He concluded that under such random excitations, the expected output power decreased with increasing nonlinearity, regardless of the bandwidth or the centre frequency of excitations.

2.3.3 Nonlinear bistable harvester

The bistable nonlinear oscillators based on the Duffing equation exhibit a potential energy profile with two potential wells separated by a potential barrier, and a negative effective stiffness coefficient in the vicinity of the potential barrier. Depending on the nature and amplitude of the external vibratory excitation, the bistable potential energy profile in an oscillator may lead to three distinct scenarios, as illustrated in Figure 2.28.

In the first case, the imparted vibrational excitation is assumed to be small, so that the kinetic energy of the oscillator is not sufficient to overcome the potential energy barrier. The oscillator is essentially confined within one of the potential wells, and performs small amplitude oscillations around one of the stable equilibria. The second scenario may occur at a vibrational excitation which imparts a level of kinetic energy very close to that of the potential energy barrier. In this scenario, depending on the initial dynamical conditions (i.e. displacement and velocity) the oscillator may be able to cross the potential barrier, or it may be confined in one of the potential wells.

This dependence of the locus of the oscillator on the uncertain nature of the initial conditions often drives the oscillator to jump between the potential wells in a chaotic or aperiodic fashion. By applying even higher vibrational excitation to the oscillator a third scenario can be obtained, where the oscillator has ample kinetic energy for smooth transition across the potential barrier. The oscillator performs large amplitude inter-well oscillation in this condition. This periodic inter-well oscillation (also known as snap-through) leads to large amplitude and high velocity operation, with the highest energy output of the three scenarios.
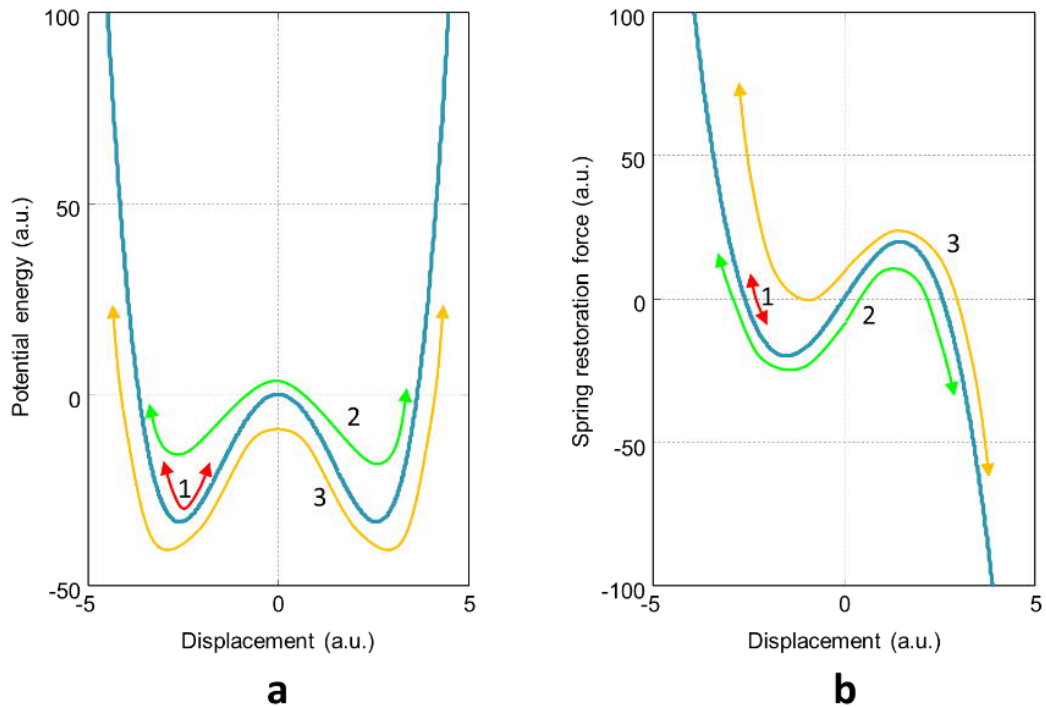
Figure 2.28: (a) Bistable potential energy with double wells, and (b) Bistable spring restoration force. Example trajectories for 1. Intra-well, 2. Chaotic inter-well and 3. Inter-well oscillations have been illustrated.

It has been recognized by Daqaq [96] that the activation energy for the inter-well oscillation condition is irrespective of the vibration frequency, and largely dependent on the vibration amplitude. This revelation suggests that the bistable oscillators could be more appropriate for many of the real life applications where the available vibration is often random or possess a broad frequency spectrum.

The theoretical and experimental investigations of bistable oscillators based on buckled beam structures and dual magnetic attractions with a ferromagnetic beam was pioneered by Tseng and Dugundji [97] and Holmes [98]. In the buckled beam based approach a horizontally suspended cantilever would be buckled at both ends such that a pitchfork bifurcation yields two stable states. The oscillator could exhibit a snap-through behaviour across a potential energy barrier between the two stable states under appropriate excitations. Magnetic attraction based bistability can be realized by positioning two magnets separated by a distance in front of a ferromagnetic beam. In a different approach, a bistable oscillator based energy harvester was developed by Cottone, et al. [99], where the authors devised a bistable system by exploiting the magnetic repulsion between a fixed

magnet and another magnet mounted on a cantilever tip. All of these mechanisms have been utilized in several iterations by various research groups.
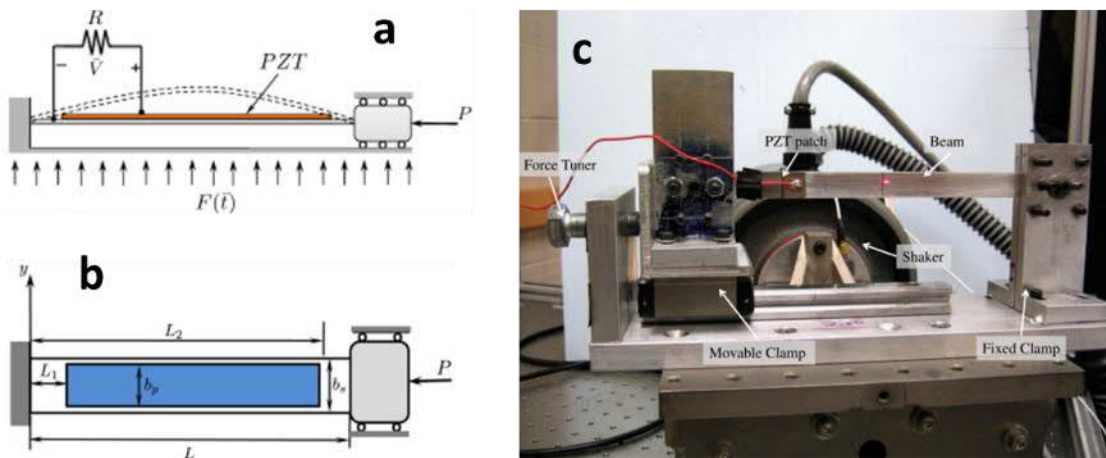
Figure 2.29: Buckled cantilever based bistable vibration energy harvester after Masana and Daqaq [[100] and [101]]. The horizontally applied buckling load induces tunable structural bistability. The PZT patch incorporates piezoelectric transduction.

The buckled beam-based approach has been one of the most popular due to the relative simplicity of the topology, and direct applicability of piezoelectric transduction in the cantilever structure. Extensive studies on the buckled cantilever-based vibration energy harvester [Figure 2.29] has been carried out by Masana and Daqaq in [100] and [101]. Their results suggested that the depth of the bistable double-well potential energy profile plays a crucial role in the overall performance of bistable energy harvesters. The extent of nonlinear bistability could be adjusted by modifying the axial buckling load, and large amplitude inter-well oscillation could be triggered even at very low frequencies.

Cottone, et al. [102] established the fact that under exponentially correlated noise vibration, the buckled cantilever-based piezoelectric energy harvester would out-perform the unbuckled cantilever by an order of magnitude. The buckled cantilever based design has also been implemented using electromagnetic transduction by Cottone, et al. [103]. However, the low vibration amplitude of the buckled beam bistable systems yield sub-optimal results in electromagnetic transduction.
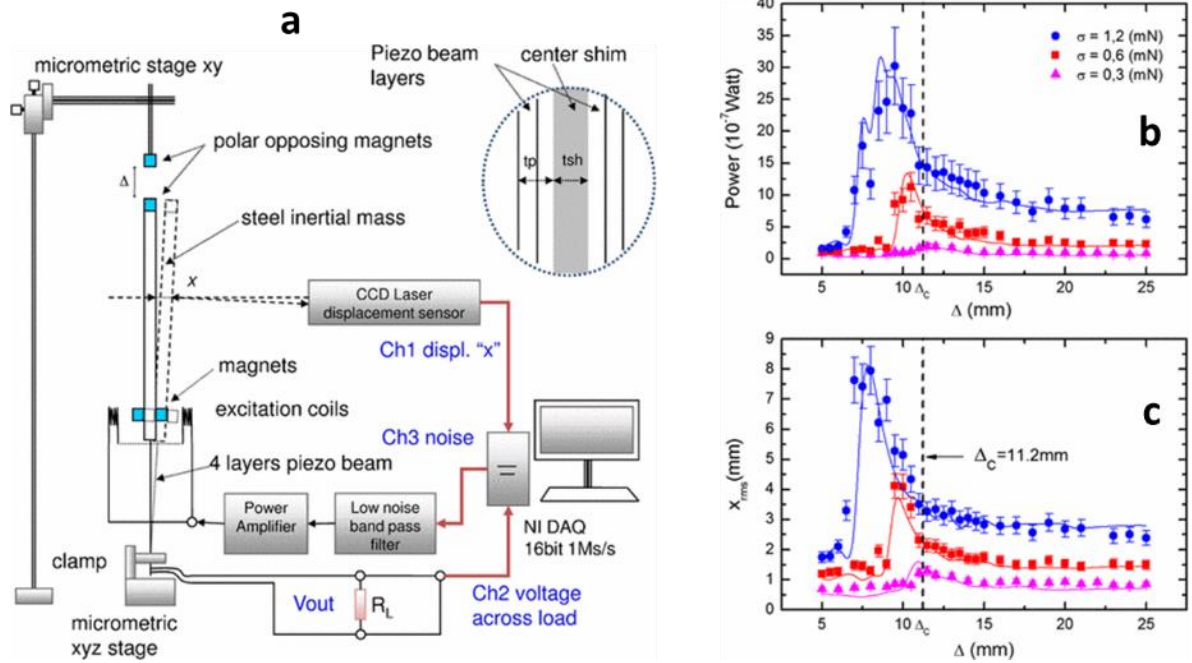
Figure 2.30: (a) Schematic layout of the experimental set up used by Cottone, et al. [99]. (b) Mean electric power, and (c) RMS position as a function of Δ for three different values of the noise standard deviation σ.

In a modified approach, Arrieta, et al. [104] used composite plate of piezoelectric laminates as a bistable energy harvester, where the achieved significantly broad spectral response at low frequencies, and high power output (> 10 mW) [Figure 2.31]. The device was further optimized by Betts, et al. [105], where the square shaped plate exhibited more uniform bistable nature over a comparable rectangular plate. An alternative configuration of axially loaded buckled cantilever was developed by Friswell, et al. [106], where the authors achieved bistable configuration by mounting a large mass on the tip of a vertically oriented piezoelectric beam. The device performed well in extremely low frequency vibrations (< 1 Hz) and the most favourable results were achieved with a tip mass that provided near-critical buckling load.

In a pioneering investigation Moon and Holmes [107] studied bistable mechanisms based on magnetic attraction between permanent magnets and ferromagnetic cantilevers, which was later extrapolated into vibration energy harvesting by Erturk and Inman [108] through piezoelectric transduction [Figure 2.32]. They achieved significantly higher power output from the high energy orbit of the bistable configuration in comparison to a similar linear device.
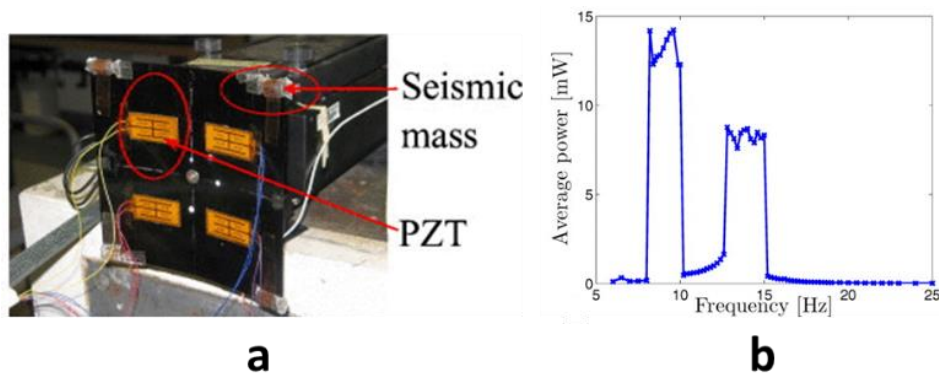
Figure 2.31: (a) Bistable composite plate enery harvester by Arrieta, et al. [104]. (b) Frequency response of the composite plate harvester at 1g acceleration.

An innovative variation of this conventional cantilever based design was developed by Galchev, et al. [109], where a magnetic coupling mechanism between two suspended magnets and a suspended magnetic mass result in a parametric frequency increased generator (PFIG), that amplified the input vibration frequency [Figure 2.33]. The device produced a broadband response in a frequency range of $20 - 60$ Hz, and harvested 13.6 µW average power at 1g acceleration.

In a seminal article Cottone, et al. [99] reported the superior performance of a magnetic repulsion based piezoelectric bistable vibration energy harvester over a similar linear device under noise infused vibrations. The intriguing results sparked the interest in such configurations among the research community, and numerous investigations followed.
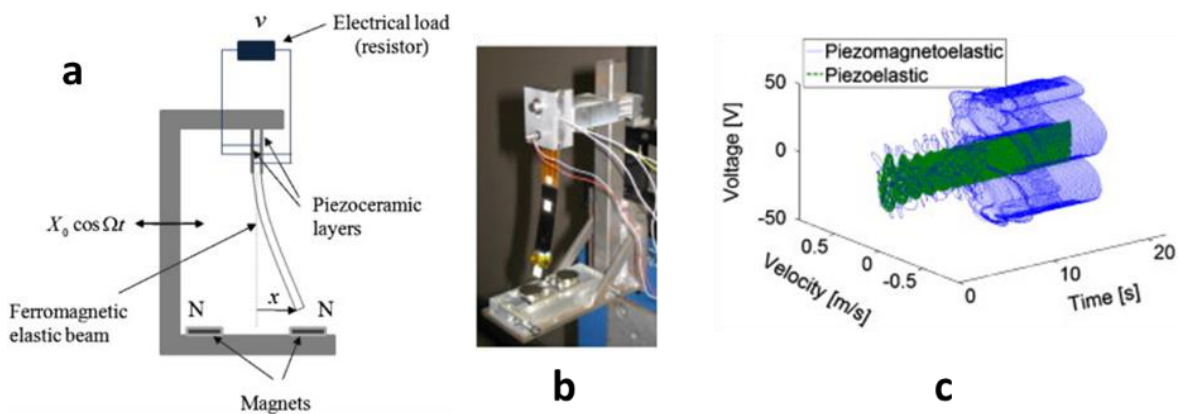
Figure 2.32: (a) Schematic diagram and (b) fabricated prototype of the piezomagnetoelastic vibration energy harvester by Erturk and Inman [108]. (c) Three-dimensional electromechanical trajectories at 0.5*g*, 8 Hz with a disturbance at *t*=11 s.
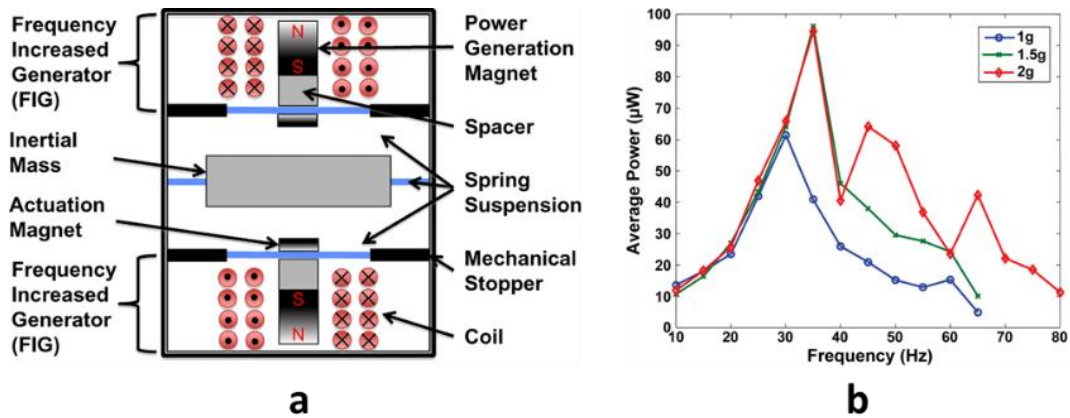
Figure 2.33: (a) Schematic representation of PFIG harvester by Galchev, et al. [109]. (b) Experimental power output at different accelerations.

Based on a structure similar to Cottone, et al. [99], a horizontally mounted piezoelectric bistable cantilever was developed by Lin and Alphenaar [110]. The prototype generated 50% higher peak voltage in comparison to a similar linear device when pink noise excitation was applied. Tang, et al. [111] attempted to find the optimal shape of the bistable potential well for low frequency applications. They determined the optimum potential profile to be in the region of transition from monostable to bistable condition, where the depth of the potential wells is shallow. These findings were applied in a wave-heave energy harvesting system, which exhibited immunity against changing input wave frequency for energy harvesting. A magnetic spring based device with electromagnetic transduction was developed and studied in separate works by Mann and Owens [112] and Sneller, et al. [113], where bistability was incorporated by repulsive interaction between the transducing magnet and externally positioned magnets. This configuration also exhibited broadening of operational frequency range due to cross-well jump of the oscillating magnet.

2.3.4 Mechanical impact induced nonlinear effect

In many mechanical systems, impact is considered an undesirable event which often induces adverse secondary effects, such as loss of energy and efficiency, wear and deterioration of parts, and noisy environment. However, the mechanics behind the phenomenon of impact has been studied in great detail, [[114], [115], [116], [117]] partly due to the abundant occurrences, and partly due to the complexity and strong dynamical nonlinearity produced by impacts. It was noted by Peterka [116] that many different types of complex periodic and chaotic impact motions could be present even for apparently simple systems under periodic excitations forces. Similar to other nonlinear systems,

mechanical systems involving impact also exhibit stable spectral region, hysteretic response, period doubling and saddle-node bifurcations.
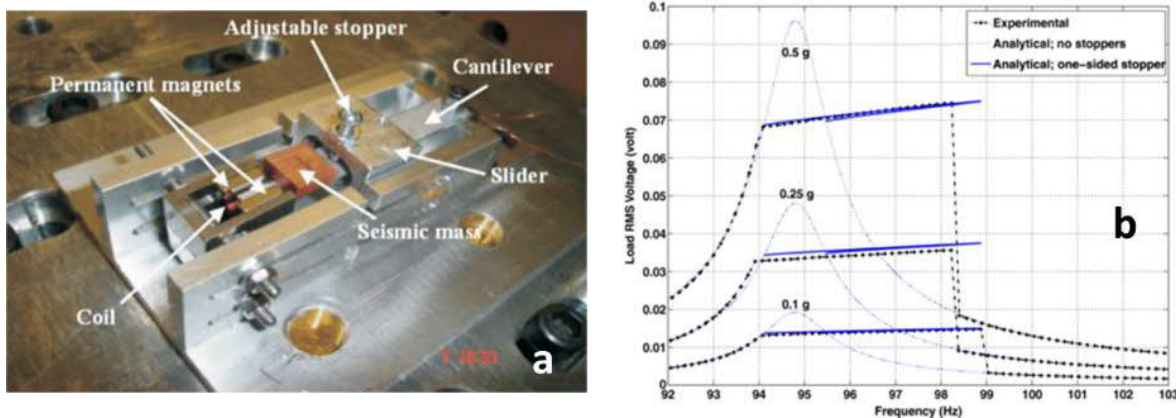
Figure 2.34: (a) Electromagnetic energy harvester with adjustable stopper for impact induced bandwidth widening effect [118]. (b) Increase in bandwdith due to impact.

The nonlinearities in mechanical impacts were utilized by Soliman, et al. [118] to broaden the bandwidth of electromagnetic vibration energy harvesters. The authors proposed a cantilever-based system where the oscillatory motion of the cantilever could be impeded by a stopper, effectively producing a wider bandwidth and hysteretic frequency response [Figure 2.34]. The prototype demonstrated an increase of 240% in bandwidth of the impact oscillator system in comparison of a conventional device.

The effect of mechanical impact in MEMS-scale vibrational energy harvesters was studied by Le and Halvorsen [119]. The authors noted that mechanical impact in micro-scale devices is often inevitable and may be leveraged to widen the operational frequency bandwidth significantly. The MEMS electrostatic energy harvesting prototype exhibited bandwidth widening under impact, however, the efficiency was adversely affected by the loss of energy upon impact.

In a different iteration of the electrostatic MEMS energy harvester, Basset, et al. [62] combined end-stopper induced mechanical impact with nonlinear electrostatic force between oscillating electrodes. They observed a 30% half power bandwidth and 2 μW output power at 1g acceleration.
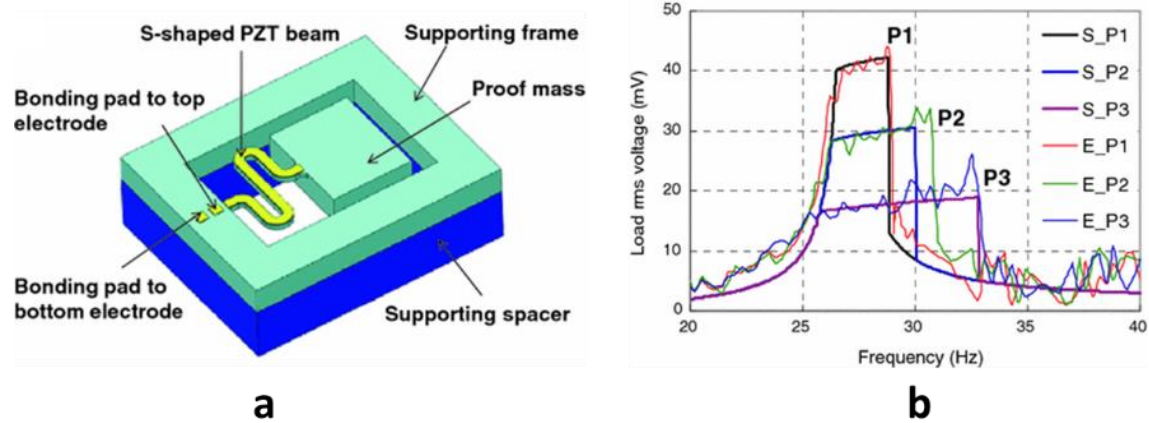
Figure 2.35: (a) Schematic diagram of piezoelectric energy harvester with S-shaped cantilever [Liu, et al. [120]]. (b) Widening of spectral response due to impact.

The impact induced hysteretic effect was also implemented in piezoelectric transduction based energy harvesting devices by Liu, et al. [120], where a large proof mass supported by an S-shaped PZT beam collided with a stopper [Figure 2.35]. The experimental results demonstrated the variability of the effective bandwidth with varying distance of the stopper.

2.4 Frequency tuning of vibration energy harvesters

While many sources generate vibrations with frequencies distributed over broad range of frequencies, many other sources produce vibrations with variable dominant frequencies that evolve in response to environmental conditions. Therefore, linear resonant oscillator based vibration energy harvesting systems are ineffective in such scenarios where there is a mismatch between the oscillator resonance frequency and the dominant frequency of available ambient vibration. One of the viable solutions to this problem is to tune the oscillator frequency such that it matches the ambient vibration frequencies. Tuning of the oscillator can be achieved by changing the mechanical characteristics (position of effective mass, equivalent spring stiffness) of the structure, or by tuning the electrical load in the circuit.
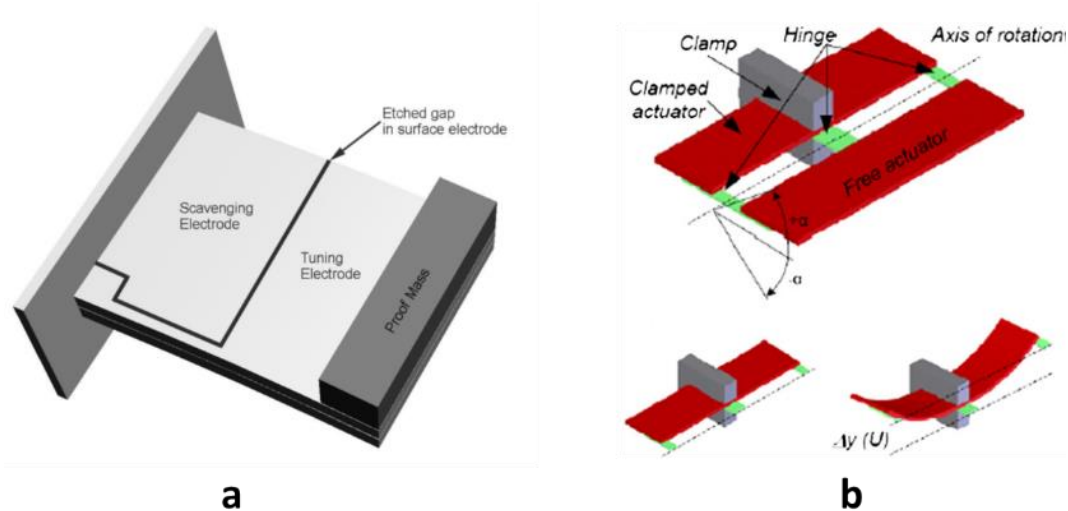
Figure 2.36: Piezoelectrically tunable energy harvester by (a) Roundy and Zhang [121], and (b) Peters, et al. [122].

2.4.1 Frequency tuning by changing mechanical characteristics

Adjustment of the resonance frequency of linear oscillators by changing mechanical characteristics can be implemented through re-positioning the effective mass or by manipulation of the spring stiffness. A piezoelectric cantilever based energy harvester with adjustable mass was reported by Wu, et al. [123], where a part of the total equivalent mass was made of a movable screw. The prototype demonstrated a frequency tunability in the range of 130 Hz to 180 Hz by moving the screw. Adjustment of spring stiffness in MEMS resonators by means of electrostatic force has been investigated by Scheibner, et al. [124] [125], and Yao and MacDonald [126]. Their studies involved tuning of the frequencies of MEMS oscillators using the variable electrostatic force between interdigitated comb electrodes by manipulation of bias voltage. One of the first piezoelectrically tuned energy harvesters was developed by Roundy and Zhang [121], where they used two separate piezoelectric patches attached to a single cantilever. While one of the patches were used for harvesting electricity, the other was used to tune the stiffness of the cantilever, and thereby the resonance frequency of the system [Figure 2.36(a)]. The oscillator was only tunable in a range of 62 − 66 Hz, and the tuning mechanism consumed more power than harvested by the generator. Since the active tuning mechanism consumed more power than that generated, the authors had concluded that a passive frequency tuning method should be more realistic. However, it has been shown later by Peters, et al. [122] that piezoelectric active tuning mechanisms could be designed to harvest more energy than expended in tuning. An improved version of this concept was realized by Peters, et al.

[127], where a clamped and a free piezoelectric actuator were connected together through piezoelectric hinges [Figure 2.36(b)]. An applied electric potential could effectively change the shape and increase the stiffness of the device. With an applied voltage of ± 5 V the device could be tuned in the range of 66 – 89 Hz, which is almost 30% of the initial resonance frequency. Similar piezoelectric stiffness manipulation for resonance frequency tuning were also investigated by Lallart, et al. [128] and Wischke, et al. [129].
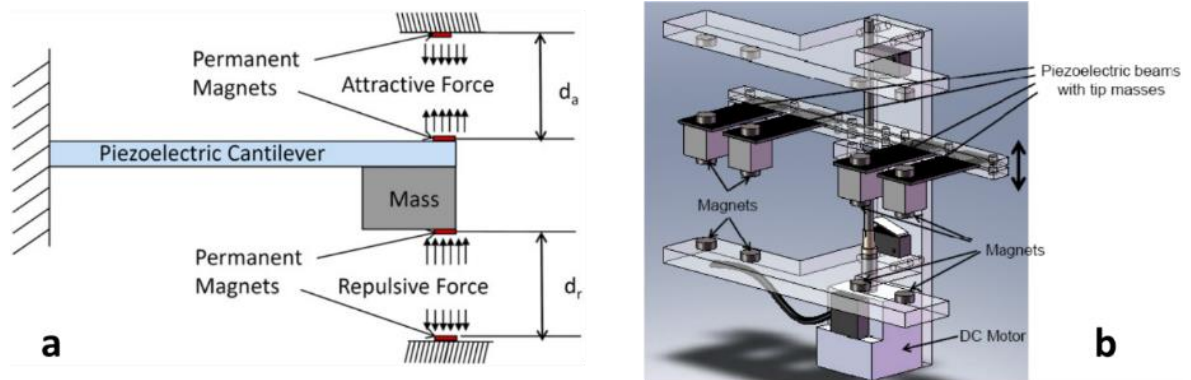
Figure 2.37: (a) Schematic diagram of a magnetically tunable piezoelectric energy harvester by Challa, et al. [130]. (b) An improved and autonomous prototype of the concept [Challa, et al. [131]].

One of the major drawbacks of implementing piezoelectric tuning for real-life application is that it is an *active* or *continuous* tuning mechanism, i.e. the piezoelectric actuator has to be powered continuously for maintaining the change in stiffness, which often lead to more power consumed in tuning than could be harvested from ambient vibration. Therefore, mechanical tuning by other methods, such as variable magnetic force was investigated by some research groups. A novel magnetic tuning mechanism was incorporated into a piezoelectric energy harvester by Challa, et al. [130]. A pair of permanent magnets bonded on a piezoelectric cantilever interacted with another pair of magnets mounted on an adjustable frame, which allowed for manipulation of the force exerted on the cantilever [Figure 2.37(a)]. This arrangement yield tunability of the resonance frequency of the piezoelectric cantilever in a range of 22 – 32 Hz around an initial resonance frequency of 26 Hz. This concept was further improved in an autonomous version of the original design [Challa, et al. [131]], where an algorithmically controlled DC stepper motor was used to manipulate the distance between the magnet arrays and tune the stiffness [Figure 2.37(b)]. The authors demonstrated that tuning over the maximum frequency range (± 25% of initial

resonance) could be performed using the energy harvested in a period of ~88 minutes at a vibrational excitation of 0.1g.
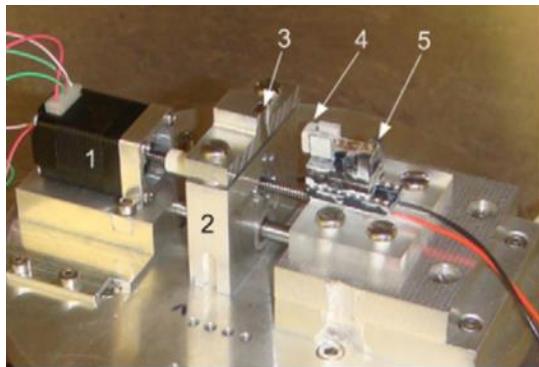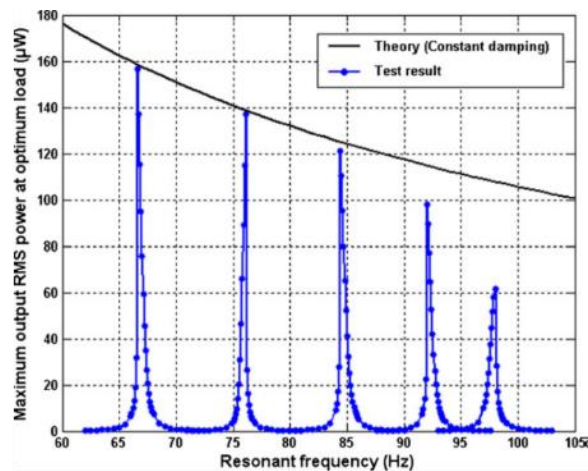
Figure 2.38: (a) Magnetically tunable energy harvester developed by Zhu, et al. [132]. (b) The device is tunable in a range of 67.6 – 98 Hz by variable magnetic force.

A simpler iteration of this magnetic tuning mechanism was developed by Zhu, et al. [132] and implemented in an electromagnetic transduction system [Figure 2.38(a)]. Their prototype demonstrated a tunability over a frequency range of 67.6 Hz to 98 Hz by the variable axial magnetic force and generated 61.6 µW – 156.6 µW power at 0.06g applied excitation [Figure 2.38(b)]. Furthermore, the authors developed a closed-loop control system Zhu, et al. [133] for fully automatic tuning of the resonance frequency in response to change in the ambient vibration frequency. This magnetic tuning architecture was also investigated by Aboulfotoh, et al. [134] and Ayala-Garcia, et al. [135] in electromagnetic devices and by Al-Ashtari, et al. [136] in a piezoelectric energy harvester.

2.4.2 Frequency tuning by electrical load variation

The electric energy generated by vibration energy harvesters are often extracted across certain optimum electrical loads, which primarily depends on the electromechanical transduction system. One of the interesting effects of varying the electrical load to a non-optimal value is a substantial modification in the electrical damping coefficient, which leads to shift in the power spectrum of the generator. Some research groups have investigated the utility of this effect to broaden the operational frequency range of vibration energy harvesters. Zhu, et al. [137] developed a detailed theoretical framework by analysing the effect of a variable capacitive load connected in parallel across a resistive

load. By varying the load capacitor value from 0 nF to 1400 nF, the researchers were able to tune the resonance frequency of the energy harvesting oscillator over a range of ~5 Hz [Figure 2.39].
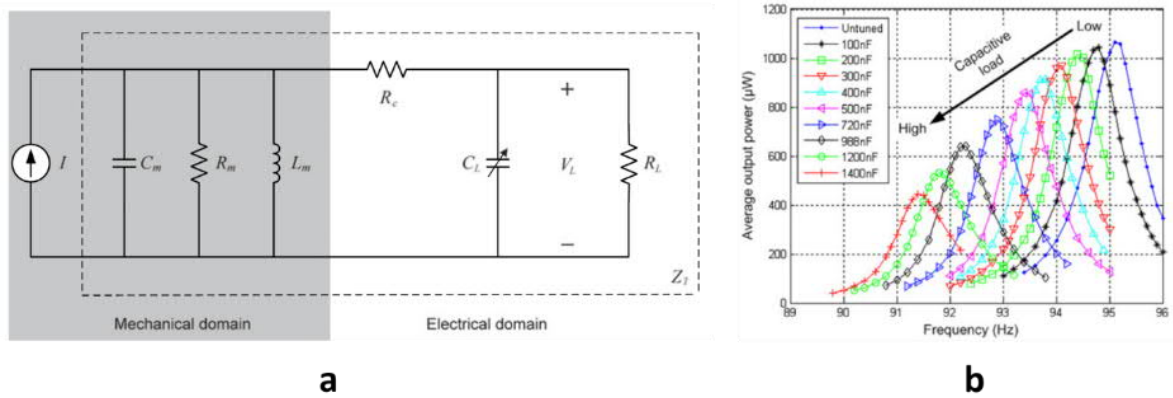
Figure 2.39: (a) Equivalent circuit model of an energy harvester with variable capacitive load [137]. (b) The effect of capacitance variation on power spectrum.

However, it was illustrated in [137] that the output power was adversely affected due to tuning by capacitive load variation, and the authors suggested that the electromechanical coupling factor should be maximized to alleviate the effect of power level attenuation. The resonance frequency tuning by electrical load variation was also investigated by Cammarano, et al. [138] and Mallick and Roy [139], where the authors used a generalized load comprising both resistive and reactive components. It was demonstrated in [138] that the half-power bandwidth could be significantly widened by using a generalized load over a conventional resistive load. A bidirectional tuning mechanism by manipulation of a complex load was developed in [139], where the authors demonstrated that the resonance frequency of the device could be tuned towards the lower frequencies by increasing the capacitive load, while it could be tuned for higher frequencies by increasing the inductive load. However, the bandwidth widening effect of frequency tuning by load variation was generally very limited (< 5 Hz) in most of the studied prototypes.

2.5 Micro-scale vibration energy harvesters

The miniaturization of vibration energy harvesters is envisaged to facilitate batch fabrication, integration with sensor and power management electronics, and significant reduction in manufacturing and deployment cost. However, with reduction in overall device size, the power generation capability of individual devices are severely diminished. In addition, miniaturization in device dimensions also result in significant increase in the operating frequency of devices, which is unsuitable for largely low frequency ambient

vibration sources. Potential solutions to this problem includes innovation in resonator design topologies, as the MEMS microfabrication techniques allow for complex spring structures. Also, the resonance frequency of such devices can be reduced by using polymer materials (e.g. PDMS, PMMA etc.) for the spring structure. Furthermore, by combining multiple micro-scale energy harvesters, the problem of diminished power output can be alleviated to some extent.

Due to the ease of integration with the standard MEMS fabrication process, electrostatic energy harvesters are prevalent at micro scale [Mitcheson, et al. [60], Basrour, et al. [61], Boisseau, et al. [58]]. Some nonlinear mechanisms arising from electrostatic force and mechanical impact [Basset, et al. [62], Le and Halvorsen [119]] and nonlinear spring topology [Nguyen, et al. [140]] have also been investigated for MEMS electrostatic micro-generators.
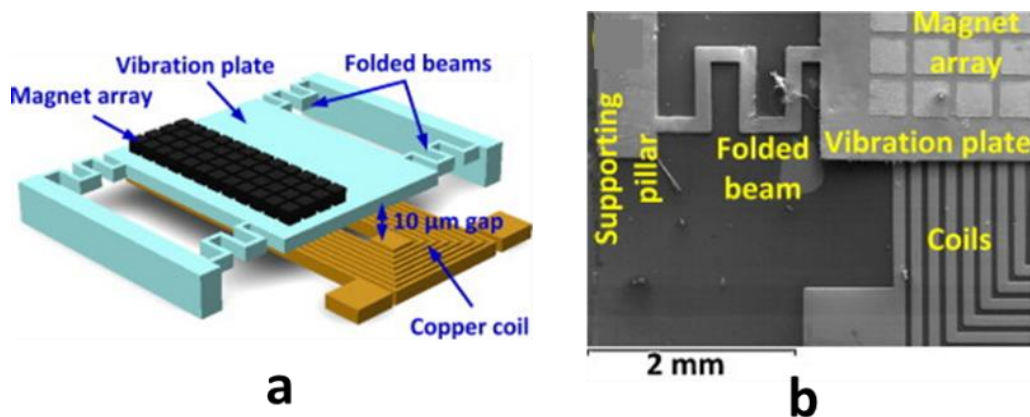
Figure 2.40: (a) MEMS electromagnetic harvester, and (b) fabricated prototype [Han, et al. [15]].

A Comprehensive review of MEMS-scale vibration energy harvesters using electromagnetic transduction has been published by Tan, et al. [141]. One of the first MEMS energy harvesters using electromagnetic transduction was developed by Williams and Yates [6], where a power output of 1 µW at a vibration of 70 Hz was predicted. Later Li, et al. [142] and Ching, et al. [143] developed MEMS energy harvesters using micro-machined silicon spring and micro-coils. The device volume was 1 cm^3, and the prototype generated 830 µW power at 110 Hz frequency, and it was able to power an FM radio and infra-red transmitter. The oscillation in these devices were in the out-of-plan direction. However, Kulkarni, et al. [144] proposed an alternative design based on in-plane oriented oscillation, also comprising silicon spring and micro-fabricated planar coils. The device

produced 586 nW at 1g acceleration and 60 Hz resonance frequency. Pioneering work on piezoelectric MEMS energy harvesters were reported by Roundy and Wright [145], where the prototype generated 375 µW from a 0.25g acceleration at 120 Hz frequency. Based on a similar piezoelectric cantilever structure, Renaud, et al. [146] developed a MEMS-scale energy harvester that generated 40 µW with a resonance frequency of 1.8 kHz. Most of these prototypes were fabricated in a semi-integrated approach, where the spring might be micro-fabricated, but the magnet, and in some instances the coils, were fabricated by conventional process.

Some of the articles published lately attempted to improve the compatibility of electromagnetic transduction with the MEMS fabrication process. Wang, et al. [9] developed a sandwich-shaped MEMS compatible device which produced 0.61 µW at 1.5g acceleration. A planar electromagnetic harvester with multipole magnetic sheet was reported by Roundy and Takahashi [147], which generated 3 V at a 260 Hz vibration frequency. Han, et al. [148] reported an integrated harvester with electroplated CoMnNiP magnet and micro-fabricated planar coil. The prototype generated 3.6×10^{-4} µW power at 1 g acceleration. In a later iteration [Figure 2.40], the power output was improved (1.12×10^{-2} µW) by using an electroplated array of magnets [Han, et al. [15]].

The cantilever-based topology is robust and most often implemented in MEMS piezoelectric energy harvesters, and is one of the easiest to fabricate. On the other hand, MEMS-scale electromagnetic devices often employ complex spring structures, magnetic materials and micro-coils that are significantly challenging to fabricate and integrate using the CMOS fabrication process. The electrostatic transduction mostly uses materials and processes that are compatible with the CMOS microfabrication techniques, and are most suitable for integration with microelectronic circuits. However, the energy harvesting capabilities of all of the transduction methods are significantly diminished with scaling down to the MEMS-scale.
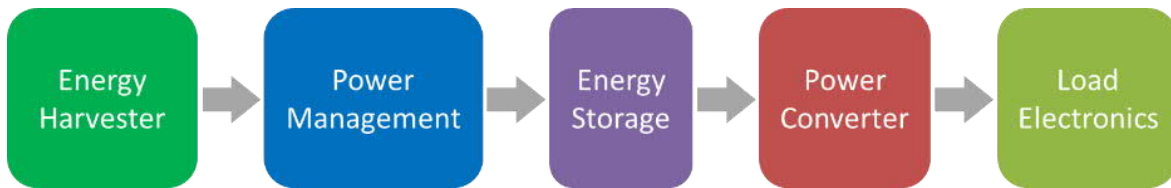
Figure 2.41: Generic path of energy flow from harvester to the load electronics

2.6 Power management of energy harvesters

In order to convert and store the electrical energy transduced from mechanical vibrations, appropriate power management circuits and energy storage components are required. The electricity generated by vibrational energy harvesters are dependent on the nature of vibration, transduction and are variable with time. Electricity generated from indirectly forced or oscillator-based harvesters are generally sinusoidal in nature, with the voltage/ current amplitude being dependent on the transduction mechanism, and the vibration frequency. On the other hand, directly forced oscillators often produce electricity in the form of short pulses. Both the regular sinusoidal and irregular pulse type electric signal are generally rectified to convert into DC signal, which is then further conditioned and stored in a battery or super-capacitor, and later converted for use with the load electronics [Figure 2.41]. However, energy is lost in each of these steps from the harvester to the load, and the principal objective of designing power management and conversion circuits is to minimize these losses to maximize the overall efficiency. A comprehensive review of the various power conditioning circuits developed for different kinetic energy harvesting systems was compiled by Szarka, et al. [149].

2.6.1 Rectification or AC – DC conversion

Most of the conventional electronic circuits require regulated DC input voltage for operation, whereas the typical vibration energy harvesting devices generate time varying voltage and currents in the form sinusoids or other complex periodic waveforms. Therefore, rectification of the output voltage from the energy harvesters is an essential first step. The most widely adopted rectification circuit consist of four diodes or transistors forming a full-wave bridge rectifier [Mitcheson, et al. [150], Figure 2.42(a)]. However, the forward bias voltage drop across diodes, and the reverse bias leakage current are the primary source of power loss in a diode based rectification circuit [Rajasekaran, et al. [151]].
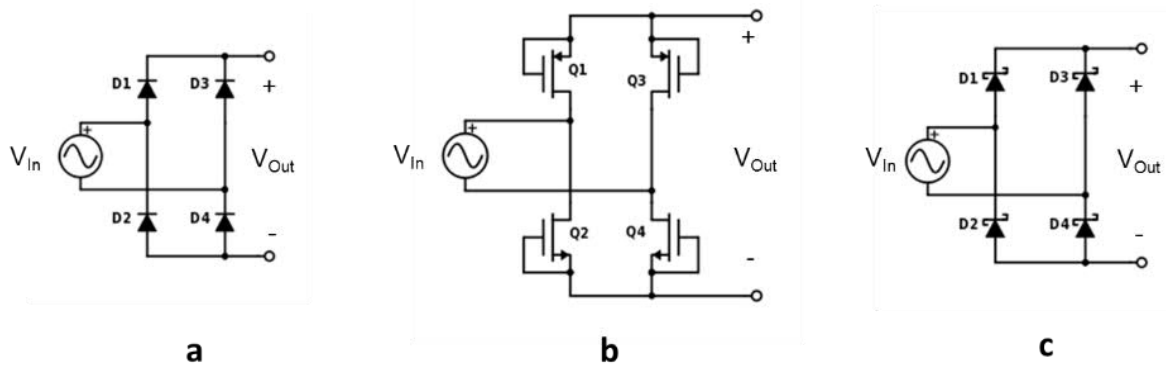
Figure 2.42: (a) Diode bridge rectifier, (b) Diode-connected MOS rectifier, (c) Schottky diode bridge rectifier.

The alternative architecture often implemented in integrated circuits involves diode-connected MOS transistors, where the source of the transistors are directly connected to the corresponding gates [Le, et al. [152], Figure 2.42(b)]. In such configurations, the gate threshold voltage may have substantial impact on the overall efficiency of the rectifier. Therefore, reduction in the forward voltage drop can increase the output voltage to some extent and boost the output power and efficiency. The Schottky diode-based rectifiers offer lower voltage drop in comparison to conventional p-n junction and diode connected rectifiers, albeit with higher reverse leakage current [Figure 2.42(c)]. In order to circumvent these issues, different gate cross-coupled MOS rectifier topologies has been proposed [Hashemi, et al. [153], Colomer-Farrarons, et al. [154]], which demonstrated an increase of $60 - 80\%$ boost in power conversion efficiency over conventional diode-bridge rectifier [Figure 2.43]. Forward voltage drop as low as 0.1 V has been achieved using such rectifier configurations, although input voltages > 1 V are still required to switch the MOS transistors ON or OFF completely during the forward or reverse cycle of the input waveform.

The rectifier topologies reported in [151] - [154] are passive in nature, i.e. no external signal is applied for switching the diodes and transistors. The rectification efficiency can be enhanced further by implementing active rectification where the diodes and transistors might be switched synchronously. This is usually implemented by driving MOSFETs through comparators that monitor the difference in source-drain voltage of transistors [Peters, et al. [155]]. However, the control circuits required for the switching introduce additional power consumption, which has been reported to be in the range of a few microwatts [155] to a few hundred nanowatts [Seeman, et al. [156]].
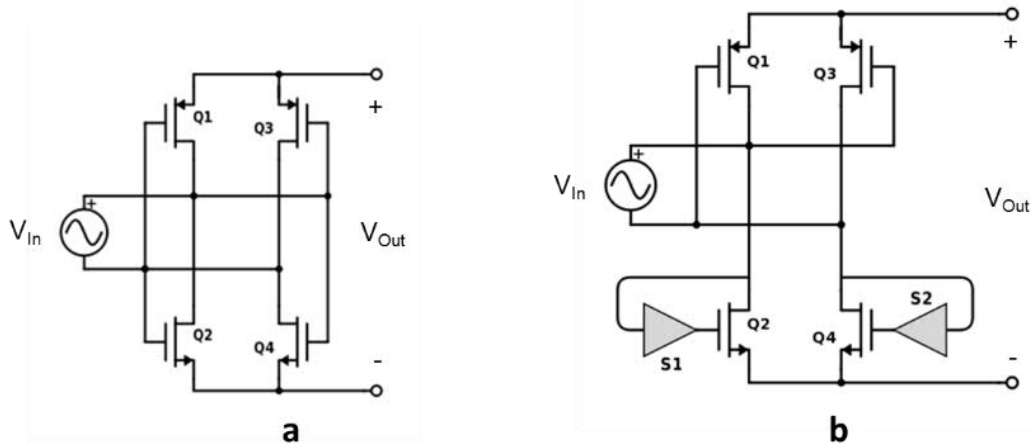
Figure 2.43: (a) Gate cross-coupled MOS rectifier, (b) Active rectifier with cross-coupled PMOS switches.

The most widely adopted active rectifier topologies include two actively switched and two gate cross-coupled MOSFETs [Figure 2.43 (b)]. The power conversion efficiencies reported for such active rectification architectures are typically $80 - 90\%$ [Bawa and Ghovanloo [157]] for light loading conditions. In general, the synchronous active rectification topologies are more efficient than the passive rectifiers. Active rectifiers, however, need to overcome the problem of cold start in a fully autonomous scenario where no power supply or previously stored energy is available to energize the switching circuits from OFF to ON state. Some researchers proposed the use of additional passive rectification components [Marinkovic, et al. [158]] due to their comparatively low start-up voltage, which could be used to initially charge up a temporary storage capacitor. An innovative solution to this problem was proposed by Ramadass and Chandrakasan [159] where the authors used a mechanically activated switch to achieve start-up voltage as low as 35 mV, which was then boost converted to 1V.

2.6.2 Voltage multiplier or switched capacitor converters

Voltage multiplier or switched capacitor circuits has been used as rectifier elements, as well as charge pumps in power conversion circuits for application in energy harvesters. Typical voltage multipliers or switched capacitor converters can be designed by combining diodes (acting as switch) and capacitors in ladder formation as shown in Figure 2.44.
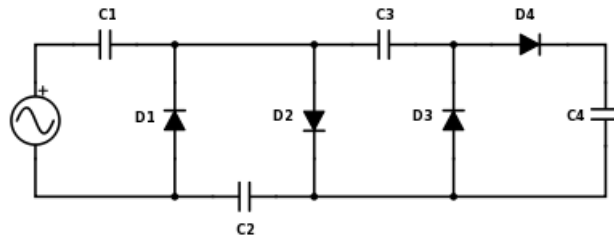
Figure 2.44: Voltage quadrupler circuit with ladder configuration

The principal sources of power loss in these switched capacitor architectures are due to the diode forward voltage drops, and losses due to capacitor charging cycles [Tse, et al. [160]]. At low frequency operations, the capacitor charging losses are predominant, while at high frequencies the diode losses are more prominent [Seeman and Sanders [161]]. Usually the passive voltage multiplier or switched capacitor circuits are deployed using low voltage drop diode equivalents or Schottky diodes, which can achieve an efficiency of ~ 65% [Torah, et al. [162]].
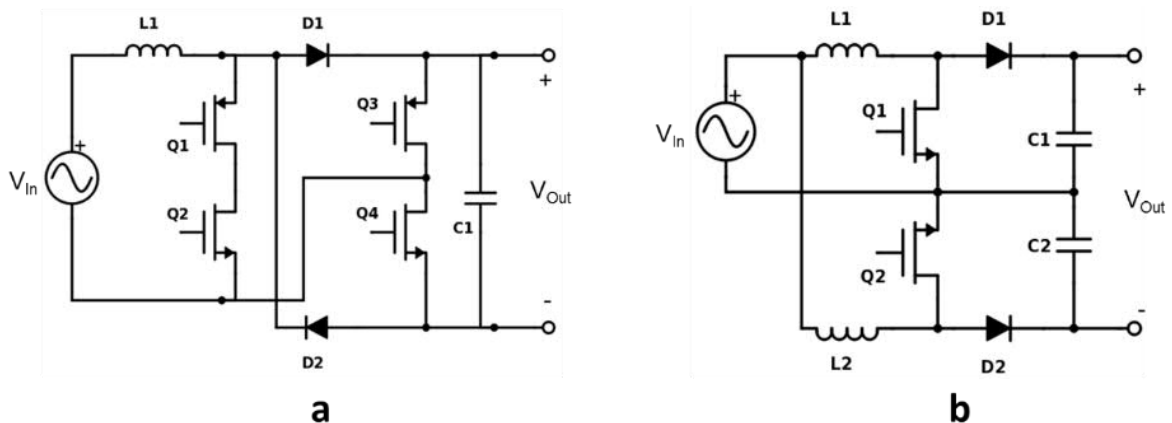
Figure 2.45: (a) Switch-mode converter developed by Dwari and Parsa [163]. (b) Dual inductor based boost converter developed by Mitcheson, et al. [164]

Switch-mode converters that require no separate rectification stage and can directly convert AC to DC can be designed by using switched inductors, which offers the benefit of more effective current and voltage regulation and can operate with very low input voltages. [Dwari and Parsa [163]] demonstrated a single inductor topology which used MOSFETs as additional secondary switches, and achieved a conversion efficiency of 60% [Figure 2.45(a)]. A dual inductor based topology combining two boost converters was developed by Mitcheson, et al. [164], which had a 44% efficiency [Figure 2.45(b)].

2.7 Benchmarking vibration energy harvesters

The comparative study of various energy harvesting devices requires identification of benchmarking parameters that take into account variables such as power output, device size, excitations, bandwidth etc. Unfortunately, the energy harvesting systems reported in the literature incorporate a plethora of transduction mechanisms, nonlinearity, and frequency tuning methods, resulting in widely variable output performances. Therefore, it is challenging to formulate a unique benchmarking parameter suitable for comparing all of the different device behaviours. In this section device performances have been compared against two widely adopted benchmarking parameters: the normalized power density (NPD), and the energy harvester figure of merit (EHFOM). The NPD, which normalizes the peak harvested power against device volume and applied acceleration, was initially proposed by Beeby, et al. [17], and has been used by several research groups in subsequent works. The EHFOM, on the other hand, was proposed by Sebald, et al. [165], and normalizes the average harvested power against the half-power bandwidth.

2.7.1 Normalized power density (NPD)

The normalized power density (NPD) [17] takes into consideration the peak power output, acceleration, and device volume [Eq. 2.33].

$$NPD = \frac{P_{Max}}{Volume \times (Acceleration)^2} \qquad 2.33$$

Where P_{Max} is the peak power at the applied vibrational acceleration. The *NPD* normalizes the output power against device size and applied vibrational acceleration. However, it does not take into consideration the operational bandwidth or the operational frequency range. A comparison of *NPD* of devices with different transduction mechanisms has been shown in Figure 2.46.

The *NPD* of the electromagnetic transducer based energy harvesters are moderately dependent on the volume of the device, which is attributable to the fact that the electromagnetic transduction strongly depends on the size of the magnet. Also, there is a clear limitation on the miniaturization of electromagnetic energy harvesters, which incorporates complex architectures, and even the MEMS scale devices are mostly semi-integrated. The *NPD* of piezoelectric energy harvesters are apparently immune to the volume scaling effect, and are suitable for miniaturization.
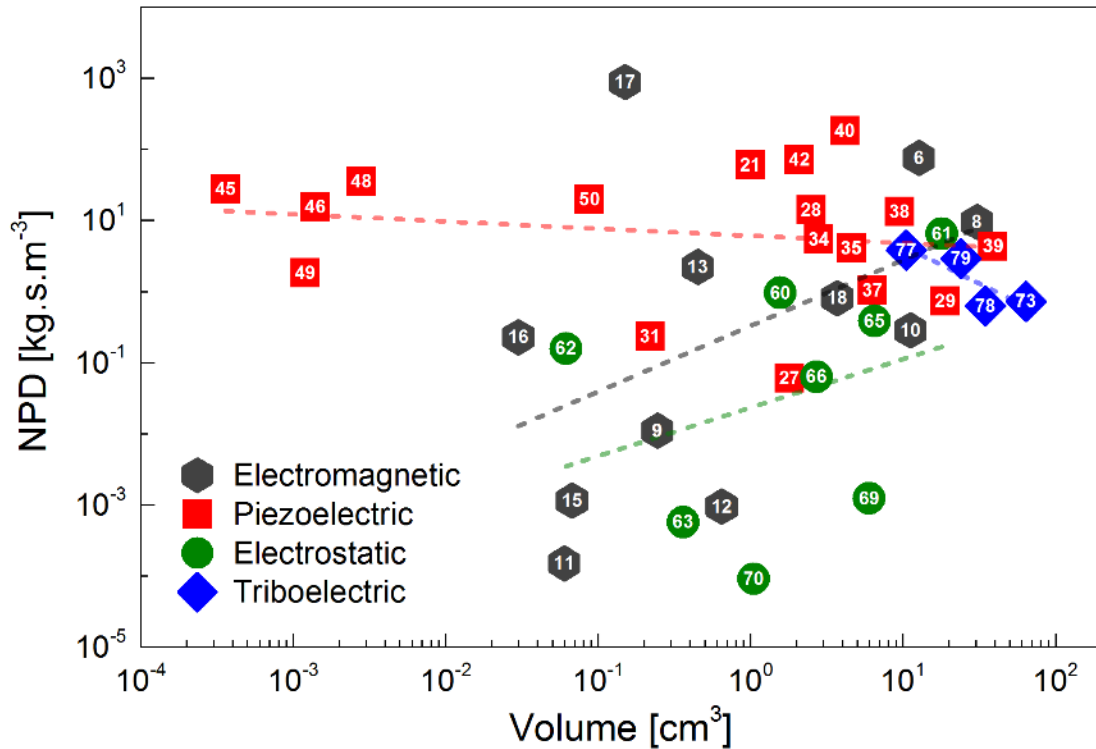
Figure 2.46: Comparison of Normalized Power Density (NPD) of devices with different transduction mechanisms. The dotted lines of the same colours as the symbols act as a guide to the eye to help follow the general trend. The numbers within the symbols correspond to the cited works listed in the references at the end of this chapter.

The *NPD* of electrostatic energy harvesters also tend to increase with volume, which can result from enhanced exchange of charge due to the larger active surface area accommodated within a larger volume. On the other hand, *NPD* of many triboelectric energy harvesters cannot be computed, since the data regarding the total volume, average power output, and frequency of applied vibration are often not reported in the literature. However, depending on the limited available data, The *NPD* of triboelectric energy harvesters exhibit a weak downward trend.

2.7.2 Energy harvester figure of merit (EHFOM)

The *NPD* does not take the operational frequency or bandwidth of devices into account, and is not suitable for benchmarking devices that are designed to exploit the ambient broadband vibrations. Sebald, et al. [165] proposed an energy harvester figure of merit (EHFOM) that takes into consideration the operational frequency and the half-power bandwidth (3dB bandwidth) of vibration energy harvesting devices,

$$EHFOM = \frac{P_{Max}}{(Acceleration)^2} \times \frac{BW_{3dB}}{f_0}$$

2.34

Where f_0 is the peak power frequency, and BW_{3dB} is the half-power bandwidth of the device at the applied vibrational acceleration. The *EHFOM* is more appropriate to compare the performances of nonlinear and tunable vibration energy harvesters that are designed to exhibit broadband response or frequency tunability.
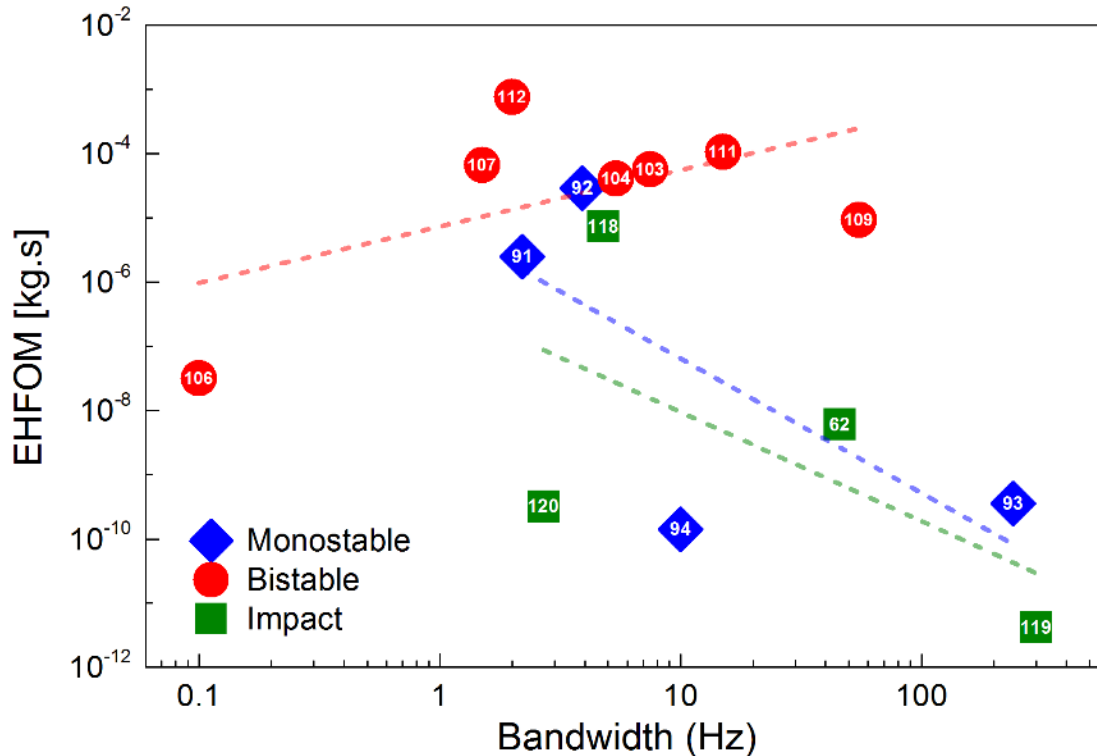
Figure 2.47: Comparison of energy harvester figure of merit (EHFOM) of devices with different nonlinear mechanisms. The dotted lines of the same colours as the symbols act as a guide to the eye to help follow the general trend. The numbers within the symbols correspond to the cited works listed in the references at the end of this chapter.

The *EHFOM*s of devices with different nonlinear mechanisms have been plotted in Figure 2.47, which shows that nonlinear bistable devices generally exhibit higher *EHFOM* than monostable and impact inducing devices. The degradation in the *EHFOM* of nonlinear monostable devices might be a result of the increasing nonlinear spring restoration force in the high energy branch of the frequency response, which limits the amplitude of motion and consequently, the harvested energy. In case of devices incorporating mechanical impact induced nonlinearity, the *EHFOM* tend to degrade with increasing bandwidth. This

might stem from the fact that broader bandwidth due to impact induced nonlinearity are usually a result of more frequent energy dissipative impacts, leading to lower harvested energy and lower *EHFOM*.

The *EHFOM*s of energy harvesting devices incorporating mechanical and electrical frequency tuning mechanisms are shown in Figure 2.48. There are only a few precedents of electrically tuned energy harvesters in literature, and the typical tuning ranges are narrow (< 10 Hz). On the other hand, several mechanical frequency tuning methods have been explored by researchers, and often exhibit much wider frequency tuning range. The *EHFOM*, however, tends to decrease with increasing tuning range, which indicates a sacrifice in harvested power when frequency tuning mechanisms are incorporated.
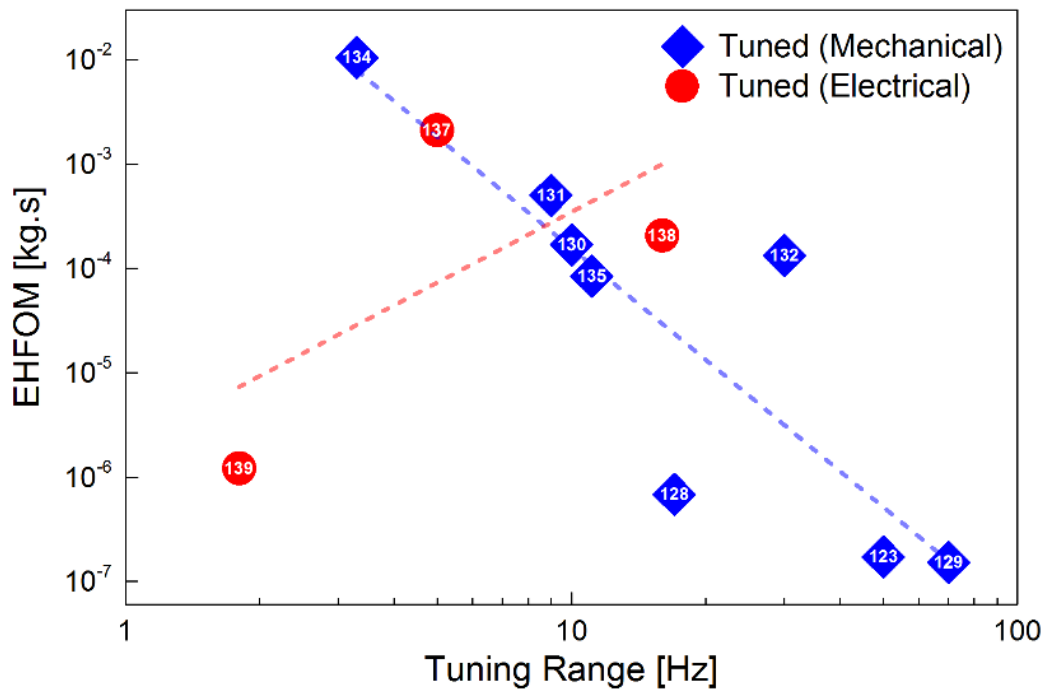
Figure 2.48: Comparison of enery harvester figure of merit (EHFOM) of devices with different frequency tuning mechanisms. The dotted lines of the same colours as the symbols act as a guide to the eye to help follow the general trend. The numbers within the symbols correspond to the cited works listed in the references at the end of this chapter.

A critical drawback of this reported *EHFOM* is the lack of normalization of device performance against device size, and might be biased to favour larger-sized devices over miniaturized ones.

2.8 Conclusion

This chapter provide a detailed overview regarding some of the key aspects of state-of-the-art in the field of vibration energy harvesting. It starts with the discussion on the various transduction mechanisms utilized to convert mechanical vibrations into electricity, and qualitatively compares the features of the transduction methods. In the next section the theoretical background of conventional linear oscillator based vibration energy harvesters are discussed, along with their application as vibration energy harvesting devices. The more advanced nonlinear oscillator based vibration energy harvesters are discussed in the following section (Section 2.3), which encompass the nonlinear Duffing monostable oscillators, bistable oscillators, and nonlinear effects induced by mechanical impacts. The application of each of these nonlinear effects in broadening the frequency bandwidth of different vibration energy harvesting devices has been illustrated. The approach of frequency tuning by various mechanical and electrical methods in order to broaden the operational frequency range vibration energy harvesters has been discussed in the next section. The discussion on micro-scale or MEMS-scale vibration energy harvesters, and the different power management circuits employed to efficiently convert harvested energy into usable electricity follows next. Finally, the issue of comparing performances of vibration energy harvesters in the scope of different transductions, nonlinearities, and frequency tuning mechanisms have been discussed. In addition to contributing a survey of the state-of-the-art vibration energy harvesting research, this chapter forms the groundwork for the work presented in the subsequent chapters of this thesis.

The study of literature in the field of vibration energy harvesters underlines the need for devices with wide frequency response, where the incorporation of nonlinearity and frequency tuning mechanisms have reported encouraging outcomes. Therefore, investigation on different nonlinearities and tuning methods, and their implementation in energy harvesting devices and systems will be presented in the subsequent chapters. The miniaturization of dynamically complex energy harvesting devices is required for economical micro-fabrication, and integration with interfacing electronics and sensor systems. However, device miniaturization leads to significant reduction in harvested power output and severely limits its applicability. Therefore, increasing the harvested energy density in MEMS-scale devices is a significant research challenge that will be investigated in this thesis. Furthermore, the issue of power management systems for processing the

harvested energy, especially at the low input voltage levels which is common in vibration energy harvesting devices, will be probed to develop effective solutions.

References

[1]   S. P. Beeby and T. O'Donnell, "Electromagnetic Energy Harvesting," in *Energy Harvesting Technologies*, S. Priya and D. J. Inman, Eds., ed Boston, MA: Springer US, 2009, pp. 129 - 161.

[2]   D. S. L. Cardwell, "On Michael Faraday, henry wilde, and the dynamo," *Annals of Science,* vol. 49, 1992.

[3]   D. Spreemann, Y. Manoli, B. Folkmer, and D. Mintenbeck, "Non-resonant vibration conversion," *Journal of Micromechanics and Microengineering,* vol. 16, pp. 169 - 173, 2006.

[4]   M. Hayakawa, "Electronic wristwatch with generator," ed: Google Patents, 1991.

[5]   K. Sasaki, Y. Osaki, J. Okazaki, H. Hosaka, and K. Itao, "Vibration-based automatic power-generation system," *Microsystem Technologies,* vol. 11, pp. 965 – 969, 2005.

[6]   C. B. Williams and R. B. Yates, "Analysis of a micro-electric generator for microsystems," *Sensors and Actuators a-Physical,* vol. 52, pp. 8-11, 1996.

[7]   C. R. Saha, T. O'Donnell, N. Wang, and P. McCloskey, "Electromagnetic generator for harvesting energy from human motion," *Sensors and Actuators A: Physical,* vol. 147, pp. 248-253, 2008.

[8]   T. von Büren and G. Tröster, "Design and optimization of a linear vibration-driven electromagnetic micro-power generator," *Sensors and Actuators A: Physical,* vol. 135, pp. 765 - 775, 2007.

[9]   P. Wang, K. Tanaka, S. Sugiyama, X. Dai, X. Zhao, and J. Liu, "A micro electromagnetic low level vibration energy harvester based on MEMS technology," *Microsystem Technologies,* vol. 15, pp. 941-951, 2009.

[10] B. Yang, C. Lee, W. Xiang, J. Xie, J. H. He, R. K. Kotlanka*, et al.*, "Electromagnetic energy harvesting from vibrations of multiple frequencies," *Journal of Micromechanics and Microengineering,* vol. 19, p. 035001, 2009.

[11] Q. Yuan, X. Sun, D. M. Fang, and H. Zhang, "Design and microfabrication of integrated magnetic MEMS energy harvester for low frequency application," in *2011 16th International Solid-State Sensors, Actuators and Microsystems Conference*, 2011.

[12] D. Hoffmann, C. Kallenbach, M. Dobmaier, B. Folkmer, and Y. Manoli, "Flexible polyimide film technology for vibration energy harvesting," *Proceedings of the PowerMEMS,* 2009.

[13] C. T. Pan, Y. M. Hwang, H. L. Hu, and H. C. Liu, "Fabrication and analysis of a magnetic self-power microgenerator," *Journal of Magnetism and Magnetic Materials,* vol. 304, pp. 394 - 396, 2006.

[14] S. Roundy and E. Takahashi, "A planar electromagnetic energy harvesting transducer using a multi-pole magnetic plate," *Sensors and Actuators A: Physical,* vol. 195, pp. 98 - 104, 2013.

[15] M. Han, Z. Li, X. Sun, and H. Zhang, "Analysis of an in-plane electromagnetic energy harvester with integrated magnet array," *Sensors and Actuators A: Physical,* vol. 219, pp. 38-46, 2014.

[16] S. Kulkarni, S. Roy, T. O'Donnell, S. Beeby, and J. Tudor, "Vibration based electromagnetic micropower generator on silicon," *Journal of Applied Physics,* vol. 99, p. 08P511, 2006.

[17] S. P. Beeby, R. N. Torah, M. J. Tudor, P. Glynne-Jones, T. O'Donnell, C. R. Saha*, et al.*, "A micro electromagnetic generator for vibration energy harvesting," *Journal of Micromechanics and Microengineering,* vol. 17, pp. 1257 – 1265, 2007.

[18] T. Galchev, H. Kim, and K. Najafi, "A Parametric Frequency Increased Power Generator for Scavenging Low Frequency Ambient Vibrations," *Procedia Chemistry,* vol. 1, pp. 1439 - 1442, 2009.

[19] Z. Hadas, C. Ondrusek, and V. Singule, "Power sensitivity of vibration energy harvester," *Microsystem Technologies,* vol. 16, pp. 691-702, 2010.

[20] D. Zhu, S. Beeby, J. Tudor, and N. Harris, "Vibration energy harvesting using the Halbach array," *Smart Materials and Structures,* vol. 21, p. 075020, 2012.

[21] S. Roundy and P. K. Wright, "A piezoelectric vibration based generator for wireless electronics," *Smart Materials and Structures,* vol. 13, pp. 1131 – 1142, 2004.

[22] S. Roundy, E. S. Leland, J. Baker, E. Carleton, E. Reilly, E. Lai*, et al.*, "Improving power output for vibration-based energy scavengers," *IEEE Pervasive Computing,* vol. 4, pp. 28-36, 2005.

[23] M. Anthony, B. Scott, and P. Shashank, "Multiple cell configuration electromagnetic vibration energy harvester," *Journal of Physics D: Applied Physics,* vol. 44, p. 295501, 2011.

[24] G. Lewin, G. H. Myers, V. Parsonnet, and K. V. Raman, "AN IMPROVED BIOLOGICAL POWER SOURCE FOR CARDIAC PACEMAKERS," *ASAIO Journal,* vol. 14, pp. 215-219, 1968.

[25] E. Häsler, L. Stein, and G. Harbauer, "Implantable physiological power supply with PVDF film," *Ferroelectrics,* vol. 60, pp. 277 - 282, 1984.

[26] N. S. Shenck and J. A. Paradiso, "Energy scavenging with shoe-mounted piezoelectrics," *IEEE Micro,* vol. 21, pp. 30-42, 2001.

[27] P. Glynne-Jones, S. P. Beeby, and N. M. White, "Towards a piezoelectric vibration-powered microgenerator," *IEE Proceedings - Science, Measurement and Technology,* vol. 148, pp. 68-72, 2001.

[28] E. Reilly, F. Burghardt, R. Fain, and P. Wright, "Powering a wireless sensor node with a vibration-driven piezoelectric energy harvester," *Smart Materials and Structures,* vol. 20, p. 125006, 2011.

[29] S. Mehraeen, S. Jagannathan, and K. A. Corzine, "Energy Harvesting From Vibration With Alternate Scavenging Circuitry and Tapered Cantilever Beam," *IEEE Transactions on Industrial Electronics,* vol. 57, pp. 820-830, 2010.

[30]   S. Adhikari, M. I. Friswell, and D. J. Inman, "Piezoelectric energy harvesting from broadband random vibrations," *Smart Materials and Structures,* vol. 18, p. 115005, 2009.

[31]   Z. Cao, J. Zhang, and H. Kuwano, "Design and characterization of miniature piezoelectric generators with low resonant frequency," *Sensors and Actuators A: Physical,* vol. 179, pp. 178 - 184, 2012.

[32]   P. Becker, E. Hymon, B. Folkmer, and Y. Manoli, "High efficiency piezoelectric energy harvester with synchronized switching interface circuit," *Sensors and Actuators A: Physical,* vol. 202, pp. 155 - 161, 2013.

[33]   S. Kim, W. W. Clark, and Q.-M. Wang, "Piezoelectric energy harvesting using diaphragm structure," in *Smart Structures and Materials 2003*, San Diego, California, United States, 2003, pp. 307 - 318.

[34]   S. Kim, W. W. Clark, and Q.-M. Wang, "Piezoelectric Energy Harvesting with a Clamped Circular Plate: Analysis," *Journal of Intelligent Material Systems and Structures,* vol. 16, pp. 847 - 854, 2005.

[35]   C. Mo, L. J. Radziemski, and W. W. Clark, "Experimental validation of energy harvesting performance for pressure-loaded piezoelectric circular diaphragms," *Smart Materials and Structures,* vol. 19, p. 075010, 2010.

[36]   C. Mo, L. J. Radziemski, and W. W. Clark, "Analysis of piezoelectric circular diaphragm energy harvesters for use in a pressure fluctuating system," *Smart Materials and Structures,* vol. 19, p. 025016, 2010.

[37]   E. Minazara, D. Vasic, F. Costa, and G. Poulin, "Piezoelectric diaphragm for vibration energy harvesting," *Ultrasonics,* vol. 44, Supplement, pp. 699 - 703, 2006.

[38]   X. Chen, T. Yang, W. Wang, and X. Yao, "Vibration energy harvesting with a clamped piezoelectric circular diaphragm," *Ceramics International,* vol. 38, Supplement 1, pp. 271 - 274, 2012.

[39]   H. W. Kim, A. Batra, S. Priya, K. Uchino, D. Markley, R. E. Newnham*, et al.*, "Energy Harvesting Using a Piezoelectric "Cymbal" Transducer in Dynamic Environment," *Japanese Journal of Applied Physics,* vol. 43, p. 6178, 2004.

[40]   B. Ren, S. W. Or, X. Zhao, and H. Luo, "Energy harvesting using a modified rectangular cymbal transducer based on 0.71Pb(Mg1/3Nb2/3)O3–0.29PbTiO3 single crystal," *Journal of Applied Physics,* vol. 107, p. 034501, 2010.

[41]   J. Feenstra, J. Granstrom, and H. Sodano, "Energy harvesting through a backpack employing a mechanically amplified piezoelectric stack," *Mechanical Systems and Signal Processing,* vol. 22, pp. 721-734, 2008.

[42]   T. B. Xu, E. J. Siochi, J. H. Kang, L. Zuo, W. Zhou, X. Tang*, et al.*, "Energy harvesting using a PZT ceramic multilayer stack," *Smart Materials and Structures,* vol. 22, p. 065015, 2013.

[43]   J. Baker, S. Roundy, and P. Wright, "Alternative Geometries for Increasing Power Density in Vibration Energy Scavenging for Wireless Sensor Networks," in *3rd International Energy Conversion Engineering Conference*, ed: American Institute of Aeronautics and Astronautics, 2005.

[44]   S. H. Kwon, Y. K. Jun, S. H. Hong, and H. E. Kim, "Synthesis and dissolution behavior of β-TCP and HA/β-TCP composite powders," *Journal of the European Ceramic Society,* vol. 23, pp. 1039 - 1045, 2003.

[45]   Y. B. Jeon, R. Sood, J. h. Jeong, and S. G. Kim, "MEMS power generator with transverse mode thin film PZT," *Sensors and Actuators A: Physical,* vol. 122, pp. 16 - 22, 2005.

[46]   H. B. Fang, J. Q. Liu, Z. Y. Xu, L. Dong, L. Wang, D. Chen*, et al.*, "Fabrication and performance of MEMS-based piezoelectric power generator for vibration energy harvesting," *Microelectronics Journal,* vol. 37, pp. 1280 - 1284, 2006.

[47]   E. E. Aktakka, R. L. Peterson, and K. Najafi, "Thinned-PZT on SOI process and design optimization for piezoelectric inertial energy harvesting," in *2011 16th International Solid-State Sensors, Actuators and Microsystems Conference*, Beijing, China, 2011, pp. 1649 - 1652.

[48]   M. Defosseux, M. Allain, E. Defay, and S. Basrour, "Highly efficient piezoelectric micro harvester for low level of acceleration fabricated with a CMOS compatible process," *Sensors and Actuators A: Physical,* vol. 188, pp. 489 - 494, 2012.

[49]   M. Marzencki, Y. Ammar, and S. Basrour, "Integrated power harvesting system including a MEMS generator and a power management circuit," *Sensors and Actuators A: Physical,* vol. 145–146, pp. 363-370, 2008.

[50]   R. Elfrink, M. Renaud, T. M. Kamel, C. d. Nooijer, M. Jambunathan, M. Goedbloed*, et al.*, "Vacuum-packaged piezoelectric vibration energy harvesters: damping contributions and autonomy for a wireless sensor system," *Journal of Micromechanics and Microengineering,* vol. 20, p. 104001, 2010.

[51]   Z. L. Wang and J. Song, "Piezoelectric Nanogenerators Based on Zinc Oxide Nanowire Arrays," *Science,* vol. 312, pp. 242-246, 2006.

[52]   J. Song, J. Zhou, and Z. L. Wang, "Piezoelectric and Semiconducting Coupled Power Generating Process of a Single ZnO Belt/Wire. A Technology for Harvesting Electricity from the Environment," *Nano Letters,* vol. 6, pp. 1656–1662, 2006.

[53]   P. X. Gao, J. Song, J. Liu, and Z. L. Wang, "Nanowire Piezoelectric Nanogenerators on Plastic Substrates as Flexible Power Sources for Nanodevices," *Advanced Materials,* vol. 19, pp. 67-72, 2007.

[54]   X. Wang, J. Song, J. Liu, and Z. L. Wang, "Direct-Current Nanogenerator Driven by Ultrasonic Waves," *Science,* vol. 316, pp. 102-105, 2007.

[55]   Y. Hu, Y. Zhang, C. Xu, L. Lin, R. L. Snyder, and Z. L. Wang, "Self-powered system with wireless data transmission," *Nano Lett,* vol. 11, pp. 2572-2577, 2011.

[56]   Y. Hu, C. Xu, Y. Zhang, L. Lin, R. L. Snyder, and Z. L. Wang, "A Nanogenerator for Energy Harvesting from a Rotating Tire and its Application as a Self-Powered Pressure/Speed Sensor," *Advanced Materials,* vol. 23, pp. 4068 – 4071, 2011.

[57]   L. Lin, Y. Hu, C. Xu, Y. Zhang, R. Zhang, X. Wen*, et al.*, "Transparent flexible nanogenerator as self-powered sensor for transportation monitoring," *Nano Energy,* vol. 2, pp. 75-81, 2013.

[58] S. Boisseau, G. Despesse, and B. A. Seddik, "Electrostatic Conversion for Vibration Energy Harvesting," in *Small-Scale Energy Harvesting*, M. Lallart, Ed., ed InTech: InTech Open, 2012.

[59] F. U. Khan and M. U. Qadir, "State-of-the-art in vibration-based electrostatic energy harvesting," *Journal of Micromechanics and Microengineering,* vol. 26, p. 103001, 2016.

[60] P. Mitcheson, A. Holmes, E. Yeatman, T. Green, and P. Miao, "Micro-Machined Variable Capacitors for Power Generation," in *Electrostatics 2003*, 2004, pp. 53-58.

[61] S. Basrour, J. J. Chaillout, B. Charlot, G. Despesse, T. Jager, J. M. Leger*, et al.*, "Fabrication and characterization of high damping electrostatic micro devices for vibration energy scavenging," in *Symposium on Design, Test, Integration and Packaging of MEMS/MOEMS (DTIP 2005), June 1-3*, Montreux, Switzerland, 2005, pp. 386-390.

[62] P. Basset, D. Galayko, F. Cottone, R. Guillemet, E. Blokhina, F. Marty*, et al.*, "Electrostatic vibration energy harvester with combined effect of electrical nonlinearities and mechanical impact," *Journal of Micromechanics and Microengineering,* vol. 24, p. 035001, 2014.

[63] D. Hoffmann, B. Folkmer, and Y. Manoli, "Analysis and characterization of triangular electrode structures for electrostatic energy harvesting," *Journal of Micromechanics and Microengineering,* vol. 21, p. 104002, Oct 2011.

[64] D. H. Choi, C. H. Han, H. D. Kim, and J. B. Yoon, "Liquid-based electrostatic energy harvester with high sensitivity to human physical motion," *Smart Materials and Structures,* vol. 20, p. 125012, 2011.

[65] Y. Naruse, N. Matsubara, K. Mabuchi, M. Izumi, and S. Suzuki, "Electrostatic micro power generation from low-frequency vibration such as human motion," *Journal of Micromechanics and Microengineering,* vol. 19, p. 094002, 2009.

[66] M. Edamoto, Y. Suzuki, N. Kasagi, K. Kashiwagi, Y. Morizawa, T. Yokoyama*, et al.*, "Low-Resonant-Frequency Micro Electret Generator for Energy Harvesting Application," in *2009 IEEE 22nd International Conference on Micro Electro Mechanical Systems*, 2009, pp. 1059-1062.

[67] V. N. Kestelman, L. S. Pinchuk, and V. A. Goldade, *Electrets In Engineering: Fundamentals and Applications*, 1 ed. vol. 1. New York: Springer US, 2000.

[68] S. Bauer, "Electrets for biomedical applications," in *2011 - 14th International Symposium on Electrets*, Montpellier, France, 2011, pp. 229-230.

[69] H. Lo and Y. Tai, "Parylene-HT-based electret rotor generator," in *2008 IEEE 21st International Conference on Micro Electro Mechanical Systems*, Wuhan, China, 2008, pp. 984-987.

[70] Y. Suzuki, D. Miki, M. Edamoto, and M. Honzumi, "A MEMS electret generator with electrostatic levitation for vibration-driven energy-harvesting applications," *Journal of Micromechanics and Microengineering,* vol. 20, p. 104002, 2010.

[71] J. Henniker, "Triboelectricity in Polymers," *Nature,* vol. 196, p. 474, 1962.

[72] D. K. Davies, "Charge generation on dielectric surfaces," *Journal of Physics D: Applied Physics,* vol. 2, p. 1533, 1969.

[73]   J. Chen, G. Zhu, W. Yang, Q. Jing, P. Bai, Y. Yang, *et al.*, "Harmonic-resonator-based triboelectric nanogenerator as a sustainable power source and a self-powered active vibration sensor," *Adv Mater,* vol. 25, pp. 6094–6099, 2013.

[74]   Z. L. Wang, "Triboelectric Nanogenerators as New Energy Technology for Self-Powered Systems and as Active Mechanical and Chemical Sensors," *ACS Nano,* vol. 7, pp. 9533–9557, 2013.

[75]   X. Wen, W. Yang, Q. Jing, and Z. L. Wang, "Harvesting Broadband Kinetic Impact Energy from Mechanical Triggering/Vibration and Water Waves," *ACS Nano,* vol. 8, pp. 7405–7412, 2014.

[76]   S. Wang, S. Niu, J. Yang, L. Lin, and Z. L. Wang, "Quantitative Measurements of Vibration Amplitude Using a Contact-Mode Freestanding Triboelectric Nanogenerator," *ACS Nano,* vol. 8, pp. 12004–12013, 2014.

[77]   J. Yang, J. Chen, Y. Yang, H. Zhang, W. Yang, P. Bai, *et al.*, "Broadband Vibrational Energy Harvesting Based on a Triboelectric Nanogenerator," *Advanced Energy Materials,* vol. 4, p. 1301322, 2014.

[78]   W. Yang, J. Chen, Q. Jing, J. Yang, X. Wen, Y. Su, *et al.*, "3D Stack Integrated Triboelectric Nanogenerator for Harvesting Vibration Energy," *Advanced Functional Materials,* vol. 24, pp. 4090–4096, 2014.

[79]   W. Tang, T. Jiang, F. R. Fan, A. F. Yu, C. Zhang, X. Cao, *et al.*, "Liquid-Metal Electrode for High-Performance Triboelectric Nanogenerator at an Instantaneous Energy Conversion Efficiency of 70.6%," *Advanced Functional Materials,* vol. 25, pp. 3718–3725, 2015.

[80]   J. Yang, J. Chen, Y. Liu, W. Yang, Y. Su, and Z. L. Wang, "Triboelectrification-Based Organic Film Nanogenerator for Acoustic Energy Harvesting and Self-Powered Active Acoustic Sensing," *ACS Nano,* vol. 8, pp. 2649–2657, 2014.

[81]   X. Fan, J. Chen, J. Yang, P. Bai, Z. Li, and Z. L. Wang, "Ultrathin, Rollable, Paper-Based Triboelectric Nanogenerator for Acoustic Energy Harvesting and Self-Powered Sound Recording," *ACS Nano,* vol. 9, pp. 4236–4243, 2015.

[82]   S. G. Kim, S. Priya, and I. Kanno, "Piezoelectric MEMS for energy harvesting," *MRS Bulletin,* vol. 37, pp. 1039-1050, 2012.

[83]   T. O'Donnell, C. Saha, S. Beeby, and J. Tudor, "Scaling effects for electromagnetic vibrational power generators," *Microsystem Technologies,* vol. 13, pp. 1637–1645, 2007.

[84]   G. Zhu, B. Peng, J. Chen, Q. Jing, and Z. Lin Wang, "Triboelectric nanogenerators as a new energy technology: From fundamentals, devices, to applications," *Nano Energy,* vol. 14, pp. 126-138, 2015.

[85]   Z. L. Wang, J. Chen, and L. Lin, "Progress in triboelectric nanogenerators as a new energy technology and self-powered sensors," *Energy & Environmental Science,* vol. 8, pp. 2250-2282, 2015.

[86]   M. Ericka, D. Vasic, F. Costa, and G. Poulain, "Predictive energy harvesting from mechanical vibration using a circular piezoelectric membrane," in *IEEE Ultrasonics Symposium, 2005.*, 2005, pp. 946-949.

[87] E. P. James, M. J. Tudor, S. P. Beeby, N. R. Harris, P. Glynne-Jones, J. N. Ross*, et al.*, "An investigation of self-powered systems for condition monitoring applications," *Sensors and Actuators A: Physical,* vol. 110, pp. 171-176, 2004.

[88] X. Cao and Y. k. Lee, "Design and Fabrication of Mini Vibration Power Generator System for Micro Sensor Networks," in *2006 IEEE International Conference on Information Acquisition*, Shandong, China, 2006, pp. 91-95.

[89] A. H. Nayfeh and D. T. Mook, "Conservative Single-Degree-of-Freedom Systems," in *Nonlinear Oscillations*, ed: Wiley-VCH Verlag GmbH, 2007.

[90] M. F. Daqaq, R. Masana, A. Erturk, and D. Dane Quinn, "On the Role of Nonlinearities in Vibratory Energy Harvesting: A Critical Review and Discussion," *Applied Mechanics Reviews,* vol. 66, p. 040801, 2014.

[91] B. P. Mann and N. D. Sims, "Energy harvesting from the nonlinear oscillations of magnetic levitation," *Journal of Sound and Vibration,* vol. 319, pp. 515-530, 2009.

[92] P. Constantinou, P. H. Mellor, and P. D. Wilcox, "A Magnetically Sprung Generator for Energy Harvesting Applications," *IEEE/ASME Transactions on Mechatronics,* vol. 17, pp. 415-424, 2012.

[93] B. Marinkovic and H. Koser, "Smart Sand—a wide bandwidth vibration energy harvesting platform," *Applied Physics Letters,* vol. 94, p. 103505, 2009.

[94] D. Mallick, A. Amann, and S. Roy, "A nonlinear stretching based electromagnetic energy harvester on FR4 for wideband operation," *Smart Materials and Structures,* vol. 24, p. 015013, 2015.

[95] M. F. Daqaq, "Response of uni-modal duffing-type harvesters to random forced excitations," *Journal of Sound and Vibration,* vol. 329, pp. 3621-3631, 2010.

[96] M. F. Daqaq, "Transduction of a bistable inductive generator driven by white and exponentially correlated Gaussian noise," *Journal of Sound and Vibration,* vol. 330, pp. 2554-2564, 2011.

[97] W. Y. Tseng and J. Dugundji, "Nonlinear Vibrations of a Buckled Beam Under Harmonic Excitation," *Journal of Applied Mechanics,* vol. 38, pp. 467-476, 1971.

[98] P. Holmes, "A Nonlinear Oscillator with a Strange Attractor," *Philosophical Transactions of the Royal Society of London. Series A, Mathematical and Physical Sciences,* vol. 292, pp. 419-448, 1979.

[99] F. Cottone, H. Vocca, and L. Gammaitoni, "Nonlinear energy harvesting," *Physical Review Letters,* vol. 102, p. 080601, 2009.

[100] R. Masana and M. F. Daqaq, "Electromechanical Modeling and Nonlinear Analysis of Axially Loaded Energy Harvesters," *Journal of Vibration and Acoustics,* vol. 133, p. 011007, 2011.

[101] R. Masana and M. F. Daqaq, "Relative performance of a vibratory energy harvester in mono- and bi-stable potentials," *Journal of Sound and Vibration,* vol. 330, pp. 6036-6052, 2011.

[102] F. Cottone, L. Gammaitoni, H. Vocca, M. Ferrari, and V. Ferrari, "Piezoelectric buckled beams for random vibration energy harvesting," *Smart Materials and Structures,* vol. 21, p. 035021, 2012.

[103]   F. Cottone, P. Basset, H. Vocca, L. Gammaitoni, and T. Bourouina, "Bistable electromagnetic generator based on buckled beams for vibration energy harvesting," *Journal of Intelligent Material Systems and Structures,* vol. 25, pp. 1484-1495, 2013.

[104]   A. F. Arrieta, P. Hagedorn, A. Erturk, and D. J. Inman, "A piezoelectric bistable plate for nonlinear broadband energy harvesting," *Applied Physics Letters,* vol. 97, p. 104102, 2010.

[105]   D. N. Betts, H. A. Kim, C. R. Bowen, and D. J. Inman, "Optimal configurations of bistable piezo-composites for energy harvesting," *Applied Physics Letters,* vol. 100, p. 114104, 2012.

[106]   M. I. Friswell, S. F. Ali, O. Bilgen, S. Adhikari, A. W. Lees, and G. Litak, "Non-linear piezoelectric vibration energy harvesting from a vertical cantilever beam with tip mass," *Journal of Intelligent Material Systems and Structures,* vol. 23, pp. 1505-1521, 2012.

[107]   F. C. Moon and P. J. Holmes, "A magnetoelastic strange attractor," *Journal of Sound and Vibration,* vol. 65, pp. 275-296, 1979.

[108]   A. Erturk and D. J. Inman, "Broadband piezoelectric power generation on high-energy orbits of the bistable Duffing oscillator with electromechanical coupling," *Journal of Sound and Vibration,* vol. 330, pp. 2339-2353, 2011.

[109]   T. Galchev, H. Kim, and K. Najafi, "Micro Power Generator for Harvesting Low-Frequency and Nonperiodic Vibrations," *Journal of Microelectromechanical Systems,* vol. 20, pp. 852-866, 2011.

[110]   J.-T. Lin and B. Alphenaar, "Enhancement of Energy Harvested from a Random Vibration Source by Magnetic Coupling of a Piezoelectric Cantilever," *Journal of Intelligent Material Systems and Structures,* vol. 21, pp. 1337-1341, 2010.

[111]   L. Tang, Y. Yang, and C.-K. Soh, "Improving functionality of vibration energy harvesters using magnets," *Journal of Intelligent Material Systems and Structures,* vol. 23, pp. 1433-1449, 2012.

[112]   B. P. Mann and B. A. Owens, "Investigations of a nonlinear energy harvester with a bistable potential well," *Journal of Sound and Vibration,* vol. 329, pp. 1215-1226, 2010.

[113]   A. J. Sneller, B. A. Owens, and B. P. Mann, "Experimental Investigations of a Bistable Energy Harvester," in *Structural Dynamics and Renewable Energy, Volume 1: Proceedings of the 28th IMAC, A Conference on Structural Dynamics, 2010*, T. Proulx, Ed., ed New York, NY: Springer New York, 2011, pp. 211-217.

[114]   J. M. T. Thompson and R. Ghaffari, "Chaotic dynamics of an impact oscillator," *Physical Review A,* vol. 27, pp. 1741-1743, 1983.

[115]   S. W. Shaw, "Forced vibrations of a beam with one-sided amplitude constraint: Theory and experiment," *Journal of Sound and Vibration,* vol. 99, pp. 199-212, 1985.

[116]   F. Peterka, "Bifurcations and transition phenomena in an impact oscillator," *Chaos, Solitons & Fractals,* vol. 7, pp. 1635-1647, 1996.

[117]   N. Hinrichs, M. Oestreich, and K. Popp, "Dynamics of oscillators with impact and friction," *Chaos, Solitons & Fractals,* vol. 8, pp. 535-558, 1997.

[118] M. S. M. Soliman, E. M. Abdel-Rahman, E. F. El-Saadany, and R. R. Mansour, "A wideband vibration-based energy harvester," *Journal of Micromechanics and Microengineering,* vol. 18, p. 115021, 2008.

[119] C. P. Le and E. Halvorsen, "MEMS electrostatic energy harvesters with end-stop effects," *Journal of Micromechanics and Microengineering,* vol. 22, p. 074013, 2012.

[120] H. Liu, C. Lee, T. Kobayashi, C. J. Tay, and C. Quan, "A new S-shaped MEMS PZT cantilever for energy harvesting from low frequency vibrations below 30 Hz," *Microsystem Technologies,* vol. 18, pp. 497-506, 2012.

[121] S. Roundy and Y. Zhang, "Toward self-tuning adaptive vibration-based microgenerators," 2005, pp. 373-384.

[122] C. Peters, D. Maurath, W. Schock, and Y. Manoli, "Novel electrically tunable mechanical resonator for energy harvesting," in *Proc. PowerMEMS 2008*, 2008, pp. 253-256.

[123] X. Wu, J. Lin, S. Kato, K. Zhang, T. Ren, and L. Liu, "A frequency adjustable vibration energy harvester," *Proceedings of PowerMEMS,* pp. 245-248, 2008.

[124] D. Scheibner, J. Mehner, D. Reuter, U. Kotarsky, T. Gessner, and W. Dötzel, "Characterization and self-test of electrostatically tunable resonators for frequency selective vibration measurements," *Sensors and Actuators A: Physical,* vol. 111, pp. 93-99, 2004.

[125] D. Scheibner, J. Mehner, D. Reuter, T. Gessner, and W. Dötzel, "A spectral vibration detection system based on tunable micromechanical resonators," *Sensors and Actuators A: Physical,* vol. 123–124, pp. 63-72, 2005.

[126] J. J. Yao and N. C. MacDonald, "A micromachined, single-crystal silicon, tunable resonator," *Journal of Micromechanics and Microengineering,* vol. 5, pp. 257-264, 1995.

[127] C. Peters, D. Maurath, W. Schock, F. Mezger, and Y. Manoli, "A closed-loop wide-range tunable mechanical resonator for energy harvesting systems," *Journal of Micromechanics and Microengineering,* vol. 19, p. 094004, 2009.

[128] M. Lallart, S. R. Anton, and D. J. Inman, "Frequency self-tuning scheme for broadband vibration energy harvesting," *Journal of Intelligent Material Systems and Structures,* vol. 21, pp. 897-906, 2010.

[129] M. Wischke, M. Masur, F. Goldschmidtboeing, and P. Woias, "Electromagnetic vibration harvester with piezoelectrically tunable resonance frequency," *Journal of Micromechanics and Microengineering,* vol. 20, p. 035025, 2010.

[130] V. R. Challa, M. G. Prasad, Y. Shi, and F. T. Fisher, "A vibration energy harvesting device with bidirectional resonance frequency tunability," *Smart Materials and Structures,* vol. 17, p. 015035, 2008.

[131] V. R. Challa, M. G. Prasad, and F. T. Fisher, "Towards an autonomous self-tuning vibration energy harvesting device for wireless sensor network applications," *Smart Materials and Structures,* vol. 20, p. 025004, 2011.

[132] D. Zhu, S. Roberts, M. J. Tudor, and S. P. Beeby, "Design and experimental characterization of a tunable vibration-based electromagnetic micro-generator," *Sensors and Actuators A: Physical,* vol. 158, pp. 284-293, 2010.

[133] D. Zhu, S. Roberts, J. Tudor, and S. Beeby, "Closed loop frequency tuning of a vibration-based micro-generator," in *PowerMEMS 2008*, Sendai, Japan, 2008, pp. 229-232.

[134] N. A. Aboulfotoh, M. H. Arafa, and S. M. Megahed, "A self-tuning resonator for vibration energy harvesting," *Sensors and Actuators A: Physical,* vol. 201, pp. 328-334, 2013.

[135] I. N. Ayala-Garcia, P. D. Mitcheson, E. M. Yeatman, D. Zhu, J. Tudor, and S. P. Beeby, "Magnetic tuning of a kinetic energy harvester using variable reluctance," *Sensors and Actuators A: Physical,* vol. 189, pp. 266-275, 2013.

[136] W. Al-Ashtari, M. Hunstig, T. Hemsel, and W. Sextro, "Frequency tuning of piezoelectric energy harvesters by magnetic force," *Smart Materials and Structures,* vol. 21, p. 035019, 2012.

[137] D. Zhu, S. Roberts, T. Mouille, M. J. Tudor, and S. P. Beeby, "General model with experimental validation of electrical resonant frequency tuning of electromagnetic vibration energy harvesters," *Smart Materials and Structures,* vol. 21, p. 105039, 2012.

[138] A. Cammarano, S. G. Burrow, D. A. W. Barton, A. Carrella, and L. R. Clare, "Tuning a resonant energy harvester using a generalized electrical load," *Smart Materials and Structures,* vol. 19, p. 055003, 2010.

[139] D. Mallick and S. Roy, "Bidirectional electrical tuning of FR4 based electromagnetic energy harvesters," *Sensors and Actuators A: Physical,* vol. 226, pp. 154-162, 2015.

[140] D. S. Nguyen, E. Halvorsen, G. U. Jensen, and A. Vogl, "Fabrication and characterization of a wideband MEMS energy harvester utilizing nonlinear springs," *Journal of Micromechanics and Microengineering,* vol. 20, p. 125009, 2010.

[141] Y. Tan, Y. Dong, and X. Wang, "Review of MEMS Electromagnetic Vibration Energy Harvester," *Journal of Microelectromechanical Systems,* vol. 26, pp. 1-16, 2017.

[142] W. J. Li, Z. Wen, P. Wong, G. M. Chan, and P. Leong, "A micromachined vibration-induced power generator for low power sensors of robotic systems," in *World Automation Congress: 8th International Symposium on Robotics with Applications*, 2000, pp. 16-21.

[143] N. N. H. Ching, H. Y. Wong, W. J. Li, P. H. W. Leong, and Z. Wen, "A laser-micromachined multi-modal resonating power transducer for wireless sensing systems," *Sensors and Actuators A: Physical,* vol. 97–98, pp. 685-690, 2002.

[144] S. Kulkarni, E. Koukharenko, R. Torah, J. Tudor, S. Beeby, T. O'Donnell, *et al.,* "Design, fabrication and test of integrated micro-scale vibration-based electromagnetic generator," *Sensors and Actuators A: Physical,* vol. 145–146, pp. 336-342, 2008.

[145] S. Roundy and P. K. Wright, "A piezoelectric vibration based generator for wireless electronics," *Smart Materials and Structures,* vol. 13, pp. 1131–1142, 2004.

[146] M. Renaud, K. Karakaya, T. Sterken, P. Fiorini, C. Van Hoof, and R. Puers, "Fabrication, modelling and characterization of MEMS piezoelectric vibration harvesters," *Sensors and Actuators A: Physical,* vol. 145–146, pp. 380-386, 2008.

[147] S. Roundy and E. Takahashi, "A planar electromagnetic energy harvesting transducer using a multi-pole magnetic plate," *Sensors and Actuators A: Physical,* vol. 195, pp. 98-104, 2013.

[148] M. Han, Q. Yuan, X. Sun, and H. Zhang, "Design and Fabrication of Integrated Magnetic MEMS Energy Harvester for Low Frequency Applications," *Journal of Microelectromechanical Systems,* vol. 23, pp. 204-212, 2014.

[149] G. D. Szarka, B. H. Stark, and S. G. Burrow, "Review of Power Conditioning for Kinetic Energy Harvesting Systems," *IEEE Transactions on Power Electronics,* vol. 27, pp. 803-815, 2012.

[150] P. D. Mitcheson, E. M. Yeatman, G. K. Rao, A. S. Holmes, and T. C. Green, "Energy Harvesting From Human and Machine Motion for Wireless Electronic Devices," *Proceedings of the IEEE,* vol. 96, pp. 1457-1486, 2008.

[151] A. Rajasekaran, A. Hande, and D. Bhatia, "Buck-boost converter based power conditioning circuit for low excitation vibrational energy harvesting," in *3rd Annual Austin Conference on Integrated Circuits and Systems, Austin, TX*, 2008.

[152] T. T. Le, H. Jifeng, A. v. Jouanne, K. Mayaram, and T. S. Fiez, "Piezoelectric micro-power generation interface circuits," *IEEE Journal of Solid-State Circuits,* vol. 41, pp. 1411-1420, 2006.

[153] S. Hashemi, M. Sawan, and Y. Savaria, "A novel low-drop CMOS active rectifier for RF-powered devices: Experimental results," *Microelectronics Journal,* vol. 40, pp. 1547-1554, 2009.

[154] J. Colomer-Farrarons, P. Miribel-Catala, A. Saiz-Vela, M. Puig-Vidal, and J. Samitier, "Power-Conditioning Circuitry for a Self-Powered System Based on Micro PZT Generators in a 0.13-μm Low-Voltage Low-Power Technology," *IEEE Transactions on Industrial Electronics,* vol. 55, pp. 3249-3257, 2008.

[155] C. Peters, O. Kessling, F. Henrici, M. Ortmanns, and Y. Manoli, "CMOS Integrated Highly Efficient Full Wave Rectifier," in *2007 IEEE International Symposium on Circuits and Systems*, 2007, pp. 2415-2418.

[156] M. D. Seeman, S. R. Sanders, and J. M. Rabaey, "An ultra-low-power power management IC for energy-scavenged Wireless Sensor Nodes," in *2008 IEEE Power Electronics Specialists Conference*, 2008, pp. 925-931.

[157] G. Bawa and M. Ghovanloo, "Analysis, design, and implementation of a high-efficiency full-wave rectifier in standard CMOS technology," *Analog Integrated Circuits and Signal Processing,* vol. 60, pp. 71–81, 2009.

[158] D. Marinkovic, A. Frey, I. Kuehne, and G. Scholl, "A New Rectifier and Trigger Circuit for a Piezoelectric Microgenerator," *Procedia Chemistry,* vol. 1, pp. 1447-1450, 2009.

[159] Y. K. Ramadass and A. P. Chandrakasan, "A Battery-Less Thermoelectric Energy Harvesting Interface Circuit With 35 mV Startup Voltage," *IEEE Journal of Solid-State Circuits,* vol. 46, pp. 333-341, 2011.

[160] C. K. Tse, S. C. Wong, and M. H. L. Chow, "On lossless switched-capacitor power converters," *IEEE Transactions on Power Electronics,* vol. 10, pp. 286-291, 1995.

[161] M. D. Seeman and S. R. Sanders, "Analysis and Optimization of Switched-Capacitor DC-DC Converters," *IEEE Transactions on Power Electronics,* vol. 23, pp. 841-851, 2008.

[162] R. Torah, P. Glynne-Jones, M. Tudor, T. O. Donnell, S. Roy, and S. Beeby, "Self-powered autonomous wireless sensor node using vibration energy harvesting," *Measurement Science and Technology,* vol. 19, p. 125202, 2008.

[163] S. Dwari and L. Parsa, "Efficient low voltage direct AC/DC converters for self-powered wireless sensor nodes and mobile electronics," in *INTELEC 2008 - 2008 IEEE 30th International Telecommunications Energy Conference*, 2008.

[164] P. D. Mitcheson, T. C. Green, and E. M. Yeatman, "Power processing circuits for electromagnetic, electrostatic and piezoelectric inertial energy scavengers," *Microsystem Technologies,* vol. 13, pp. 1629–1635, 2007.

[165] G. Sebald, H. Kuwano, D. Guyomar, and B. Ducharne, "Experimental Duffing oscillator for broadband piezoelectric energy harvesting," *Smart Materials and Structures,* vol. 20, p. 102001, 2011.

3 THEORETICAL AND EXPERIMENTAL TECHNIQUES

This chapter gives a general overview of the theoretical and experimental techniques and instruments used in this dissertation. The description of research methodology follows the sequence of device modelling and simulation, fabrication and characterization techniques.

3.1 Modelling and simulation techniques

This section discuss the modelling and simulation techniques and software tools used in the dissertation work. Modelling and simulation tools are extensively used in engineering and scientific research to estimate and optimize the response of conceptual devices and systems prior to fabrication and characterization. The simulation results often provide insight into system behaviours that are difficult to achieve by solving system equations using classical methods.

3.1.1 COMSOL Multiphysics

The COMSOL Multiphysics software package is a finite element (FEM) partial differential equation (PDE) solution tool [1]. The software has several add-on modules, among which the structural mechanics, MEMS, and AC/DC modules has been extensively used for this dissertation work.

The laws of physics are generally expressed as partial differential equations in space and time dependent problems. In the context of simple geometrical space and boundary conditions, such equations can be solved analytically to derive closed-form solutions. However, real life engineering problems often involve complex geometrical structures, and the mathematical model can include a complex combination of differential and algebraic

equations (DAEs). Therefore, exact solutions of such real life problems are often prohibitively complicated and time consuming, or even non-existent. In such scenarios the FEM method can be used to divide the complex geometry in numerous simpler geometric blocks (such as, triangle, quadrilateral, tetrahedron, hexagon etc.), which is known as meshing. Following meshing, the proper boundary conditions are applied at the appropriate meshes and nodes, and the material properties are defined. Then the governing PDE or ODE is approximately solved using numerical techniques at each node of the mesh geometry. These nodal solutions can be used to calculate the value of a desired quantity at any point inside each mesh element, and therefore be interpolated over the entire geometrical domain of the problem.
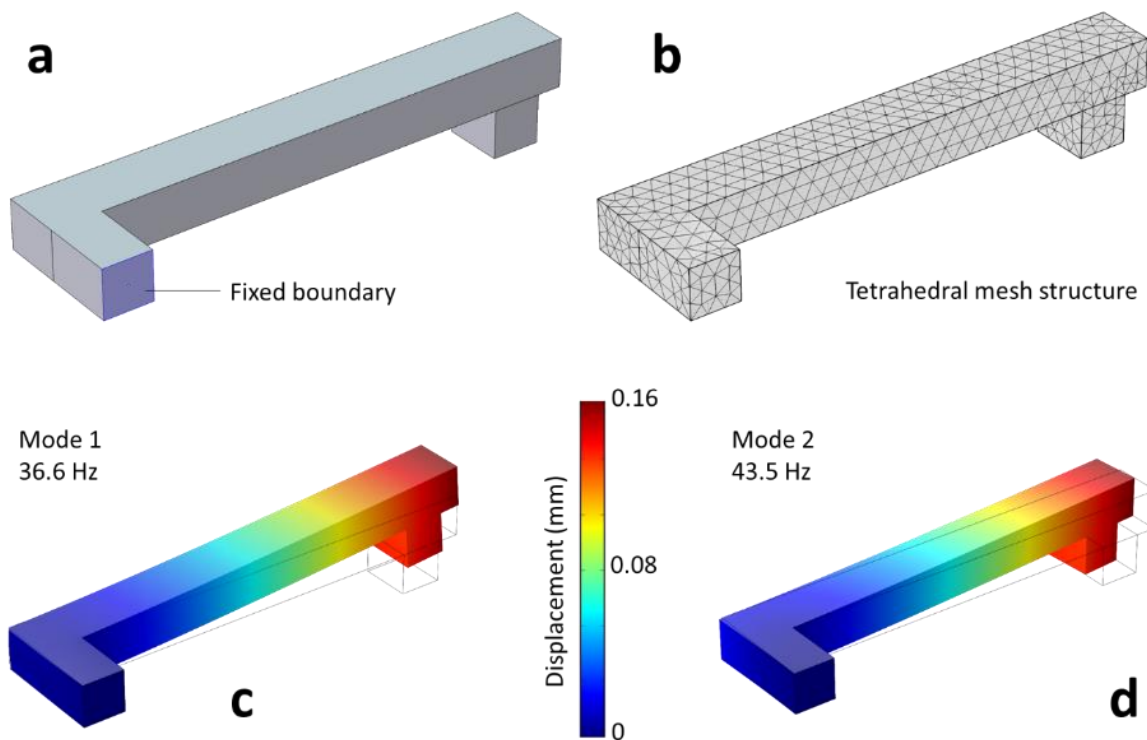
Figure 3.1: (a) COMSOL Multiphysics model of an L-shaped polysilicon cantilever structure. (b) Cantilever divided into tetrahedral meshes to use FEA. (b) Result of Eigen frequency analysis showing the first two vibrational modes.

In this dissertation work the COMSOL Multiphysics software package is used for 2D and 3D modelling and simulation of complex geometrical structures. The model parameters extracted from these simulations (e.g. linear and nonlinear stiffness, stationary response, Eigen modes, frequency response etc.) are then used in the numerical model to solve the system equation in MatLab.

3.1.2 Ansoft Maxwell

The Ansoft Maxwell is a software package that uses finite element analysis (FEA) to solve electromagnetic problems. Similar to other FEA tools, Maxwell divides any complex geometry into a number of simpler geometric blocks (i.e. meshing). Following meshing, appropriate initial and boundary conditions and material properties are incorporated, and the Maxwell's equations are solved at the appropriate meshes and nodes. These nodal solutions are then combined to generate the solution of the problem over the entire geometry. The software offers the choice of electrostatic, magnetostatic, eddy current and magnetic transient solvers to solve a problem, and uses the appropriate set of equations.
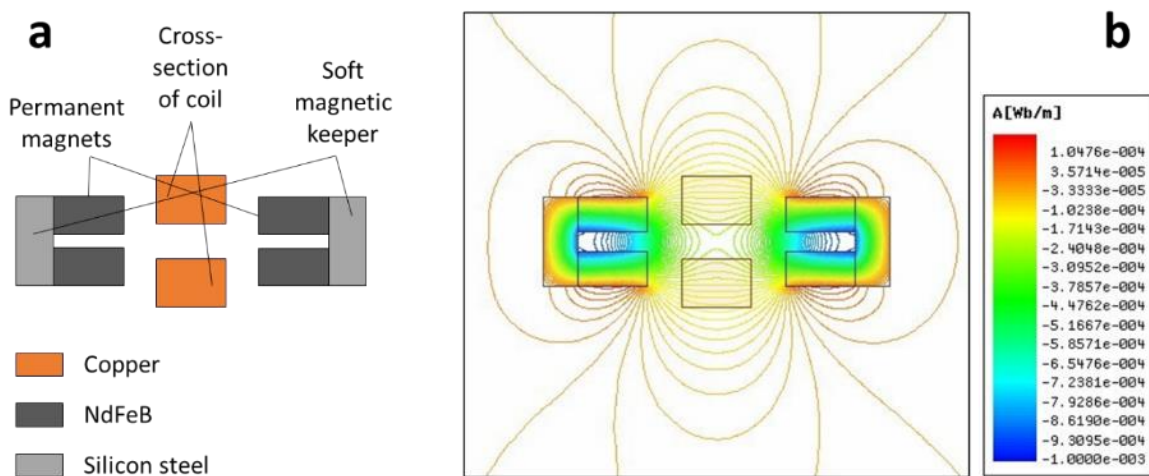
Figure 3.2: (a) 2D Cross-sectional view of a magnet-coil assembly for electromagnetic transduction. (b) Ansoft Maxwell simulation showing the distribution of magnetic flux.

In the context of this dissertation, the Ansoft Maxwell software has been used to obtain the magnetic field and flux distributions, and flux linkage gradients in numerous electromagnetic transduction architectures. The model parameters extracted from these simulations are then used in a numerical model to solve the system equation in MatLab.

3.1.3 MatLab/ Simulink

MatLab (acronym for Matrix Laboratory, developed by MathWorks Inc.) is a high level programming language designed for scientific and technical computation. Simulink (also developed by MathWorks Inc.) is a block diagram based graphical environment for multi-domain simulation and model-based design applications. Simulink is usually integrated with MatLab, and incorporates MatLab algorithms into models, and exports simulation results to MatLab for further analysis and post processing. MatLab/ Simulink integrates

programming, computation, modelling and visualization in a user-friendly platform, and is widely used in academia and industry . Optional features in MatLab includes a number of application-specific solutions called toolboxes, which are an extensive collection of MatLab functions that can be used to solve specific classes of problems. Areas in which toolboxes are available include communication systems, control systems, digital signal processing, image processing, symbolic math, neural networks and fuzzy logic etc. In this dissertation, MatLab has been used to solve systems of partial differential equations derived from the analytical models of energy harvesting devices. The 4th order Runge-Kutta method was used to numerically solve the differential equations, and graphical tools were used to visualize the simulation results. In addition, MatLab was extensively used for post-processing, analysis and visualization of the experimental datasets.

3.1.4 SPICE

SPICE (acronym for Simulation Program with Integrated Circuit Emphasis) is a general-purpose open source circuit simulation program. In addition to the open source version, many proprietary versions of the program (such as, OrCAD PSPICE, LTSpice, National Instruments MultiSim etc.) has been developed by various organizations. The program includes the models for common passive and active electronic devices. In addition, several electronic device and integrated circuit manufacturers provide SPICE models for many of their products. In most of the modern SPICE circuit simulation program, a circuit is generally described in the form of a netlist, which is a text description of all the circuit components and their connecting nodes. The SPICE program analyses the netlist using circuit equations and algorithms, and provide graphic visualization of the results. LTSpice has been used in this dissertation work to design and simulate power management circuits and estimate the behaviour of the circuit under different input excitations.

3.2 Fabrication techniques

This section gives an overview of the techniques and instruments used to fabricate the devices developed and studied in this thesis. The meso-scale device structures were fabricated by laser micromachining of FR4 sheets, and manually assembled to sintered NdFeB micro-magnets and wire-would micro-coils. The MEMS scale devices were fabricated on silicon by using photolithography, DRIE, sputtering, electrodeposition, PECVD etc.

3.2.1 Laser micromachining

Since its invention in the mid-1950s one of the most prolific is usage of laser have been in the industrial manufacturing and micromachining applications. While industrial machining by laser was first commercially introduced in the early 1970s, laser micromachining is a more recent development, first demonstrated in the 1980s. [Herziger [2]]. In general, laser micromachining works by focusing a high intensity laser beam through optical systems onto a substrate or workpiece, usually mounted on a computer controlled platform. The laser optics and the motion of the platform can be controlled by computer to trace out and cut a CAD (computer aided design) generated pattern in the substrate or workpiece material.
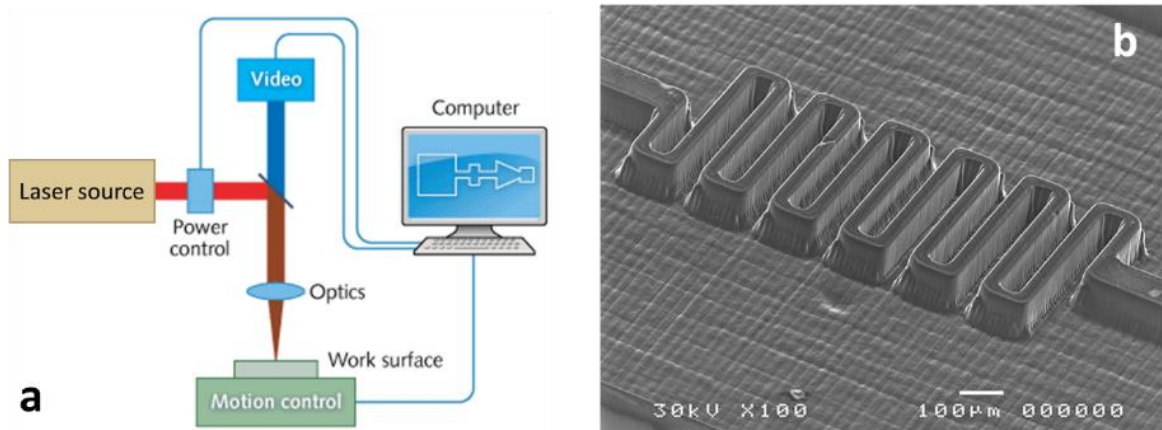
Figure 3.3: (a) Schematic diagram of laser micro-machining system [3]. (b) serpentine spring pattern laser micro-machined on diamond [4].

The first industrial applications of laser micromachining involved continuous wave (CW) lasers and microsecond pulsed laser, which often resulted in rough edge and extensive heat affected zone when applied to create micro-scale features [Steen [5]]. The uneven edges in micro-structures produced by continuous and micro-second pulsed lasers was a result of excessive heat concentration in the substrate at the point of incidence of the laser. This issue has been resolved in recent years by the introduction of pico-second pulsed laser and lately, the ultra-fast femto-second lasers [Chichkov, et al. [6]], which enabled the micro-machining of features as small as a few microns in a variety of materials (e.g. metals, semiconductors, ceramics, diamond etc.). The laser micro-machining technique has been used in this dissertation to fabricate complex linear and nonlinear spring designs in FR4 sheets. FR4 is a flame-retardant composite (glass fibre embedded in epoxy resin system) material, which is widely used in the electronics industry as printed circuit board (PCB).

The FR4 spring structures are then assembled with permanent magnets and coils to form the energy harvesting devices.

3.2.2 Photolithography

The literal meaning of the term 'photolithography' is 'writing on stone with light' [Latin], and this technique is extensively used in the microelectronics industry to pattern microscopic structures onto different substrates. In the photolithography process a photoresist (a photoactive organic compound) is first spread (or spin-coated) onto a substrate (usually a wafer of silicon or other material) surface.
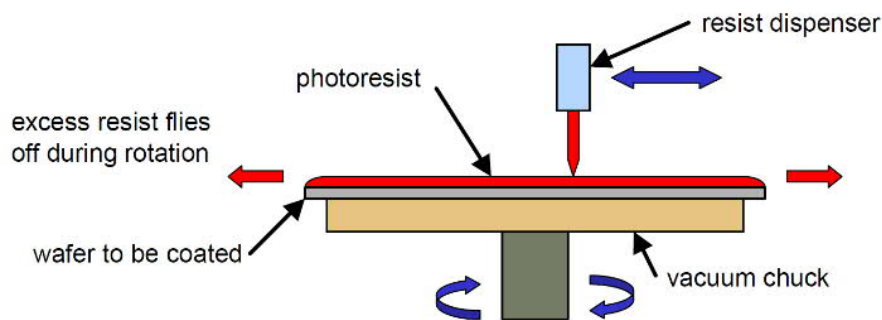
Figure 3.4: Spin-coating of photoresist on wafer.

The thickness of the photoresist coating is usually determined by the viscosity of the photoresist solution and the spin speed, and is in the range of $1 - 2$ µm for most microelectronic fabrication process steps. However, thicker resist coatings ($10 - 100$ µm) might be required for special processes (e.g. use of photoresist pattern as mould for electrodeposition), and can be achieved by multiple spin-coating steps. The photoresist coated substrate is then prebaked using convection oven, or IR lamps or hotplate (typically 80ºC – 90ºC) in order to evaporate the photoresist solvent material and densify the resist. The pattern or features of the intended device are pre-printed in a photomask, which is essentially a glass plate with features printed using metal (e.g. chromium) such that UV light can be completely blocked selectively.

(X, Y, θ) alignment of mask to substrate

UV exposure illumination

Chrome on glass photomask

Photoresist
Substrate

Latent image created on photoresist after exposure

Wet chemical development

Negative Photoresist
Photoresist is photopolymerized where exposed and rendered insoluble to the developer solution.

Positive Photoresist
Exposure decomposes a development inhibitor and developer solution only dissolves photoresist in the exposed areas.

Figure 3.5: The photolithography process.

The photomask is then exposed UV and the photoresist-coated substrate are then loaded in projection system with mask alignment mechanism which allows for accurate alignment of the substrate with the photomask. Then the UV lamp is turned on with a predefined intensity and duration, which is primarily determined by the requirements of the photoresist. The UV exposure creates latent image of the photomask patterns on the photoresist layer, which is then developed in a chemical bath. Depending on the photoresist type (negative or positive) a negative or a positive pattern of the photomask is left on the substrate after development. This pattern is then used for subsequent micro-fabrication steps involving deposition of new material layers, doping, or etching of existing layers. Typical micro-fabrication process flow often involve several photolithography steps using different photomask layouts to create complex device structures. The photolithography techniques has been extensively used in this dissertation work to transfer the patterns of springs and planar micro-coils onto silicon wafers and metallic seed layers in the microfabrication of silicon springs and micro-coils. A Karl-Suss mask aligner with mercury lamp (minimum feature size 0.5 µm) was used for the UV photolithography in this dissertation.
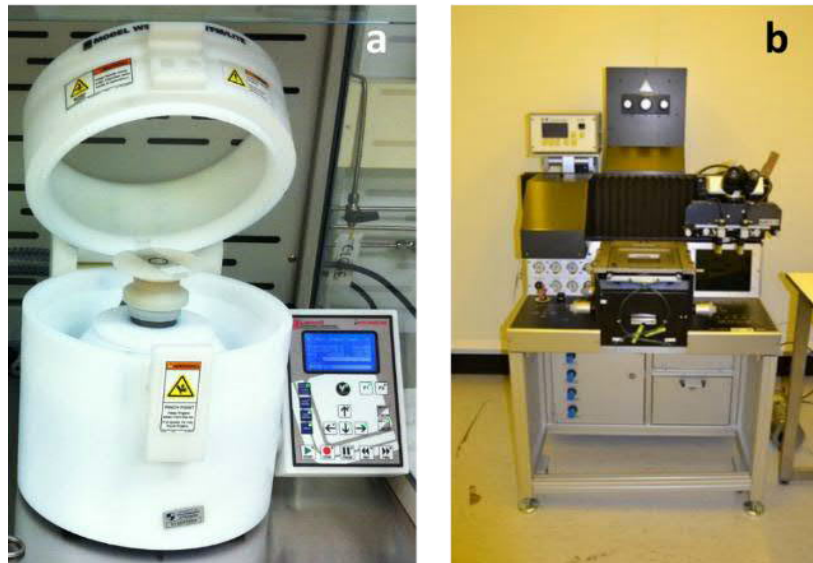
Figure 3.6: (a) Laurell WS 650 spin coater. (b) Karl-Suss MA6 mask aligner.

3.2.3 Deep reactive ion etching (DRIE)

The deep reactive ion etching (DRIE) is a process to create high aspect ratio features in silicon. The process is also known as the Bosch process, after the German company Robert Bosch GmbH which patented the process [7]. The process works by repetitively alternating between two phases, etching and passivation in a time-multiplexed fashion, which is also known as the time-multiplexed deep etching (TMDE) process [Ayón, et al. [8]].
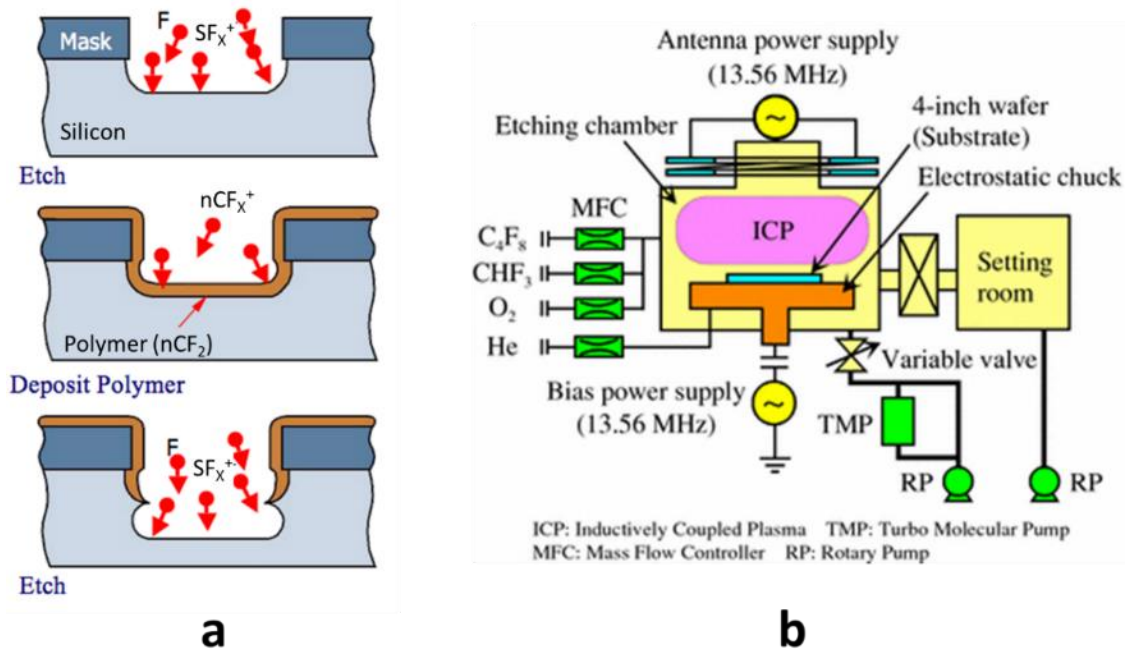
Figure 3.7: Illustration of the DRIE process [9]. (b) Schematic diagram of DRIE system for borosilicate glass [Akashi and Yoshimura [10]].

The typical silicon DRIE process uses three process gases, SF_6 for the reactive etch, C_4F_8 for the passivation, and helium for wafer cooling. The DRIE etching systems use a high density inductively coupled plasma (ICP), while the process cycles between SF_6 etch of silicon, and C_4F_8 passivation to protect the surrounding side-walls. The etched profile, silicon etch rate, and mask erosion rate are dependent on the process/recipe gas switching
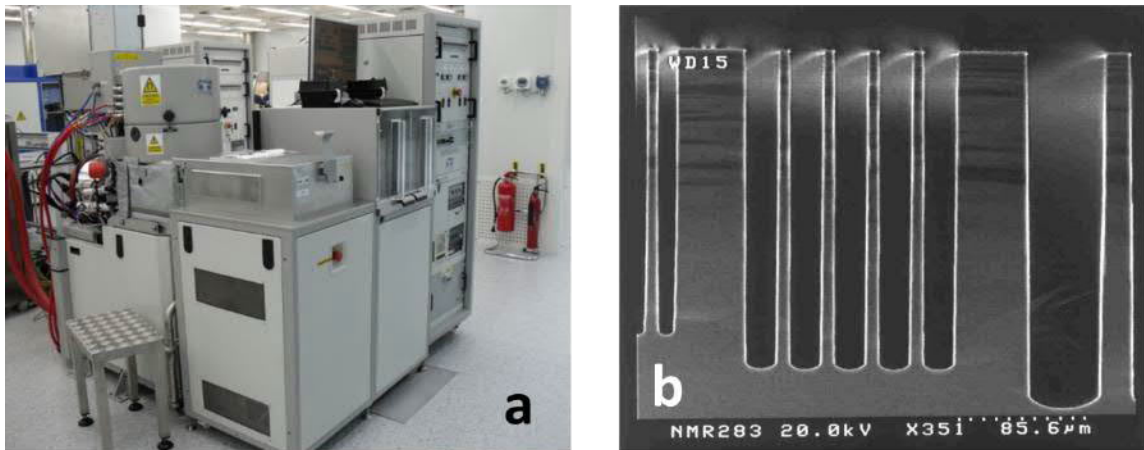

Figure 3.8: (a) SPTS DRIE system. (b) High aspect ratio features in silicon by DRIE.

In this dissertation work, the DRIE technique has been used to etch high aspect ratio spring structures in silicon and silicon-on-insulator (SOI) substrates.

3.2.4 Sputter deposition

The sputter deposition process can be used to coat virtually anything with high quality thin films of a wide range of materials, including solid metal or alloy and a variety of compounds. Sputter deposition is a physical vapour deposition (PVD) method of depositing thin films by sputtering, i.e. ejecting material from a target (or source), which is then deposited onto a substrate [Behrisch [11]]. Both DC and RF magnetron sputtering methods are widely used to deposit various materials [Kelly and Arnell [12]].

A typical magnetron sputtering system consists of a vacuum chamber, magnetron guns, vacuum pumps, a process gas supply system, power supplies and a computer control system. The target material are placed on a magnetron cathode, and the chamber is evacuated at ultra-high vacuum (UHV) condition to reduce impurities, which is then re-filled with the process gas (usually argon).
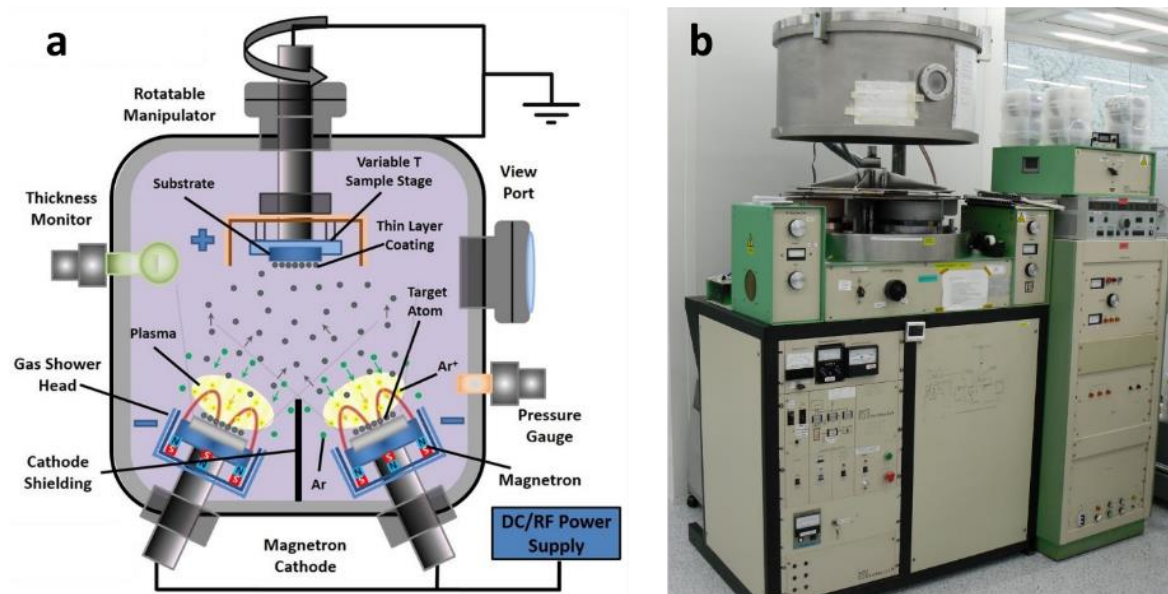
Figure 3.9: (a) Schematic diagram of a magnetron sputtering system [13]. (b) The Nordiko 2550 sputtering system.

High electric potential is then applied between the target material and the substrate, and free electrons within sputtering chamber are accelerated. The magnetic fields produced by the magnetron keeps the energized electrons confined near the target surface. The electrons then collide with the process gas atoms and create positively charged ions, which are accelerated towards the target surface and dislodge or sputter off surface atoms. The sputtered atoms then travel to the substrate and are deposited to form a thin layer of the target material. On the other hand, some of the ionized process atoms recombine with the free electrons, giving away the plasma glow. The sputter deposition technique has been used in this dissertation work to deposit seed layers (titanium and copper) on silicon substrate for subsequent electrodeposition process. Also, the sputter deposition technique has been used for deposition of aluminium nitride insulation between subsequent planar micro-coil layers.

3.2.5 Electrodeposition

The electrodeposition (or electrolytic deposition) technique is widely used to deposit a variety of metals and alloys on other substrates for numerous applications in industry and research [Paunovic, et al. [14]]. In the microelectronics industry, electrodeposition has been in use over the last few decades to produce the interconnections of multilayer microchips and the wiring of printed circuits [Dini and Snyder [15]]. Other notable use of

electrodeposition technique include the development of thin films of advanced magnetic materials and materials for thermoelectric energy harvesting devices.
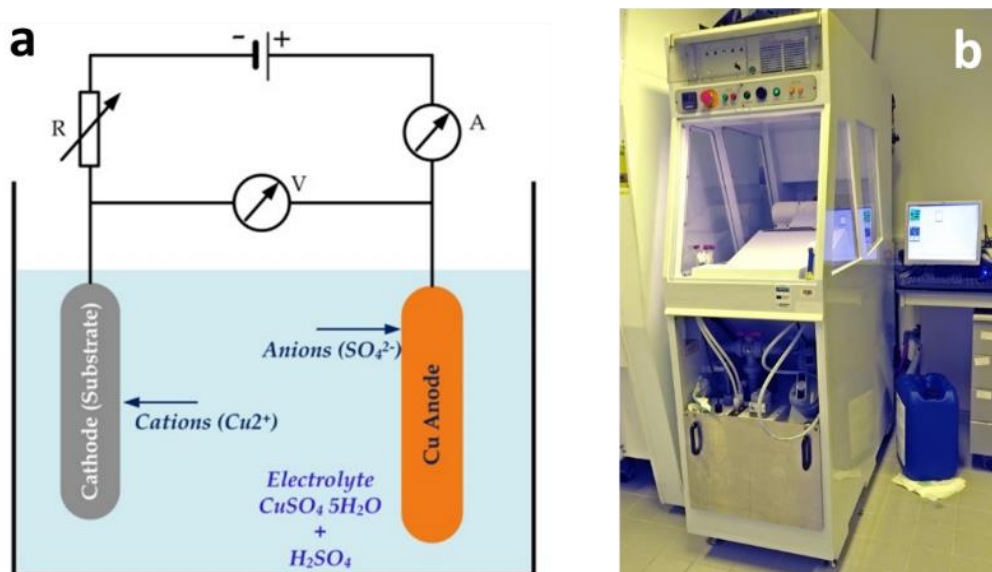
Figure 3.10: (a) Schematic representation of electrodeposition of copper [[Atteq Rehman and Lee [16]]]. (b) Digital Matrix electrodeposition system.

The electrodeposition process is a method of ionic transfer of metals from a target material to a substrate material via a fluid solution. In the electrodeposition of copper, for example, pure copper is used as the anode in an acidic plating bath (aqueous solution of copper sulphate and sulfuric acid), while the substrate material is connected to the cathode. On application of electric potential between the anode and cathode, sulphate anions react with the copper anode and dissolves it, while copper cations are deposited on the substrate surface. In order to improve the uniformity and planarity of the electroplated surface, additives such as glycol, gelatine, urea etc. can be included in the plating bath [Yokoi [17]]. The electrodeposition technique has been used in this dissertation work to develop spiral planar micro-coils for energy harvesting devices.

3.2.6 Plasma enhanced chemical vapour deposition (PECVD)

A plasma is an ionised phase of gas, which is often defined as the fourth state of matter. Chemical vapour deposition (CVD) processes assisted by plasma can deposit many types of thin films at much lower temperatures than would be possible by conventional CVD [[Guo, et al. [18]]]. In PECVD systems reactant gases are passed through a low pressure electric discharge plasma. An external RF power source provide the energy to sustain the ionised state of atoms. A typical PECVD system is shown in Figure 3.11, where plasma is generated between a grounded electrode and an RF energized electrode. The capacitive

coupling between the electrodes generates plasma in the reactant agents, and facilitates deposition of materials on the substrate surface. The major benefits of using PECVD over conventional CVD is the low temperature (200° C – 300°C) operation, which is useful for fabrication of many devices that might otherwise be damaged in high temperature (600° C – 800°C) conventional CVD. The materials typically deposited using PECVD include polysilicon, silicon nitride, silicon oxide, silicon oxy-nitride, silicon carbide etc. The silicon source is usually provided by silane (SiH_4), which is combined with an oxygen source gas to form silicon dioxide or a nitrogen gas source to produce silicon nitride.
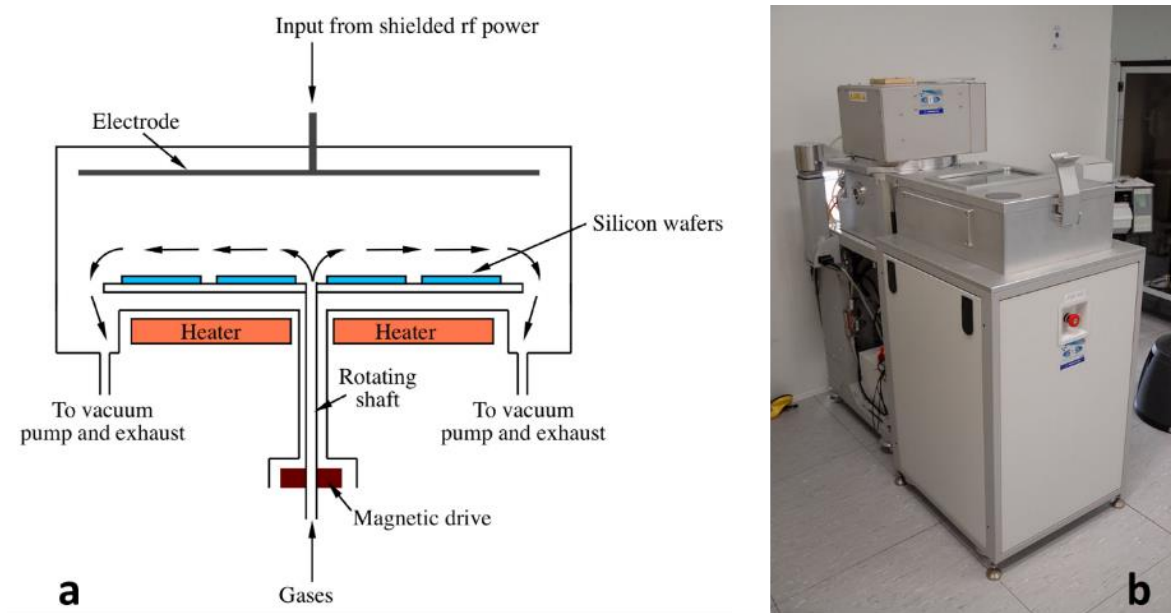
Figure 3.11: (a) Schematic representation of a radial flow PECVD reactor [19]. (b) STS Multiplex PECVD machine.

In this dissertation work the PECVD process was used to deposit silicon oxide and silicon nitride dielectric materials as insulation layer between micro-coil layers.

3.3 Characterization techniques

This section provides an overview of the characterization techniques used in this dissertation. After fabrication, different crucial components of the MEMS-scale devices are observed and characterized using advanced microscopy techniques. The fabricated device components are then assembled to form the complete device prototypes, and both MEMS-scale and meso-scale devices are characterized using vibration test setup.

3.3.1 Scanning electron microscope (SEM)

The scanning electron microscope (SEM) is a tool widely used in academia and industry to observe specimen surfaces. The SEM works by irradiating a specimen with a fine electron beam (i.e. an electron probe), which cause emission of secondary electrons from the specimen surface. Two dimensional scanning (raster scanning) of the specimen surface with the electron probe and detection of the secondary electrons can be used to rendered a highly detailed image of the specimen surface topography.
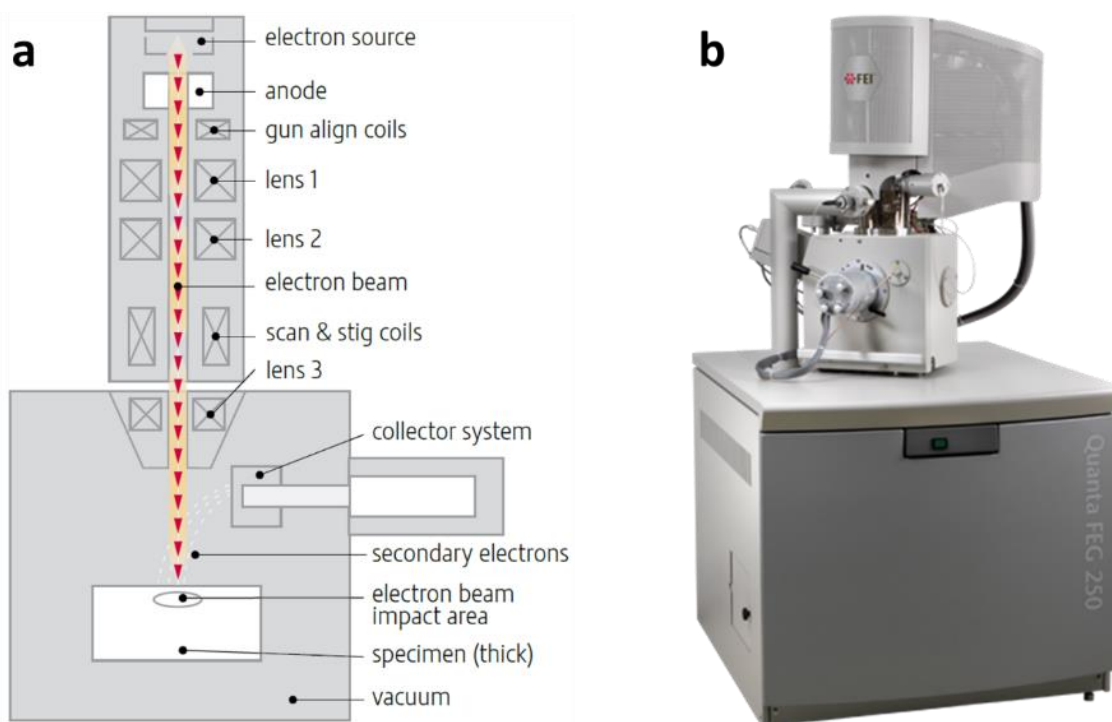
Figure 3.12: (a) Schematic construction of an SEM (scanning electron microscope) [20]. (b) FEI Quanta 250 FEG SEM.

The essential components of an SEM include an electron gun for generation of the electron beam, alignment and scanning coils for scanning of the electron beam over the specimen surface, and lens systems for focusing the electron beam. When the incident electron beam enters the specimen surface, secondary electrons are produced from the valence band of the surface atoms, which are detected by the secondary electron detector. Some of the incident electrons are scattered by the specimen atoms, and are picked up by the back-scattered electron detector. The back-scattered electrons possess higher energy, and the relative intensity of the back-scattered electrons tends to increase with the atomic number of the elements in the specimen. Therefore, secondary electron detector and the back-scattered electrons detector information can be combined to visualize the surface topography as well

as material variation in the specimen surface. In this dissertation SEM has been used to observe the micro-fabricated components (i.e. silicon springs and planar micro-coils) of the vibration energy harvesters.

### 3.3.2 Energy dispersive X-ray spectroscopy (EDX or EDS)

As specimens are irradiated by electron beams in an SEM, incident electrons enter the specimen and interact with the surface atoms. This interaction result in emission of secondary electrons from the valence bands, as well as the inner shells of the constituent atoms. When electrons are ejected from the inner shells, electrons from the outer shells often jump down into the vacant inner shells, and emit excess energy as X-rays. These X-rays are called characteristic X-rays since their energies (wavelengths) correspond to the energy difference between the outer shell and inner shell electrons. These X-rays are characteristic of individual elements, and can be analysed to determine the constituent elements in a specimen. Characteristic X-rays emitted by the electrons in the K-shell are called 'K-lines'; similarly, characteristic X-rays emitted by L and M-shells are called the 'L-lines' and 'M-lines' respectively.

The EDX (or EDS) analysis can be applied in three modes to determine the elemental constituents of a specimen. The point analysis can be used to irradiate a certain point in the specimen to obtain a characteristic X-ray spectrum, while line analysis is used to determine the one-dimensional distribution of elements. A two-dimensional area mapping of X-ray spectrum can be used to map the distribution of elements in a specimen surface. The EDX analysis capabilities are incorporated in most of the modern SEM systems. In this dissertation EDX mapping has been used to determine the step coverage of dielectric materials in fabricated ultra-dense micro-coil prototypes.

3.3.3 Focused ion beam (FIB) instrument

The SEM uses electron beams to non-destructively probe into the surface topologies in great details. A focused ion beam (FIB) instrument is very similar in construction to that of an SEM, only it uses a focused beam of ions rather than electrons. Since even the lightest ions are at least 2,000 times heavier than electrons, a beam of ions can have much higher momentum and kinetic energy than a beam of electrons. Therefore, when a beam of ions is incident on a specimen, it may dislodge some atoms in the point of impact. This principle

is utilized in FIB instruments to 'mill' a specimen or make a precise cross-section for observation under SEM or TEM (transmission electron microscope).
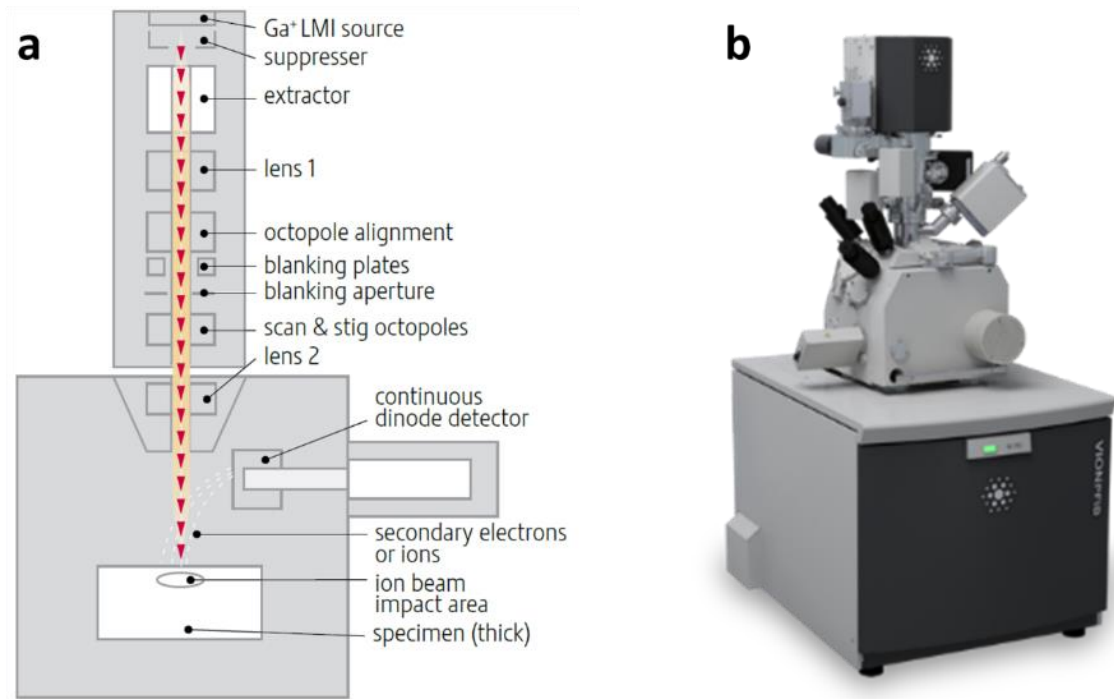
Figure 3.13: (a) Schematic construction of an FIB (focused ion beam) instrument [21]. (b) FEI Vion PFIB.

Most of the FIB instruments used in academia and industry use liquid metal ion sources (Ga^+). The ions ejected by the ion source are then accelerated by an arrangement of suppresser and extractor. The beam of ions is then focused using magnetic lenses and aligned using octo-pole arrangements onto the work area in the specimen, and very precise nano-machining can be executed by carefully controlling the beam energy and intensity. In addition to milling the work area, ion beam assisted chemical vapour deposition can be used to deposit certain materials on the work area with nanometre precision. In many FIB instruments, SEM and EDX capabilities are incorporated to facilitate characterization of the FIB-milled area or cross-section. The FIB instrument has been used in this dissertation work to make precise cross-sections of micro-coil prototypes and determine the conformity of the insulating dielectric layers between copper coil layers.

3.3.4 Vibration test set up

The demand for high speed operation combined with the trend to use lightweight materials in the modern industrial machinery necessitates extensive dynamic characterization, of

which vibration testing and analysis is an integral part. The vibrations experienced by devices and component during practical operations are emulated in labs by using electromagnetic shakers, and devices under test are subject to the generated vibrations for characterization.
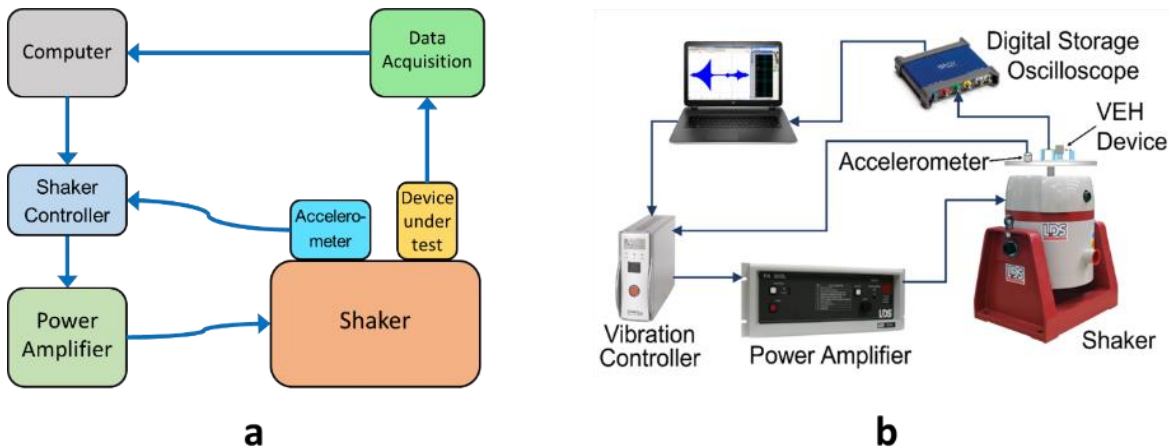
Figure 3.14: (a) Generic configuration of vibration test setup. (b) Brüel & Kjær vibration test equipment configured for testing vibration energy harvesting devices.

In order to produce a predefined vibration characteristics, electromagnetic shakers are used which convert electrical signals into mechanical movements in a controlled manner. The electromagnetic shaker is the principal component in a vibration test setup, which operates on principles similar to that of a loud speaker. The movements in the shaker are produced by currents passing through a coil in a magnetic field, where the force accelerating the moving element is determined by the drive current and the magnetic flux. The drive current fed to the shaker is generated by a power amplifier, which amplifies the signal generated by a computer-controlled signal generator. The signal generator generates the excitation signal in response to the feedback of an accelerometer mounted on the vibrating element, which completes a feedback control loop. The feedback control loop ensures that the acceleration and frequency of the vibration produced by the shaker is stable and controllable through a software program. In addition to the generation of harmonic sinusoidal vibrations, many test setups have the capability of generating shock and random vibrations for different types of characterization. The vibration energy harvesting devices developed in this dissertation work has been tested by using a Brüel & Kjær shaker system comprising of an LDS V455 shaker, a PA1000L power amplifer and an LDS Comet shaker controller. A piezoelectric accelerometer (DeltaTron 4517-002) is attached on the shaker platform and the acceleration is fed back to the shaker controller. The vibration energy

harvesting device to be characterized is mounted on the shaker platform, and subject to harmonic sinusoidal excitation or random vibration. The output of the energy harvester is recorded by a digital storage oscilloscope and stored in a computer. The vibration test setup has been extensively used in this dissertation work to characterize the energy harvesting devices under various excitation conditions.

3.4 Conclusion

The analytical and experimental techniques used in the present dissertation has been discussed in this chapter. The techniques has been categorized as the modelling and simulation techniques, fabrication techniques and characterization techniques. The first section gives an overview of the finite element modelling and simulation tools and numerical simulation techniques such as COMSOL Multiphysics, Ansoft Maxwell, MatLab, LTSpice etc. The next section briefly discuss the device fabrication techniques such as laser micromachining, photolithography, and different etching and deposition techniques that has been used to fabricate the prototypes. The final section presents the advanced microscopy and characterization tool and feedback-controlled vibration test setup which has been extensively used for characterization of the devices under different conditions.

References

[1]   Available: https://www.comsol.com/

[2]   G. Herziger, "Physics Of Laser Materials Processing," in *1986 International Symposium/Innsbruck*, 1986.

[3]   Available: http://www.industrial-lasers.com

[4]   Available: http://www.oxfordlasers.com

[5]   W. M. Steen, "Laser material processing—an overview," *Journal of Optics A: Pure and Applied Optics,* vol. 5, p. S3, 2003.

[6]   B. N. Chichkov, C. Momma, S. Nolte, F. von Alvensleben, and A. Tünnermann, "Femtosecond, picosecond and nanosecond laser ablation of solids," *Applied Physics A,* vol. 63, pp. 109-115, 1996.

[7]   F. Laermer and A. Schilp, "Method of anisotropically etching silicon," ed: Google Patents, 1996.

[8]   A. A. Ayón, R. Braff, C. C. Lin, H. H. Sawin, and M. A. Schmidt, "Characterization of a Time Multiplexed Inductively Coupled Plasma Etcher," *Journal of The Electrochemical Society,* vol. 146, pp. 339-349, 1999.

[9]   (2014). *Fabricating MEMS and Nanotechnology* [Online]. Available: https://mems-exchange.org

[10]   T. Akashi and Y. Yoshimura, "Deep reactive ion etching of borosilicate glass using an anodically bonded silicon wafer as an etching mask," *Journal of Micromechanics and Microengineering,* vol. 16, p. 1051, 2006.

[11]   R. Behrisch, "Introduction and overview," in *Sputtering by Particle Bombardment I: Physical Sputtering of Single-Element Solids*, R. Behrisch, Ed., Springer, Berlin, Heidelberg, 1981.

[12]   P. J. Kelly and R. D. Arnell, "Magnetron sputtering: a review of recent developments and applications," *Vacuum,* vol. 56, pp. 159-172, 2000.

[13]   *UHV Magnetron Sputtering System (MDS)*. Available: http://www.adnano-tek.com/

[14]   M. Paunovic, M. Schlesinger, and D. D. Snyder, "Fundamental Considerations," in *Modern Electroplating*, ed: John Wiley & Sons, Inc., 2010.

[15]   J. W. Dini and D. D. Snyder, "Electrodeposition of Copper," in *Modern Electroplating*, ed: John Wiley & Sons, Inc., 2010.

[16]   Atteq Rehman and S. H. Lee, *Crystalline Silicon Solar Cells with Nickel/Copper Contacts*: InTech, 2015.

[17]   M. Yokoi, "Supression Effect and Additive Chemistry," in *Copper Electrodeposition for Nanofabrication of Electronics Devices*, K. Kondo, R. N. Akolkar, D. P. Barkey, and M. Yokoi, Eds., ed New York, NY: Springer New York, 2014.

[18]   L. Guo, M. Kondo, M. Fukawa, K. Saitoh, and A. Matsuda, "High Rate Deposition of Microcrystalline Silicon Using Conventional Plasma-Enhanced Chemical Vapor Deposition," *Japanese Journal of Applied Physics,* vol. 37, pp. 116-118, 1998.

[19]   H. O. Pierson, "CVD Processes and Equipment," in *Handbook of Chemical Vapor Deposition (CVD) (Second Edition)*, ed Norwich, NY: William Andrew Publishing, 1999, pp. 108-146.

[20]   *Scanning Electron Microscopes : Quanta SEM for Materials Science* [Webpage]. Available: https://www.fei.com

[21]   *Focused Ion Beam Microscope : V400ACE Focused Ion Beam*. Available: https://www.fei.com/

4 WIDEBAND NONLINEAR BISTABLE GENERATOR

This chapter presents the development of a meso-scale nonlinear bistable vibration energy harvesting device in order to achieve wider bandwidth. In the first section, the design and fabrication method of the prototype bistable vibration energy harvesting (VEH) device has been described. The developed prototype is then investigated through analytical modelling, numerical simulation and experimental validation, which produced broad frequency responses. In the next section, the bistable VEH prototype is probed further by combining the effect of mechanical impact with bistable nonlinearity which exhibits even further bandwidth broadening effect. This is again validated through a detailed theoretical framework, numerical simulation and experimental results. The device performances are benchmarked along with other published works against appropriate figures of merit.

4.1 Design and fabrication of bistable energy harvester

The device consisting of FR4 material, neodymium-iron-boron (NdFeB) magnets and copper wire-wound coil employ electromagnetic transduction for conversion of mechanical energy into electrical energy. Figure 4.1 shows the schematic diagram and the magnetic flux pattern in a vertical cross-section through the centre of the coil. The device is based on a folded beam structure made out of a FR4 sheet (300 µm thickness) processed by laser machining. FR4 was chosen for the oscillator as the Young's modulus of this material is low (~ 21 GPa), resulting in large amplitude oscillation at low frequency.

A folded cantilever structure was designed, which further lowers the operating frequency, while keeping the device dimension small. The centre of the folded arm cantilever is bonded to the base, while the rest of the structure is free to oscillate. Four sintered neodymium (NdFeB) magnets (4mm × 2mm × 1mm) are bonded in opposite polarization using epoxy adhesive to the FR4 cantilever on both sides of a slot.
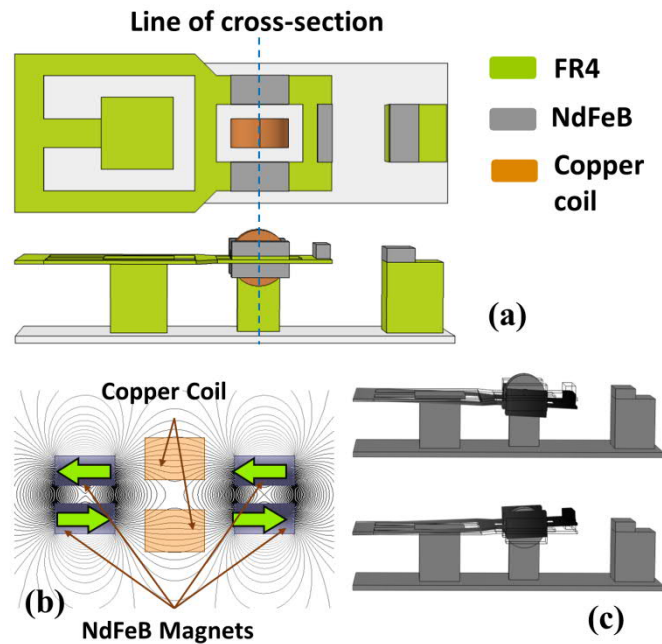
Figure 4.1: (a) Top and side schematic view of electromagnetic bistable vibration energy harvesting device, (b) Magnetic flux lines in a vertical cross-section through the dotted line in (a). Arrows denote the magnetic pole (N-S) orientation. (c) Static equilibria positions of the deflected device in bistable configuration.

Such arrangement of magnets results in oppositely oriented magnetic fields, producing a region of high flux gradient within the slot. A precision machine-wound enamelled copper wire coil (2500 turns, inner diameter 1.15 mm, outer diameter 4mm, 110 µH inductance, and 770 Ω resistance) is placed in the slot between the magnets. A fifth NdFeB magnet (4mm × 1mm × 1mm) is bonded at the end of the cantilever, with its north pole facing the outward direction. Another magnet (4mm × 2mm × 1mm) is placed in front of the cantilever in such a way that it exerts a repulsive force on the magnet at the end of the cantilever. This magnetic repulsive force results in a reduced effective spring constant of the FR4 cantilever, and introduces nonlinearity into the system. This magnetically introduced nonlinearity can be controlled by adjusting the gap between the repulsive magnets. Figure 4.2 shows the complete fabricated device. A micro-positioning stage was used to precisely control the gap between the repulsive magnets (not shown in Figure 4.2). The magnetic dipole moments of the repulsively oriented magnets were determined by FEA tools (Ansoft Maxwell).
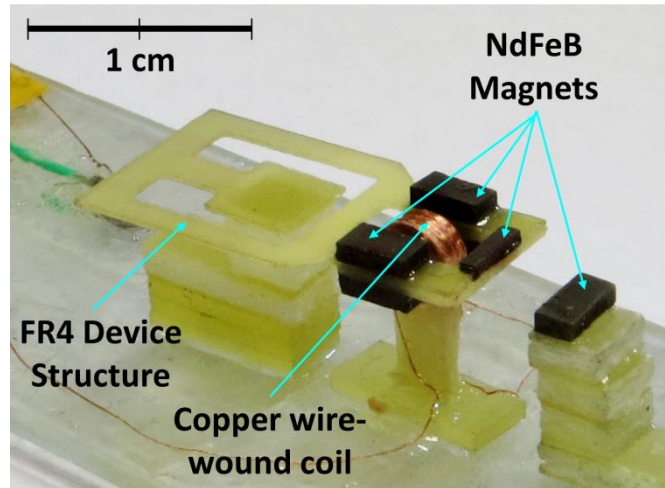
Figure 4.2: Fabricated EM-VEH device on FR4

4.2 Nonlinear bistable vibration energy harvester

The effect of the depth of the potential well on the performance of an electromagnetic bistable VEH in a moderately low frequency (10–40 Hz) and low acceleration (0.2–0.6 g) vibration environment has been studied in this work. In order to harvest vibration energy from low frequency vibrations FR4 (PCB material, Young's modulus ~21 GPa) has been chosen as the structural material for the oscillator. A folded-arm cantilever structure is designed for the oscillator, reducing even further the linear resonance frequency, while keeping the device footprint (11 mm × 22 mm) relatively small. Piezoelectric transduction is the most widely employed transduction mechanism for the reported bistable energy harvesting devices. However, due to the very high internal impedance of piezoelectric materials the resulting output current is very low. Also, the brittleness and degradation of piezoelectric materials over time adversely affect the long-term performance and reliability of piezoelectric transduction. The reported device circumvents the issues posed by piezoelectric transduction by implementing electromagnetic (EM) transduction. The device has been analytically modelled and numerically simulated across a range of excitation conditions. The simulation results have been validated against experimental results from extensive measurements using the fabricated device. In particular, the dependence of the power–frequency response and Q-factor of the device on the potential well profile has been investigated to demonstrate that under low to medium excitation levels, a shallower bistable potential well is preferable from an energy harvesting point of view.

4.2.1 Analytical modelling and Numerical simulation

The device can be modelled as a spring-mass-damper system combined with a bistable potential well created by the magnetic repulsion force. The equivalent mass of the system, linear spring constant and total damping coefficient is denoted by M, k and D respectively (Figure 4.3). The distance between the centres of the repulsively positioned magnets is denoted by d. A periodic external force F due to the external vibration is applied in the vertical direction. The resulting displacement of the mass M from the initial equilibrium position is denoted by $z(t)$ and the distance between the centres of the repulsive magnets becomes r.
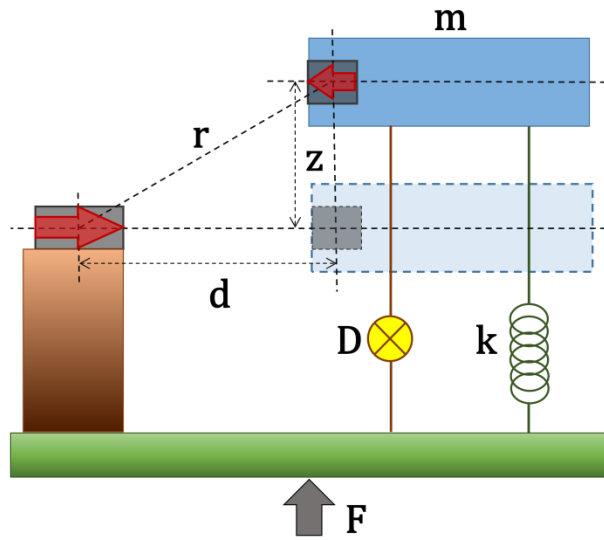
Figure 4.3: Schematic diagram of the equivalent spring-mass-damper system with repulsively positioned magnets.

It is assumed that the repulsive magnets remain anti-parallel at all times, i.e. no angular motion of the cantilever-mounted movable magnet is taken into account. If the magnetic dipole moments of the two repulsively positioned magnets are denoted by m_1 and m_2 respectively, then the magnetic interaction potential can be obtained from Furlani [1] and Yung, et al. [2] as,

$$U_m = -\frac{\mu_0}{4\pi r^3}[3(\vec{m}_1.\vec{e}_r)(\vec{m}_2.\vec{e}_r) - \vec{m}_1.\vec{m}_2] \tag{4.1}$$

where μ_0 is the permeability of air, $r = \sqrt{z^2 + d^2}$ is the distance between the centres of the magnetic dipoles and $\vec{e}_r$ is the unit vector along $\vec{r}$. Since the dipoles are assumed to be

parallel and anti-parallel to the horizontal direction, $\vec{m}_1 = m_1\vec{e}_x$ and $\vec{m}_2 = -m_2\vec{e}_x$, where $\vec{e}_x$ is the unit vector along the horizontal direction. Also,

$$\vec{m}_1.\vec{e}_r = m_1\vec{e}_x.\left(\frac{d\vec{e}_x + z\vec{e}_z}{r}\right) = m_1\frac{d}{r} \tag{4.2}$$

and similarly,

$$\vec{m}_2.\vec{e}_r = -m_2\frac{d}{r} \tag{4.3}$$

where $\vec{e}_z$ is the unit vector along the vertical direction. Equations 4.1 - 4.3 can be combined to obtain,

$$U_m = -\frac{\mu_0}{4\pi r^3}\left[3\left(m_1\frac{d}{r}\right)\left(-m_2\frac{d}{r}\right) + m_1m_2\right] \tag{4.4}$$

Or,

$$U_m = \frac{\mu_0}{4\pi r^3}\left[3m_1m_2\left(\frac{d}{r}\right)^2 - m_1m_2\right]$$

$$= \frac{\mu_0 m_1 m_2}{4\pi}\frac{(2d^2 - z^2)}{(z^2 + d^2)^{5/2}} = C\frac{(2d^2 - z^2)}{(z^2 + d^2)^{5/2}} \tag{4.5}$$

where $C = (\mu_0 m_1 m_2)/4\pi$ is a constant pre-factor. The dynamical equation of the system can be represented as follows,

$$M\ddot{z} + kz + D\dot{z} + \frac{\partial}{\partial z}U_m(z) = F \tag{4.6}$$

At sufficiently small gap distances (d) the total mechanical potential energy ($U(z)$) and restoring force ($F_{Rest}(z)$) can be expressed as,

$$U(z) = \frac{1}{2}kz^2 + C\frac{(2d^2 - z^2)}{(z^2 + d^2)^{5/2}} \tag{4.7}$$

and,

$$F_{Rest}(z) = -\frac{\partial}{\partial z}U(z) = -kz - C\frac{3z(z^2 - 4d^2)}{(z^2 + d^2)^{7/2}} \tag{4.8}$$

The eq. 4.7 and 4.8 represent a bistable nonlinear dynamical system with a potential barrier at initial equilibrium ($z = 0$) and two potential wells on either sides of the barrier [Figure 4.4]. The dependence of the potential energy profile and restoring force on the gap between the repulsively arranged magnets is depicted in Figure 4.4. As d is gradually decreased from a higher value to a lower value, the potential energy at the initial equilibrium position ($z = 0$) becomes larger and two potential wells are developed on either sides of the equilibrium. Thus, the system which was initially linear, with a monostable parabolic potential profile, evolves into a bistable system with two stable positions. Also, the restoring force changes from the linear pattern into a nonlinear form with decreasing values of d. Thus, the potential energy and restoring force in the system can be modified by adjusting the gap between the repulsively oriented magnets.

Table 4.1: Identified system parameters used in numerical simulation

Symbol	Quantity	Value/ Magnitude
m	Equivalent mass	2.664×10^{-4} kg
k	Equivalent spring coefficient	13.61 N/m
L	Length of cantilever	16.5×10^{-3} m
w	Distance of wall (base) from the cantilever	3.5×10^{-3} m
m_0	Dipole moment of tip magnet	3.6×10^{-3} A.m^2
m_1	Dipole moment of front magnet	7.8×10^{-3} A.m^2
ξ	Mechanical damping coefficient	5.263×10^{-3}
R_{Coil}	Resistance of copper coil	770 Ω
N	No. of turns in coil	2500
R_{Load}	Optimum load resistance	1000 Ω

When an external periodic vibration force is applied to the system, the equivalent mass starts to oscillate within one of the potential wells of the system. This 'intra-well' oscillation is of relatively small amplitude and the energy produced by the harvester is typically small in this situation. If the applied force is large enough, the equivalent mass accumulates sufficient kinetic energy enabling it to overcome the potential barrier. The mass then starts to oscillate between the two potential wells, performing large amplitude

'inter-well' oscillations. This large amplitude inter-well oscillation results into higher magnetic flux linkage gradient in an electromagnetic transduction system, which is favourable from the energy harvesting point of view.
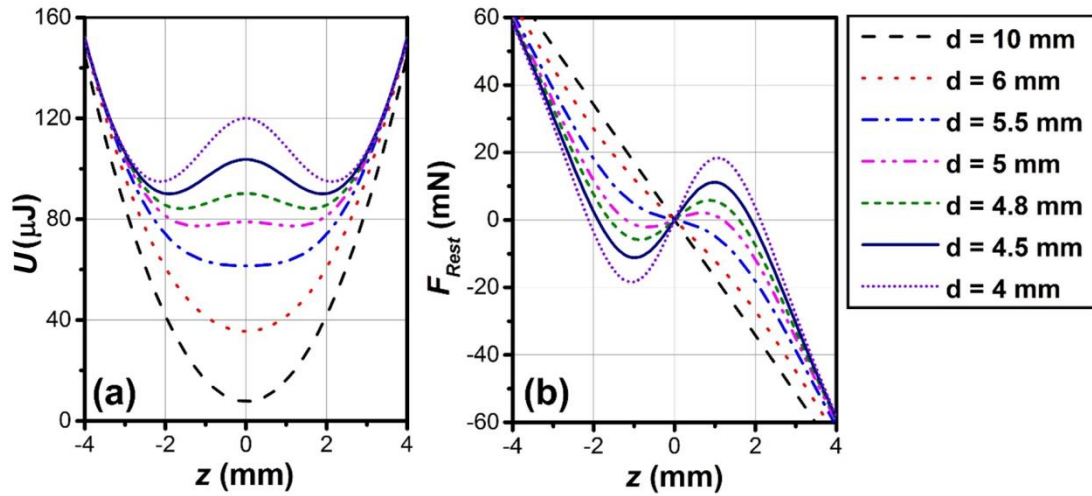
Figure 4.4: Variation of the (a) potential energy (*U*) and (b) restoring force (*F$_{Rest}$*) with vertical displacement (*z*) of the oscillator.

As the equivalent mass, i.e. the four-pole magnet assembly oscillates vertically under the influence of the applied vibration force, it induces a current in the coil. Using Kirchhoff's voltage law, electrical subsystem can be expressed as,

$$L\dot{I} + \dot{\phi} + I(R_{Coil} + R_{Load}) = 0 \qquad \text{4.9}$$

where ϕ is the total magnetic flux across all turns of the coil, R_{Load} is the load resistance, I is the induced current, and R_{Coil} and L represent the resistance and inductance of the coil respectively.

The undamped natural frequency, equivalent mass and effective spring constant of the oscillator model consisting of the FR4 folded cantilever and NdFeB magnets were determined using COMSOL Multiphysics. The maximum von Mises stress produced in the device structure was obtained from simulation [Figure 4.5(a)] and it was found to be less than the yield stress of FR4 (450 – 650 MPa). Ansoft Maxwell was used to obtain the magnetic flux linkage gradient across the coil [Figure 4.5(b)]. The one dimensional analytical model [eq. 4.6 and 4.9] was numerically solved using explicit 4th order Runge-Kutta method in MATLAB with the parameters listed in Table 4.1.
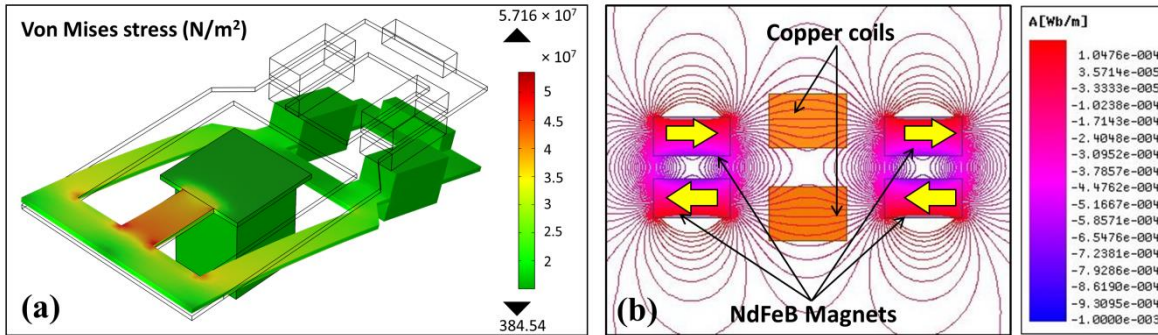
Figure 4.5: (a) von Mises stress in the deflected device. (b) magnetic flux lines in a vertical cross-section through the centre of the coil. Arrows denote the magnetic poles (N-S) orientation.

4.2.2 Experimental results and Discussions

The device was characterized for different excitation conditions using a vibration test set up consisting of a computer controlled shaker with accelerometer feedback. The harvester was subjected to sinusoidal base excitations at fixed acceleration values, whilst the frequency was varied at a constant rate. The base accelerations were chosen in a range from 0.2g to 0.6g, while the base excitation frequencies were slowly varied from 10 Hz to 50 Hz (forward sweep) and from 50 Hz to 10 Hz (backward sweep). The voltage waveform generated by the device was observed on a digital storage oscilloscope [Figure 4.6(a)].
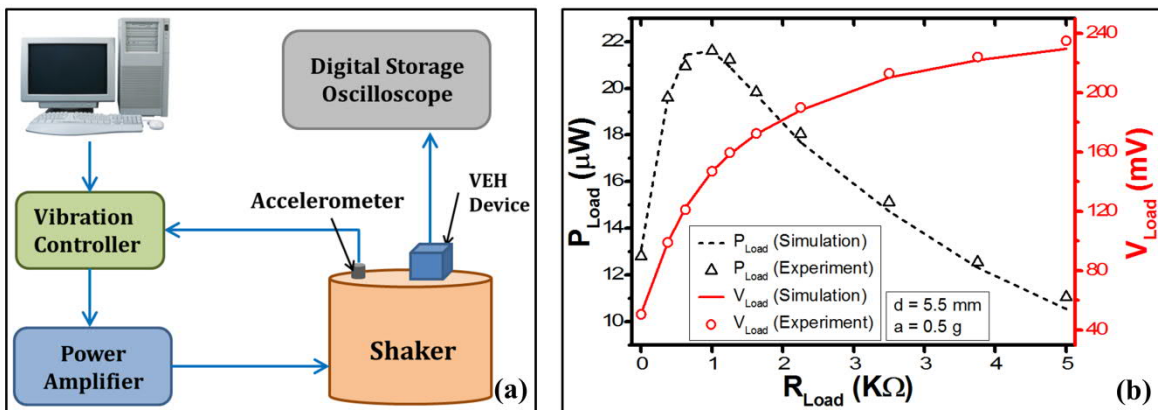
Figure 4.6: (a) Experimental test set up, (b) Variation of load power and load voltage with varying resistive load.

While FR4 has been used in very few works [3], [4], [5], [6] as a structural material for VEH devices, it is relatively unexplored compared to other conventional materials such as metals, silicon and polymers. The yield stress of FR4 is in the range of $450 - 650$ MPa (N/m^2) and the maximum von Mises stress as observed from COMSOL simulations of the

model is 57.16 MPa (N/m²). During the experiments, low to moderate accelerations (up to 0.6g) were applied and the device was operated for 6 – 8 hours each day over a period of four weeks (More than 10 million cycles). So far, no degradation (fracture, crack) in the device structure has been detected by optical observation.

In the first set of experiments, the output voltage was measured across various resistive loads, ranging from 200 Ω to 5 kΩ, while the device was excited at 0.5g acceleration near the peak power frequency. The optimum load resistance was found to be 1 kΩ experimentally, across which the device generated a peak optimum power of 22 µW and peak load voltage of 150 mV at an acceleration of 0.5g [Figure 4.6(b)]. The plots in Figure 4.6(b) represent the data collected for a bistable configuration (d = 5.5 mm). The same experiment was repeated for a linear configuration (d = 10 mm), which produced a variation of load power (P_{Load}) and load voltage (V_{Load}) with varying load resistance (R_{Load}), which is very similar to that given in Figure 4.6(b). This is primarily due to the fact that the electromagnetic coupling between the coil and magnets is small and is insensitive to the mechanical nonlinearity in the system.

The effect of varying the distance d between the repulsive magnets (i.e. changing nonlinearity) was studied under fixed acceleration values (0.2g, 0.4g, 0.6g) and a fixed load resistance of 1 kΩ, while the frequency was swept in both forward and reverse directions. Under 0.2g acceleration, at large gap distances (d = 10 mm) the resulting power-frequency response shows linear resonant behavior [Figure 4.7(b)], i.e. a sharp peak at the resonance frequency and almost identical response in up and down frequency sweeps. As d is gradually decreased to 5 mm, the repulsive force between the magnets increased, creating a bistable system with two shallow potential wells on either side of the initial equilibrium. Also, increased magnetic repulsion force cause a drop in the effective spring constant which is evident from the gradual shift of the linearized resonance frequency. The frequency response in this condition represents hysteretic behavior in a region bounded by two saddle node points (jump frequencies) in forward and reverse frequency sweeps. While in up sweep the response traces a high energy branch with a peak load power of 8 µW and a wider bandwidth (~5 Hz), during down sweep it follows a low energy orbit. The jump frequency and peak power in up sweep is larger than the same in down sweep, i.e. the power frequency response gives a nonlinear hardening response (i.e. frequency response tilted towards higher frequencies). Due to the bistable nonlinearity

brought into effect by the repulsive magnetic force, the frequency response in this configuration also produces a small jump in power near a frequency of 12.5 Hz, which can be attributed to the super harmonic resonances. As demonstrated by Masana and Daqaq [7], the superharmonic responses can be utilized to harvest power at frequencies much lower than the fundamental frequency of a bistable device.
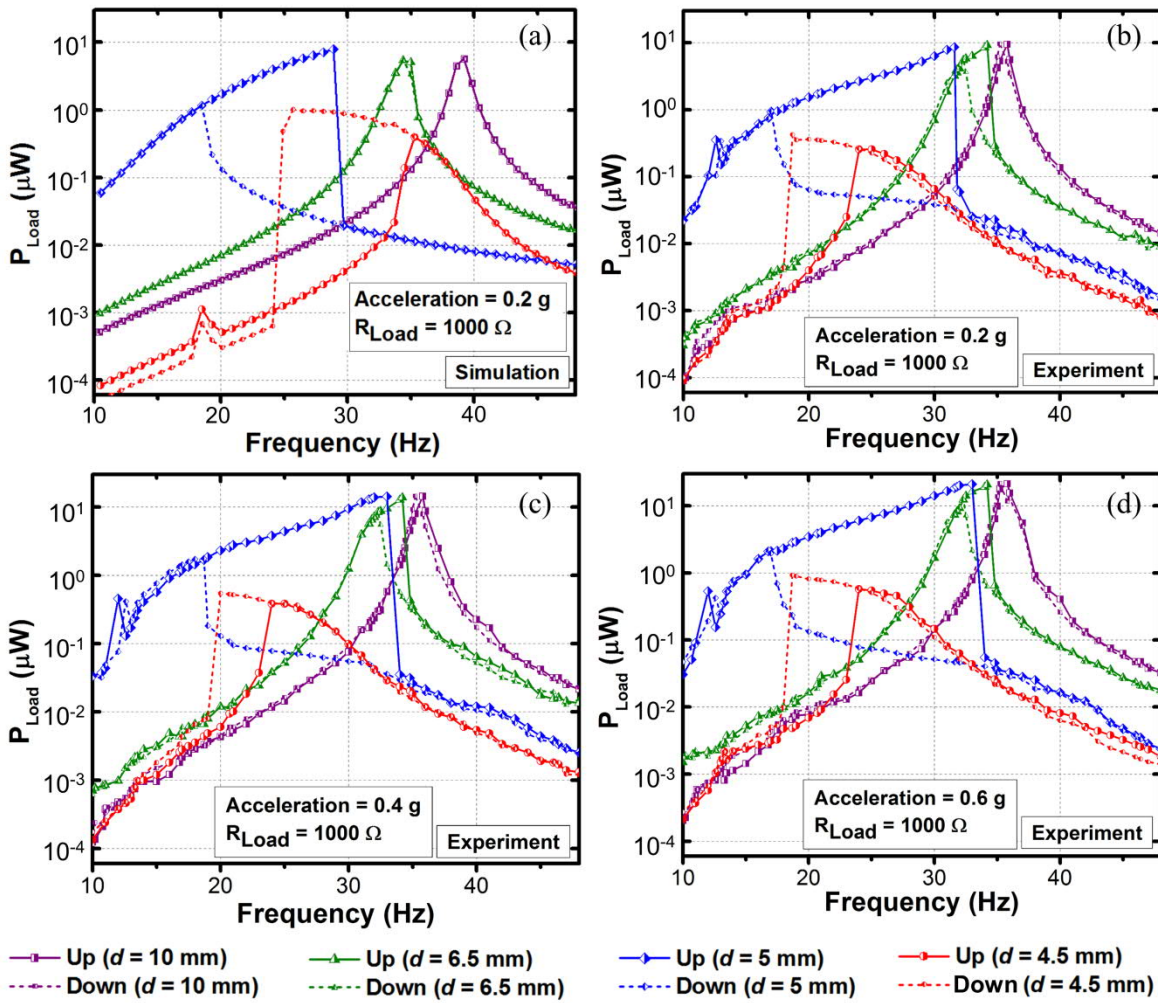
Figure 4.7: **Frequency sweep responses at different accelerations for different gap distances between repulsively arranged magnets. (a) Simulated response at 0.2g acceleration, (b) Experimental response at 0.2g acceleration, (c) Experimental response at 0.4g acceleration, (d) Experimental response at 0.6g acceleration.**

As the gap is reduced further (d = 4.5 mm), the potential barrier between the wells becomes even higher, and the oscillator becomes confined within a single potential well, performing small amplitude oscillations resulting in a small amount of power being generated. In addition, the device represents a softening nonlinear behavior (i.e. frequency response tilted towards lower frequencies) due to confinement in a single potential well,

i.e. the peak power level in the downward frequency sweep becomes larger than the same in upward sweep.

The effect of increasing the acceleration (0.4g, 0.6g) on the device performance was studied at the same gap distances (d = 10 mm, 5 mm, 4.5 mm) as described previously. The power frequency responses for each of these cases were similar to that observed in Figure 4.7(b), except for an enhancement in the harvested power. In addition, for d = 5 mm, the jump frequency in the up sweep increased slightly, thus marginally increasing the bandwidth to about 6 Hz. For d = 4.5 mm, even at the highest applied excitation (0.6g), the oscillator is still confined in a potential well and performs low energy intra-well oscillations. From an energy harvesting point of view, the inter-well oscillation in the case of shallow potential wells (for d = 5 mm) is more desirable than the intra-well oscillation in a deeper potential well (for d = 4.5 mm). This is because with decreasing d, the height of the potential barrier between them is increased, which inhibits large amplitude inter-well oscillations of the VEH system. Hence, for the application of bistable VEH systems in vibrational environments with low to medium acceleration values, as studied in this work (0.2g – 0.6g), it is critical to design a potential energy profile that allows the oscillator to perform large amplitude inter-well oscillations.

The phenomenon of confinement in a single potential well (for d = 4.5 mm) is also indicated in the simulated voltage vs. position plots (Figure 4.8) taken near the jump frequencies in an up sweep. The loops on both sides of the voltage–position plot for d = 5 mm occur due to the fact that at large amplitude vibrations, the magnet assembly travels beyond the range of influence of the coil, abruptly reverting the flux linkage gradient.
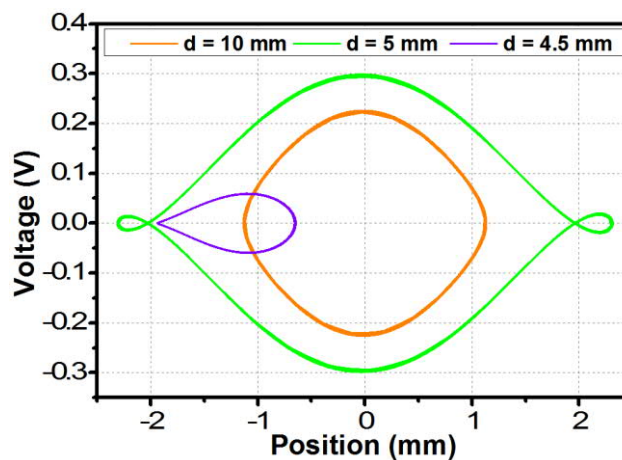

**Figure 4.8: Voltage vs. position plots at a = 0.2 g acceleration**

The Q-factor (quality factor) of a linear resonant system can be defined as the ratio of energy stored vs energy dissipated in each oscillatory cycle, which typically indicates the sharpness of the system frequency response. However, for a nonlinear non-resonant system the Q-factor of the device, as an approximation, was determined by observing the decay in the open circuit voltage signal after abruptly stopping the shaker near the peak power frequency (Figure 4.9(a)). As the gap distance (*d*) was decreased in steps, the Q-factor was found to decrease from about 90 to 95 (*d* = 11.5–8.5 mm) to the range of 50–60 (*d* = 5–4.5 mm) (Figure 4.9(b)). The lower Q factors at closer gaps between the magnets can be attributed to the reduced contribution of the linear stiffness factor due to repulsive interaction between the oppositely oriented magnets. While a lower Q factor is beneficial for a system with a wider bandwidth, it also indicates a lower peak power at similar excitation conditions. Thus, proper adjustment of the potential energy profile by regulating the gap distance (*d*) is also crucial to achieve a wide bandwidth while maintaining a reasonably high Q factor.
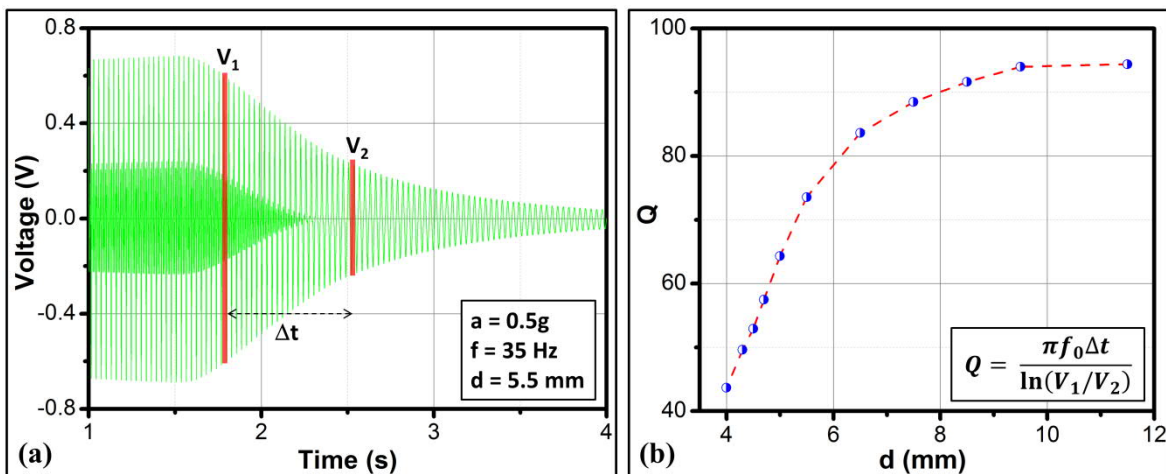
Figure 4.9: **(a) Voltage decay plot after turning off the excitation at d = 6 mm, a = 0.5 g, f = 35 Hz and (b) variation of Q-factor with gap between repulsive magnets.**

Figure 4.10 shows the frequency response of the open circuit voltage generated by the energy harvester when d is 5 mm under an acceleration of 0.5 g. The open circuit voltages have been shown at different frequencies during an upward and downward frequency sweep in Figure 4.10(b)–(h). As the up sweep frequency is gradually increased from lower values, the peak to peak open circuit voltage increases to almost ±0.75 V until the jump frequency at 35 Hz. The amplitude of vibration also increases with increasing frequency, and the magnet assembly moves beyond the range of influence of the coil. Thus, the flux

linkage gradient changes direction and accordingly, the voltage time trace develops small fluctuating peaks (Figure 4.10(d)).
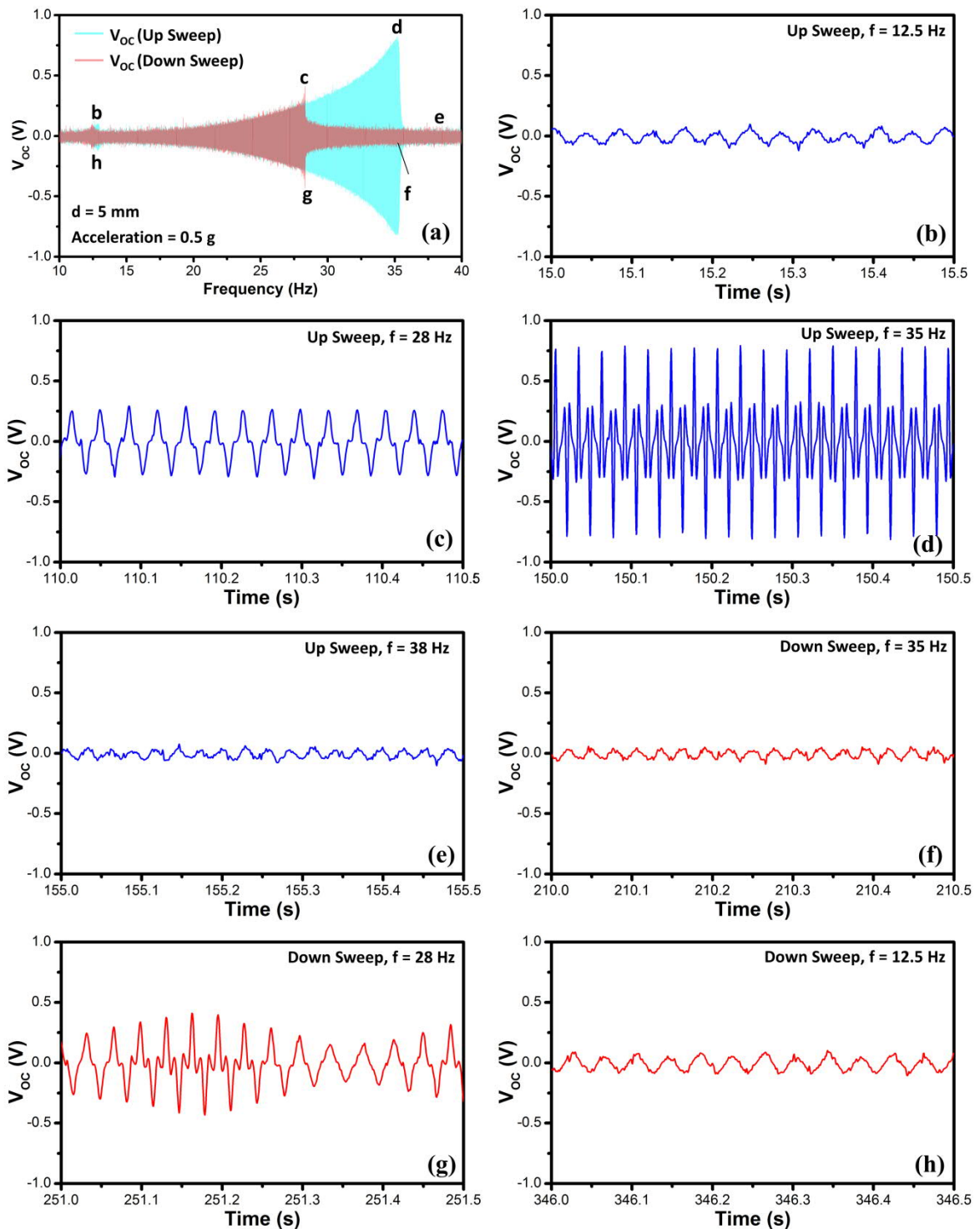
Figure 4.10: (a) Open circuit voltage vs. frequency plot at d = 5 mm, a = 0.5 g, (b) V_{OC} at f = 12.5 Hz, (c) V_{OC} at f = 28 Hz, (d) V_{OC} at f = 35 Hz, (e) V_{OC} at f = 38 Hz, (f) V_{OC} at f = 35 Hz, (g) V_{OC} at f = 28 Hz, and (h) V_{OC} at f = 12.5 Hz.

During the down sweep of the frequency the generated voltage is low; however, the oscillator suddenly jumps to oscillate with higher amplitude at 28 Hz (Figure 4.10(g)). The jump frequencies at 35 Hz and 28 Hz are the saddle node points in the open circuit voltage frequency response. A small rise in peak to peak open circuit voltage is observed near 12.5 Hz in both up and down sweeps, which can be attributed to the super-harmonic resonance phenomenon of nonlinear oscillators.

4.3 Nonlinear vibration energy harvester combining bistable nonlinearity and mechanical impact

In this section the combined effect of magnetically induced bistable nonlinearity and mechanical impact has been investigated through analytical modelling, numerical simulation, experimental validation and analysis. The mechanical impact phenomenon generally occurs under large amplitude vibration, especially when the size of the device is small and the space available for movement of the oscillatory mass is limited. However, the impact phenomenon can be realized even under small amplitude harmonic vibrations in small size devices if the conditions of resonance are satisfied (for linear devices), or the initial conditions for high energy large amplitude oscillation are met (for nonlinear devices). The effect of mechanical impact on the frequency response of linear and nonlinear oscillations of vibration energy harvesting devices have been studied in this section.

The folded cantilever structure introduced in the previous section [4.2] has been used here, which allows for relatively low frequency operation within a relatively small footprint due to the use of low Young's modulus FR4 material. Similar to the previous section, the bistable nonlinearity is introduced into the system by a pair of repulsively oriented NdFeB permanent magnets [Figure 4.2]. A second nonlinear mechanism, i.e. mechanical impact between the oscillator and the base is also taken into account. Based upon the theoretical discussion in subsection 4.2.1, a more elaborate analytical model has been developed which incorporates the impact effect and angular motion of the movable magnet. The effects of bistable nonlinearity and mechanical impact have been experimentally investigated individually and in conjunction at different acceleration levels.

4.3.1 Theoretical Methods and Numerical Analysis

The theory of operation of the device can be explained with the help of a linear oscillator consisting of a spring-mass-damper system in conjunction with a bistable potential well created by the force of magnetic repulsion, as explained in 4.2.1. The equivalent mass of the system, linear spring constant and total damping coefficient are denoted by M, k and D respectively. The cantilever onto which the magnets are attached can be modelled to be hinged at one end and the other end is allowed to move up and down in the vertical Z direction. Another repulsively oriented magnet is placed in front of the magnet on cantilever in such a way that the centers of the magnets are a distance 'd' apart. On application of an external periodic force F in the vertical (Z) direction, the mass moves periodically in the vertical direction. As the free end is deflected from the initial equilibrium position to a distance 'z' in the vertical direction, the cantilever is rotated by an angle 'θ' with respect to the equilibrium position. [Figure 4.11]. The displacement of the mass M from its equilibrium position is denoted by z(t).
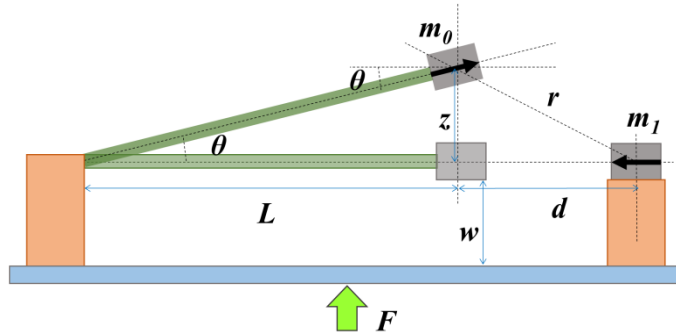
Figure 4.11: Schematic diagram of the bistable VEH system with repulsively positioned magnets

If the magnetic dipole moments of the repulsively oriented magnets are denoted by $\vec{m}_0$ and $\vec{m}_1$ respectively, then, $\vec{m}_0 = m_0 \cos\theta\, \vec{e}_x + m_0 \sin\theta\, \vec{e}_z$ and $\vec{m}_1 = -m_1 \vec{e}_x$, where $\vec{e}_x$ and $\vec{e}_z$ are the unit vectors along the horizontal (X) and vertical (Z) direction respectively [Figure 4.11]. From [1] and [2] the magnetic interaction potential can be expressed as,

$$U_m = -\frac{\mu_0}{4\pi r^3}[3(\vec{m}_0 \cdot \vec{e}_r)(\vec{m}_1 \cdot \vec{e}_r) - \vec{m}_0 \cdot \vec{m}_1] \qquad 4.10$$

where $r = \sqrt{z^2 + d^2}$ is the distance between the centres of the magnetic dipoles and $\vec{e}_r$ is the unit vector along $\vec{r}$. Also,

$$\vec{m}_0 . \vec{e}_r = \frac{m_0}{r}(d \cos \theta + z \sin \theta)$$

4.11

and,

$$\vec{m}_1 . \vec{e}_r = -m_1 \frac{d}{r}$$

4.12

and similarly,

$$\vec{m}_0 . \vec{m}_1 = -m_0 m_1 \cos \theta$$

4.13

Equations. (4.10), (4.11), (4.12) and (4.13) can be combined to obtain,

$$U_m(z) = \frac{\mu_0 m_0 m_1}{4\pi r^5}[(2d^2 - z^2)\cos\theta + 3dz\sin\theta]$$

$$= \frac{C}{L}\left[\frac{(2d^2 - z^2)\sqrt{L^2 - z^2} + 3dz^2}{(z^2 + d^2)^{5/2}}\right]$$

4.14

where $C = +\frac{\mu_0 m_0 m_1}{4\pi}$ is a positive constant pre-factor, and μ_0 is the permeability of air.

The vertical force acting on the cantilever due to magnetic dipole interaction is given by,

$$F_m(z) = -\frac{\partial}{\partial z}U_m(z)$$

$$= -\frac{C}{L}\left[-\frac{5z}{(d^2 + z^2)^{7/2}}\left(3dz^2 + (2d^2 - z^2)\sqrt{L^2 - z^2}\right)\right.$$

$$\left. + \frac{1}{(d^2 + z^2)^{5/2}}\left(6dz - 2z\sqrt{L^2 - z^2} - \frac{z(2d^2 - z^2)}{\sqrt{L^2 - z^2}}\right)\right]$$

4.15

When $z \geq -w$, the dynamical equation of the system can be formulated as,

$$M\ddot{z} + kz + D\dot{z} + \frac{\partial}{\partial z}U_m(z) = F\sin(\omega_0 t)$$

4.16

In order to model the effect of mechanical impact in the nonlinear bistable system, a rigid wall (glass) at a distance 'w' from the mass can be considered. Under low to moderate harmonic excitation (0.2g – 0.5g) the oscillator does not hit the wall. However, with increasing acceleration (0.6g – 1.5g) the amplitude of oscillation increases and the mass starts to collide with the wall as the excitation frequency approaches the peak power

frequency. For higher applied accelerations the oscillator collides with the rigid wall at $z = -w$ when the oscillation amplitude is $> w$. If the oscillator collides with the wall at the time t_c, then [Dankowicz and Jerrelind [8]],

$$\lim_{t \to t_c^-} z(t) = -w \qquad\qquad 4.17$$

and,

$$\lim_{t \to t_c^-} \dot{z}(t) \leq 0 \qquad\qquad 4.18$$

Then, after the collision at $t = t_c$,

$$\lim_{t \to t_c^+} z(t) = -w \qquad\qquad 4.19$$

and,

$$\lim_{t \to t_c^+} \dot{z}(t) = -C_{Rest} * \left[\lim_{t \to t_c^-} \dot{z}(t)\right] \qquad\qquad 4.20$$

where C_{Rest} is the 'coefficient of restitution' for the inelastic impact between mass and the wall. In other words, on each impact with the wall, the motion of the mass is stopped at $z(t) = -w$, and the velocity of the mass is changed to $-C_{Rest} * \dot{z}(\mathrm{t})$. This is imposed as a boundary condition in the numerical model which is simulated using explicit 4th order Runge-Kutta method in MATLAB.

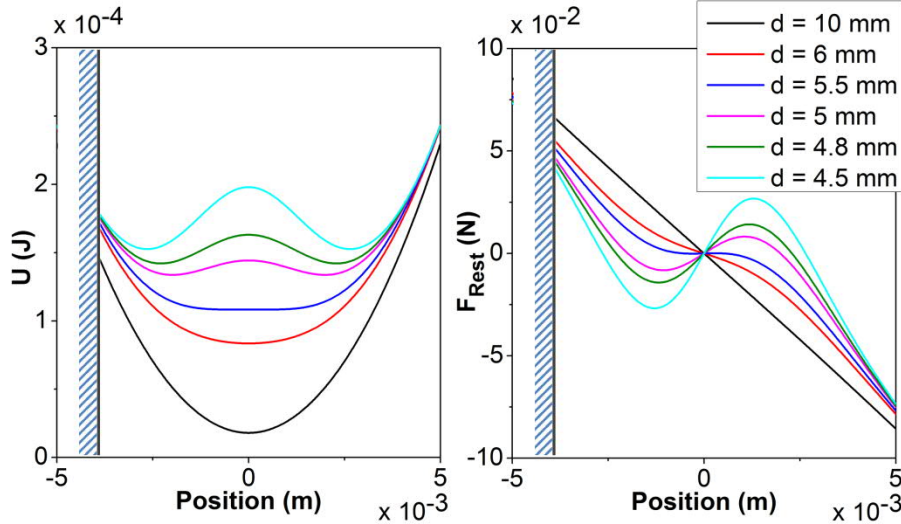Now, the total potential energy and restoring force can be obtained as,

$$U(z) = \frac{1}{2}kz^2 + \frac{C}{L}\left[\frac{(2d^2 - z^2)\sqrt{L^2 - z^2} + 3dz^2}{(z^2 + d^2)^{5/2}}\right] \qquad\qquad 4.21$$

and,

$$F_{Rest}(z) = -\frac{\partial}{\partial z}U(z) \qquad\qquad 4.22$$

The dependence of potential energy and restoring force on the distance between the repulsively arranged magnets is shown in Figure 4.12. The nature of the potential function can be controlled by manipulating the gap distance between the repulsive magnets. Specifically, when the gap is large, the potential represents a parabola, which is typical of a linear oscillator. As the gap between the magnets is reduced, two new equilibrium positions appear on either sides of a potential barrier at the centre. The peak of this central

potential barrier becomes higher if the magnets are brought even closer together. This evolution in potential energy profile is also apparent in the restoring force, which goes from linear to nonlinear with decreasing gap between the repulsive magnets.

Figure 4.12: Variation of potential energy (U (z)) and restoring force (F_{Rest}(z)) with d. The wall position is at z = -3.5 × 10^{-3} m.

When the system is subject to the external periodic force *F* due to ambient vibration, the mass can oscillate around the new stable equilibrium positions in each potential well, representing intra-well oscillation. If *F* is high enough to overcome the potential barrier in between the potential wells, the mass starts to jump from one potential well to the other, producing large amplitude inter-well oscillation. From energy harvesting point of view, the harvester would generate higher energy when it oscillates between the two potential wells, instead of oscillating within a single potential well. On collision with the rigid wall during large amplitude inter-well oscillation, the potential energy becomes discontinuous following impact (Figure 4.12). A similar discontinuity is also observed for the restoring force.

The oscillation of the four-pole magnet assembly (equivalent mass *M*) across the copper coil changes the magnetic flux linkage across the coil. Thus, current will be induced into the coil, resulting in an electromagnetic damping force on the magnet assembly moving with respect to the fixed coil. The total damping coefficient *D* in eq. 4.16 can be divided into two components [eq. 4.23], the parasitic damping coefficient, D_P and electromagnetic damping coefficient, D_{EM}.

$$D = D_{EM} + D_P \qquad \text{4.23}$$

If ϕ is the magnetic flux across the coil then the flux linkage gradient is represented by $\frac{d\phi}{dz}$, and the voltage induced across the coil is given by the well-known Faraday's law,

$$V_{Ind} = -\dot{\phi} = -\frac{d\phi}{dt} = -\left(\frac{d\phi}{dz}\right)\left(\frac{dz}{dt}\right) = -\left(\frac{d\phi}{dz}\right)\dot{z} \qquad \text{4.24}$$

When a load resistance R_{Load} is connected across the output, then, from Kirchhoff's voltage law,

$$L\dot{I} + V_{Ind} + (R_{Coil} + R_{Load})I = 0 \qquad \text{4.25}$$

Or,

$$L\dot{I} - \dot{\phi} + (R_{Coil} + R_{Load})I = 0 \qquad \text{4.26}$$

where L and R_{Coil} are, respectively, the inductance and resistance of the coil. The eq. 4.26 can be rearranged as,

$$\frac{dI}{IR_O - \dot{\phi}} = -\frac{1}{L}dt \qquad \text{4.27}$$

where $R_O = R_{Coil} + R_{Load}$ represents the total effective resistance in the circuit. Integrating both sides of eq. 4.27 yields,

$$\frac{1}{R_O}\ln(IR_O - \dot{\phi}) = -\frac{1}{L}t + A \qquad \text{4.28}$$

where A is a constant. Considering the initial current in the coil as I_0 (at $t = 0$, $I = I_0$), the constant A can be obtained from eq. 4.28 as,

$$A = \frac{1}{R_O}\ln(I_0 R_O - \dot{\phi}) \qquad \text{4.29}$$

Substituting A in eq. 4.28 and rearranging yields,

$$\frac{1}{R_O}\left[\ln(IR_O - \dot{\phi}) - \ln(I_0 R_O - \dot{\phi})\right] = -\frac{1}{L}t \qquad \text{4.30}$$

Which is equivalent to,

$$\ln\left(\frac{IR_O - \dot{\phi}}{I_0 R_O - \dot{\phi}}\right) = -\frac{R_O}{L}t \qquad \text{4.31}$$

Or,

$$\frac{IR_O - \dot{\phi}}{I_0 R_O - \dot{\phi}} = e^{-\frac{R_O}{L}t}$$

4.32

Rearranging eq. 4.32 yields I as a function of time,

$$I(t) = \frac{\dot{\phi}}{R_O} + \left(I_0 - \frac{\dot{\phi}}{R_O}\right)e^{-\frac{R_O}{L}t}$$

4.33

For a fixed rate of change of ϕ, the $I(t)$ relaxes to the value,

$$I(t) = \frac{\dot{\phi}}{R_O}$$

4.34

with a relaxation time $\tau_{Rel} = L/R_O$, which is of the order of μs in the experimental set up. Since τ_{Rel} is much faster than the rate of change of ϕ, it essentially implies that that I adiabatically relaxes to $\dot{\phi}/R_O$.

The electromagnetic force F_{EM} acting on the magnet assembly due to the current (I) induced in the coil can be calculated from the approximation of a coil moving relatively in a single direction through a magnetic field varying in the direction of movement, which is given by [Saha [9]],

$$F_{EM} = I\frac{d\phi}{dz} = D_{EM}\dot{z}$$

4.35

The parasitic damping coefficient D_P is related to the open circuit quality factor Q_{OC} by [Saha [9]],

$$D_P = \frac{M\omega_n}{Q_{OC}}$$

4.36

where ω_n is the natural resonance frequency of the oscillator. In general, the unloaded quality factor Q_{OC} is the lumped representative of different parasitic dissipation mechanisms such as material loss, thermos-elastic loss, clamping loss, surface loss, viscous loss etc. However, detailed analysis and modelling of the various parasitic loss mechanisms are beyond the scope of the present work.

The electrical power generated in the coil is given by [Saha [9]],

$$P_{EM} = F_{EM}\dot{z} = D_{EM}(\dot{z})^2$$

4.37

The average load power across the load resistance R_{Load} is given as a time integral over an interval from t to $t+T$, where T is the time period of natural oscillation of the harvester [Saha [9]].

$$P_{Load} = \frac{R_{Load}}{R_{Coil} + R_{Load}} \frac{1}{T} \int_{t}^{t+T} P_{EM} dt \qquad 4.38$$

The device model was simulated with the help of FEA tools and numerical techniques. COMSOL Multiphysics was used to determine the undamped natural frequency, equivalent mass and effective spring constant of the oscillator model consisting of the FR4 folded cantilever and NdFeB magnets. The magnetic flux linkage gradient across the coil was obtained from Ansoft Maxwell. The equation of motion of the system was solved numerically using explicit 4th order Runge-Kutta method in MATLAB to obtain the voltage and power generated in the system.

4.3.2 Experimental Methods

The base of the energy harvester was attached to a Brüel & Kjær (LDS V455) permanent magnet shaker with accelerometer feedback, which produced vibration in the vertical direction [Figure 4.13]. The harvester and accelerometer were mounted on the shaker controlled by an LDS Comet vibration controller. The output from the controller was fed to a power amplifier (LDS PA 1000L) and the amplifier output was used to excite the shaker.
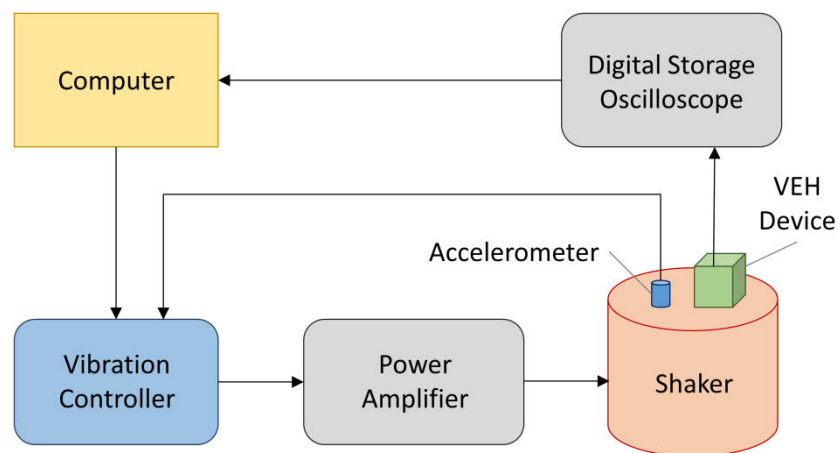
**Figure 4.13: Experimental test set up**

The harvester was subjected to sinusoidal base excitation at fixed acceleration values, while the frequency was varied at a constant rate (0.167 Hz/s). Since the dynamical model of the device considered is nonlinear which might result into multiple co-existing solutions depending upon the initial conditions, frequency sweeps are performed in both forward

(low to high) and reverse (high to low) directions. The base accelerations were chosen in a range from 0.2g to 1.5g, while the base excitation frequencies were varied from 10 to 50 Hz. The output voltage and current were measured across various resistive loads, ranging from 50 Ω to 5 KΩ. The output signal from the energy harvester was recorded via a digital storage oscilloscope.

4.3.3 Results and Discussions

Initially the experiment was performed to obtain the optimum load resistance, across which the generator produces maximum power. Figure 4.14 shows the variation of generated peak load power and load voltage for varying resistive loads at a fixed acceleration value (0.4g). The optimum load resistance was found to be about 1000 Ω, at which a peak load power of 14 µW and RMS load voltage of 150 mV was produced. The results from numerical analysis match fairly accurately with the experimental data. The power density calculated from this data is 1.45 µW per cm^3 per m/s^2.
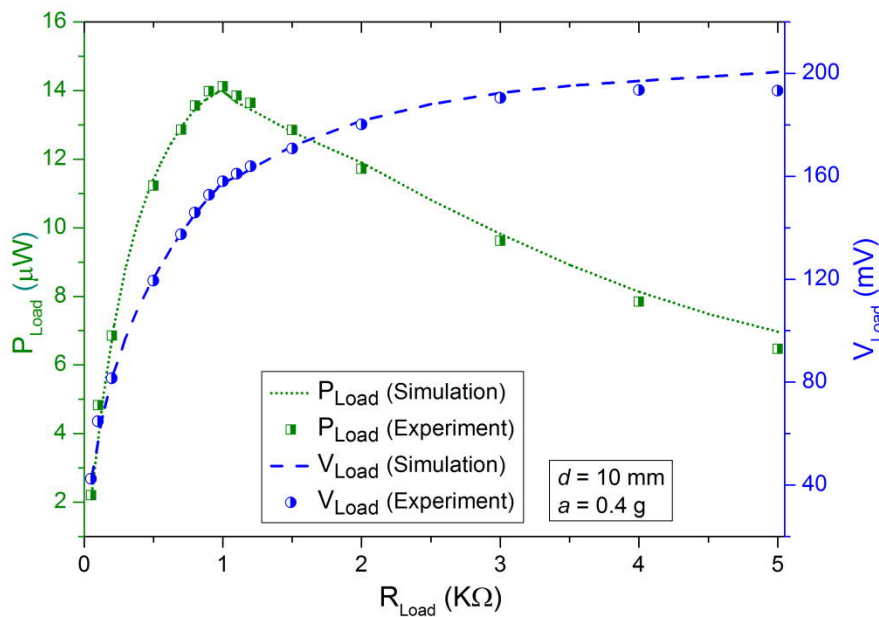
Figure 4.14: Variation of load power and load voltage with varying resistive load

The effect of varying distances (*d*) between the repulsively positioned magnets in front of the cantilever was studied under a fixed acceleration value of 0.2g and load resistance of 1 kΩ. For simulation, the frequency of the external force (equivalent mass × 0.2g, for instance) was swept upward (10 Hz to 50 Hz) and downward (50 Hz to 10 Hz). At each frequency, the steady state time series of load voltage is stored, from which the RMS voltage and load power is obtained. Then, the load power is plotted for each corresponding

frequency to generate the load power-frequency response plot. Experimentally, the VEH device is excited at a fixed acceleration (0.2g, for instance) and the frequency of the vibration was swept up and down. During the sweep the voltage time series generated by the device across a load resistance was recorded at each frequency. The RMS voltages are then computed over a moving time window which is 1/2000th (0.25 s) of the total frequency sweep duration. The load power is calculated from the RMS voltage and plotted against the corresponding frequency values.
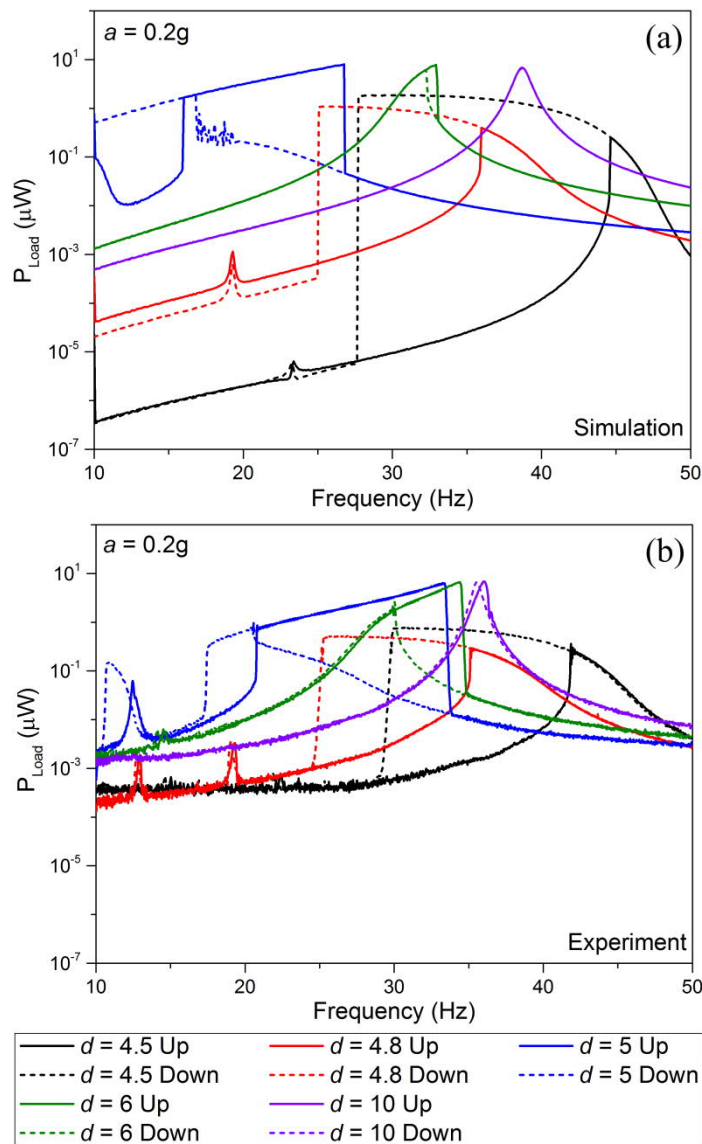

Figure 4.15: (a) Simulated and (b) Experimental frequency sweep responses for different values of d (a = 0.2g, R_{Load} = 1 KΩ).

Figure 4.15 shows the simulated and experimental power vs. frequency sweep plots for different separation distances between the magnets. The acceleration in each case was

fixed at 0.2g, and the frequency was varied from low to high (up-sweep) and high to low (down sweep) values. At a separation of 10mm between the repulsive magnets, the force due to repulsion is negligible. Thus, the potential energy function is parabolic and similar to that of a linear oscillator system with a single parabolic potential well. The frequency sweep response in this case represents a sharp resonance peak, characteristic of a linear oscillator. The simulated linear resonance frequency was 39 Hz, while the same from experiment was found to be 36 Hz. This slight mismatch in linear resonance frequency can be attributed to the imperfections in manual assembly and the resulting asymmetry in the fabricated device.
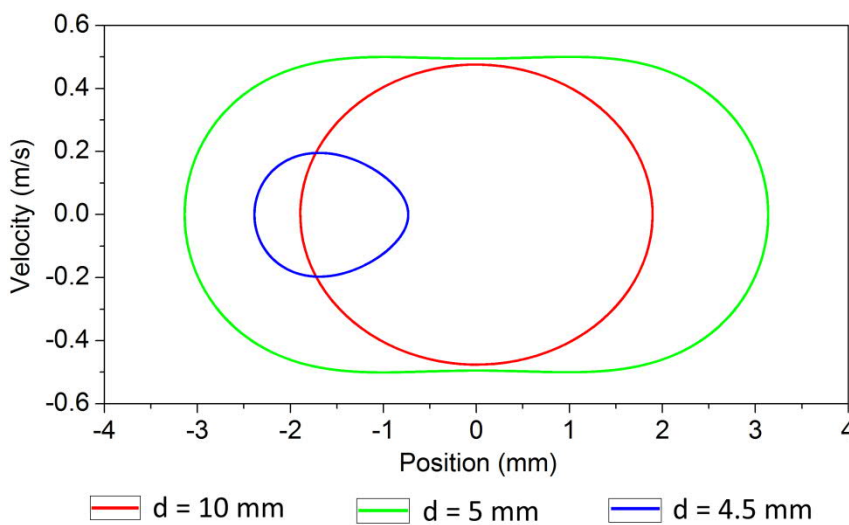
Figure 4.16: Phase plots near jump frequencies in up sweep for different distances between repulsively positioned magnets

As the gap between the magnets is reduced to 5 mm, the force of repulsion increases, forming a bistable system with two shallow potential wells on either sides of the initial equilibrium. The increased magnetic repulsion force causes a drop in the effective spring constant and introduces a nonlinear spring force into the system. This is evident from the gradual shift of the linearized resonance frequency towards lower frequency values. As the excitation frequency is slowly varied from low to higher values, the output power gradually increases, and then jumps abruptly to a very small value at a certain frequency. On the other hand, as the frequency was gradually decreased from high to lower value, the output power follow a low energy path, and then jumps up at another frequency to merge with the up sweep response. Thus, a hysteresis loop is represented by the up and down frequency sweep responses. Figure 4.15 displays that there is good qualitative agreement between the simulated and experimental results. However, the frequency responses at $d = 5$

mm show that there is a difference of about 7 Hz between the simulated and experimental jump frequency in up sweep. This discrepancy can be attributed to the simplicity of the one dimensional numerical model, whereas the real device is a complex three dimensional system.

As the distance between the magnets is made even smaller (4.5 mm), the bistable potential wells on either sides of the central position become even deeper (Figure 4.12). A situation is reached when the kinetic energy of the oscillator due to external vibrational force is not sufficient to overcome the potential barrier and the beam gets confined within a single potential well. This confinement of the oscillator in a potential well results into softening spring behaviour [Nguyen and Halvorsen [10] , Masana and Daqaq [11]]. In this condition, the amplitude of oscillation and subsequently, the power generated by the harvester is very small. Figure 4.15 also reveals small super-harmonic resonance peaks near 1/3rd of the resonance frequency. This super-harmonic resonance peaks are characteristic of a nonlinear dynamic system, which can be tapped to harvest energy from low frequency vibrations [Masana and Daqaq [7] , Harne and Wang [12]] of a device with smaller foot-print and relatively high resonance frequency.

In order to visualize the confinement of the oscillator in a single potential well at smaller values of *d*, the phase plots (velocity vs position) [Figure 4.16] were obtained near the up sweep jump frequencies from numerical simulations. At *d* = 10 mm, there is no bistability in the system and correspondingly, the amplitude of oscillation is relatively small. When *d* is reduced to 5 mm, two shallow potential wells are created on either sides of the equilibrium position (z = 0) and the mass oscillates between the two potential wells, performing large amplitude inter-well oscillation. As *d* is further reduced to 4.5 mm, the potential barrier becomes too high for the oscillator to overcome and small amplitude intra-well oscillation is initiated. This is evident from Figure 4.16 as the oscillator is confined in a potential well on the left hand side and no more crosses the equilibrium position at *z* = 0.

In order to study the effect of mechanical impact on the VEH's performance, higher vibrational accelerations are applied so that the amplitude of oscillation increases and the oscillator collides with the base. Figure 4.17 shows the variation of the load power in both forward and reverse frequency sweep at different acceleration values, when *d* = 10 mm. At low acceleration values (0.2g, 0.4g) the power response depicts a linear resonant nature, with resonance frequency at 39 Hz for simulation, and at 36 Hz for experiments.
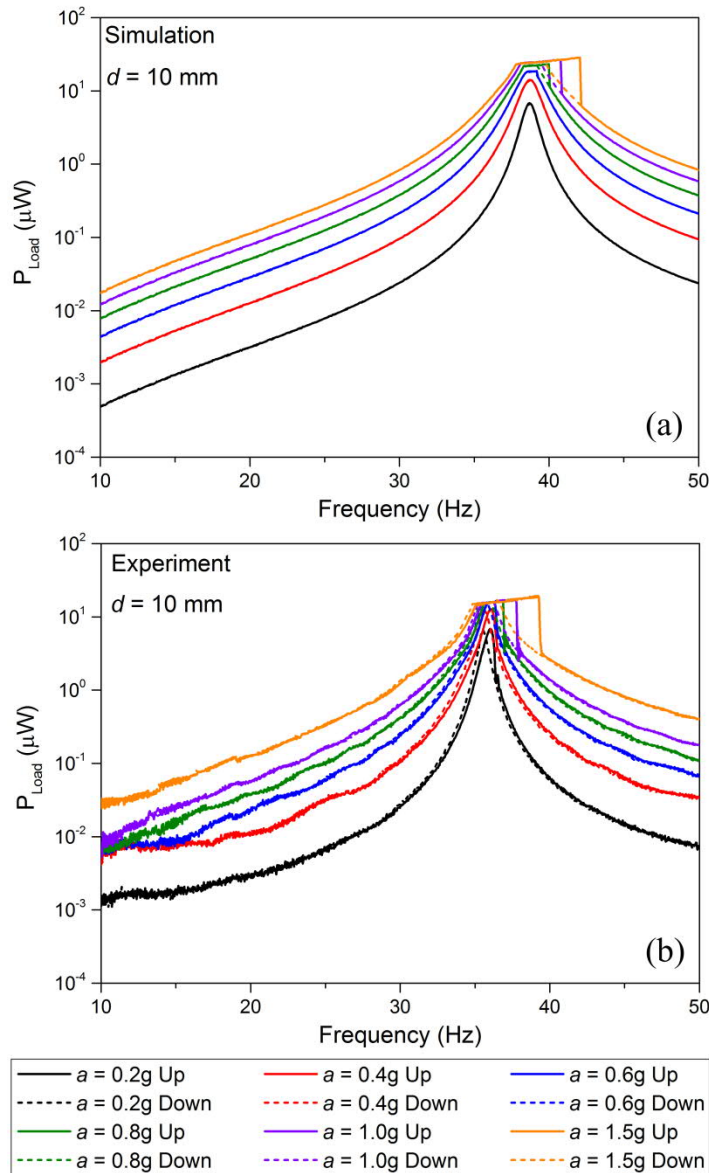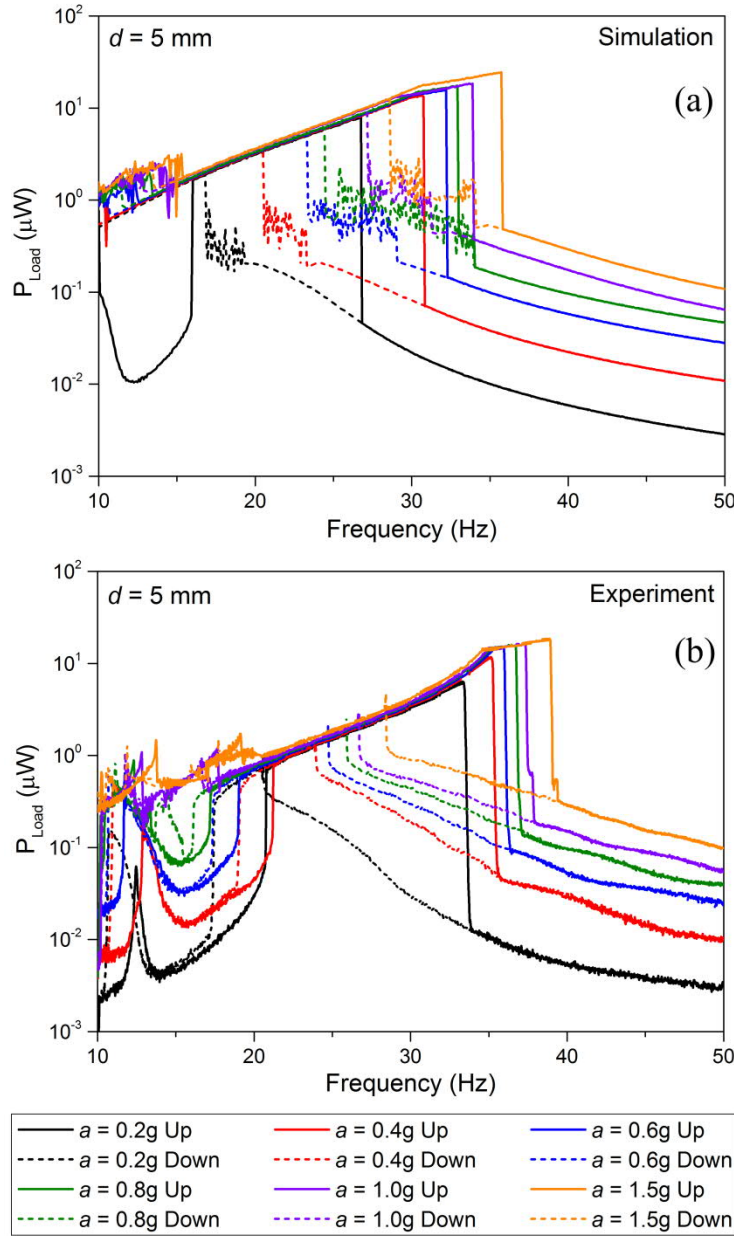
Figure 4.17: (a) Simulated and (b) Experimental frequency sweep responses for different acceleration values (d = 10 mm, R_{Load} = 1 kΩ, w = 3.5mm)

As the acceleration is increased in steps (0.6g, 0.8g, 1.0g, 1.5g), the peak of the frequency response in upward frequency sweep get flattened due to abrupt change in the dynamics of the oscillator as it starts colliding with the base at higher acceleration. This effect was explored by some researchers [[13] , [14]] to widen the frequency response of VEH devices by using mechanical stoppers to change the stiffness of the oscillator on impact. In the present device, however, the base of the oscillator serves as the mechanical stopper, and the nonlinearity incorporated by the impact broadens the operational bandwidth in this case.
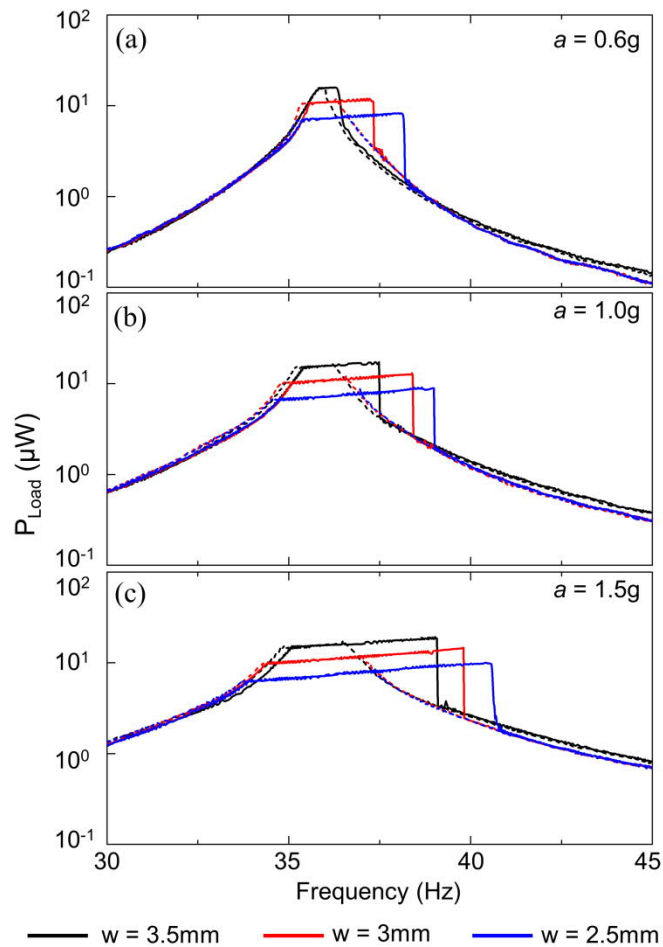
Figure 4.18: Experimental frequency responses for different wall distances (*w*) at (a) *a* = 0.6g, (b) *a* = 1g, and (c) *a* = 1.5g, for *d* = 10 mm.

The effect of varying wall distances on the frequency response of the VEH is shown in Figure 4.18. In order to vary the wall distance from the oscillator, small pieces of diced glass slides of the appropriate thickness were placed at the impact point on the base. At a fixed vibrational acceleration, the frequency response become broader as the wall was brought closer in steps, resulting in early onset of mechanical impact and increase in the up sweep jump frequencies. Furthermore, as the acceleration is increased keeping the wall distance fixed, the frequency response broadened even further. However, the output power level also became lower with bringing the wall closer. This is due to the fact that the impact limits the amplitude of the VEH oscillator and some energy is dissipated in the system on every impact.

Figure 4.19: (a) Simulated and (b) Experimental frequency sweep responses for different acceleration values (d = 5 mm, R_{Load} = 1 kΩ, w = 3.5 mm).

The effect of mechanical impact on the frequency sweep response for the nonlinear bistable configuration (d = 5 mm) is depicted in Figure 4.19. As the input acceleration is increased from 0.2g to 1.5g in steps, the peak output power gradually increases from 6.4 µW to about 18.6 µW. However, beyond an acceleration value of 0.6g, the amplitude of oscillation becomes very large near the resonance frequency and the free end of the cantilever collides with the base of the energy harvester. Again, this collision changes the system dynamics, which is manifested in the increase in the jump frequency during up

sweep. In this configuration the device exploits both the effects of bistability and mechanical impact to achieve a wider frequency bandwidth.
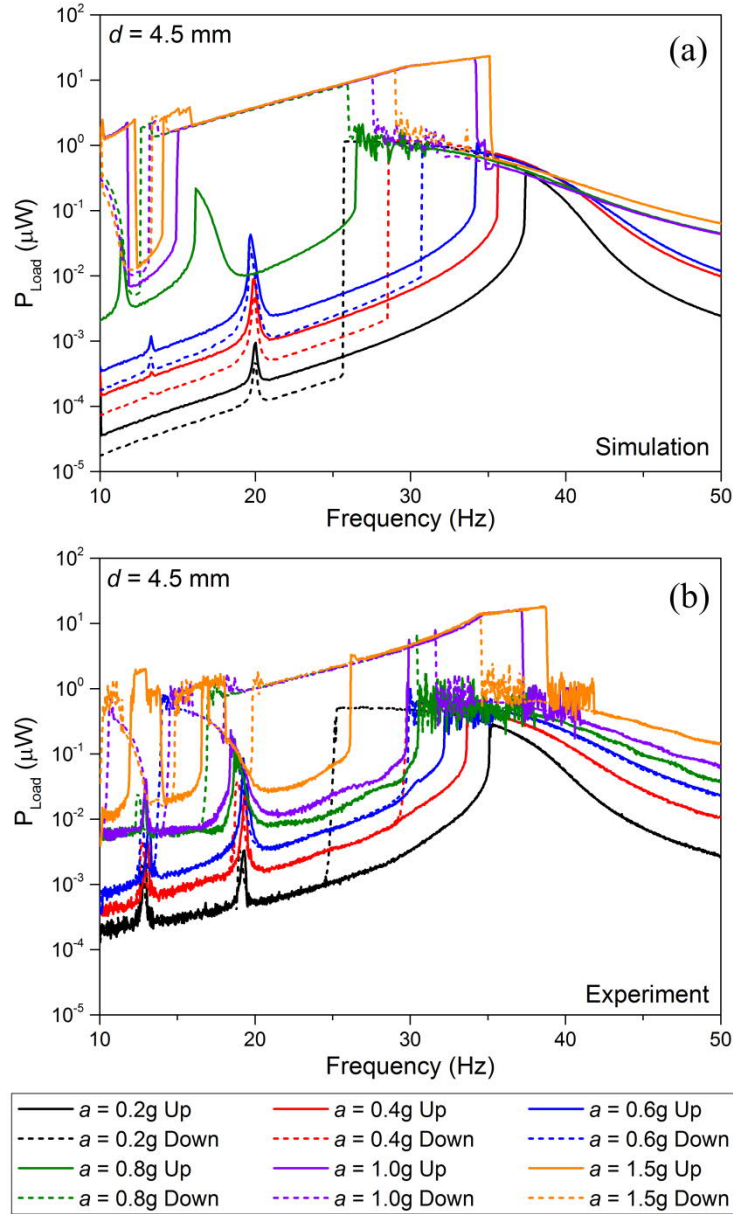
Figure 4.20: (a) Simulated and (b) Experimental frequency sweep responses for different acceleration values (d = 4.5 mm, R_{Load} = 1 kΩ, w = 3.5 mm).

As the potential barrier is made even higher (d = 4.5 mm), under low to medium applied accelerations (0.2g, 0.4g, 0.6g), the device initially remain confined in one potential well, resulting in softening spring behaviour [Nguyen and Halvorsen [10]; Masana and Daqaq [11]] (Figure 4.20). At an applied acceleration of 0.8g, the device response becomes chaotic in the frequency range 30 – 37 Hz, in up and down sweep, as it starts to oscillate intermittently between the potential wells (Figure 4.20(b)). The chaotic inter-well motion is shown in Figure 4.21. As the acceleration is increased even further (1.0g, 1.5g), the

oscillator starts inter-well motion and collides with the base during up sweep as it approaches the jump frequency. As a result of the impact, the frequency response in up sweep is broadened, which is evident from the increase in the jump frequency. After the jump the inter-well motion become chaotic, and is finally diminished to confinement in a potential well.
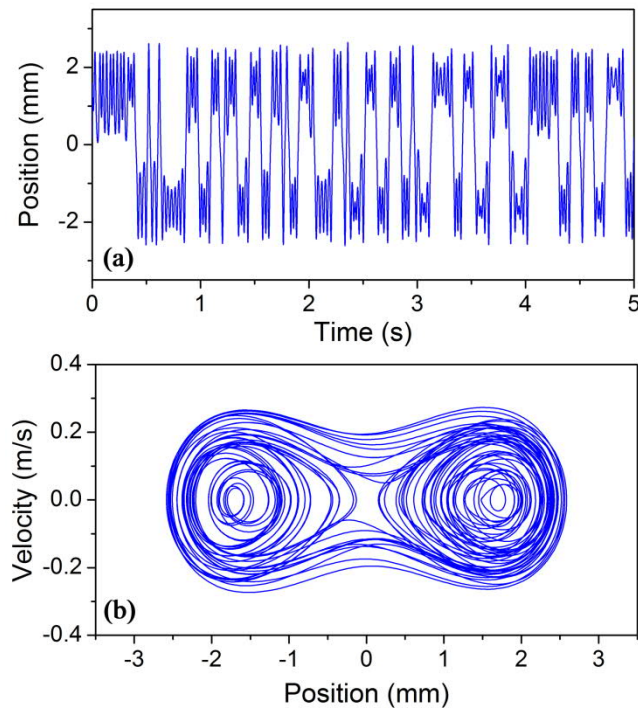
Figure 4.21: Simulated (a) Position vs time, (b) Phase plot (Velocity vs Position) for *d* = 4.5 mm, *a* = 0.8g, *f* = 30 Hz, *w* = 3.5 mm.

Figure 4.22(a) shows the variation of bandwidth (BW) for different gap distances at different applied accelerations. A threshold load power level of 5 µW (~ 0.1 V over 1 KΩ load for a coil of 770 Ω resistance) was considered to obtain the bandwidth and the average load power was calculated over the range of bandwidth. For *d* = 10 mm, the broadening in bandwidth is almost linear with increasing acceleration and reaches a maximum of 6 Hz at *a* = 1.5g. While the broadening in bandwidth up to *a* = 0.6g can be attributed to the increased power level, from *a* = 0.8g onwards, the bandwidth increases primarily due to impact. The average load power, on the other hand, increases at a faster rate at lower accelerations (0.2g – 0.6g), and the rate of increase in power diminishes with increasing acceleration and become almost flat at higher accelerations (*a* = 1.2g, 1.5g). When the potential wells are shallow (*d* = 6 mm, 5mm), the bandwidth widening at low accelerations (0.2g to 0.6g) are due to the nonlinearity effected by increased magnetic repulsive force.
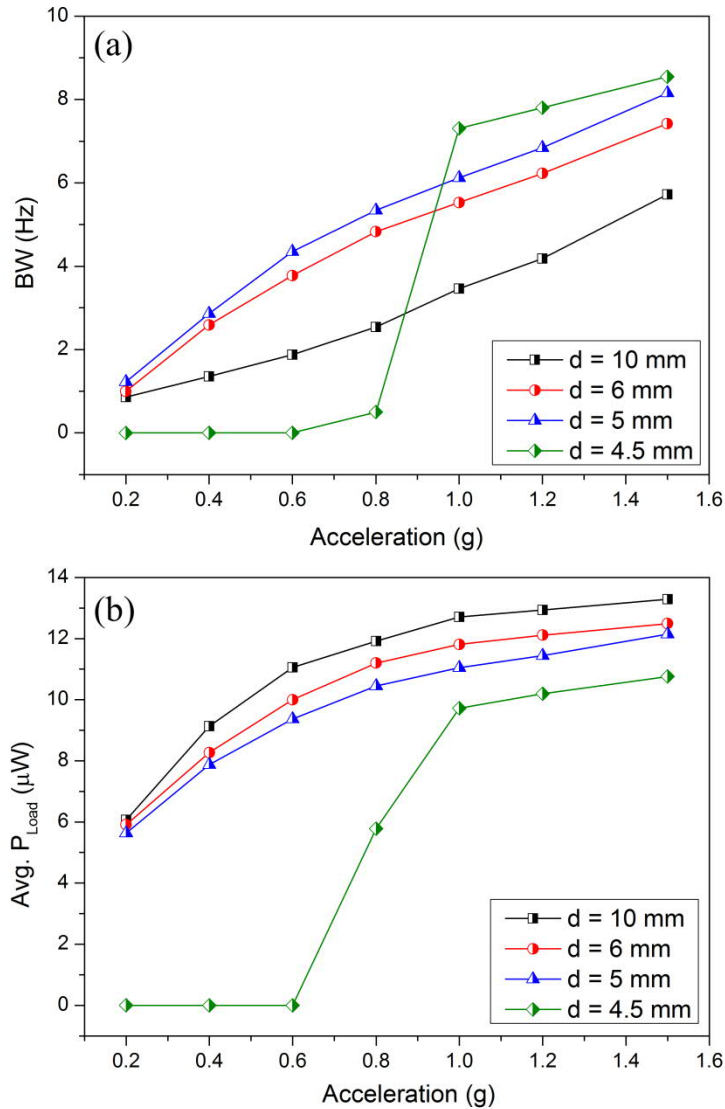
Figure 4.22: Variation of (a) bandwidth (BW) and (b) average load power (Avg. P$_{Load}$) with acceleration for different values of *d* (R = 1 KΩ, *w* = 3.5 mm).

At higher accelerations (0.8g to 1.5g), the oscillator collides with the base and the combined effect of bistability and impact increases the bandwidth to almost 8 Hz. The average load power over the frequency range of bandwidth also increases and follows a pattern almost similar to the linear (*d* = 10 mm) condition. The average load powers in this case, however, remain slightly less than that in the linear case. This decline in power level can be attributed to the fact that increased magnetic repulsion at smaller *d* decreases the velocity of the oscillator and induced voltage in the coil, resulting in lower power output. As the potential wells are made even deeper (*d* = 4.5 mm), for low accelerations (0.2g to 0.6g) the oscillator remain confined in one potential well, generating power less than the threshold value. Hence, the calculated BW in these conditions is zero, as shown in Figure 4.22. At 0.8g, the power level rises just above the threshold value and the BW is slightly

above zero. For higher accelerations (1g to 1.5g) the oscillator performs large amplitude inter-well oscillation and collides with the base. Again, the combined effect of bistability and mechanical impact broadens the frequency range to more than 8.5 Hz. As a result of the diminished velocity due to increased magnetic repulsion, the average load power in this case is almost 2.5 µW less than that for the linear case. An abrupt jump in BW and average load power is observed for d = 4.5mm at 1g acceleration, which indicate the activation of large amplitude inter-well oscillation.

In order to enhance the performance of the VEH, a second version of the prototype (P2) is developed. In this prototype two soft magnetic steel plates on both sides of the magnet assembly are used to concentrate the flux lines (Figure 4.23(a)) through the coil. Furthermore, the gap between the magnet assembly and the coil was reduced to 0.5mm, which initially was 1mm for P1, the first prototype. These adjustments enhance the flux linkage gradient through the coil and results in higher output power while operating under the same conditions.
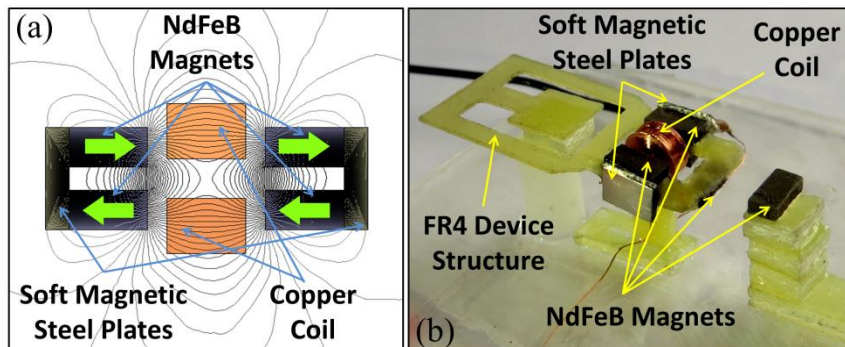
Figure 4.23: (a) Magnetic flux lines through the cross-section in the magnet-coil assembly in P2, (b) Fabricated prototype (P2) of the EM-VEH device.

From the experiments it was found that at the same applied vibrational acceleration, P2 generated at most 1.8 times higher power in comparison to P1, while the bandwidth remains almost the same (Figure 4.24).
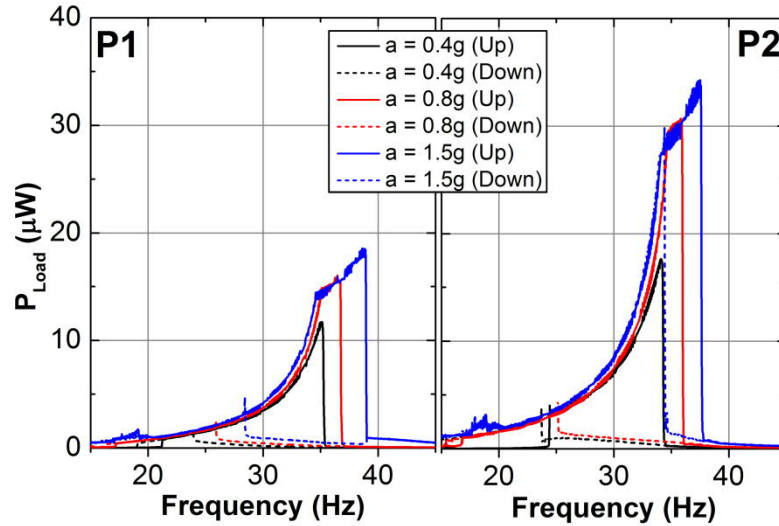
Figure 4.24: Comparison of output load power in P1 and P2 under the same vibrational acceleration. P2 produces almost 1.8 times higher power than P1.

The maximum efficiencies (η) of the P1 and P2 devices can be computed using the following equation,

$$\eta = \frac{Output\ Electrical\ Power}{Input\ Mechanical\ Power} = \frac{P_{Max}}{MA\dot{z}}$$

<div align="right">4.39</div>

Where M is the effective mass, A is the applied acceleration, and $\dot{z}$ is the peak velocity of the oscillator at the applied acceleration. Considering the device output and simulated velocity at 0.8g acceleration, the efficiencies of P1 and P2 are obtained as 3.5% and 8.1% respectively. The size of the devices are comparable to AAA size batteries (length 4.5cm, diameter 1 cm), which has an energy content of approximately 1.3Wh (4680 Joule) for Li-ion chemistry. In order to generate the same amount of energy at a constant rate of 31.2 µW (maximum output of P2) the prototype 2 will take approximately 4.8 years.

A comparative study of performances of P1 and P2 and other reported devices require identification of an appropriate figure of merit (FOM) that would compare performances of different devices regardless of the size and operating conditions. In a previous work, Sebald, et al. [15] defined an *FOM* as,

$$FOM = \frac{P_{MAX}}{A_0^2} * \frac{BW}{f_0}$$

<div align="right">4.40</div>

where P_{MAX} is the maximum power achieved by the device, A_0 is the acceleration due to vibration and BW is the half-power bandwidth defined as,

$$BW = f_2 - f_1$$

<div align="right">4.41</div>

where f_1 and f_2 are the half power cut-off frequencies and f_0 is the resonant frequency of the device. This definition of *FOM* has been used earlier by a few researchers [Basset, et al. [14], Yuichi, et al. [16],]. However, this metric is less appropriate to compare devices of different volume and weight, as it does not offer normalization regarding device size. In general, larger and heavier devices tend to produce much higher power than smaller and lighter devices. Also, this *FOM* fails to properly acknowledge a device with relatively flat response, since it considers only the peak power (P_{MAX}). Hence, a modified FOM_{VEH} is developed where the device mass and overall response is taken into account. In case of the wideband nonlinear generators, the use of average power over the frequency range of bandwidth (P_{AvgBW}) is more appropriate instead of the peak power. Since the total volume of a device is rarely reported in literature, the effective mass of an oscillator based device can be considered as an approximate representative of the device size. Therefore, it is recommended that the total expression should be divided by the effective mass of the device. The FOM_{VEH} in eq. 4.40 is further multiplied by ($f_2 - f_1$) to remove the dimension of time from the expression. Thus, the modified *FOM* is given by,

$$FOM_{VEH} = \frac{P_{AvgBW}}{MA_0^2} * \frac{BW^2}{f_0} \qquad\qquad 4.42$$

The modified FOM_{VEH} takes into account the effective mass of the device, and the average power produced by the device over the frequency range of bandwidth, and normalizes over the applied acceleration and frequency regime. A comparison of FOM_{VEH} of different reported nonlinear devices and this work is shown in Table 4.2. The modified FOM_{VEH} for most of the devices fall in the range from 10^{-5} to 10^{-3}. The Table 4.2 also compares the FOM_{VEH} for the different possible configurations of the two prototypes (P1 and P2) operating under the same vibrational acceleration (0.5g). Comparing the FOM_{VEH} of P1 and P2 in Table 4.2, it can be found that P2 achieve FOM_{VEH} 30% − 50% higher than that achieved by P1 in the same condition. For the linear versions of both P1 and P2, the FOM_{VEH} is the lowest, as the bandwidth is very small. As mechanical impact is incorporated by moving the wall closer to the oscillator in three steps (w = 3.5, 3 and 2.5 mm), the FOM_{VEH} was found to increase for the linear configuration due to broader bandwidth, despite lower output power. The bistable configurations of both P1 and P2 show a fairly large FOM_{VEH} compared to the corresponding linear ones, offering fairly wide bandwidth and reasonable amount of power. When mechanical impact is incorporated in the bistable configuration, the bandwidth increased, while the output power decreased

with decreasing wall distance. Furthermore, the FOM_{VEH} of bistable + impact configurations is found to be lower than the bistable-only configuration for w = 3.5, 2.5 mm for both P1 and P2, but higher than the bistable ones at w = 3 mm, implying an optimized adjustment.

Table 4.2: Comparison of *Figure of Merit (FOM)* of some of the reported devices with this work

References	Equivalent mass (kg)	Acceleration (m/s²)	f_0 (Hz)	$f_2 - f_1$ (Hz)	$P_{Avg.BW}$ (W)	FOM_{VEH}
Stanton [17], (PZ)	5.5×10^{-3}	10	14.78	2.5	5.50×10^{-4}	4.23×10^{-4}
Soliman [13], (EM)	3.8×10^{-3}	1	94.8	4.79	7.26×10^{-5}	4.62×10^{-3}
Cottone [18], (EM)	72.3×10^{-3}	5	45	7.5	6×10^{-3}	4.15×10^{-3}
Basset [14], (ES)	6.6×10^{-5}	10	162	40	1.60×10^{-6}	2.39×10^{-3}
Le [19], P1 (ES)	2.8×10^{-6}	55	1220	300	5.10×10^{-8}	4.44×10^{-4}
Le [19], P2 (ES)	1.2×10^{-6}	3.1	670	140	1.05×10^{-8}	2.66×10^{-3}
This work, P1 (Linear) (EM)	2.66×10^{-4}	5	36	1.1	11×10^{-6}	5.56×10^{-5}
This work, P1 (Linear+Impact [w = 3.5mm]) (EM)	2.66×10^{-4}	5	36	1.5	9.6×10^{-6}	9.02×10^{-5}
This work, P1 (Linear+Impact [w = 3mm]) (EM)	2.66×10^{-4}	5	36	2.18	8.94×10^{-6}	1.77×10^{-4}
This work, P1 (Linear+Impact [w = 2.5mm]) (EM)	2.66×10^{-4}	5	36	3.6	6.15×10^{-6}	3.33×10^{-4}
This work, P1 (Bistable) (EM)	2.66×10^{-4}	5	36	3.64	1.09×10^{-5}	6.03×10^{-4}
This work, P1(Bistable +Impact [w = 3.5mm]) (EM)	2.66×10^{-4}	5	36	3.8	9.56×10^{-6}	5.77×10^{-4}
This work, P1(Bistable +Impact [w = 3mm]) (EM)	2.66×10^{-4}	5	36	6.32	7.53×10^{-6}	1.26×10^{-3}
This work, P1(Bistable +Impact [w = 2.5mm]) (EM)	2.66×10^{-4}	5	36	7.81	3.96×10^{-6}	1.01×10^{-3}
This work, P2 (Linear) (EM)	2.78×10^{-4}	5	35.2	1.08	1.48×10^{-5}	7.06×10^{-5}
This work, P2 (Linear + Impact [w = 3mm]) (EM)	2.78×10^{-4}	5	35.2	2.1	1.19×10^{-5}	2.15×10^{-4}
This work, P2 (Bistable) (EM)	2.78×10^{-4}	5	35.2	3.51	1.46×10^{-5}	7.35×10^{-4}
This work, P2(Bistable +Impact[w = 3.5mm]) (EM)	2.78×10^{-4}	5	35.2	3.72	1.32×10^{-5}	7.47×10^{-4}
This work, P2(Bistable +Impact[w = 3mm]) (EM)	2.78×10^{-4}	5	35.2	6.17	1.15×10^{-5}	1.79×10^{-3}
This work, P2(Bistable +Impact[w = 2.5mm]) (EM)	2.78×10^{-4}	5	35.2	7.68	6.38×10^{-6}	1.54×10^{-3}

Therefore, considering the trade-off relations between harvested power and bandwidth, it is important to properly adjust the distance of the impact point (wall distance *w*) in bistable VEH devices exploiting impact induced bandwidth widening technique. In applications where wider bandwidth is preferred over high power output, the impact induced bandwidth widening can be employed along with bistable nonlinearity. However, this method of broadening the bandwidth may not be appropriate for situations where high power is needed, rather than the wider bandwidth.

Although FR4 materials have been used for energy harvesting devices in a few previous works [42 - 46], the behaviour of this material in long duration vibrational environment is relatively unexplored. During experiments the device was subject to high acceleration (up to 1.5g) vibration for several days. So far, no degradation (fracture, crack) in the device structure has been observed. Furthermore, close observation of the impact regions also do not suggest any fragmentation or chipping. Hence, it is established that FR4 is robust enough to withstand vibrations and moderate level of mechanical impacts over a fairly long period of operation.

The performance of the nonlinear broadband energy harvesters described in this chapter cannot be compared to the commercially available linear energy harvesters, such as the Perpetuum 6600 series. These devices employ electromagnetic transduction, and include the power management circuits within a hermetically sealed stainless steel enclosure [20]. The Perpetuum energy harvesters are designed to operate at a certain resonance frequency, and are optimized to harvest very large energy (~ 5 mW) at relatively small vibrational excitation (~ 0.05g), albeit over a very narrow bandwidth (< 2 Hz). On the contrary, the devices presented in this chapter (and subsequent chapters in this thesis) employ fundamentally different nonlinear mechanisms to broaden the bandwidth by means of hysteretic frequency response. The broadband behaviour demonstrated by these nonlinear devices are appropriate for vibration scenarios with relatively wide-ranging frequencies or variable frequencies, which is in contrast with the requirement of resonant condition for commercial linear energy harvesters.

4.4 Conclusion

This chapter described the development, analysis, fabrication, and characterization of a meso-scale nonlinear bistable vibration energy harvesting device. The device comprises a

laser micro-machined FR4 folded arm spring structure, NdFeB magnets, soft magnetic steel and wire-wound copper micro-coil. The use of FR4 material and the folded arm spring design allows for a moderately low vibration frequency within a relatively small device footprint. The bistable nonlinear mechanism is incorporated by repulsive magnetic interaction at the free end of the FR4 spring structure, which can be controlled by manipulating the gap distance between the pair of repulsive magnets. At an appropriate gap distance between the magnets, this bistable nonlinearity widens the operational bandwidth of the system by up to 3.4 Hz at 0.4g acceleration with respect to the linear counterpart, while generating almost similar level of power (11.71 µW). As the driving frequency approached the jump frequency, the oscillator started to vibrate at large amplitude, and the high flux gradient magnet assembly travelled beyond the range of influence of the coil. This resulted in an abrupt reversal of flux linkage gradient across the coil, giving rise to small peaks in the open circuit voltage response. Also, it was demonstrated numerically and experimentally that in order to harvest a significant level of energy and achieve a broader frequency bandwidth in a low acceleration and low frequency vibration environment, the depth of the potential well should be made shallower to facilitate inter-well jumping. An optimized prototype improved the performance by almost 60% (18.73 µW) in the same operational conditions (0.4g acceleration). On increasing the input acceleration beyond 0.4g, the oscillation amplitude becomes limited by collision with the base, abruptly changing the dynamics of the system on impact. The impact induced change in dynamics increases the peak power frequency, widening the bandwidth even further up to 8 Hz. Therefore, the reported device utilizes the effects of both nonlinearity and stiffness change on mechanical impact to achieve a fairly wideband operation. The operational frequency range of the prototypes (30 – 40 Hz) falls within the range of vehicle induced (10 – 100 Hz) and human motion induced (10 – 50 Hz) vibrations [Chapter 1: Section 1.3.1]. Therefore, the devices could be useful to power low power and low duty cycle wireless sensor applications such as, temperature and humidity sensing, pollutant sensing, ambient light sensing etc.

The performances of different configurations of the nonlinear bistable VEH device prototype is compared with that of other reported devices against an appropriate *Figure of Merit*, which normalizes the device output against the respective size and operating frequency. This approach to benchmarking the device performances show that the

combined effect of bistable nonlinearity is beneficial in certain circumstances where wider bandwidth is preferred over high power.

This work demonstrates the capability of FR4 based nonlinear bistable EM harvesters to generate usable amount of power from low frequency vibrations over a wider frequency range compared to linear devices. Optimization of the device structure and magnet-coil assembly could further enhance the output power and operational frequency range of the device.

References

[1]   E. P. Furlani, *Permanent Magnet and Electromechanical Devices: Materials, Analysis, and Applications*: Elsevier Science, 2001.

[2]   K. W. Yung, P. B. Landecker, and D. D. Villani, "An Analytic Solution for the Force Between Two Magnetic Dipoles," *Magnetic and Electrical Separation,* vol. 9, pp. 39-52, 1998.

[3]   D. Mallick, A. Amann, and S. Roy, "A nonlinear stretching based electromagnetic energy harvester on FR4 for wideband operation," *Smart Materials and Structures,* vol. 24, p. 015013, 2015.

[4]   G. Hatipoglu and H. Ürey, "FR4-based electromagnetic energy harvester for wireless sensor nodes," *Smart Materials and Structures,* vol. 19, p. 015022, 2010.

[5]   E. Sardini and M. Serpelloni, "An efficient electromagnetic power harvesting device for low-frequency applications," *Sensors and Actuators A: Physical,* vol. 172, pp. 475-482, 2011.

[6]   D. Mallick and S. Roy, "Bidirectional electrical tuning of FR4 based electromagnetic energy harvesters," *Sensors and Actuators A: Physical,* vol. 226, pp. 154-162, 2015.

[7]   R. Masana and M. F. Daqaq, "Energy harvesting in the super-harmonic frequency region of a twin-well oscillator," *Journal of Applied Physics,* vol. 111, p. 044501, 2012.

[8]   H. Dankowicz and J. Jerrelind, "Control of near-grazing dynamics in impact oscillators," *Proceedings of the Royal Society A: Mathematical, Physical and Engineering Science,* vol. 461, p. 3365, 2005.

[9]   C. R. Saha, "Modelling Theory and Applications of the Electromagnetic Vibrational Generator," in *Sustainable Energy Harvesting Technologies - Past, Present and Future*, D. Y. K. Tan, Ed., InTech, Available from: http://www.intechopen.com/books/sustainable-energy-harvesting-technologies-

past-present-and-future/modelling-theory-and-applications-of-the-electromagnetic-vibrational-generator: InTech, 2011.

[10] D. S. Nguyen and E. Halvorsen, "Analysis of vibration energy harvesters utilizing a variety of nonlinear springs," *Proceedings of the PowerMEMS,* vol. 10, pp. 331-334, 2010.

[11] R. Masana and M. F. Daqaq, "Relative performance of a vibratory energy harvester in mono- and bi-stable potentials," *Journal of Sound and Vibration,* vol. 330, pp. 6036-6052, 2011.

[12] R. Harne and K. Wang, "On the fundamental and superharmonic effects in bistable energy harvesting," *Journal of Intelligent Material Systems and Structures,* vol. 25, pp. 937-950, 2013.

[13] M. S. M. Soliman, E. M. Abdel-Rahman, E. F. El-Saadany, and R. R. Mansour, "A wideband vibration-based energy harvester," *Journal of Micromechanics and Microengineering,* vol. 18, p. 115021, 2008.

[14] P. Basset, D. Galayko, F. Cottone, R. Guillemet, E. Blokhina, F. Marty*, et al.*, "Electrostatic vibration energy harvester with combined effect of electrical nonlinearities and mechanical impact," *Journal of Micromechanics and Microengineering,* vol. 24, p. 035001, 2014.

[15] G. Sebald, H. Kuwano, D. Guyomar, and B. Ducharne, "Experimental Duffing oscillator for broadband piezoelectric energy harvesting," *Smart Materials and Structures,* vol. 20, p. 102001, 2011.

[16] T. Yuichi, S. Eisaku, K. Fumiya, H. Hirotaka, S. Kazufumi, S. Kenji*, et al.*, "Lead-Free Piezoelectric MEMS Energy Harvesters of (K,Na)NbO 3 Thin Films on Stainless Steel Cantilevers," *Japanese Journal of Applied Physics,* vol. 52, p. 09KD13, 2013.

[17] S. C. Stanton, C. C. McGehee, and B. P. Mann, "Nonlinear dynamics for broadband energy harvesting: Investigation of a bistable piezoelectric inertial generator," *Physica D: Nonlinear Phenomena,* vol. 239, pp. 640-653, 2010.

[18] F. Cottone, P. Basset, H. Vocca, L. Gammaitoni, and T. Bourouina, "Bistable electromagnetic generator based on buckled beams for vibration energy harvesting," *Journal of Intelligent Material Systems and Structures,* vol. 25, pp. 1484-1495, 2013.

[19] C. P. Le and E. Halvorsen, "MEMS electrostatic energy harvesters with end-stop effects," *Journal of Micromechanics and Microengineering,* vol. 22, p. 074013, 2012.

[20] Perpetuum Limited, *Vibration Energy Harvesters*, 2013, Available: https://perpetuum.com/download/veh-vibration-energy-harvester-datasheet/?wpdmdl=913

5 COMBINED NONLINEAR ENERGY HARVESTER

This chapter presents the development of a meso-scale combined nonlinear vibration energy harvesting device where bistable nonlinearity and monostable quartic nonlinearity has been combined in a single device topology. Through extensive numerical simulations and experimental procedures, it has been demonstrated that the combined nonlinear device performs better than the individual nonlinear systems in both harmonic and band-limited random vibration conditions. In addition, some critical inconsistencies between the theoretical treatment and application of bistable nonlinearity in the field of vibration energy harvesting have been investigated. The first section describes the background and motivation for the development of a combined nonlinear vibration energy harvesting system. The structural design and fabrication of the combined nonlinear device topology is described in the next section. The third section deals with the analytical modelling and numerical simulation of the combined nonlinear system. The experimental results and analysis are presented in the fourth section. Finally, the concluding remarks are presented.

5.1 Combined nonlinear energy harvester - Background

The general composition of VEHs often includes a mechanical oscillator and a transducer (electromagnetic, piezoelectric, electrostatic, triboelectric etc.). The conventional linear resonant oscillator based VEHs [Kulkarni, et al. [1] , Beeby, et al. [2]] are unable to efficiently convert real-world nonstationary and broadband natural vibrations into electricity due to their characteristically narrow frequency bandwidth. In this context, recently, the nonlinear oscillator based VEH systems have attracted considerable attention due to their inherent capability to improve the off-resonance performance compared to a linear resonant system [Cottone, et al. [3], Erturk, et al. [4], Erturk and Inman [5]]. The nonlinear Duffing equation [Nayfeh and Mook [6]] forms the theoretical basis of nonlinear vibration energy harvesters, which can take the monostable-quartic (single-well) or the

bistable-quartic (double-well) form depending on the nature of the potential energy profile. The monostable-quartic (MQT) potential nonlinearity can be implemented in VEHs through specially designed stretchable spring arms which induce cubic nonlinear restoring force or through nonlinear magnetic levitation force [Marinkovic and Koser [7], Mann and Sims [8], Mallick, et al. [9]]. However, the high energy branch of motion of the quartic systems is largely dependent on the initial conditions and can only be achieved through proper frequency sweep. Furthermore, usually the nonlinear components of the spring force come into effect at large deflection or large limit cycle oscillations (LCO), which can be triggered at relatively large vibrational acceleration.

Physical realization of bistable Duffing oscillator based VEHs has been attempted through repulsive magnetic interaction [Ferrari, et al. [10], Podder, et al. [11], [12]] or by using buckled cantilever designs [Masana and Daqaq [13], Cottone, et al. [14], Cottone, et al. [15]]. However, in practice, the bistability induced through repulsive magnetic interaction are not bistable-quartic (BQT), but rather bistable-quadratic (BQD) in nature, where the oscillators follow quadratic potential profile at large deflections. This fundamental difference in the large deflection behaviors of the theoretically defined bistable-quartic Duffing VEHs and the experimentally deployed bistable-quadratic VEHs lead to substantially different frequency spectrum and energy harvesting performance. This work explicitly highlights these differences and their effects through numerical simulation and experimental validation, which has long been overlooked in the vibration energy harvesting literature. The buckled beam induced bistability, on the other hand, produces quartic potentials due to stretching deformation leading to bistable-quartic (BQT) system. However, the buckled beam based BQT systems also suffer from very small oscillation amplitude, limiting the power output severely [Vocca, et al. [16]], and the lack of dynamical adjustability or tunability of the quartic potential, which is governed largely by the mechanical properties of the beam.

In this work a novel VEH device topology is introduced where magnetic repulsion induced bistability is combined with stretching induced quartic potential in a single design with a tunable bistable-quartic (BQT) potential profile to enhance the performance across the vibrational spectrum. Furthermore, this device topology allows activation of the individual bistable-quadratic (BQD) or monostable-quartic (MQT) nonlinearities, or their simultaneous activation leading to a bistable-quartic (BQT) nonlinear potential, while other

parameters remain unaffected. Therefore, this device topology also offers the unique opportunity to make proper unbiased comparison of the performances of VEHs in different nonlinear potential energy profiles. The proposed VEH system induces bistability through repulsive interaction of permanent magnets and administers quartic potentials by stretching of clamped-constrained beams, which exhibits substantially larger amplitude oscillation across the double potential wells in comparison to the clamped-clamped buckled beam based BQT devices. The numerical simulation and experimental results show significant improvement in spectral response of the BQT device in comparison to the BQD and MQT, particularly in the lower frequency domain of the vibrational excitation. The enhanced performance of the BQT device in the lower frequency domain is advantageous in real application scenario since most of the naturally occurring mechanical vibration energy is available in the lower range of the spectrum. Comparison of the harmonic frequency responses of the VEH systems reveals that the BQT device efficiently combines the beneficial features of the BQD (large amplitude oscillation at the lower end of spectrum) and MQT (large harmonic oscillation at high frequencies) devices to generate higher overall power across the vibrational spectrum. In band limited random vibration scenario, the BQT VEH produces more power over broader frequency range, resulting into larger average power than the BQD and MQT VEHs.

5.2 Design of combined nonlinear generator

An important aspect of this work is to understand the fundamental differences in the three types of nonlinear VEHs and a comparative study of their performances under identical excitation conditions. In order to compare the relative performances of the different nonlinear VEHs, a VEH system has been engineered that can be transformed into BQD, BQT or MQT by simple alterations, while keeping the equivalent mass and underlying linear stiffness constant. The proposed bistable-quartic (BQT) VEH system, comprising of laser micro-machined FR4 device structure, miniaturized wire-wound copper coil and NdFeB permanent magnets is shown in Figure 5.1(a). The pair of repulsively positioned magnets at the vertically movable constrained end of the device structure produces the bistability, whereas the stretching of a pair of clamped-constrained FR4 cantilevers arranged on either sides of the transducing magnet-coil assembly contributes to the cubic nonlinear stiffness (Figure 5.1(b)).
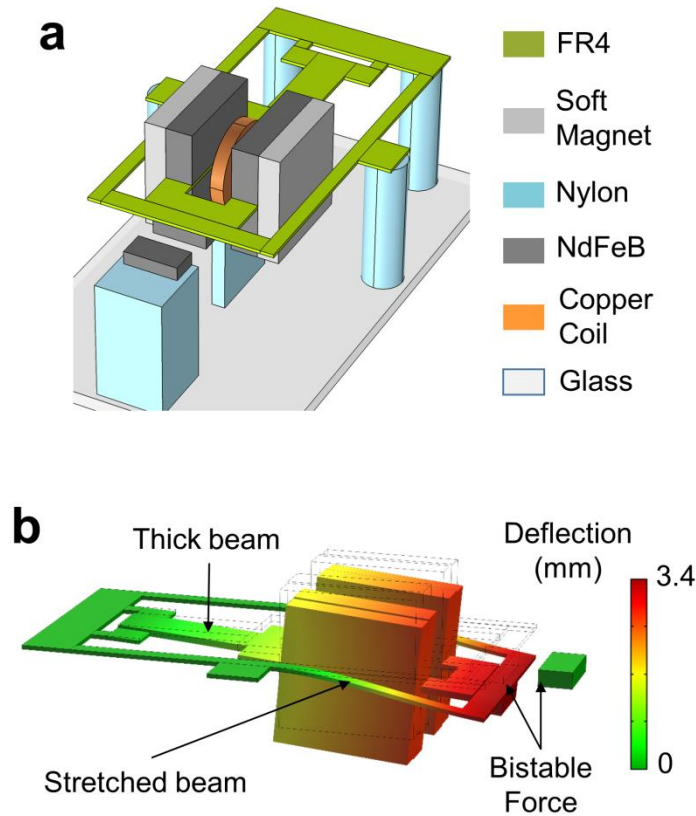
Figure 5.1: (a) Combined nonlinear vibration energy harvester architecture. (b) Simulated deflection of the VEH device. The clamped-constrained sections of the oscillator structure get stretched at larger deflections.

The BQT system can be transformed into a monostable-quartic (MQT) system by increasing the gap between repulsive magnets sufficiently or a bistable-quadratic (BQD) system by removing the pair of clamped-constrained beams, while keeping the linear stiffness unaffected. The resulting simulated potential energy and restoring force profiles of the different nonlinear VEH configurations (MQT, BQD and BQT) are shown in Figure 5.2(a) and (b), where the corresponding linear potential and stiffness are also shown as reference. It can be observed that the BQT potential energy and restoring force profiles are considerably modified including two favorable features from that of the BQD and MQT systems. The first is the reduced relative depth of the bistable potential wells with respect to the potential crest [Figure 5.5] leading to a potential energy profile with relatively even or flat bottom. The second is the higher restoring force due to the steeply rising cubic nonlinear force when the oscillator is further away from the equilibrium position. These beneficial factors enable the BQT system to swing from one bistable potential well to the other even at low vibrational accelerations and perform large amplitude inter-well

oscillation, leading to superior performance of the BQT system over the others.
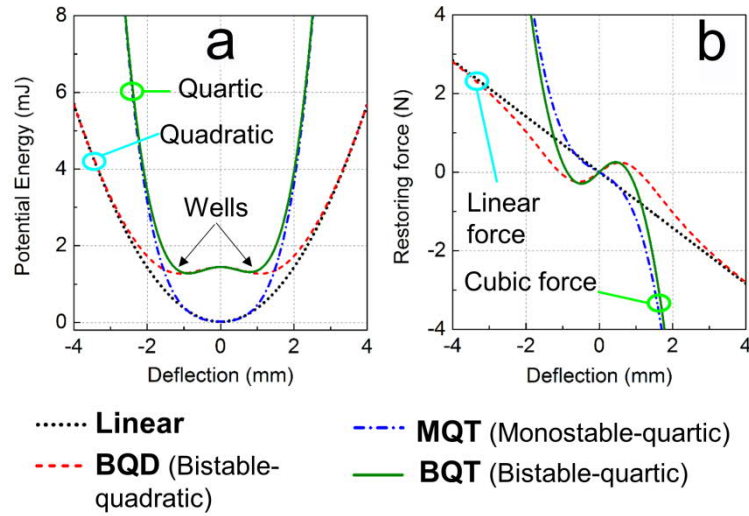
Figure 5.2: Variation of (a) potential energy and (b) restoring force plots for the linear, monostable-quartic (MQT), bistable-quadratic (BQD), and bistable-quartic (BQT) systems. MQT follows linear and BQT follows bistable potentials at small deflections. At large deflections both MQT and BQT follow quartic potential.

In the context of VEH systems, bistable nonlinearity can be realized by repulsive magnetic force between a pair of permanent magnets, or through buckling of clamped-clamped cantilevers under critical buckling load. At small deflections, the oscillators in both cases experience two potential wells and negative stiffness on either sides of the equilibrium point. At large deflections, however, the effect of magnetic repulsion is negligible and the oscillator experiences a quadratic potential due to the linear stiffness of the cantilever resulting a bistable-quadratic (BQD) oscillator. On the other hand, the buckled beam based bistable oscillator experiences stretching under deflections and experiences quartic potential producing a bistable-quartic (BQT) oscillator. However, the buckling based VEH suffers from very small oscillation amplitude and proportionally small harvested power compared to the magnetic repulsion induced bistability. The small amplitude oscillation in buckling induced bistable-quartic VEHs is avoided in the proposed BQT VEH system by introducing bistability through magnetic repulsion in a clamped-constrained beam architecture. The proposed BQT nonlinear mechanism can be further modified by bringing in even more stable states (tristable, multistable etc.), degrees of freedom (multimode vibration) and be miniaturized to the micro-scale.

5.3 Fabrication of combined nonlinear generator

The fabricated BQT VEH device is shown in Figure 5.3. The device structure is made of FR4 (PCB) material using laser micromachining process. The Young's modulus of FR4 is relatively low (21 – 24 GPa) in comparison to other commonly used metallic alloys, which implies applicability in low frequency vibrations. In addition, FR4 is a low density (1.85 g/cc) yet mechanically robust material with high yield strength (450 – 650 MPa), capable of sustaining long-term oscillatory stress.
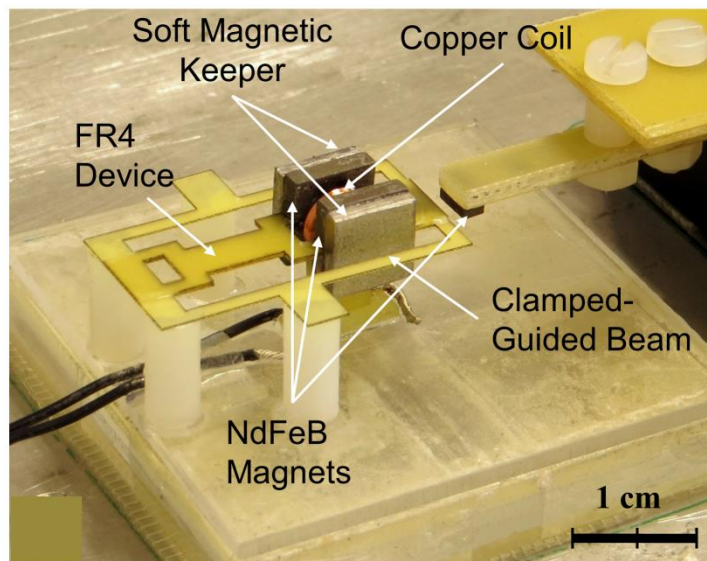
Figure 5.3: Fabricated combined nonlinear vibration energy harvesting device. The external repulsive magnet is mounted on a micro-positioning stage for precise control of gap distance.

Furthermore, FR4 is relatively tolerant to variations in environmental conditions, such as temperature and humidity, which makes it an excellent material to use in unpredictable and potentially hazardous conditions. In the course of the experiments the FR4 based beam structure has been subject to more than 10 million cycles of oscillation, without any damage or degradation in performance, which validates the long-term reliability of the material for VEH applications. The bistable-quartic spring design has been laser micromachined from FR4 sheets of thickness 0.2 mm and 0.5 mm. Four NdFeB magnets (8mm × 4mm × 2mm (↑), the '↑' denotes the magnetization axis direction) are arranged on both sides of a slot in the device structure in such a way that a high flux gradient is created within the slot. Furthermore, two high permeability soft magnetic steel blocks (8mm × 8mm × 1.6mm) are used on both sides of the magnet assembly to intensify the magnetic

flux in the slot. A coil wound using 30 μm diameter enameled copper wire (6.5 mm outer diameter, 1.15 mm inner diameter, 1 mm thickness, 2500 turns, 720 Ω resistance) is placed at the midpoint of the slot within the high flux gradient magnet assembly. The entire device is supported on four cylindrical nylon spacers, two of which are attached at the fixed end. The other two spacers are attached to the mid-points of two longitudinal beams which are carved on each side of the device structure. It was found that when the mass (magnet assembly) oscillates vertically, a part of the two beams are subject to bending as well as longitudinal stretching deformation, which introduce a nonlinear restoring force dependent upon the third power of the displacement. The middle portion of the beam supporting the magnets is designed to be thicker (0.5 mm) in comparison to the stretchable sections (0.2 mm) of the beam. Another NdFeB magnet (4mm × 2mm (↑) × 1mm) with polarity along the longitudinal direction is attached at the tip of the device structure. In order to incorporate bistability, an additional NdFeB magnet (4mm × 2mm (↑) × 1mm) is mounted on a micro-positioning stage and positioned in opposite polarity to the tip magnet. This arrangement exerts adjustable repulsive force on the tip magnet and induces bistable nonlinearity into the system dynamics.

5.4 Analytical modelling of combined nonlinear generator

The fundamental distinction among different nonlinear mechanisms in the BQD, MQT and BQT systems can be analytically described through the generalized equation of the Duffing potential energy ($U_D(y)$) and the corresponding spring reaction force ($F_D(y)$) as given by [Cottone, et al. [3], Daqaq, et al. [17]],

$$U_D(y) = \frac{1}{2}ay^2 + \frac{1}{4}by^4 \qquad\qquad 5.1$$

$$F_D(y) = -\frac{\partial}{\partial y}U_D(y) = -ay - by^3 \qquad\qquad 5.2$$

where a and b are independent parameters and y represents the displacement or deflection of the oscillator. Depending upon the values of a and b the potential energy function can represent either a linear ($a > 0$, $b = 0$), monostable-quartic ($a > 0$, $b > 0$) or bistable-quartic ($a < 0$, $b > 0$) potential energy profile [17]. The linear oscillator follows a quadratic potential and linear stiffness profile for the entire range of displacements. In the vicinity of

the initial equilibrium $\left(|y| \ll \sqrt{a/b}\right)$ position, the potential energy $(U_D(y))$ and restoring force $(F_D(y))$ profiles of the MQT oscillator is approximately similar to that of the linear oscillator. However, within the same region, $(U_D(y))$ and $(F_D(y))$ for the BQT oscillator represents double-well potential and negative stiffness. For large displacements $\left(y \in \left\{y < -\sqrt{a/b}\right\} \cup \left\{y > \sqrt{a/b}\right\}\right)$ both the theoretical MQT and BQT oscillators produces quartic potential and cubic restoring force profiles, which are significantly steep in comparison to the potential and restoring force of the linear and BQD oscillators.

One of the most widely exploited method of incorporation of bistable nonlinearity in VEH systems is by using repulsively positioned magnets such that pitchfork bifurcation is induced as the distance between the magnets is reduced below a critical limit [Stanton, et al. [18]]. While the dynamical behavior of such functional bistable oscillators are governed by the relative heights of the potential barrier and wells near the small deflection region, it is dominated by the regular linear quadratic potential at large deflections where the repulsive interactions between the magnets is negligible. This configuration of bistable and quadratic potentials produces interesting dynamical phenomena e.g. hysteresis in frequency sweep responses, cross-well jump and chaotic oscillations etc. However, it should be noted while the small deflection behavior in both the analytically described BQT oscillator and experimentally realized BQD oscillators are essentially similar, the large deflection behaviors are substantially different. The large deflection behavior in the BQT oscillator is influenced by the cubic stiffness, while that for the BQD oscillator is governed by the linear stiffness. This difference in the large deflection behavior of the theoretically investigated BQT oscillator and the experimentally deployed BQD oscillator leads to remarkably different frequency responses and energy harvesting capabilities, which has not been appreciated in previous works. In fact, many of the reported works use Duffing BQT oscillator in numerical simulations as the quartic term arises from the Taylor series expansion of magnetic repulsion potential in small deflection regime, but use BQD oscillator in experiments since it naturally occurs when an oscillator with quadratic potential is made bistable through repulsive magnetic interactions.
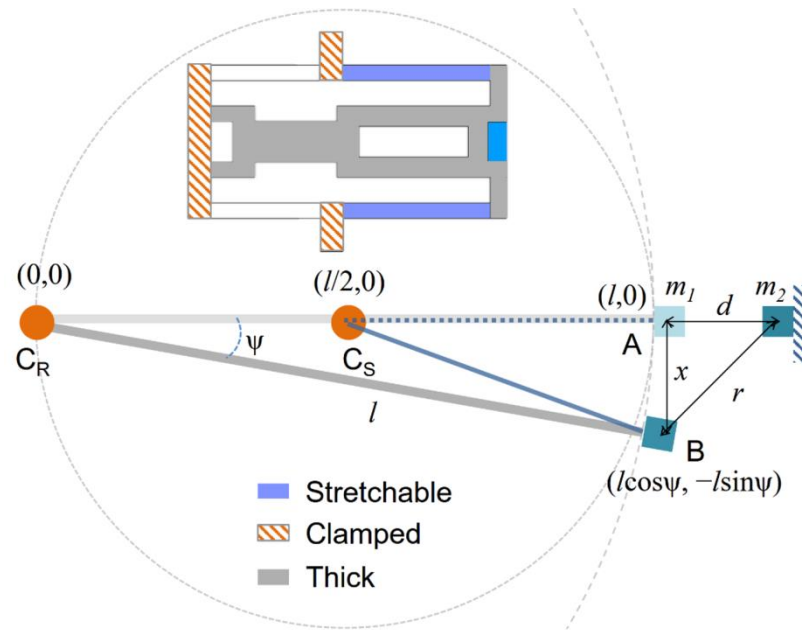
Figure 5.4: Schematic model of the BQT oscillator. The thick, stretchable and clamped sections of the spring structure has been identified.

In order to understand the principal source of nonlinear spring reaction force in our BQT system, let us consider the simplified schematic model as in Figure 5.4. The spring structure consists of a thick section which has a fixed length l, and a thin section of length $l/2$, which is assumed to be stretchable under longitudinal strain. The thick section (section C_RA of length l and thickness t_R) and the stretchable thin section (section C_SA of length $l/2$ and thickness t_S, $t_R \simeq 2.5t_S$) of the beam are conjoined at the movable end A. The thick section and the stretchable sections of the structure are clamped at the other end at different points (C_R and C_S respectively) such that the stretchable part is approximately half the length of the thick part. Under sufficient vibrational excitation, the movable conjoined end is subject to vertical deflection ($x \simeq l \sin \psi$ for small deflections), and is constrained to move along the conjoined end of the thick beam. Therefore, the conjoined end of the thin stretchable beam is also constrained to move along with the thick beam, which exerts longitudinal stretching strain in the stretchable section of the beam. The longitudinal stretching strain generates a nonlinear cubic force-displacement relationship or quartic potential condition in the device structure. Considering the angular deflection of the thick section to be ψ, the stretched length of the stretchable beam (length $l/2$) can be estimated as,

$$\Delta l = \left| l\left(\cos\psi - \frac{1}{2}\right), l\sin\psi \right| - \frac{l}{2} \simeq \frac{l}{2}\left(\sqrt{1 + 2\psi^2} - 1\right) \simeq \frac{x^2}{2l} \qquad 5.3$$

where the approximations are true for small angle ψ. Then, for an elastic beam (of length $l/2$) within the limit of elasticity, the energy stored due to the stretching component of strain can be expressed as [Landau, et al. [19], Senturia [20]],

$$U_S(x) = \frac{1}{2}\frac{Ew_s t_s}{l/2}(\Delta l)^2 = \frac{Ew_s t_s}{4l^3}x^4 = \frac{1}{4}k_n x^4 \qquad 5.4$$

where E is the modulus of elasticity (Young's modulus) of FR4 material, w_S and t_S are the width and thickness of the stretchable beams respectively, and k_n represents the nonlinear spring coefficient due to stretching of the beams. The total strain energy due to bending of the thick and stretchable beam sections can be approximated by considering the Eular-Bernoulli beam formulation for linear elastic solids as [Mallick, et al. [9], Senturia [20]],

$$U_B(x) = \frac{1}{2}kx^2 \qquad 5.5$$

where k is the total linearized stiffness coefficient due to bending of the beam. The magnetic interaction potential energy ($U_m(x)$) due to the repulsive arrangement can be determined by considering dipole-dipole interaction between the tip magnets as [Podder, et al. [12]],

$$U_m(x) = \frac{\mu_0 m_1 m_2}{4\pi l}\left[\frac{(2d^2 - x^2)\sqrt{l^2 - x^2} + 3dx^2}{(x^2 + d^2)^{5/2}}\right] \qquad 5.6$$

where μ_0 is the permeability of air, m_1 and m_2 are the magnetic dipole moments of the repulsively oriented magnet pair, d is the horizontal gap distance between the centers of the magnets when they are anti-parallel and in front of each other and r is the distance between the centers of the oppositely polarized tip magnet and external magnet at the deflected position B (Figure 5.4). The intensity of repulsive magnetic force on the tip of the cantilever can be controlled by altering d, the gap between the tip magnet and the externally positioned magnet. Therefore, the magnetic interaction potential and its contribution to the total mechanical potential energy and restoring force can also be modified by adjusting d.

The total elastic potential energy ($U(x)$) and spring reaction force ($F_R(x)$) taking into consideration the effects of bending, stretching and repulsive magnetic interaction simultaneously can be expressed as,

$$U(x) = U_B(x) + U_S(x) + U_m(x) \qquad 5.7$$

$$F_R(x) = -\frac{\partial}{\partial x}U(x) = -kx - k_n x^3 - \frac{\partial}{\partial x}U_m(x) \qquad 5.8$$

In the proposed BQT system the quartic and bistable potentials can be manipulated independent of each other. The effect of nonlinear force contribution due to magnetic repulsion induced bistable nonlinearity and stretching induced cubic force nonlinearity on the potential energy ($U(x)$) and restoring force ($F_R(x)$) are illustrated in Figure 5.5 (a-d) for different gap (d) distances between the repulsive magnets. In the absence of the clamped-constrained cantilevers, the oscillator is subject to a quadratic potential or linear force (Figure 5.5 (a, b)). On the other hand, the inclusion of the clamped-constrained cantilevers subjects the oscillator to a quartic potential or cubic force (Figure 5.5 (c, d)). The repulsive interaction between the magnets is negligible for larger gap ($d \geq$ 5mm), resulting in monostable quadratic (Figure 5.5 (a)) or quartic (Figure 5.5 (c)) potentials, and linear (Figure 5.5 (b)) or cubic (Figure 5.5 (d)) stiffness profiles. For smaller gaps ($d \leq$ 4.5mm), the repulsive interaction becomes significant and a bistable condition is produced due to a pitch-fork bifurcation. The resulting potential energy profiles exhibit two potential energy minima (Figure 5.5 (a, c)) and negative stiffness (Figure 5.5 (b, d)), characteristic of bistable systems.

In the BQD configuration [Figure 5.5 (a, b)], the potential function is quadratic and the stiffness is almost linear at large deflections ($x >$ 2mm). Contrastingly, the BQT configuration at similarly large deflections follows a quartic Duffing potential and cubic nonlinear stiffness. The most advantageous consequences of designing a BQT oscillator by combining double-well potentials and cubic stiffness is the modest decrease in the relative height of the potential crest (Figure 5.5 (c)) with respect to the potential wells and higher restoring force (Figure 5.5 (d)) at large deflections. The resulting reduced potential barrier can be traversed by the oscillator at lower amplitude vibrations, triggering large amplitude inter-well motion that produces higher energy.
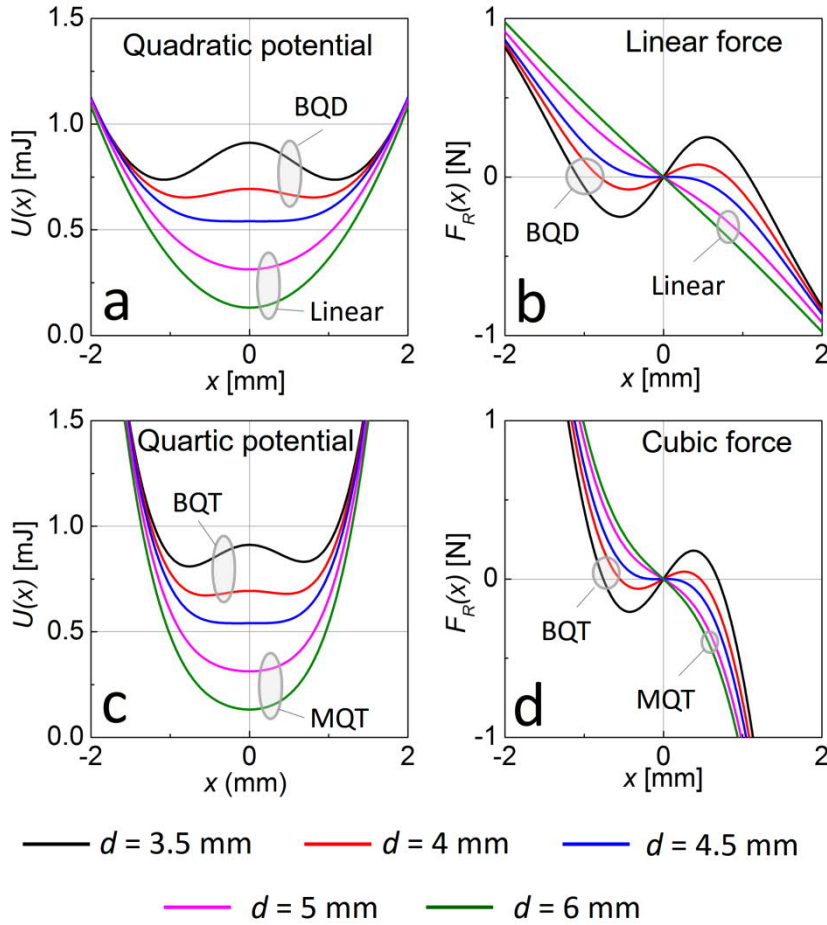
Figure 5.5: Variation of potential energy function [*U(x)*] and restoring force [*F_R(x)*] for different values of *d*. (a) Quadratic potential, (b) Quadratic force, (c) Quartic potential, (d) Quartic force.

Taking into account the bistable-quartic nonlinearity produced by combining the cubic stiffness and bistable double-well potentials, the complete dynamical system equation can be expressed as,

$$M\ddot{x} + kx + k_n x^3 + \frac{\partial}{\partial x}U_m(x) + 2M\xi\omega\dot{x} + \gamma I = -M\ddot{z} \qquad 5.9$$

where *M* is the equivalent mass of the system, ξ is the mechanical damping coefficient, γ is the electromagnetic coupling factor, *I* is the current induced in the coil and, $z = Z_0 \sin \omega t$ is the displacement due to external vibration. The angular frequency of the external vibration is denoted by ω. If the total resistive load combining the coil resistance and the load resistance in the electrical circuit is denoted by *R*, the electrical circuit can be represented as [Podder, et al. [12], Cottone, et al. [15]],

$$L\dot{I} + RI = \gamma\dot{x}$$

<div align="right">5.10</div>

where L denotes the inductance of the coil. Eq. (5.9) and (5.10) are solved numerically using explicit fourth-order Runge-Kutta method in MATAB to obtain the voltage and power generated in the system.

5.5 Numerical simulation of combined nonlinear generator

The dynamical equation of the bistable-quartic combined nonlinear system was solved numerically using 4th order Runge-Kutta method in Matlab. The equivalent mass (M), magnetic dipole moments (m_1, m_2), mechanical damping factor (D), total circuit resistance (R) and coil inductance (L) were measured. While the Eq (5.4) and (5.5) explains the mechanisms of the quartic and quadratic potentials, they do not take into account the details of the geometry of the device. Therefore, for numerical simulations the linear and nonlinear spring constants (k and k_n, respectively) were determined from more accurate FEA analysis using COMSOL Multiphysics. The electromagnetic coupling factor ($\gamma(z) = d\phi/dz$) is determined from FEA analysis using Ansoft Maxwell, where ϕ denotes the magnetic flux linkage. The electromagnetic coupling factor (γ) is found to be a polynomial function ($\gamma(z) = B_1 + 3B_3z^2 + 5B_5z^4$, where $B_1 = 5.94$ Wb/m; $B_3 = -3.26 \times 10^5$ Wb/m^3; $B_5 = 5.39 \times 10^9$ Wb/m^5) dependent upon the deflection (z). These parameter values determining the magnetic flux distribution across the coil were put in the ODE (5.9) and solved numerically in Matlab. The parameters used in the numerical simulation are given in the Table 5.1.

The numerical simulation results (Figure 5.6)) exhibit much higher power (~10 times) in the lower frequency domain (10 – 30 Hz) for the BQD and BQT systems in comparison to the MQT VEH. Moreover, in the high frequency regime (> 60 Hz), the BQT system exhibits high peak power frequency and high peak power level almost similar to the MQT system. Therefore, the proposed BQT system essentially combines the beneficial features of the BQD (higher power in low frequencies) and MQT (high peak power in high frequencies) systems to provide a generally improved response. Subsequently, the simulation results are validated against the test results of the fabricated prototypes of bistable-quadratic, monostable-quartic and bistable-quartic VEH devices.

Table 5.1: Parameters used in the numerical simulations

Parameters	Symbols	Value	Unit
Elasticity modulus (Young's modulus) of FR4	E	19×10^9	Pa
Stretchable beam thickness	t_S	2×10^{-4}	m
Stretchable beam width	w_S	2×10^{-3}	m
Thick beam thickness	t_R	5×10^{-4}	m
Thick beam width	w_R	4×10^{-3}	m
Thick beam length	l	20×10^{-3}	m
Equivalent mass	M	3.56×10^{-3}	kg
Linear spring coefficient	k	440	N/m
Nonlinear spring coefficient	k_n	5.88×10^8	N/m^3
Dipole moments of magnets in bistable configuration	m_1, m_2	12.64×10^{-3}	A·m^2
Gap distance between bistable magnets	d	variable	m
Mechanical damping coefficient	ξ	0.012	-
Inductance of the coil	L	3.425×10^{-3}	H
Resistance of the coil	R_{Coil}	710	Ohm
Load resistance	R_{Load}	3000	Ohm
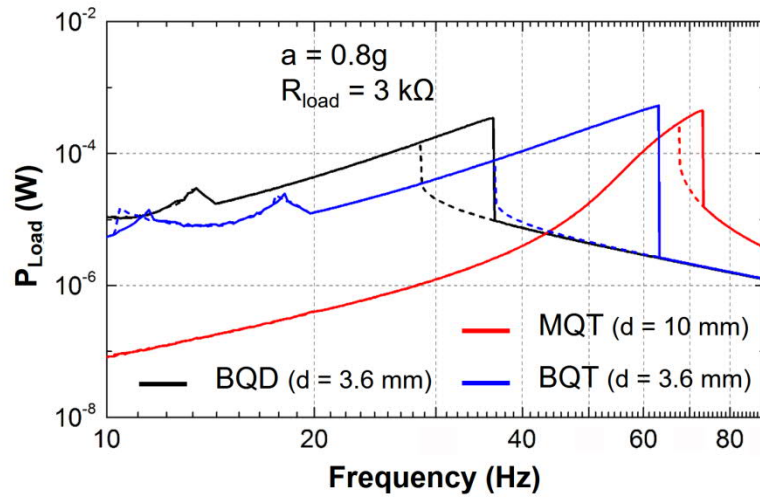
Figure 5.6: Numerically simulated frequency responses for the BQD (bistable-quadratic), MQT (monostable-quartic) and BQT (bistable-quartic) VEHs. The solid and dashed lines represent the forward sweep response and the reverse sweep responses.

5.6 Experimental results and discussions

The base of the fabricated VEH prototypes was attached to a Brüel & Kjær shaker (LDS V455) with accelerometer (DeltaTron Type 4517-002) feedback. The shaker was controlled by an LDS Comet vibration controller and the output from the controller was amplified using a power amplifier (LDS PA 1000L) before feeding to the shaker. Different vibrational accelerations (0.02g – 1.6g) with a frequency range of 10 Hz to 90 Hz in both forward and reverse frequency sweep (sweep rate of 0.333 Hz/s) was used to excite the device. The band-limited random vibration test was performed using vibration that generated a flat power spectral density (PSD) profile over the frequency band (10 – 100 Hz). The output time traces of the VEH device and the shaker were recorded using a data acquisition system (Picoscope 3000 series). The external repulsive magnet was mounted onto a micro-positioning stage (Newport) to exercise precise control over the gap between the repulsively positioned magnets. A variable resistance box (Centrad) was used to vary the resistive load across the energy harvester output terminals.

5.6.1 Experimental optimization of electrical load

The experimental test set up comprising of computer controlled shaker, accelerometer and oscilloscope used for the electrical characterization of the VEHs is shown in Figure 5.7(a). In the first set of experiments, the optimal resistive load for all the nonlinear (BQD, MQT and BQT) VEH configurations is determined. The pair of clamped-constrained beams in

the BQT device structure was discarded in the BQD configuration to avoid the stretching effect, and relatively thicker supportive beam is used to ensure that the linearized resonance frequency for all the configurations remain nearly same (~ 45 Hz). The excitation frequency in each configuration is ramped up to the jump frequency in the forward sweep and is held constant at a value proximal to the jump frequency.

It is shown in Figure 5.7 (b) that for all the configurations, the peak load power reaches the maximum values at 3 kΩ, the optimum load resistance of the system, which indicate that the effective electrical damping is independent of the mechanical damping in the system. Henceforth the optimum 3 kΩ load resistance has been used for all the subsequent experiments on all nonlinear VEH configurations. The forward sweep jump frequencies (f_{Peak}) at 0.8g acceleration for the BQD, MQT and BQT combined configurations are 38.2 Hz, 73.35 Hz and 65.06 Hz respectively, and the peak load power (peak P_{Load}) at the same acceleration for these three device configurations are 0.487 mW, 1.073 mW and 0.835 mW respectively. The peak efficiencies of each of these configurations can be computed using the eq. 4.39, and are found to be 6.7%, 13.4% and 10.6% respectively for the BQD, MQT and BQT configurations [Table 5.2].

Table 5.2: Efficiency of different energy harvester configurations

Device	Effective mass [kg]	Acceleration [m/s²]	Velocity [m/s]	Mechanical Power [mW]	Electrical Power [mW]	Efficiency [%]
Bistable Quadratic (BQD)	0.00356	8	0.25	7.24	0.487	6.7
Monostable Quartic (MQT)	0.00356	8	0.28	8.01	1.073	13.4
Bistable Quartic (BQT)	0.00356	8	0.3	7.89	0.835	10.6

The dimensions of the prototypes (2.8cm × 2cm × 2.2 cm) are comparable to the dimensions of standard AA size batteries (length 5cm, diameter 1.4 cm) with an energy content of 2.9 Wh (10440 J) for lithium ion chemistry. At the power levels outlined in Table 5.2, it will take approximately 248 days, 113 days, and 145 days respectively for the BQD, MQT and BQT devices to harvest as much energy as a Li-ion AA battery.
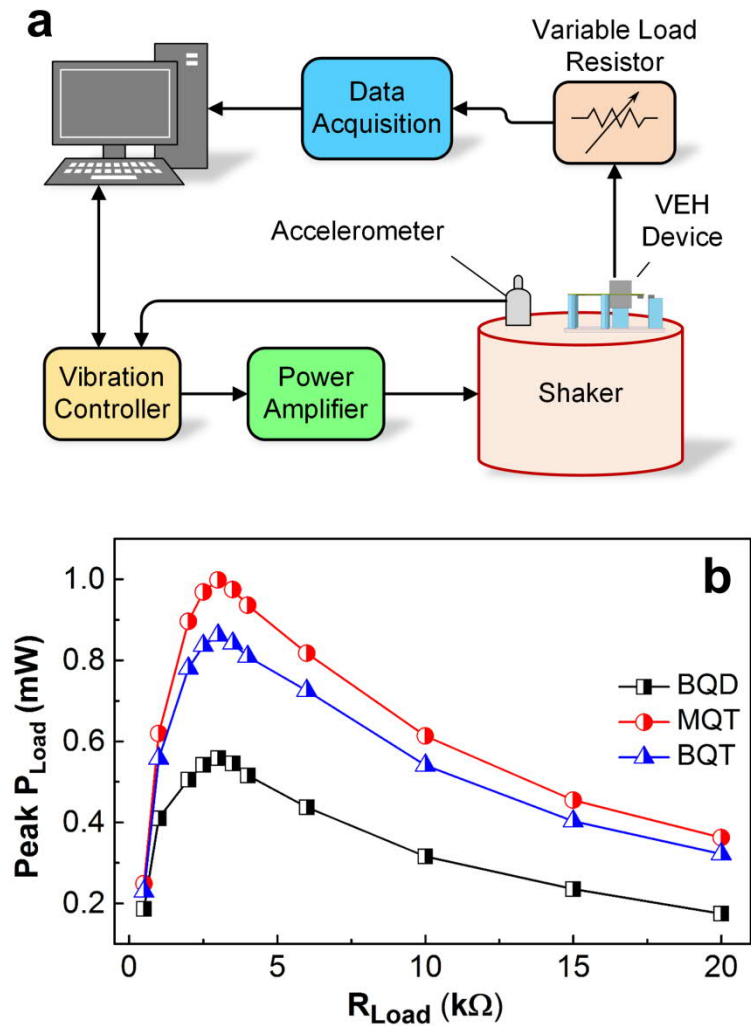
Figure 5.7: (a) Vibration test setup comprising computer controlled electromagnetic shaker, accelerometer, VEH device and digital storage oscilloscope. (b) Variation of peak load power (Peak P_{Load}) with load resistance (R_{Load}) for the BQD, MQT and combined BQT configurations at 0.8g harmonic acceleration.

5.6.2 Response to harmonic frequency sweep excitations

The harmonic frequency responses of the different nonlinear VEH configurations were obtained from vibrational frequency sweeps in the forward (10 Hz – 90 Hz) and reverse (90 Hz – 10 Hz) directions while keeping the acceleration constant. The frequency response plots for the BQD, MQT and BQT configurations at geometrically increasing vibrational accelerations (0.2g, 0.4g, 0.8g and 1.6g) are illustrated in Figure 5.8. While the gap between the repulsively positioned magnets is fixed at $d = 10$ mm for the MQT configuration, it is set at $d = 3.6$ mm for the BQD and BQT configurations.
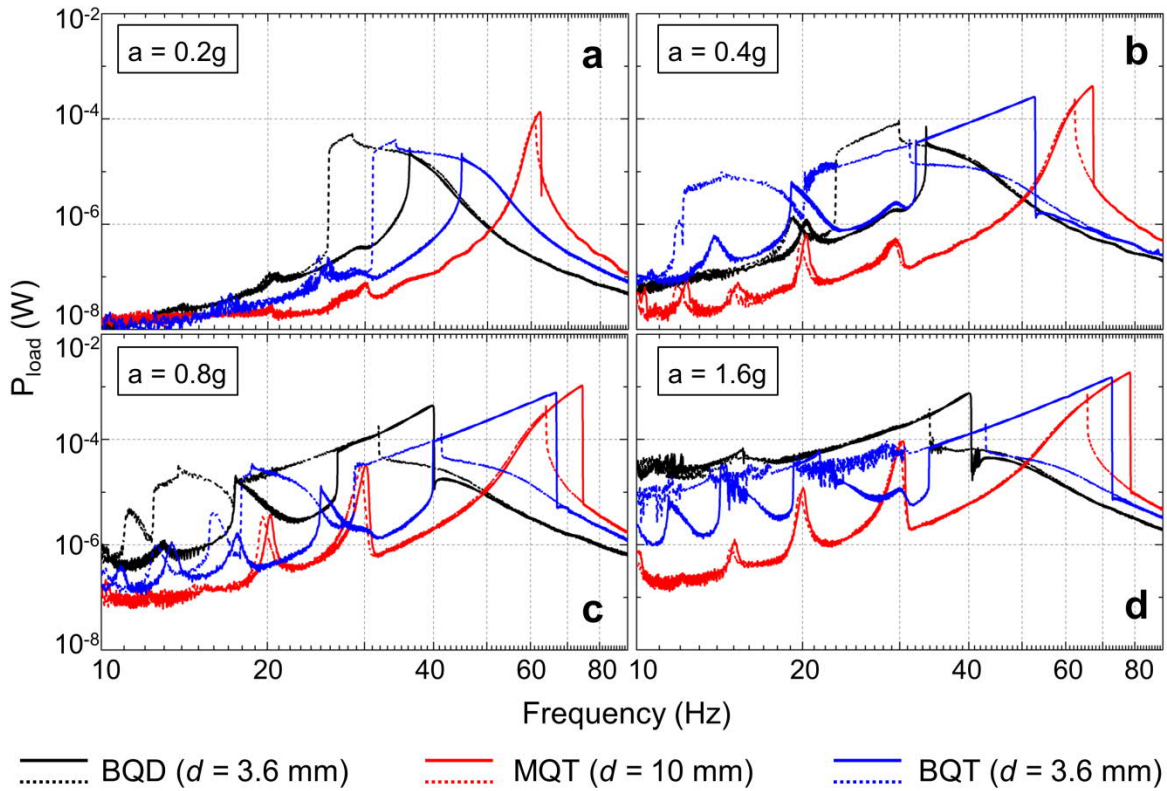
Figure 5.8: Experimental frequency responses for the BQD (*d* = 3.6 mm), MQT (*d* = 10 mm), and BQT (*d* = 3.6 mm) configurations at different accelerations. Solid lines represent the forward sweep response [10 Hz – 90 Hz] and dashed lines denote the reverse sweep response [90 Hz – 10 Hz]. At low acceleration (0.2g) BQD and BQT VEHs are confined in a single potential well and exhibit softening response leaning towards the left. At higher accelerations (0.4g, 0.8g, 1.6g) the BQD and BQT configurations perform consistent inter-well jumps in the high-energy branch. At 1.6g acceleration, both BQD and BQT VEHs perform chaotic inter-well motion in the low (10 – 30 Hz) frequencies. The MQT device produces hardening frequency response leaning towards the right and super harmonic peaks in the low (10 – 30 Hz) frequencies.

At 0.2g, the BQD and BQT VEHs produces hysteretic frequency responses tilted towards the left with softening characteristics [Nguyen and Halvorsen [21]], which is typical of low amplitude intra-well oscillation. This type of small limit-cycle intra-well oscillation indicates that 0.2g vibrational acceleration is inadequate for the bistable oscillators to overcome the potential barrier and the oscillator essentially remain confined within a potential well. Contrastingly, the MQT VEH produces mildly hysteretic hardening response [[21]] by oscillating with small amplitude near the bottom of the single potential well (Figure 5.5 (c)). As the vibrational acceleration is increased in geometric progression

(0.4g, 0.8g), the BQD and BQT VEHs eventually escape the potential well under suitable initial conditions and perform large amplitude (large limit-cycle) inter-well motions producing broadband hardening response. The MQT oscillator also produces hardening response at higher accelerations, albeit over a narrower frequency range. Additionally, all the nonlinear VEH configurations exhibit super-harmonic peaks at lower frequencies which become more prominent with increasing accelerations. At 1.6g acceleration, the bistable VEHs generate higher power in the low frequency regime (10 – 30 Hz) than the monostable one by performing large amplitude chaotic inter-well oscillations. In the high frequency regime (60 – 80 Hz) the BQT VEH produces large power similar to the MQT device, which is much higher than that from the BQD VEH. Therefore, it is experimentally validated that the BQT VEH combines the beneficial features of the BQD and MQT VEHs in the low and high frequency domains respectively to harvest higher energy over the entire frequency range.

A figure of merit (FOM) for the comparison of the relative performances of the different VEHs should be able to determine the probability of generating sufficient power to meet certain threshold conditions over the entire frequency range of interest. Since the perception of frequency naturally occur in the logarithmic scale (e.g. pitch of music, color of light, mechanical vibration etc.), the logarithm of vibrational frequency should be incorporated in the FOM expressed as,

$$
\begin{aligned}
M &= \frac{1}{\ln\left(f_N/f_0\right)} \int_{f=f_0}^{f_N} \theta(P_L(f) - P_{Th}) d(\ln f) \\
&= \frac{1}{\ln\left(f_N/f_0\right)} \int_{f=f_0}^{f_N} \frac{\theta(P_L(f) - P_{Th})}{f} df
\end{aligned}
$$

5.11

where f_0 and f_N are the lower and upper limits of the frequency and θ is the Heaviside function defined as,

$$
\theta(P) = \begin{cases} 1, & P \geq 0 \\ 0, & P < 0 \end{cases}
$$

5.12

where P is the difference between load power $P_L(f)$ and threshold power P_{Th} given by,

$$
P = P_L(f) - P_{Th}
$$

5.13

In other words, the function M estimates the probability of the load power P_L being higher than the threshold level P_{Th} over the frequency range $f = [f_0, f_N]$. The threshold power P_{Th} is determined by the minimum requirements of the power management electronics of the device driven by the VEH and typically ranges from very low ($\sim$ 1 μW) to very high ($\sim$ hundreds of μW) values. Since frequencies in our experiments are sampled in equal steps over the entire range, M can be approximated as,

$$M = \frac{1}{\ln\left(f_N/f_0\right)} \left[\sum_{n=0}^{N-1} \frac{\theta(P_L(f_n) - P_{Th})}{f_n} \right] (f_{n+1} - f_n) \qquad 5.14$$

where f_n is the n-th frequency value.
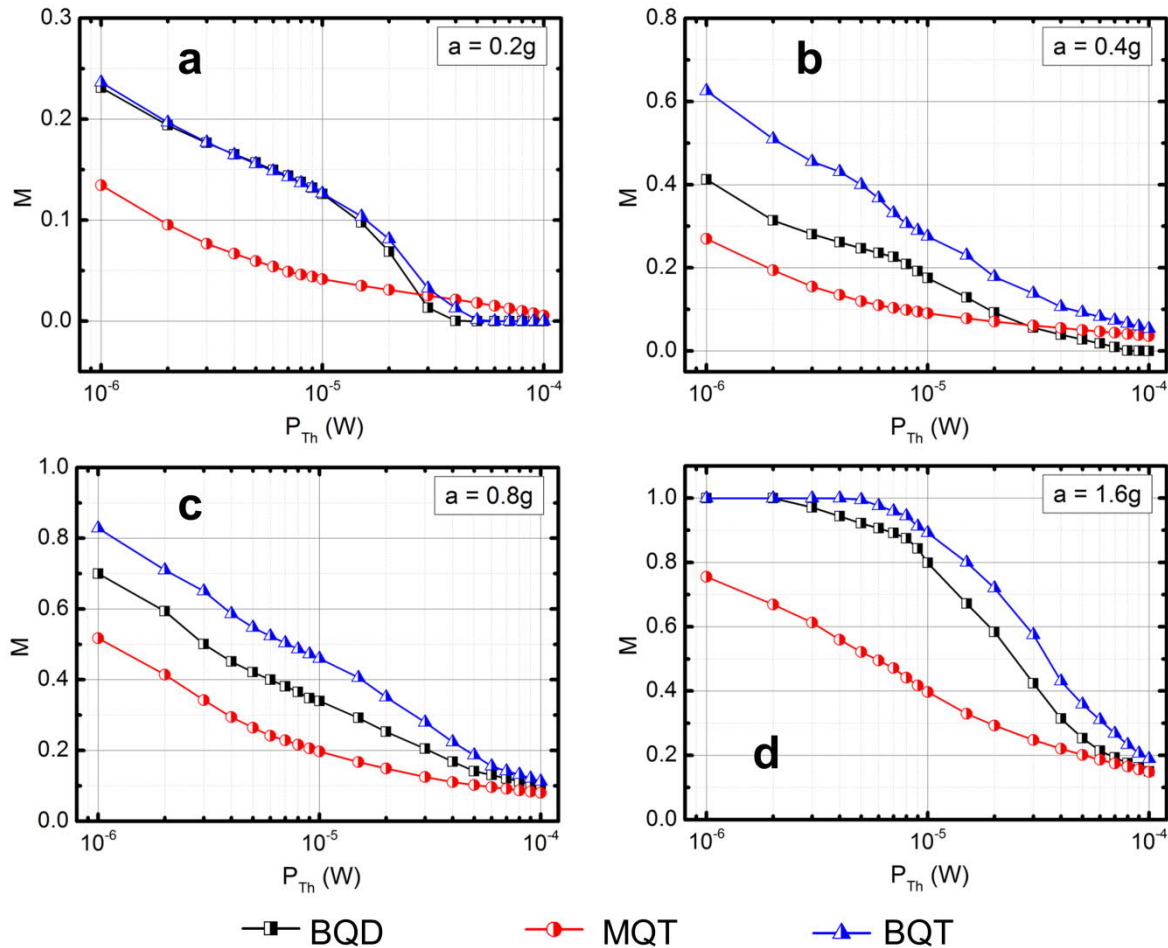
Figure 5.9: Variation of M (normalized probability for $P_{Load} \geq P_{Th}$ over the frequency sweep) with threshold power (P_{Th}) for BQD, MQT and BQT VEH configurations.

The variation of *M* over different values of logarithmically varying threshold power at geometrically increasing accelerations is shown in Figure 5.9, where *M* increases with increasing acceleration for all the nonlinear VEH configurations. On the other hand, as the required P_{Th} is increased logarithmically at fixed accelerations, a smaller segment of the frequency response meets the required power level leading to decreasing the probability *M*. The Figure 5.9 shows that for all acceleration values the probability of the BQT VEH to be able to generate load power beyond the threshold value is higher than both BQD and MQT VEHs. The higher probability of harvesting larger than threshold power in the BQT VEH system originates from the combined effect of large amplitude inter-well motion at low frequencies (feature of BQD) and nonlinear cubic stiffness induced large amplitude motion (feature of MQT) in the BQT system.

Another FOM in terms of energy generating capabilities can be defined as the normalized power integral (*NPI*) which computes the amount of usable load power above the threshold power level given by,

$$NPI = \frac{1}{\ln\left(f_N/f_0\right)} \int\limits_{f=f_0}^{f_N} P_L(f)[\theta(P_L(f) - P_{Th})]d(\ln f)$$

$$= \frac{1}{\ln\left(f_N/f_0\right)} \int\limits_{f=f_0}^{f_N} \frac{P_L(f)[\theta(P_L(f) - P_{Th})]}{f} df$$

5.15

which, due to equidistant frequency steps, can be approximated as,

$$NPI = \frac{1}{\ln\left(f_N/f_0\right)} \left[\sum_{n=0}^{N-1} \frac{P_L(f_n)[\theta(P_L(f_n) - P_{Th})]}{f_n}\right](f_{n+1} - f_n)$$

5.16

In other words, the *NPI* determines the total usable load power generated above the threshold power level. This FOM appreciates the efficacy of a VEH system in most practicable situations where the generated power is stored in charge storage devices (super-capacitors or rechargeable batteries) after proper conditioning.
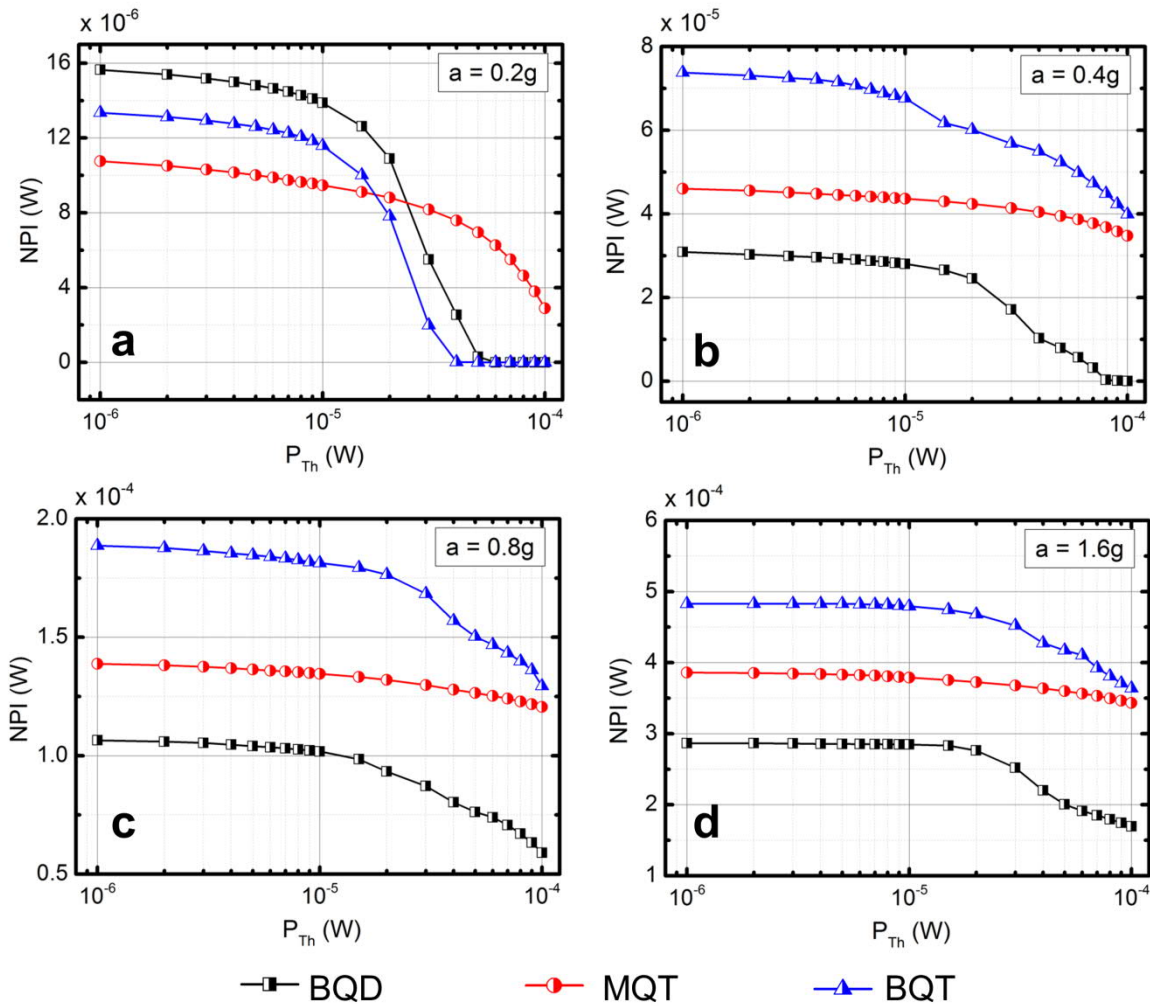
Figure 5.10: Variation of *NPI* (normalized power density over the frequency sweep) with threshold power (P$_{Th}$) for BQD, MQT and BQT VEH configurations.

The variation of *NPI* over logarithmically varying P_{Th} are shown in Figure 5.10, where the *NPI* is increasing with the geometrically increasing accelerations. At a fixed acceleration, however, the *NPI* gradually decreases as the P_{Th} is logarithmically increased. This is a result of decreasing the probability of the load power P_L being higher than the threshold P_{Th} as it is gradually increased. At low acceleration ($a = 0.2$g) the *NPI* for both BQD and BQT are larger than that of MQT when the threshold P_{Th} is less than 20 µW. This is a manifestation of the fact that the BQD and BQT harmonic frequency responses tend to be above P_{Th} at more segments of the response than the MQT VEH. As P_{Th} is increased gradually beyond 20 µW, the frequency response is unable to cross the threshold level after $P_{Th} = 50$ µW and results into zero *NPI*. At higher accelerations, (Figure 5.10.(b), (c), (d)) the *NPI* levels for BQT is higher than that for both BQD and BQT, which indicates higher power harvesting capability for the BQT VEH. This enhancement of *NPI* can be attributed

to the fact that the BQT configuration leads to higher power in the low frequency regime (due to bistable nonlinearity), while maintaining the high energy branch of the frequency response similar to MQT (due to quartic potential) in the high frequency regime.
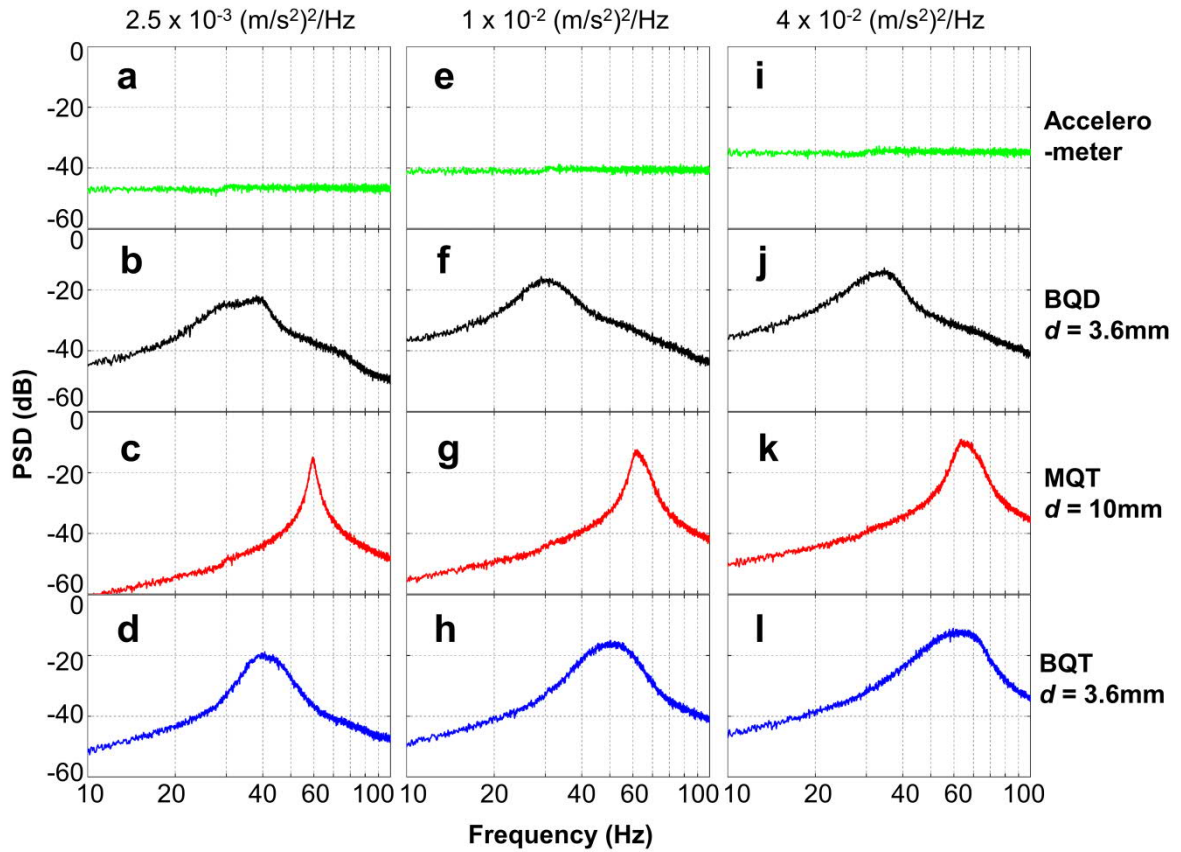
Figure 5.11: Power spectral density (PSD) vs frequency plots for the BQD, MQT and BQT configurations under band limited (10-110 Hz) random vibrations of 2.5×10⁻³ (m/s²)²/Hz, 1×10⁻² (m/s²)²/Hz, and 4×10⁻² (m/s²)²/Hz average PSD.

5.6.3 Band-limited random frequency response

The performances of all the different configurations of the proposed VEH device in random vibration environment are evaluated in applied bandlimited (10 Hz – 110Hz) random vibrations with low (2.5×10^{-3} $(m/s^2)^2/Hz$, or 0.5 m/s² RMS), medium (1×10^{-2} $(m/s^2)^2/Hz$, or 1m/s² RMS), and high (4×10^{-2} $(m/s^2)^2$ /Hz, or 2 m/s² RMS) accelerations for 500 seconds. The resulting PSDs of the input vibrational excitations reveal an uniform distribution of vibrational energy across the spectrum (Figure 5.11 (a),(e),(i)). The resulting PSDs of the BQD device produce relatively broadened responses with a peak between 30 Hz – 40 Hz for all accelerations (Figure 5.11 (b),(f),(j)). At all acceleration levels, the MQT variant of the device produces steep peaks near 60 Hz (Figure 5.11

(c),(g),(k)), which implies higher peak power but reduced low frequency responses. Contrastingly, in the BQT configuration, the peak is flattened with higher power in the lower frequency domain for all accelerations (Figure 5.11 (d),(h),(l)), implying more uniformly distributed energy harvesting capabilities across the spectrum. This is attributable to the higher nonlinear restoring force and lowering of the bistable potential barrier height (Figure 5.5 (c),(d)) due to incorporation of quartic potential, which enable the oscillator to perform inter-well jump at all vibrational accelerations.
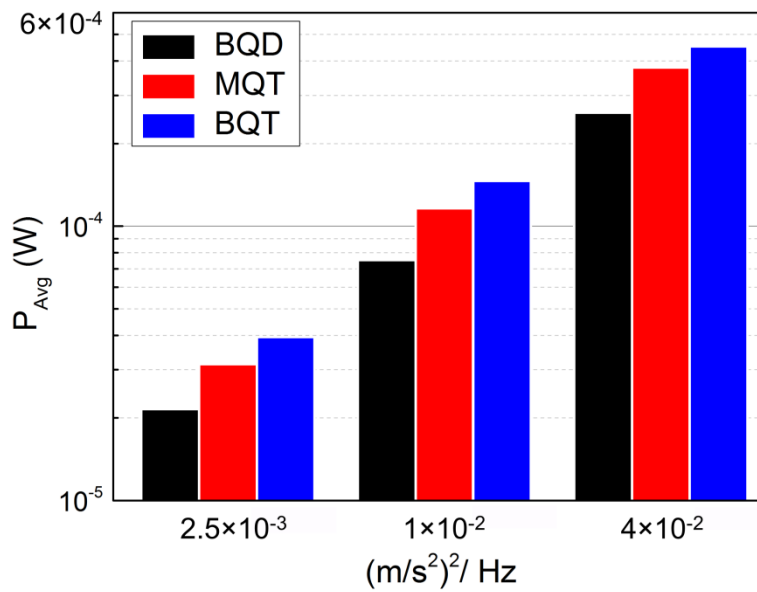
Figure 5.12: Comparison of average harvested power (P_{Avg}) for the BQD, MQT and BQT configurations subject to band limited (10-110 Hz) random vibrations of 2.5×10^{-3} (m/s²)²/Hz, 1×10^{-2} (m/s²)²/Hz, and 4×10^{-2} (m/s²)²/Hz average PSD.

Unsurprisingly, the peak power generated by the BQT VEH is smaller in comparison to the MQT at all accelerations, similar to the observation made previously in case of harmonic excitation (Figure 5.7 (b)). However, comparisons of the average load power (P_{Avg}) over the entire time series of the random vibrations exhibit that the P_{Avg} for the BQT device is higher than that of the BQD and MQT configurations (Figure 5.12). The broader frequency spectrum and lower peak power and still higher average power in the BQT configuration implies that the harvested energy is spread out more uniformly over the frequency range even in random vibrations.

5.7 Conclusions

In many vibration energy harvesting literature, the use of nonlinear bistable-quartic Duffing oscillator based theoretical framework and the practical implementation using magnetic repulsion induced bistable-quadratic nonlinear device leads to critical inconsistencies in the large deflection characteristics and performances of the reported VEHs. Through a specially designed BQT oscillator based VEH this work has demonstrated that the fundamentally different large deformation behavior leads to significant enhancement in the performance of the BQT device in comparison to both BQD and MQT devices. The proposed novel BQT VEH prototype is fabricated using laser micro-machined spring structure where quartic potential is induced through a pair of clamped-constrained cantilevers and bistability is introduced by the repulsive interaction between discrete permanent magnets and transduction is incorporated electromagnetically. The ability to manipulate the magnetically induced bistability and stretching induced quartic potential independently yields the opportunity for comparative study of the nonlinear effects on the performances of the BQD, BQT and MQT VEHs.

The numerical simulations and experimental harmonic frequency sweep responses reveal that the beneficial features of the BQD (large amplitude chaotic oscillations at low frequency) and MQT (large amplitude harmonic oscillation in the high energy branch at high frequencies) devices are combined in the BQT device, leading to superior performance. Both the probability of generating at least the threshold power and the temporal average of generated power are higher in the BQT device than BQD and MQT devices at all accelerations. Additionally, under bandlimited random vibration the BQT device attains a broader power spectral density and spectral average power in comparison to the other nonlinear systems. These performance enhancements are attributable to the moderate reduction in bistable potential barrier height and higher restoring force at large deflections due to coupling of magnetic repulsion induced bistability into a stretching induced quartic potential system. Through numerical simulations and experimental results it has been established that the favorable features of nonlinear BQD and MQT systems can be integrated in a combined bistable-quartic (BQT) potential system to enhance the overall performance over the entire vibrational frequency spectrum. The proposed BQT nonlinear device topology could be further modified for implementation in other transduction (piezoelectric, electrostatic, triboelectric etc.) mechanisms for different wideband practical application scenario and miniaturized to the micro-scale. The technique of exploiting the

advantages of different nonlinear mechanisms by combining them in a single system could be extended even further towards sensors and accelerometer applications where large amplitude oscillation over broad spectrum of vibrations is necessary. The developed prototypes operate over a frequency range from $30 - 80$ Hz, which make them suitable for low power sensor applications in moving vehicles, machine monitoring in manufacturing plants etc.

References

[1]   S. Kulkarni, S. Roy, T. O'Donnell, S. Beeby, and J. Tudor, "Vibration based electromagnetic micropower generator on silicon," *Journal of Applied Physics,* vol. 99, p. 08P511, 2006.

[2]   S. P. Beeby, R. N. Torah, M. J. Tudor, P. Glynne-Jones, T. O'Donnell, C. R. Saha*, et al.*, "A micro electromagnetic generator for vibration energy harvesting," *Journal of Micromechanics and Microengineering,* vol. 17, pp. 1257 – 1265, 2007.

[3]   F. Cottone, H. Vocca, and L. Gammaitoni, "Nonlinear Energy Harvesting," *Physical Review Letters,* vol. 102, p. 080601, 2009.

[4]   A. Erturk, J. Hoffmann, and D. J. Inman, "A piezomagnetoelastic structure for broadband vibration energy harvesting," *Applied Physics Letters,* vol. 94, p. 254102, 2009.

[5]   A. Erturk and D. J. Inman, "Broadband piezoelectric power generation on high-energy orbits of the bistable Duffing oscillator with electromechanical coupling," *Journal of Sound and Vibration,* vol. 330, pp. 2339-2353, 2011.

[6]   A. H. Nayfeh and D. T. Mook, "Forced Oscillations of Systems Having a Single Degree of Freedom," in *Nonlinear Oscillations*, ed: Wiley-VCH Verlag GmbH, 2007, pp. 161-257.

[7]   B. Marinkovic and H. Koser, "Smart Sand—a wide bandwidth vibration energy harvesting platform," *Applied Physics Letters,* vol. 94, p. 103505, 2009.

[8]   B. P. Mann and N. D. Sims, "Energy harvesting from the nonlinear oscillations of magnetic levitation," *Journal of Sound and Vibration,* vol. 319, pp. 515-530, 2009.

[9]   D. Mallick, A. Amann, and S. Roy, "A nonlinear stretching based electromagnetic energy harvester on FR4 for wideband operation," *Smart Materials and Structures,* vol. 24, p. 015013, 2015.

[10]   M. Ferrari, V. Ferrari, M. Guizzetti, B. Andò, S. Baglio, and C. Trigona, "Improved energy harvesting from wideband vibrations by nonlinear piezoelectric converters," *Sensors and Actuators A: Physical,* vol. 162, pp. 425-431, 2010.

[11]   P. Podder, A. Amann, and S. Roy, "A bistable electromagnetic micro-power generator using FR4-based folded arm cantilever," *Sensors and Actuators A: Physical,* vol. 227, pp. 39-47, 2015.

[12] P. Podder, A. Amann, and S. Roy, "Combined Effect of Bistability and Mechanical Impact on the Performance of a Nonlinear Electromagnetic Vibration Energy Harvester," *IEEE/ASME Transactions on Mechatronics,* vol. 21, pp. 727-739, 2016.

[13] R. Masana and M. F. Daqaq, "Electromechanical Modeling and Nonlinear Analysis of Axially Loaded Energy Harvesters," *Journal of Vibration and Acoustics,* vol. 133, p. 011007, 2011.

[14] F. Cottone, L. Gammaitoni, H. Vocca, M. Ferrari, and V. Ferrari, "Piezoelectric buckled beams for random vibration energy harvesting," *Smart Materials and Structures,* vol. 21, p. 035021, 2012.

[15] F. Cottone, P. Basset, H. Vocca, L. Gammaitoni, and T. Bourouina, "Bistable electromagnetic generator based on buckled beams for vibration energy harvesting," *Journal of Intelligent Material Systems and Structures,* vol. 25, pp. 1484-1495, 2013.

[16] H. Vocca, F. Cottone, I. Neri, and L. Gammaitoni, "A comparison between nonlinear cantilever and buckled beam for energy harvesting," *The European Physical Journal Special Topics,* vol. 222, pp. 1699-1705, 2013.

[17] M. F. Daqaq, R. Masana, A. Erturk, and D. Dane Quinn, "On the Role of Nonlinearities in Vibratory Energy Harvesting: A Critical Review and Discussion," *Applied Mechanics Reviews,* vol. 66, p. 040801, 2014.

[18] S. C. Stanton, C. C. McGehee, and B. P. Mann, "Nonlinear dynamics for broadband energy harvesting: Investigation of a bistable piezoelectric inertial generator," *Physica D: Nonlinear Phenomena,* vol. 239, pp. 640-653, 2010.

[19] L. D. Landau, L. P. Pitaevskii, A. M. Kosevich, and E. M. Lifshitz, *Theory of Elasticity*: Elsevier Science, 2012.

[20] S. D. Senturia, *Microsystem design*: Kluwer Academic Publishers, 2001.

[21] D. S. Nguyen and E. Halvorsen, "Analysis of vibration energy harvesters utilizing a variety of nonlinear springs," *Proceedings of the PowerMEMS,* vol. 10, pp. 331-334, 2010.

6 NONLINEAR SILICON MEMS ENERGY HARVESTER

One of the major challenges to be resolved for successful widespread implementation of vibration energy harvesting systems is the miniaturization and integrated or semi-integrated fabrication of such devices, while still being capable of harvesting useful amount of energy. This chapter describes the works related to the development of MEMS scale vibration energy harvester. In the first section an electromagnetic transduction based MEMS vibration energy harvester is described, comprising silicon spring structure, sintered NdFeB micro-magnet and planar double layer micro-coil. The fabricated device exhibits nonlinear response, primarily due to the inherent stretching effect in the spiral spring arms. At large deflections, this effect is combined with a second nonlinear effect, the mechanical impact between the vibrating magnet and the micro-coil. In the second section the nonlinear MEMS energy harvester is combined with a magnetic repulsion induced frequency tuning mechanism. The frequency tuning effect is incorporated by precise manipulation of the distance, and thereby the repulsion force, between the transducing magnet and a screw mounted tuning magnet. The results show that the tuning mechanism is capable of modifying the frequency response significantly. The fabrication method and experimental results for the MEMS vibration energy harvesters are discussed in detail, and finally the concluding remarks are presented.

6.1 Nonlinear MEMS micro-power generator

A nonlinear MEMS electromagnetic vibration energy harvester which combines structural nonlinearity with mechanical impact is described in this section. This section describes the development of a nonlinear MEMS electromagnetic micro-power generator consisting of a silicon-on-insulator (SOI) spiral spring, double layer micro-coils and miniaturized NdFeB magnets. Furthermore, with respect to the spiral silicon spring based VEH, four different square micro-coil topologies with different copper track width and number of turns have

been investigated to determine the optimal coil dimensions. The micro-generator with the optimal micro-coil generated 0.68 micro-watt load power over an optimum resistive load at 0.1g acceleration, leading to normalized power density of 3.5 kg.s/m^3. At higher accelerations the load power increased, and the vibrating magnet collides with the planar micro-coil producing wider bandwidth. The design methodology of the nonlinear micro-power generator is first explained, followed by detailed discussion on the micro-fabrication process. In the following subsections, the experimental results and discussions are presented.

6.1.1 Design of the nonlinear MEMS micro-power generator

The proposed micro electromagnetic vibrational energy harvester comprise of silicon spring, tiny NdFeB magnets and double-layer planar copper micro-coil. The spring constitutes of four spiral-shaped silicon cantilever beams Figure 6.1. While one end of each of the beams is clamped to a square shaped silicon frame, the other end is terminated into a central silicon paddle. In this spring architecture, while the surrounding silicon frame is kept fixed or stationary, the central paddle is suspended by the four spiral silicon springs and is movable under external excitation such as vibration.
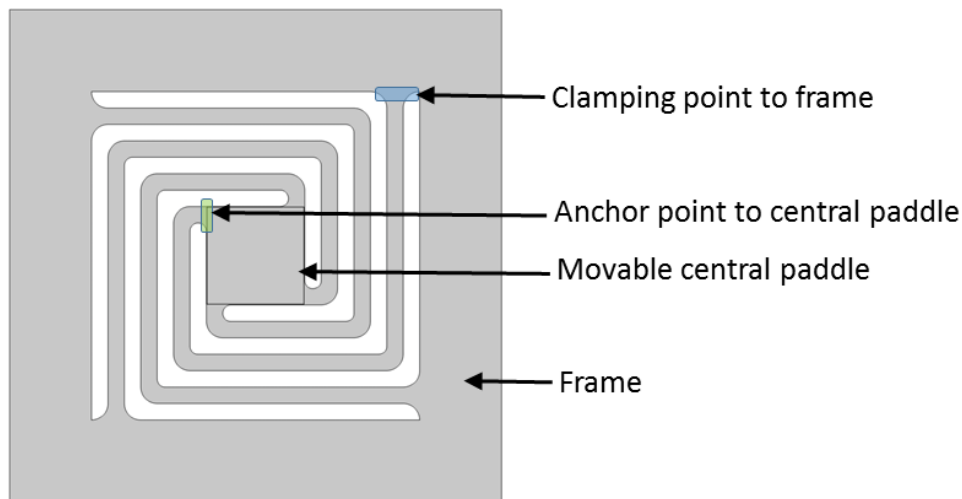
Figure 6.1: SOI spring architecture. The clamping and anchoring points of the spring arms are defined in the diagram.

The movable central paddle can support a sintered NdFeB magnet, which can be attached to the paddle such that the motion of the paddle is not obstructed. The silicon frame and magnet assembly is mounted onto a Perspex supporting structure [Figure 6.2(a)]. A micro-fabricated double-layer planar micro-coil is placed underneath the suspended magnet in

such a way that oscillation of the magnet induces flux linkage gradient in the micro-coil. The vertical oscillation of the movable frame creates mechanical stress in the spring arms, and it is important to keep the induced stress as low as possible, since high stress adversely affects the long-term reliability of the device. Figure 6.2(b) exhibits the simulated stress profile in the silicon spring structure when the central pad is deflected by 1 mm. The maximum stress (750 MPa) is shown to be well below the yield stress of silicon (7000 MPa). Therefore, it can be speculated that the springs would be able to sustain the oscillations induced by mechanical vibrations.
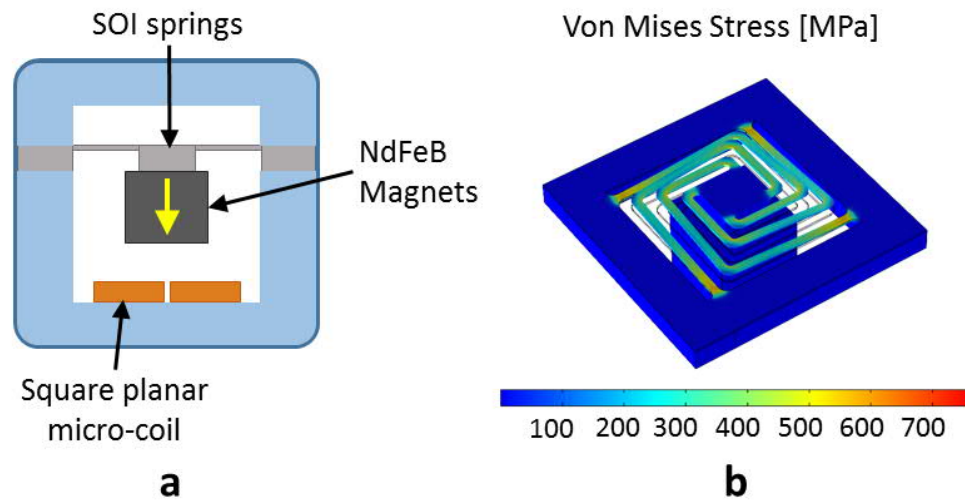
Figure 6.2: (a) Schematic diagram of the proposed micro-EMVEH, (b) mechanical simulation showing the von Mises stress distribution.

6.1.2 Fabrication of the MEMS micro-power generator

The three essential components forming the nonlinear micro-EMVEH are the spiral silicon spring, the double-layer planar micro-coil and the miniaturized NdFeB magnets. Standard silicon MEMS microfabrication processes are used to fabricate the silicon springs and micro-coils. Post-fabrication, these two components are joined together with the sintered NdFeB magnet to form the complete nonlinear micro-EMVEH system.

A. Fabrication of silicon spring

The spiral silicon spring fabrication process steps are shown in Figure 6.3, which starts with a double-side polished SOI (Silicon-On-Insulator) wafer of 50 μm thick Si device layer, 3 μm thick buried SiO_2 layer and 450 μm thick Si handling layer (Figure 6.3(a)). The process of double side polishing of silicon wafer reduces the mechanical stress in the wafer

due to surface irregularities. In the first step, oxide layers are grown on the front and backside of the SOI wafer by wet thermal oxidation (Figure 6.3(b)). Second, the HiPR 6512 positive photoresist is spin-coated on the device layer side and the spiral spring patterns are transferred onto the Si device layer top oxide by using the first mask. The HiPR 6512 is an advanced g-line (436 nm UV) and i-line (365 nm UV) compatible positive photoresist that can produce near vertical profiles down to 0.5 μm resolution. Then, using PERIE (Plasma Enhanced Reactive Ion Etching) the spiral spring patterns are etched onto the device layer top oxide (Figure 6.3(c)). This process uses chemically reactive plasma to remove material from the interaction surface. In the next step, HiPR 6512 photoresist is spin-coated on the back side (Si handle layer) and the central stage and spring frames are patterned using the second photo-mask.
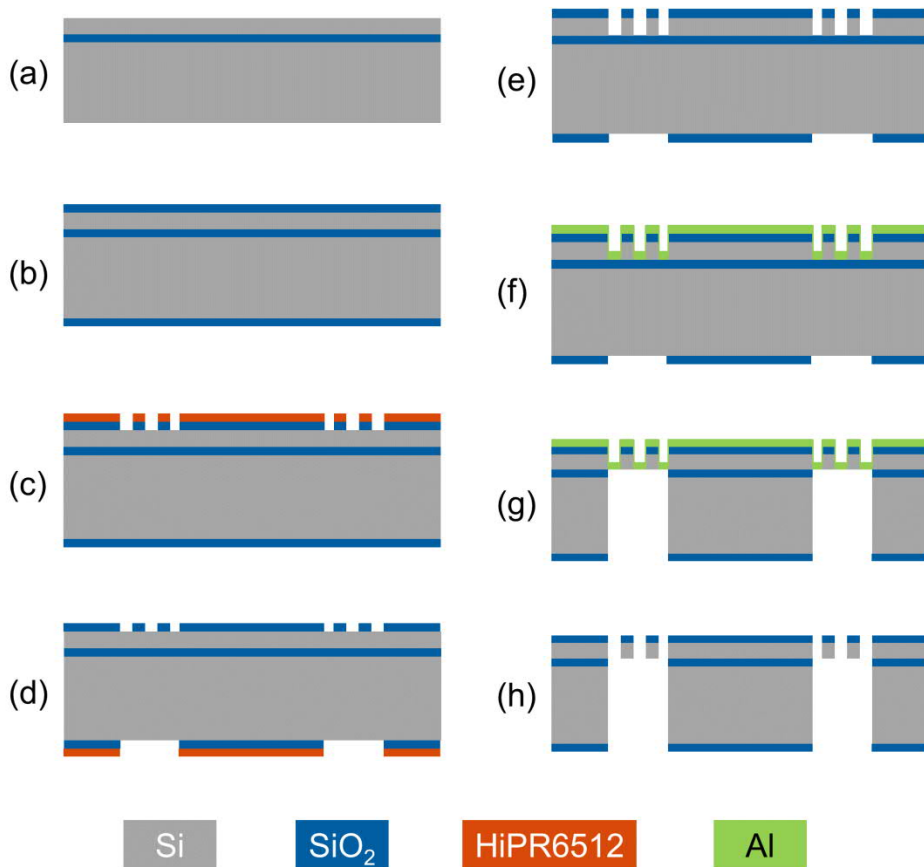
Figure 6.3: Fabrication process steps for the SOI spring structure

Next, the spring frame and central stage patterns are etched onto the backside oxide layer using PERIE (Figure 6.3(d)). The spiral spring patterns are then etched further on the device layer silicon using DRIE (Deep Reactive Ion Etching) process (Figure 6.3(e)) which is a time-multiplexed RIE combined with a sidewall passivation. The DRIE (also known as

Bosch process, after the German company Robert Bosch GmbH, which patented the process) is a standard MEMS fabrication process capable of rendering very deep (~ 600 µm) near-vertical etches profiles. After the DRIE process, the delicate spring structures are protected by sputtered aluminium (0.2 µm) and sprayed photoresist (Figure 6.3(f)).

In the next step, the handle layer is etched using DRIE to release the movable central stage (Figure 6.3(g)), followed by removal of the buried oxide layer. The wafers are then diced into an individual die size of 7mm × 7mm, where the movable central stage is 1.2 mm × 1.2 mm and is supported by four spiral springs (50 µm thick, 200 µm wide). Finally, the protective aluminium and sprayed photoresist layers are etched to release the individual silicon springs (Figure 6.3(h)). The resulting spring structure and its SEM micrograph are shown in Figure 6.4 (a) and (b) respectively.
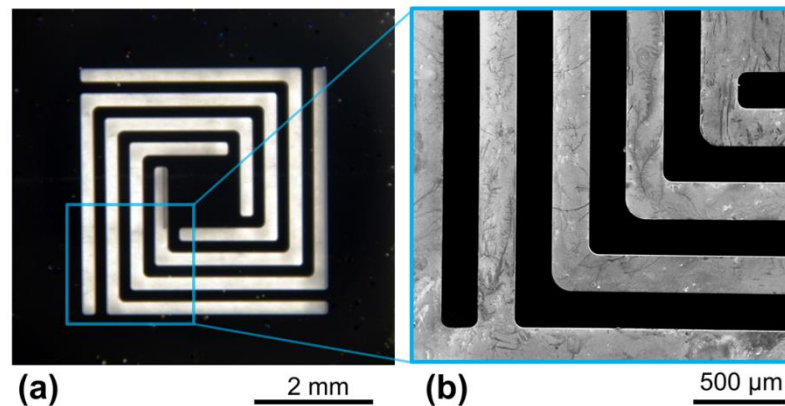
Figure 6.4: Fabricated SOI spring structure (a) Optical image, (b) SEM micrograph

B. Fabrication of planar micro-coil

The double-layer planar micro-coil fabrication steps are illustrated in Figure 6.5, which starts with silicon wafers onto which a titanium (20 nm) and copper (200 nm) seed layers are sputtered (Figure 6.5(a)). Secondly, AZ9260 positive photoresist is spin-coated on the seed layer, and the first coil layer is patterned onto the seed layer using the first mask (Figure 6.5(b)). AZ9260 is a thick film photoresist generally used in processes such as lift-off, metal (e.g. gold, copper etc.) electroplating, and MEMS processes. Following the lithography, the wafer is treated in oxygen plasma to make the metal surface hydrophilic, which facilitates the adherence of the electroplated material to the seed layer during electroplating process. The first coil layer is then electroplated to a height of 15 µm (Figure 6.5(c)). The plating bath used is a commercially available highly acidic (pH = 0) bath ($CuSO_4$, H_2SO_4, additives) manufactured by Schlotter Chemical Technology. The

electroplating process is performed in a room temperature environment using a commercial plating line while agitated mechanically.
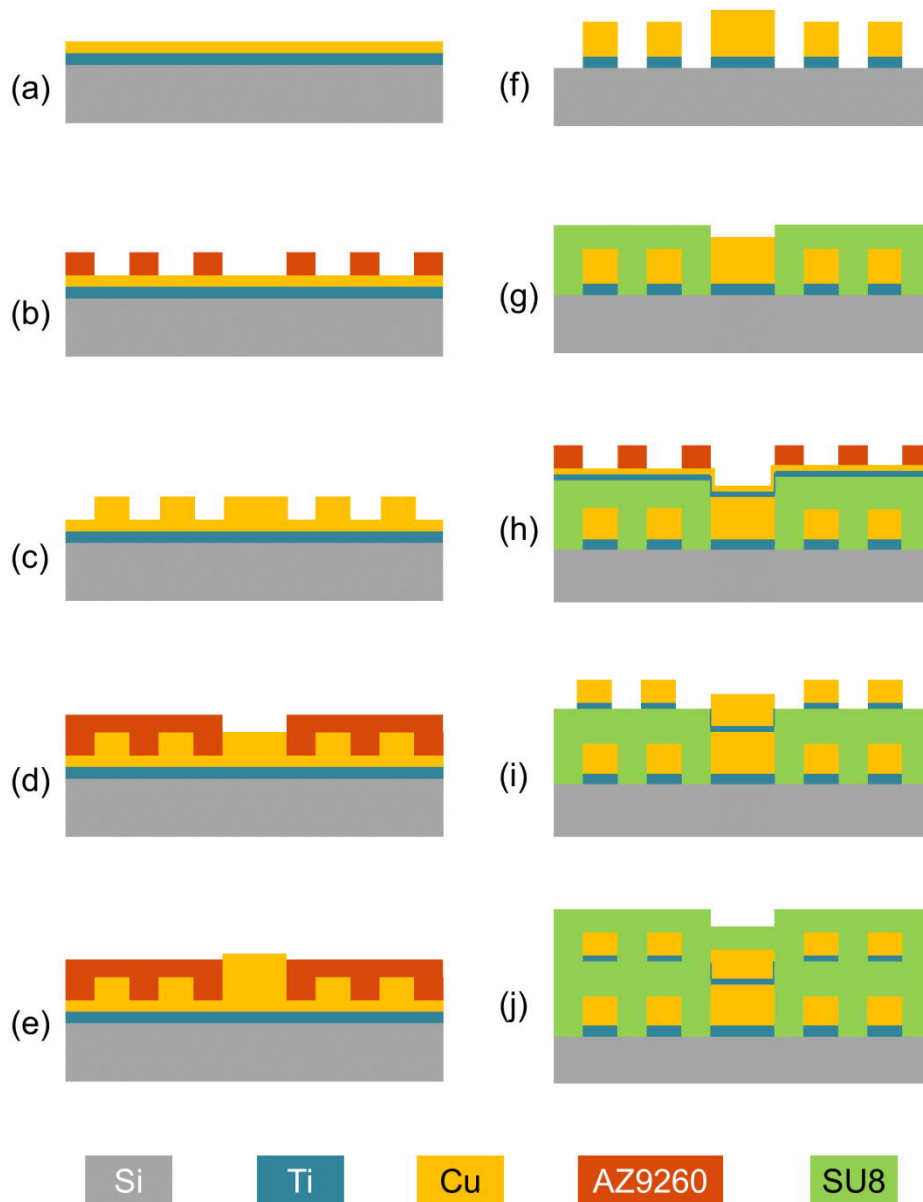
Figure 6.5: Fabrication process steps for the double-layer copper micro-coil

The AZ9260 resist is then spin-coated on top of the electroplated coil layer and a central via is then patterned (Figure 6.5(d)) and electroplated to a height of 15 μm (Figure 6.5(e)). This central via establishes the connection between the first (bottom) coil layer and the second (top) coil layer. Following electroplating the via, the photoresist is removed using acetone. Then the copper seed layer is etched using ammonium persulfate solution (20 g/ 100 ml) and the titanium layer is etched using hydrofluoric acid (HF). At this point, a spiral planar single layer coil is formed (Figure 6.5(f)) with a via at the centre.

In the next step, SU-8 photoresist is spun on top of the first coil layer as an insulation layer, and the central via is opened through photolithography (Figure 6.5(g)). Then, titanium - copper (20 nm/ 200 nm) seed layer is sputtered onto the insulating SU-8 layer for electroplating of the second coil layer. Next, AZ9260 photoresist is spin-coated and the second coil layer pattern is transferred onto the seed layer by UV-ray photolithography (Figure 6.5(h)). The second coil layer is then electroplated to a height of 12.5 μm, and the seed layer is etched after removal of the photoresist (Figure 6.5(i)). The two coil layers are designed such that the induced current flows in the same direction through the copper tracks in the two layers. The minimum copper track width and inter-track gaps are 10 μm and 10 μm respectively, while the central via has a dimension 100 μm × 100 μm. The overall area of the coils is 2.8 mm × 2.8 mm and the total number of turns is 132 with a resistance of 130 ohm. Finally, an SU-8 passivation layer is spun on top of the second coil layer (Figure 6.5(j)) to protect the coils from moisture, oxidation and shorting or damaging due to contaminants and/or handling. The two ends of the copper coils are terminated on two copper pads to provide contact with a PCB through wire bonding or soldering. Figure 6.6 shows the optical image (Figure 6.6(a)) and the two coil layers in a cross-sectional SEM micrograph (Figure 6.6(b)) of the coil area around the central via. The bottom coil layer (before fabrication of the second coil layer) is shown in Figure 6.6(c).
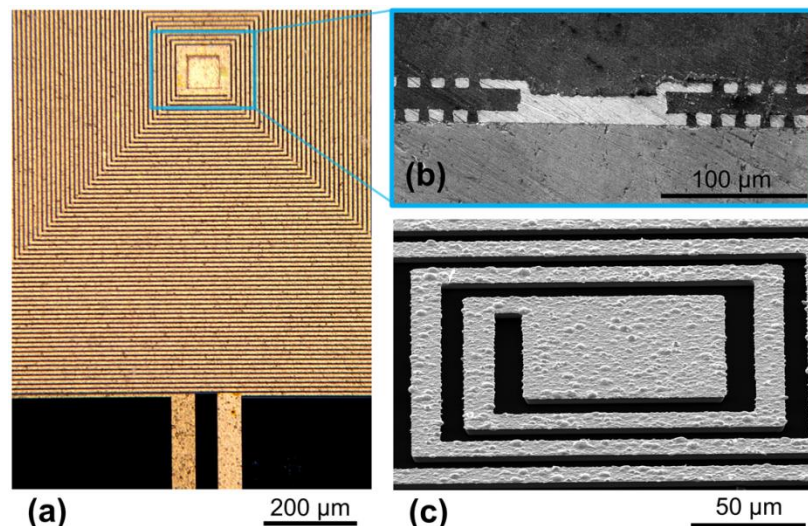
Figure 6.6: (a) Fabricated double-layer copper micro-coil, (b) SEM micrograph of the coil cross-section showing the two coil layers connected through a central via (c) SEM micrograph of the bottom layer of the coil.

C. Assembly of the MEMS micro-power generator

The silicon spring and double-layer planar micro-coils together with the miniaturized NdFeB magnets are assembled on rectangular shaped Perspex spacers to form the complete micro-EMVEH system (Figure 6.7). The planar micro-coil is bonded using epoxy adhesive on an FR4 PCB board (10mm × 15mm) with copper pads onto which the copper coil pads are wire-bonded. An NdFeB magnet (2mm × 2mm × 2mm) is bonded on one side of the movable central paddle of the silicon spring structure. The silicon spring with the NdFeB magnet is aligned above the centre of the copper coil such that the magnetic flux lines pass through the coil. Two Perspex spacers are positioned in between the coil and frame of the spring such that the vertical gap between the micro-coil plane and the magnet is 1.6mm. The magnet can move vertically (out-of-plane) and induce current in the micro-coil due to a change of magnetic flux-linkage.
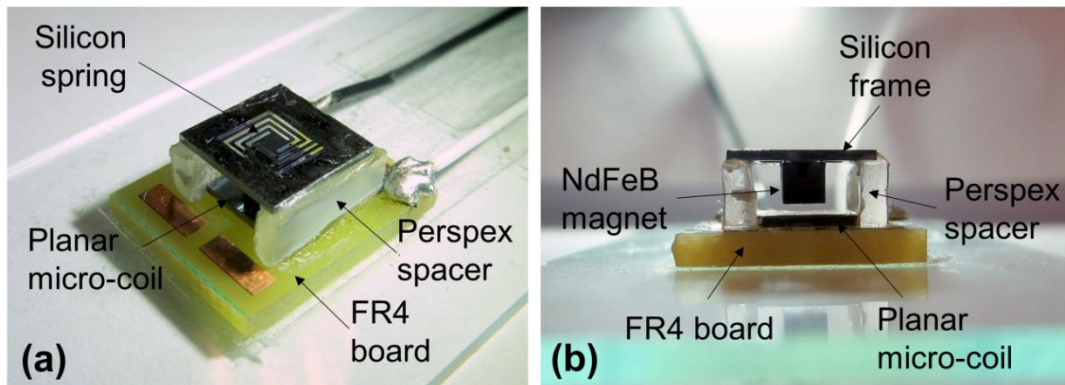
Figure 6.7: Fully assembled micro-EMVEH (a) perspective view showing the silicon spring (b) side view showing the NdFeB magnet suspended above the planar micro-coil.

6.1.3 Experimental results and discussion

In order to determine the effect of micro-coil parameters on the performance of the energy harvester, four different devices, each with the same magnet and silicon spring configurations but different micro-coils are fabricated and tested. The parameters of the different coils are given in Table 6.1.

Table 6.1: Micro-coil parameters

Coil	Copper Track width (µm)	Inter Track gap (µm)	No. of turns	Resistance (Ohm)
Type 1	15	10	104	57.7
Type 2	12.5	12.5	104	95.6
Type 3	10	10	130	131.8
Type 4	10	8	144	156

In the first set of experiments the optimum load resistances of the individual devices were obtained for a linear configuration of the device. This is achieved by applying low magnitude (0.05g) vibrational acceleration, such that the device oscillation amplitude remains small and within the linear range. The Figure 6.8 shows that with increasing load resistance, the RMS load voltage keeps on increasing, while the load power reaches maxima at different load resistances for each coil type, before falling off. It is observed that the optimum resistive load for each coil types is very close to the resistances of the individual coils (Figure 6.8(b)). This is due to the fact that the weak magnetic flux linkage between the magnet and coils result in weak electromagnetic coupling coefficient, leading to low electromagnetic damping in comparison to the mechanical damping which has negligible effect on the optimum load.
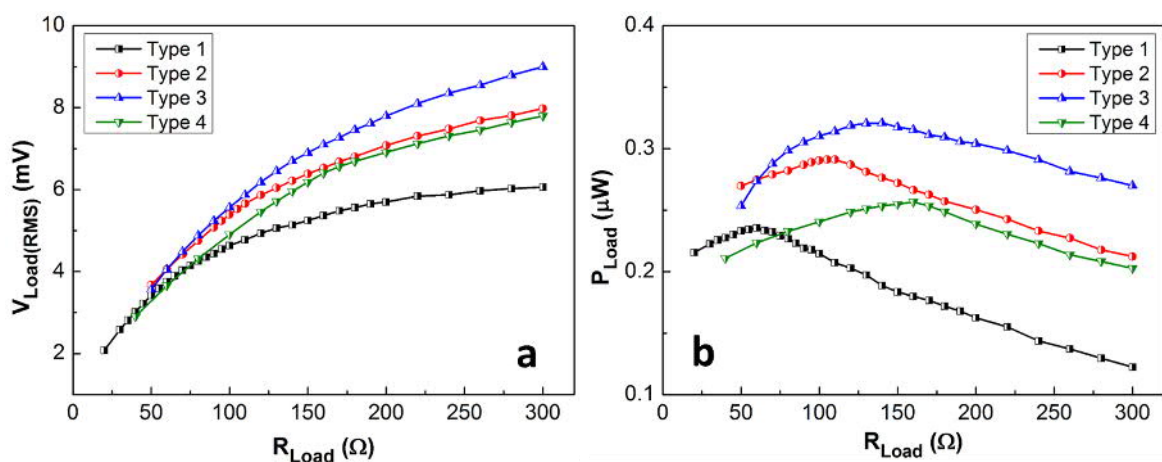
Figure 6.8: Variations of (a) RMS load voltage and (b) Load power with load resistance for different types of micro-coil at 0.05g acceleration.

The RMS load voltage and the load powers of the different devices at 0.05g acceleration are shown in Figure 6.8 (a) and (b). At 0.05g acceleration, the device with Type 3 micro-

coil generates the highest power (0.32 µW) while the device with Type 1 micro-coil produces the smallest power (0.24 µW). Experimentally, the Type 3 micro-coil is the optimum for this device as this configuration generates the highest voltage and power across the optimum load among all the configurations, which could be due to higher packing factor and optimum coil geometry.
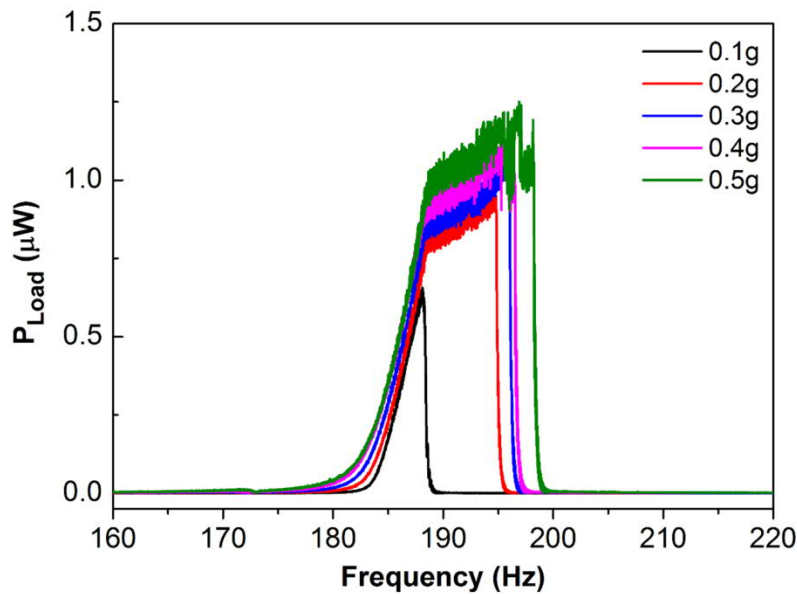
Figure 6.9: Load power vs frequency responses for different acceleration.

The experimental frequency response plots for the device with coil type 3 for different accelerations are shown in Figure 6.9, and produces 0.68 µW power at 0.1g acceleration. The response also exhibits hysteretic frequency response due to nonlinear behaviour triggered by stretching of the spiral beams. As the acceleration is increased, the oscillation amplitude of the spring increases leading to higher peak power (1.2 µW), and the magnet starts to collide with the coil underneath. These collisions occur in the acceleration range 0.2g-0.5g, and the peaks of the frequency responses for these accelerations are flattened, leading to wider bandwidth of 8-12 Hz. This type of impact induced bandwidth widening has been exploited at macro and meso-scale [Soliman, et al. [1], Podder, et al. [2]] for electromagnetic systems and at micro scale [Le and Halvorsen [3], Basset, et al. [4]] for electrostatic transduction systems previously. It is evident from Figure 6.9 that the mechanical impact phenomenon can also be utilized for bandwidth widening at micro-scale using electromagnetic transduction. This work forms the background for further development in the device topology by incorporation of magnetically induced frequency tuning and investigation of its effect on the device performance.

6.2 Magnetic tuning of nonlinear MEMS micro-power generator

One of the major concerns for implementation of vibration energy harvesters in real-life environments is the variability of frequency of vibration sources. For example, vibration data from different locations of a suspension bridge shows very different spectral characteristics (Figure 6.10).
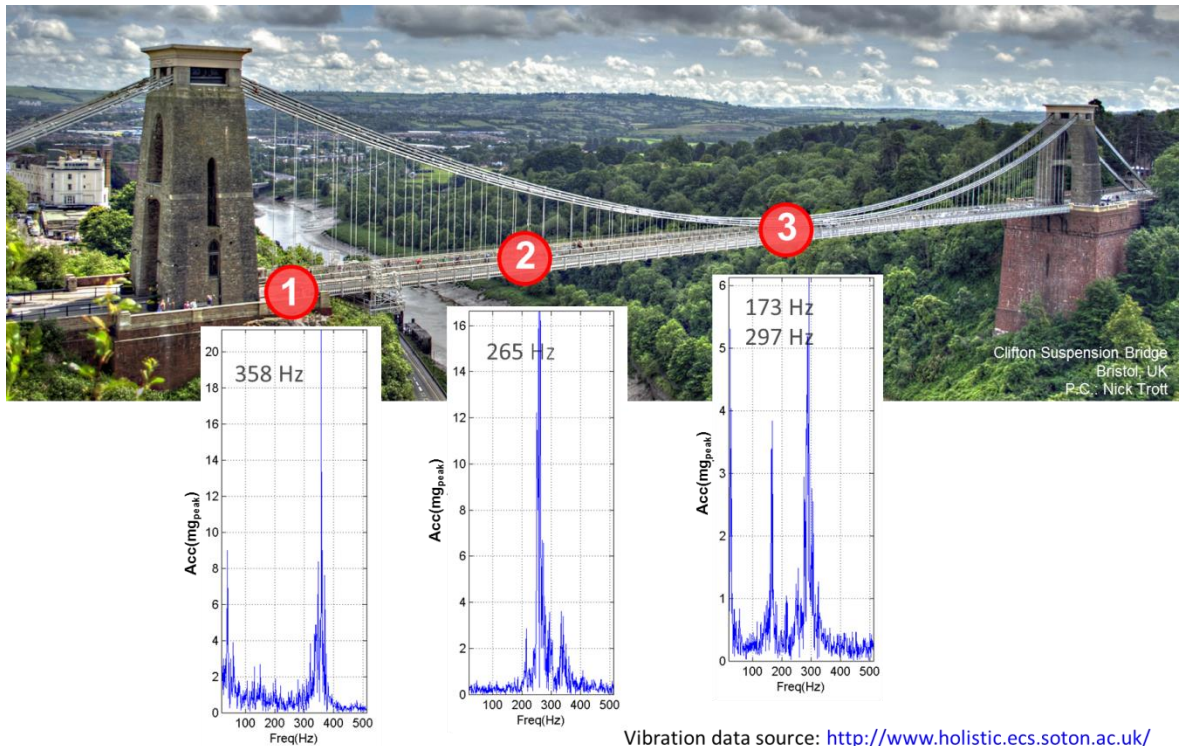
**Figure 6.10: Different vibration spectra from different parts of Clifton suspension bridge**

Therefore, it is of critical importance to the designer of a vibration energy harvester to include provisions for tunability of the device to suite different vibration environment. Various frequency tuning mechanisms (mostly mechanical tuning by manipulation of spring coefficient or the effective proof-mass) have been investigated and successfully implemented in macro-scale and meso-scale vibration energy harvesters [e.g. Gieras, et al. [5], Wu, et al. [6], Jia and Seshia [7]]. A different approach of frequency tuning by manipulation of magnetic force have also been investigated by some research groups [Zhu, et al. [8], Waleed, et al. [9], Constantinou, et al. [10]], all of which are implemented in macro or meso-scale prototypes.

In this work the effect of magnetic force tuning in an inherently nonlinear MEMS-scale electromagnetic vibration energy harvester has been investigated. The spiral silicon spring and double layer micro-coils fabricated in section 6.1.2 are used to develop the tunable micro-energy harvester. The repulsive magnetic tuning force is controllably incorporated through interaction of a pair of transducing and tuning magnets, while cubic Duffing nonlinearity is induced by stretching of clamped-constrained spiral cantilevers. The topology of the device compensates for tuning induced damping by enhanced electromagnetic coupling and increased power level. In the subsequent sections, the design of the prototype device and the associated theoretical framework are discussed, followed by a brief discussion on fabrication and assembly of the device. Finally, different tuned configurations of the prototype are characterized in various excitation conditions; analysis and discussion of the experimental results are followed by the concluding remarks. It has been demonstrated that the proposed magnetic tuning mechanism modifies the frequency responses and harvested power levels significantly and is deployable in micro-EMVEHs for post-fabrication tunability.

6.2.1 Design of magnetically tunable MEMS micro-power generator

The proposed micro electromagnetic vibrational energy harvester comprises a micro-fabricated silicon spring, miniature NdFeB magnets and a double-layer planar copper micro-coil [Figure 6.11]. The silicon spring and micro-coils are fabricated separately using standard photolithography and micro-fabrication process (described in 6.1.2) and all components are assembled to form the micro-EMVEH. The spring constitutes of four spiral-shaped silicon cantilevers supporting a vertically movable central stage within a 7mm × 7 mm footprint. The individual spring arms are of 200 μm width and 50 μm thickness. An NdFeB magnet (dimension 2mm × 2mm × 2mm) with its magnetization directed vertically is bonded to the central stage and suspended by the four spring arms. The square-shaped double-layer copper micro-coil is fabricated on a 500 μm thick silicon substrate within an area of 2.8mm × 2.8mm and has 132 turns. The electromagnetic transducing mechanism is implemented by positioning the spring-supported magnet above the coil such that most of the magnetic flux passes through the coil area. As illustrated in Figure 6.11, the frequency tuning mechanism is incorporated by another magnet positioned at an appropriate height from the transducing magnet with opposite polarity, such that the transducing and tuning magnets interact repulsively. The distance between the tuning and transducing magnets can be adjusted by a screw-mechanism.
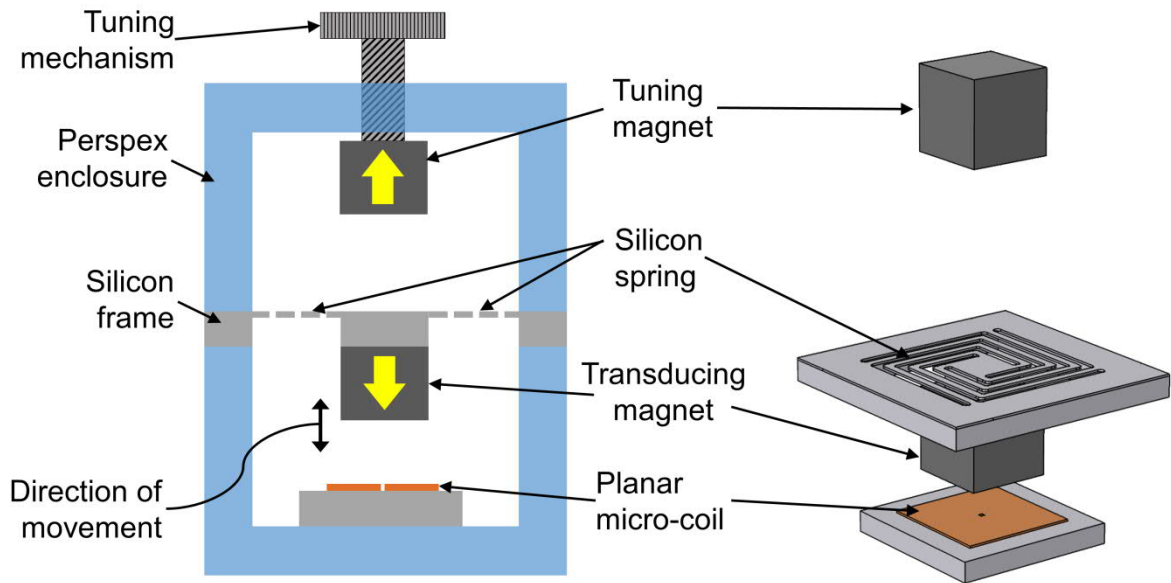
Figure 6.11: Structure of the magnetically tunable MEMS nonlinear VEH comprising of silicon spring, NdFeB magnets and planar micro-coil.

In the absence of the tuning magnet, the gap between the bottom surface of the transducing magnet and the top surface of the planar micro-coil is 1.6 mm. As the tuning magnet is incorporated with opposite polarity to that of the transducing magnet, the force of magnetic repulsion pushes the transducing magnet downward, effectively reducing the gap between the transducing magnet and the micro-coil. By adjusting the vertical distance between the tuning magnet and the silicon spring frame through the screw-mechanism, the degree of repulsive magnetic interaction and the magnitude of repulsive force can be adjusted. The distance between the tuning and transducing magnets are related to the force of repulsion and the stiffness coefficient of the spring. Therefore, the vertical displacement of the transducing magnet also deflects the spiral silicon spring vertically, and changes the linearized stiffness coefficient significantly. In this particular device, the stiffness of the silicon spring increases with deflection under magnetic repulsion, and the resonant vibration peak is shifted to higher frequencies. The entire device including the transduction assembly, tuning magnet and screw-mechanism are enclosed in a Perspex frame.

6.2.2 Numerical modelling and simulation

FEA simulation tools are used to determine the vibrational modes in the silicon spring structure and the electromagnetic coupling factor in the transducing magnet-coil assembly. The primary mode of vibration of the designed spiral spring structure depends on the location of different modal frequencies in the vibration spectrum and the direction of the

applied excitation relative to the spring. The first four fundamental modes of vibration of the spring structure are shown in Figure 6.12. The first two modes (176.9 Hz and 176.92 Hz) are combinations of lateral and torsional (with axis along the spring plane) motion of the equivalent mass and are identical in nature due to the structural symmetry in the spring topology. The third mode (201.53 Hz) is a vertically oriented out-of-plane translational motion normal to the plane of the spring. This is the intended primary vibration mode and produces the maximum relative displacement between the coil and the transducing magnet. The fourth mode (1675.42 Hz) is a torsional motion with its axis along the normal to the spring-plane. Since the mode III is the intended vibration mode, the vibrational excitation supplied during experimental studies are oriented along this direction (i.e. out-of-plane) only. However, imperfections introduced during the manual assembly of the prototype may create microscopic asymmetries in the device structure, which can potentially contribute to distribution of the applied vibration force into components that might excite vibrational modes other than mode III.

(a) Mode I : 176.9 Hz

(b) Mode II : 176.92 Hz

(c) Mode III : 201.53Hz

(d) Mode IV : 1675.42 Hz
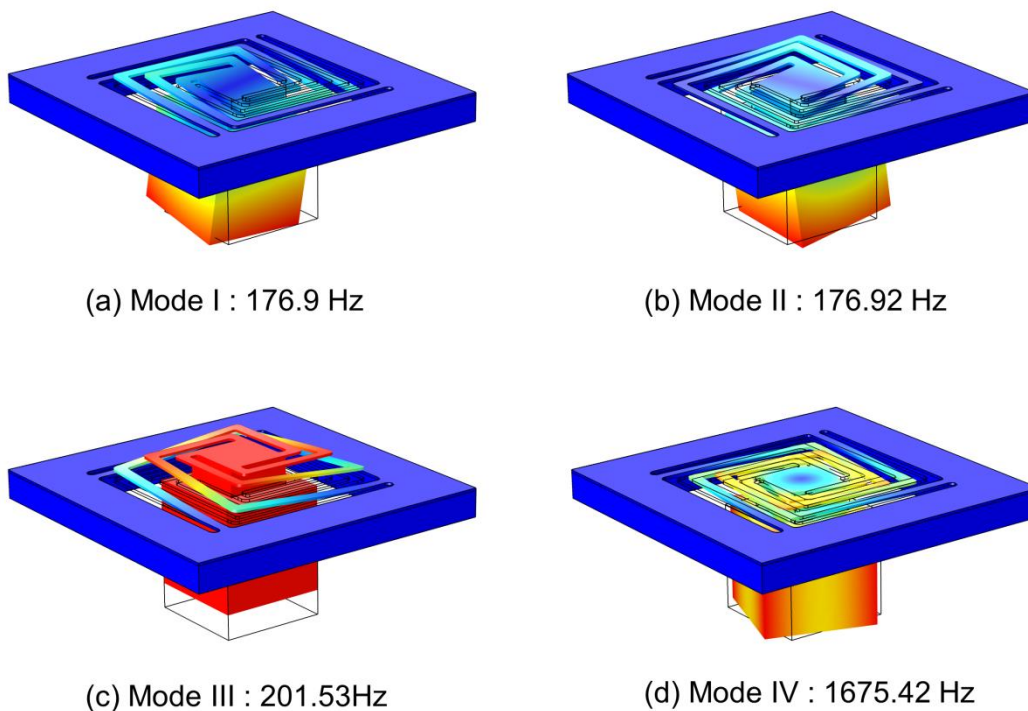
Figure 6.12: The first four fundamental modes of the micro-EMVEH. (a, b) Modes I and II are combination of lateral and torsional motion. (c) Mode III is a translational motion normal to the plane of the spring. (d) Mode IV is a torsional oscillation with axis normal to the plane of the spring.

An experimental frequency sweep of the external vibration in the vertical direction (i.e. along the oscillation direction of mode III) can excite the different vibrational modes at their respective frequencies, which can be discerned from the resulting frequency response. The distributions of the magnetic flux density at different stages of a typical oscillation cycle are studied using COMSOL MultiPhysics (Figure 6.13). This study reveals both the variation of the repulsive magnetic force between the transducing and tuning magnets, and the variation of the magnetic flux linkage between the transducing magnet and the planar coil. While the tuning magnet is assumed to be fixed at a certain height from the coil base, the transducing magnet is allowed to move along the vertical direction along a line connecting the centres of the magnets and the planar coil. Initially, the transducing magnet is positioned very close to the micro-coil at a height of 0.1 mm from coil base. It can be observed from Figure 6.13 that a significant amount of the magnetic flux intersects the coil, and produce the maximum magnetic flux linkage. At this position, the distance between the transducing and tuning magnets is maximum, and the magnetic repulsion force is the smallest.
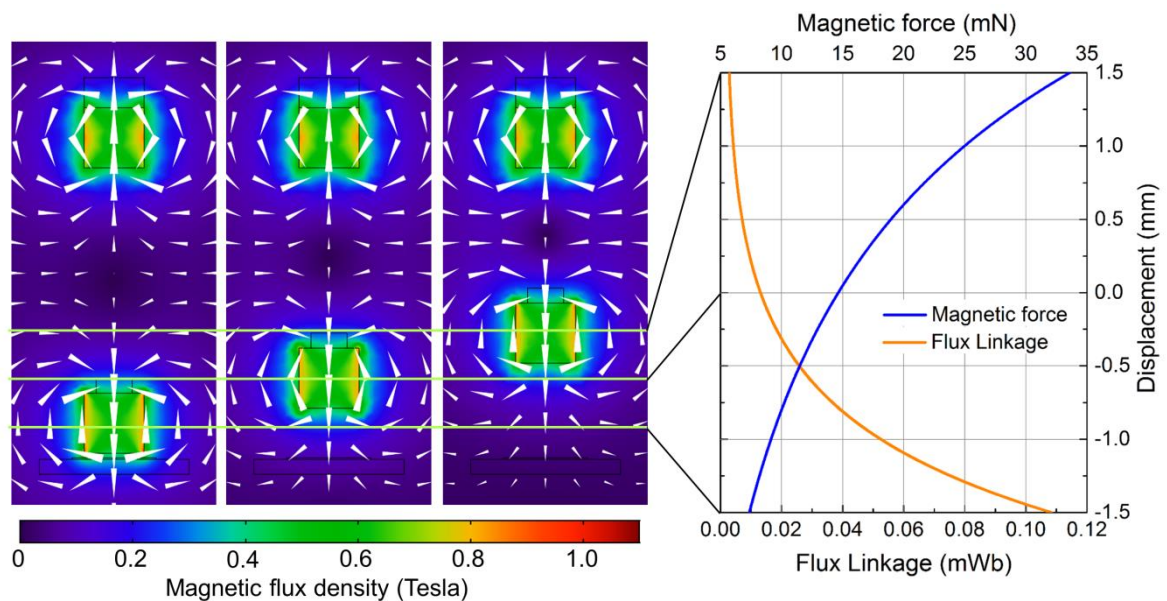
Figure 6.13: Magnetic flux distribution at different positions of the transducing magnet ($z = −1.5$mm, 0 mm, +1.5 mm). Magnetic field directions are denoted by white arrows. The magnetic flux linkage through the coil varies exponentially, while the magnetic force decreases with distance from the coil.

During an oscillation cycle, as the transducing magnet moves vertically upward and away from the coil plane, the magnetic flux intersecting the coil decreases, and reaches a minima as the transducing magnet ascends to a maximum height. Simultaneously, the vertical

distance between the transducing and tuning magnet pair decreases, and the magnetic repulsion force between them increases considerably. This limits the upward movement of the transducing magnet in combination with the spring restoration force. A numerical model is developed in order to analyse the effect of magnetic tuning on the potential energy and stiffness profile of the micro-EMVEH. The developed one-dimensional model is based on the magnetic dipole-dipole interaction, forced vibration formulae and electrical circuit theory. The application of magnetic force alters the potential energy and stiffness profiles of mechanical structures, leading to the shift in the inherent linearized resonant frequency. Considering the magnetic dipole-dipole interaction, the potential energy between two oppositely polarized cuboidal magnets can be represented by the simplified mono-dimensional expression given by [Furlani [11], Podder, et al. [2]],

$$U_m(z) = \frac{\mu_0 m_1 m_2}{2\pi(d-z)^3} \qquad 6.1$$

where m_1 and m_2 are the magnetic moments of the repulsively positioned magnetic dipoles, μ_0 is the permeability of air, d is the initial distance between the magnetic dipoles and z is the displacement due to oscillation of the dipole m_1. The total mechanical potential energy including contributions from the linear and nonlinear stiffness of a generalized Duffing oscillator and the magnetic interaction potential is given by,

$$U(z) = \frac{1}{2}k_1 z^2 + \frac{1}{4}k_3 z^4 + \frac{\mu_0 m_1 m_2}{2\pi(d-z)^3} \qquad 6.2$$

where k_1 and k_3 are the linear and nonlinear cubic stiffness coefficients respectively. The corresponding restoring force can be obtained by differentiating $U(z)$ as given below,

$$F_R(z) = -\frac{\partial}{\partial z}U(z) = -k_1 z - k_3 z^3 - \frac{3\mu_0 m_1 m_2}{2\pi(d-z)^4} \qquad 6.3$$

Figure 6.14 (a) and (b) shows the variation in the potential energy and restoring force profiles due to changing gap distances between the tuning magnet (dipole moment m_2) and the silicon spring frame. At large initial d, the repulsive interaction between the transducing and tuning magnetic dipoles is negligible, and the potential energy and restoring force profiles represents that of a nonlinear cubic Duffing oscillator.
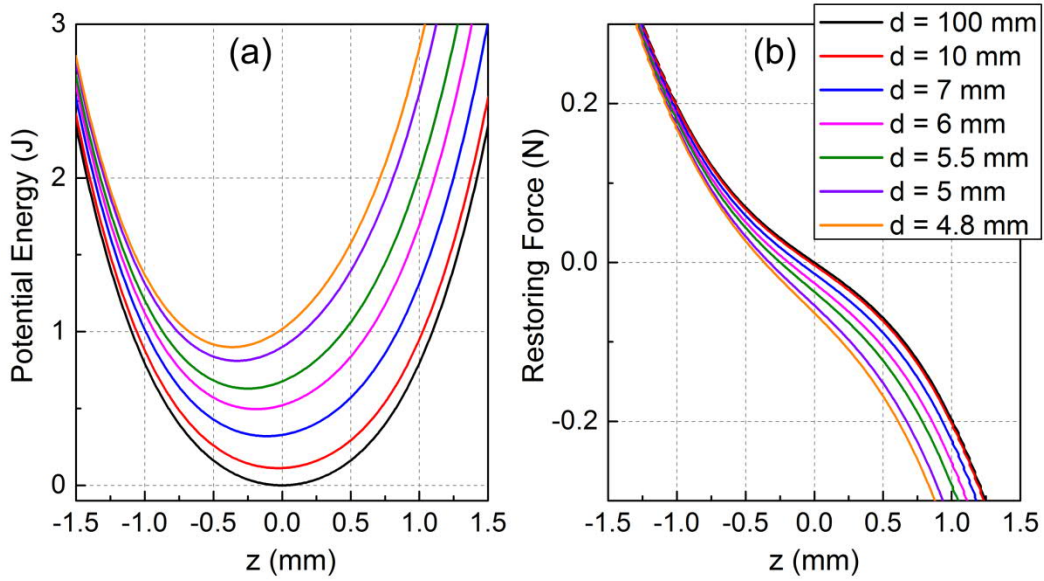
Figure 6.14: (a) Variation of the potential energy and (b) restoring force with _d_

As the gap (_d_) between the transducing and tuning magnets are decreased, the repulsive force on the transducing magnet increases, leading to a downwards deflection (z_0) of the movable central paddle supported by the spiral spring (Figure 6.15 (a)). The deflection in the spiral spring, in combination with the increased magnetic repulsion, results into substantial modification in the symmetric potential energy and restoring force profiles as they are transformed into asymmetric ones (Figure 6.14 (a) and (b)). The asymmetric potential energy and restoring force profiles also lead to an increment in the linearized stiffness coefficient (k_1'), where,

$$k_1'(d) = \left[-\frac{\partial}{\partial z} F_R(z) \right]_{z=z_0} \qquad\qquad 6.4$$

where z_0 represents the deflection of the central paddle with respect to the silicon frame [Figure 6.15 (a)]. These modifications in the potential energy and stiffness lead to shifting the linear resonant frequency (f_0') towards higher values [Figure 6.15 (b)]. Therefore, the operational frequency of the VEH device can be modified or tuned by controlling the distance between the tuning and transducing magnets. The variation of the deflection (z_0), linear spring stiffness (k_1') and linearized resonance frequency (f_0') with the gap _d_ are illustrated in Figure 6.15 (b).
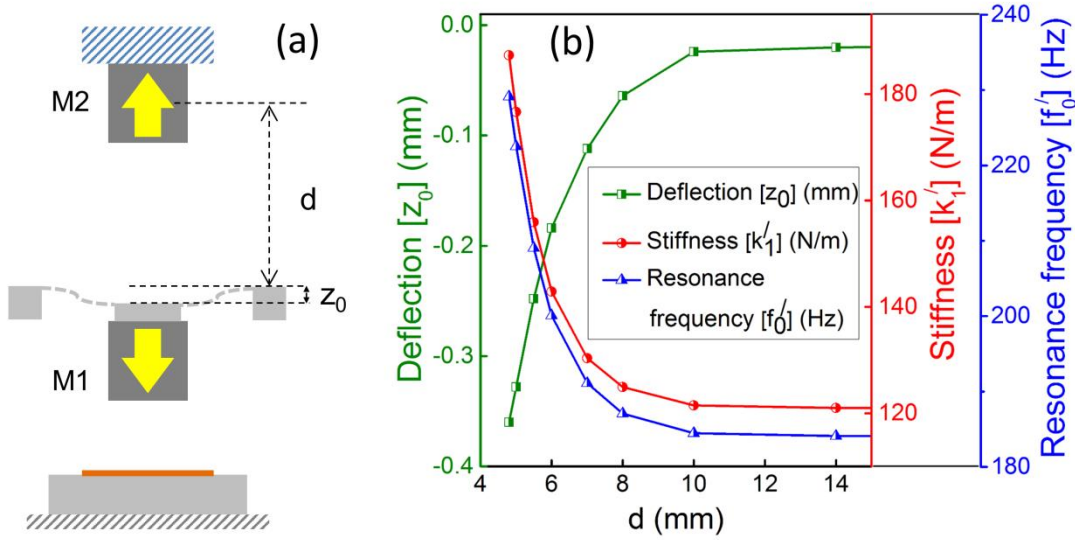
Figure 6.15: With decreasing the gap between the repulsively positioned magnets M1 and M2, the equilibrium (zero force) position is lowered (a), while the stiffness and linearized resonance frequency is increased (b).

The complete mono-dimensional dynamical equation of the system can be represented as,

$$M\ddot{z} + k_1 z + k_3 z^3 + \frac{3\mu_0 m_1 m_2}{2\pi(d-z)^4} + D\dot{z} + \gamma I = -M\ddot{y} \qquad 6.5$$

where M is the equivalent oscillating mass, D is the mechanical damping factor, γ is the electromagnetic coupling factor between the transducing magnet and coil, I is the current induced in the coil and $y = Y_0 \sin \omega t$ is the displacement of the entire system imparted by the sinusoidal vibrational excitation. If the total resistive load combining the coil resistance (R_C) and the load resistance (R_L) in the electrical circuit is denoted by R, the electrical circuit can be represented as [[12], [2]] ,

$$L\dot{I} + RI = \gamma\dot{z} \qquad 6.6$$

where L denotes the inductance of the coil. Eq. (6.5) and (6.6) are solved numerically using explicit fourth-order Runge-Kutta method in MATLAB to obtain the load voltage (V_L) and load power (P_L) generated in the system, which are expressed as,

$$V_L(t) = \gamma\dot{z} \left[\frac{R_L}{R_L + R_C} \right] \qquad 6.7$$

and,

$$P_L(t) = \frac{V_L(t)^2}{R_L} \qquad 6.8$$

where R_C and R_L represent the coil resistance and the load resistance respectively. The input mechanical power can be estimated as,

$$P_M = Force \times Velocity = Ma\dot{z}$$

6.9

where a denotes the acceleration due to applied external vibration, which remains constant during a particular frequency sweep. The efficiency (η) of conversion of mechanical power to electrical power can be estimated as,

$$\eta = P_L/P_M$$

6.10
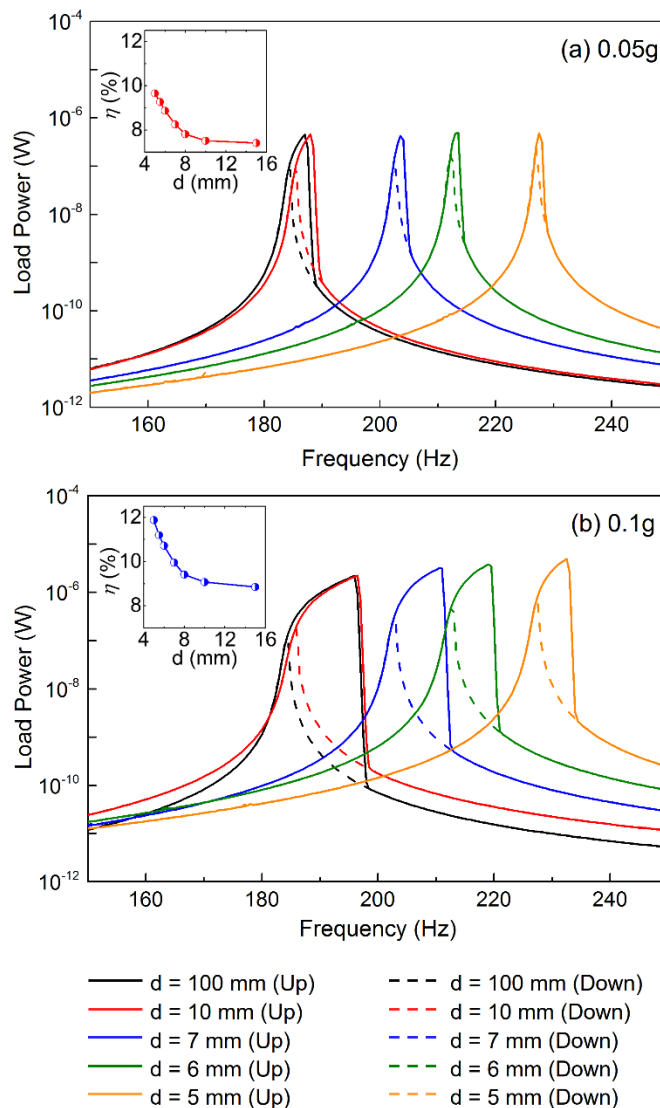
Figure 6.16: Numerically simulated load power vs. frequency plots for (a) 0.05g and (b) 0.1g acceleration.

The numerical frequency sweep responses (Figure 6.16 (a), (b)) show that with increasing acceleration, higher power is generated and the effect of cubic Duffing nonlinearity

become more prominent, which is manifested by the broadening hysteresis. Furthermore, with decreasing d, the forward sweep and reverse sweep jump frequencies shift towards the higher frequencies, which validate the frequency tuning effect of adjustable magnetic repulsion on the micro-EMVEH. In addition, the efficiency of power conversion (η) is observed to be increasing with decreasing d. This phenomenon can be attributed to the fact that with smaller d the effective gap between the transducing magnet and coil plane become smaller, leading to increment in the magnetic flux linkage gradient and moderate enhancement in the harvested power level.
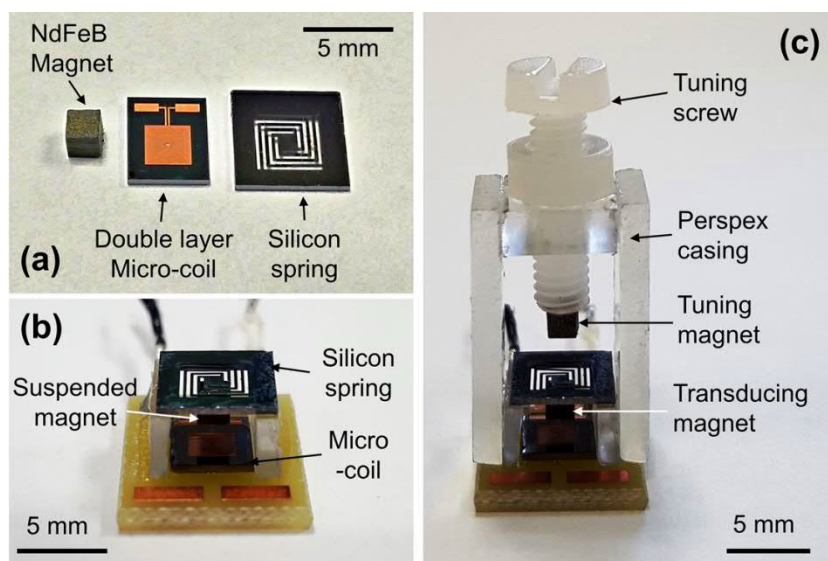
Figure 6.17: (a) The principal components of the micro-EMVEH: NdFeB magnet, double-layer planar micro-coil, and spiral silicon spring, (b) The transducer comprising the NdFeB magnet suspended by the silicon spring above the micro-coil. (c) The assembled tunable micro-EMVEH enclosed within Perspex casing; The tuning magnet is attached to the tuning screw such that it repulsively interacts with the transducing magnet.

6.2.3 Fabrication of magnetically tunable MEMS micro-power generator

The silicon springs and the double-layer micro-coils are micro-fabricated using the process flow similar to that described in section 6.1.2. Two Perspex spacers are positioned in between the coil and frame of the spring such that the vertical gap between the micro-coil plane and the magnet is 1.6 mm. However, in order to incorporate the magnetic force tunability in the device structure, a second tuning magnet is positioned above the transducing magnet. The tuning magnet is positioned in repulsive orientation with the transducing magnet and its position can be adjusted by means of screw-mechanism. This

mechanism allows for the tuning of the vibration frequency of the transducing magnet suspended from the silicon spring.

6.2.4 Experimental results and discussions

Test set-up and load optimization

The experimental set up comprises a computer controlled electromagnetic shaker (LDS V455) with an accelerometer (DeltaTron 4517-002) feedback, power amplifier (LDS PA 1000L) and oscilloscope (Picoscope 3000 series), as shown in Figure 6.18 (a). The device and the electrical loads are enclosed within a ground-connected aluminium box to minimize the effect of external electromagnetic noise on the device output. The grounded aluminium box including the device and load resistances are mounted on a vibrating stage attached to the shaker capable of generating oscillatory motion in the vertical direction. In the experiments the vibration frequency of the shaker is swept in the forward (150Hz – 250Hz) and reverse (250Hz – 150Hz) directions, while the peak-peak acceleration imparted by the shaker is maintained at a fixed value.

In order to determine the optimum resistive load for the VEH device, the device is operated in the linear regime (at low acceleration, 0.025g) at the resonance frequency (188.5 Hz) while the load is varied.
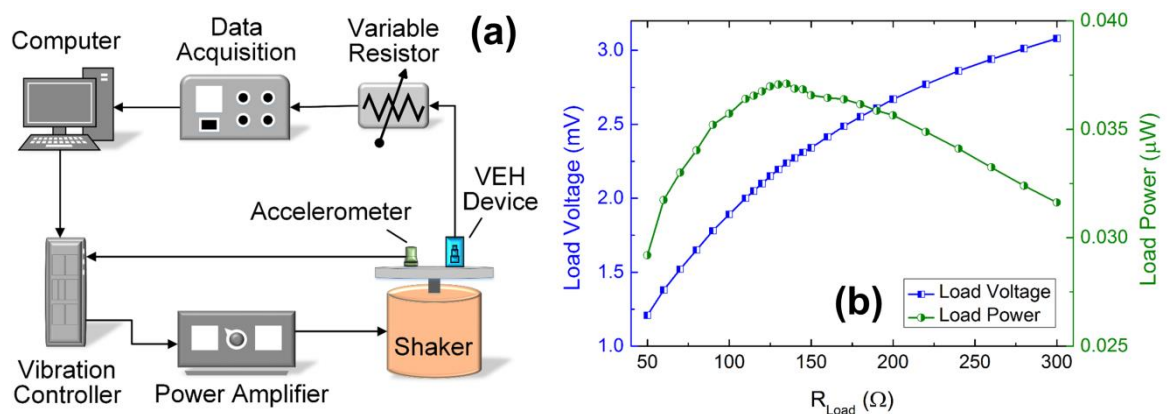
Figure 6.18: (a) Experimental vibration test set-up, (b) Variation of load voltage and load power with load resistance at *d* = 10 mm and 0.025g acceleration. The optimum load resistance is 135 Ω.

The coil type 3 [Table 6.1], with 130 turns and 132 Ω resistance was used in the tested prototype. The maximum load power of 36.6 nW at 0.025g is generated across an optimum

resistive load of 135 Ω [Figure 6.18 (b)]. The experimentally determined optimum load is very close to the resistance value of the planar micro-coil, which indicates that the electromagnetic damping factor is very small in comparison to the parasitic mechanical damping. Subsequently, 135 Ω is used as the load resistance for the remaining experiments.

Effect of increasing acceleration on frequency response

The effect of increasing the vibrational acceleration on the frequency response is shown in Figure 6.19. At low accelerations (0.025g) the response is similar to that of a linear oscillator, with a sharp peak at 188.5 Hz. At higher applied accelerations (0.05g – 0.125g), the deflection of the spiral spring becomes gradually larger. In this condition the spiral spring behaviour is dynamically analogous to that of a clamped-guided cantilever, where the four spring-arm ends anchored to the frame are clamped and the spring-arm ends concurring at the vertically movable central stage are constrained to move vertically. This configuration triggers stretching strain in addition to the bending of the spring-arms at large deflections and result into a nonlinear cubic deflection-stiffness relationship [[12], Marinkovic and Koser [13], Liu, et al. [14]]. Therefore, with higher applied acceleration, the spectral response of the device gradually moves into the nonlinear regime, effectively tilting the hysteretic frequency responses towards the higher frequencies and results in hardening spectral responses. The resulting hardening frequency responses exhibit distinctive features such as a hysteresis region, bounded by the forward and reverse sweep jump frequencies. Therefore, as depicted in Figure 6.19, with increasing acceleration, harvested power become larger and the hysteresis region widens, effectively broadening the high energy branch of the spectral response. In addition, smaller peaks (< 10 nW) appear at lower frequencies (169 Hz) that corresponds to mode I and II (torsional modes) of vibration as illustrated in Figure 6.12. This implies the existence of microscopic asymmetries in the device structure, which could have been introduced during manual assembly of the transducing magnet and silicon spring.
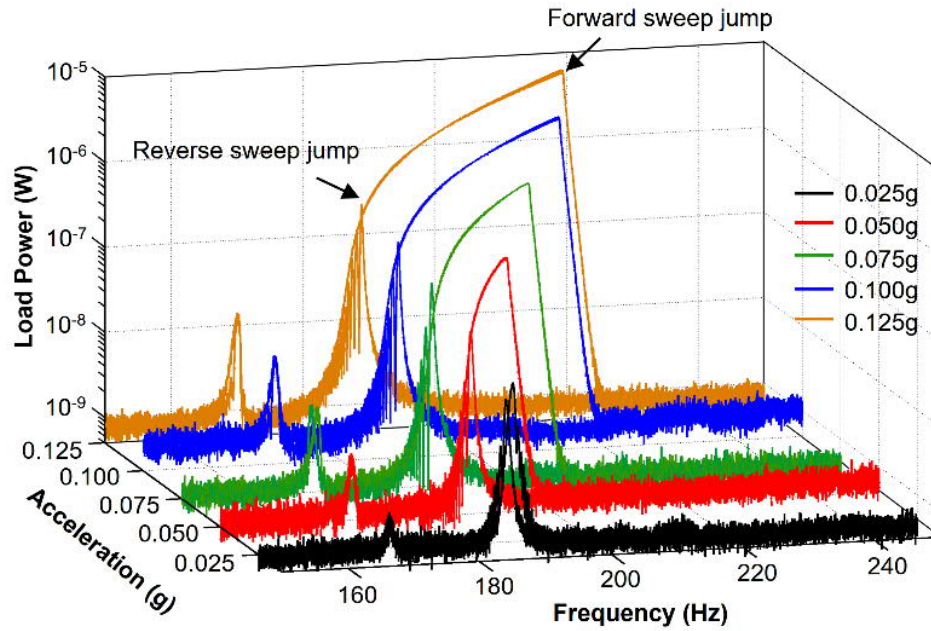
Figure 6.19: Variation of frequency responses with vibrational acceleration at *d* = 100 mm. The forward sweep jump frequency increases with acceleration, broadening the hysteresis region.

Effect of magnetic repulsion on frequency response

The magnetic repulsion force acting on the spiral silicon spring due to the interaction of the transducing and tuning magnets can be controlled by adjusting their separation through the screw-mechanism. The variations in the magnetic repulsion force on the spring leads to significant variation in the potential energy profile and the underlying linear and nonlinear stiffness of the micro-energy harvester. The effect of varying magnetic repulsion on the spectral response of the micro-EMVEH is studied by varying the vertical distance (*d*) between the tuning magnet and the frame of the silicon spring in discrete steps of 10mm, 8mm, 7mm, 6mm and 5mm, while the tuning and transducing magnets are repulsively oriented. The vibrational acceleration is also varied in steps (0.025g, 0.05g, 0.075g, 0.1g, 0.125g), while the frequency is swept linearly with time in both forward and reverse directions.
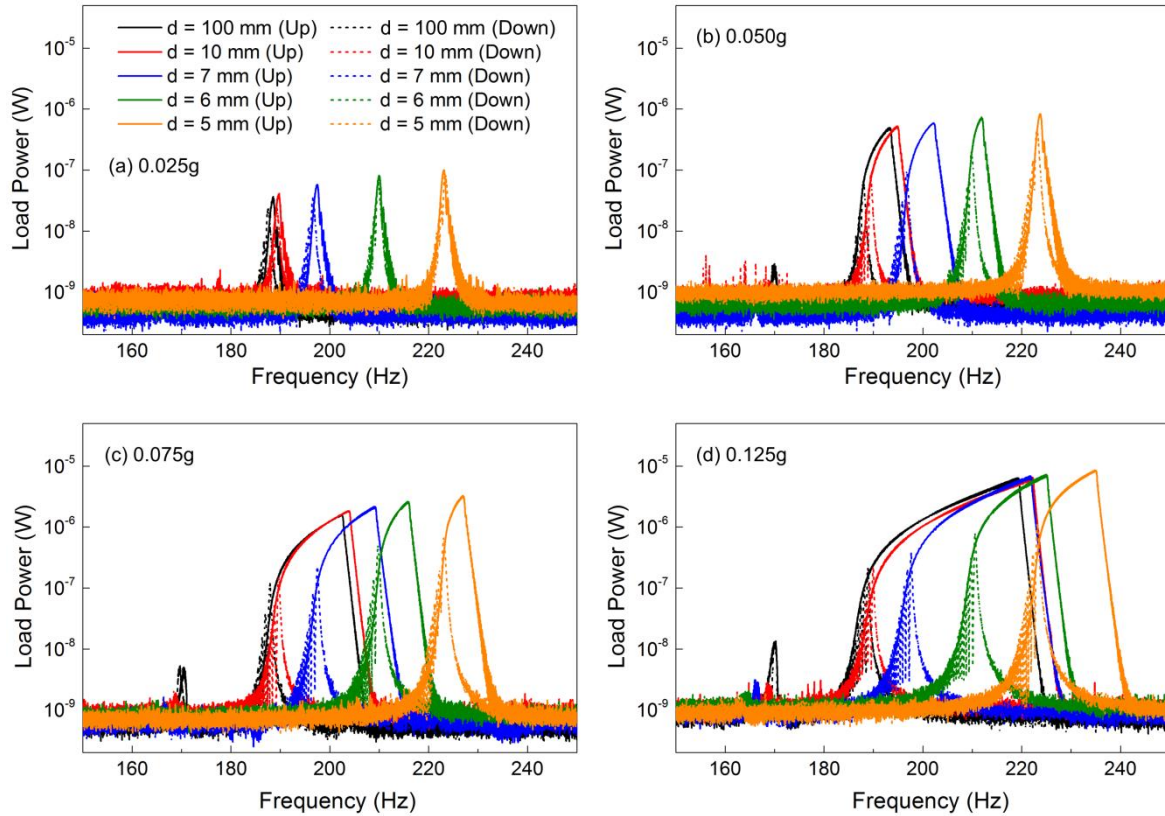
Figure 6.20: Variation of frequency responses with vibrational acceleration and gap distance _d_ between the transducing and tuning magnets.

The resulting frequency sweep responses at the lowest accelerations (0.025g) exhibit shifting of the linear resonant peaks to higher frequencies with decreasing _d_ (Figure 6.20). At higher applied accelerations, the repulsively induced spring hardening (due to decreasing _d_) results into shifting of both the forward and reverse sweep jump frequencies towards the higher range, effectively shifting the entire high energy branch and changing the hysteretic frequency width. It can be observed from Figure 6.20, that both the linear resonant and the nonlinear hardening responses are shifted towards the higher frequencies with decreasing _d_. Therefore, the magnetic repulsion induced frequency tuning mechanism can be effective on both the linear and nonlinear frequency responses. It is also illustrated in Figure 6.20 that the hysteresis region becomes narrower with decreasing _d_, i.e. stiffening spring. At the largest gap (_d_ = 100 mm) between the top magnet and the transducing magnet, smaller peaks at lower frequencies (169 Hz) can be observed for all accelerations. The origin of these peaks can be found in the first two vibrational modes which are combinations of lateral and torsional oscillations, and occurs at frequencies 176.9 Hz and 176.92 Hz respectively in the FEA simulations (Figure 6.12). This mode of vibration is weak in the applied vertically oriented out-of-plane vibration scenario and produces

negligibly small power of 6.55 nW. Furthermore, with decreasing d, the distance between the tuning magnet and the suspended transducing magnet is also reduced and the magnetic repulsion increases. The increased magnetic repulsion suppresses the combined lateral and torsional oscillation of the first vibrational modes, effectively leading to disappearance of the first peak from the frequency response (Figure 6.20).

Further analysis of results and discussion

The experimental results exhibit significant variation in the forward and reverse sweep jump frequencies, hysteresis width and peak power level over the frequency range due to different vibrational acceleration and the alteration of the distance (d) between the tuning magnet and silicon spring frame. Figure 6.21 (a) shows the variation in the peak power frequency and the forward and reverse sweep jump frequencies with acceleration and the gap d. It exhibits that the amount of shift in the peak power frequency (i.e. the forward sweep jump frequency) is maximum at the lowest acceleration level (0.025g), where the device oscillates with small amplitude in the linear regime. The shift in peak power frequency achieved in this configuration is almost 35 Hz, which is ~19% of the initial frequency (188 Hz). As the applied acceleration is increased for a particular value of d, the oscillation amplitude increases, and the cubic Duffing nonlinearity become obvious due to the stretching in the spiral spring arms. Therefore, the frequency response exhibits hysteretic properties, where the entire response is tilted towards the high frequencies with distinctive forward and reverse sweep jumps.

As d is decreased in steps, the magnetic repulsion force on the spring increases and the linearized stiffness coefficient increases, resulting in enhancement in the peak power frequency. At the smallest d, the spring stiffness is maximum, and consequently the forward sweep jump also occurs at the maximum frequency. For the smallest d, the relative change in jump frequency is almost 7.6% over that with the largest value of d. The dependence of forward and reverse sweep jump frequencies on the gap distance d and the applied acceleration is illustrated in Figure 6.21 (b). It shows that although the reverse sweep jump frequency increases with decreasing d, it remains fairly unchanged with increasing acceleration.
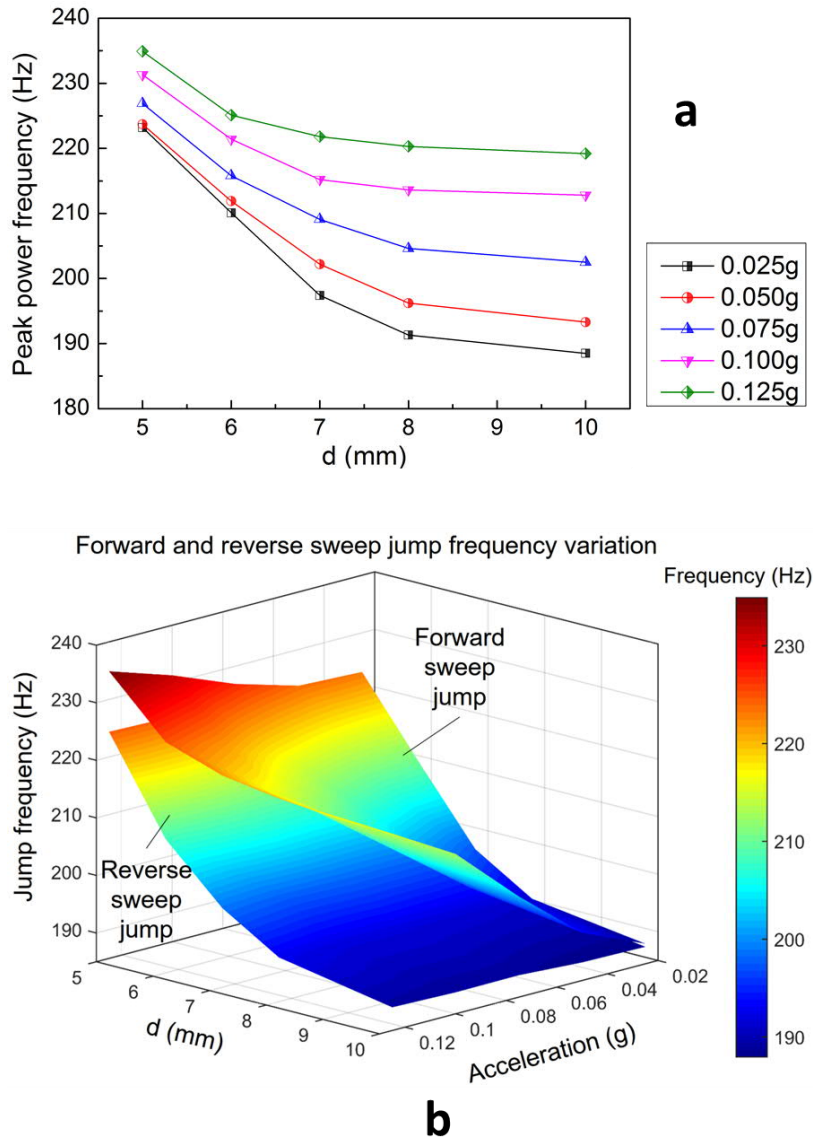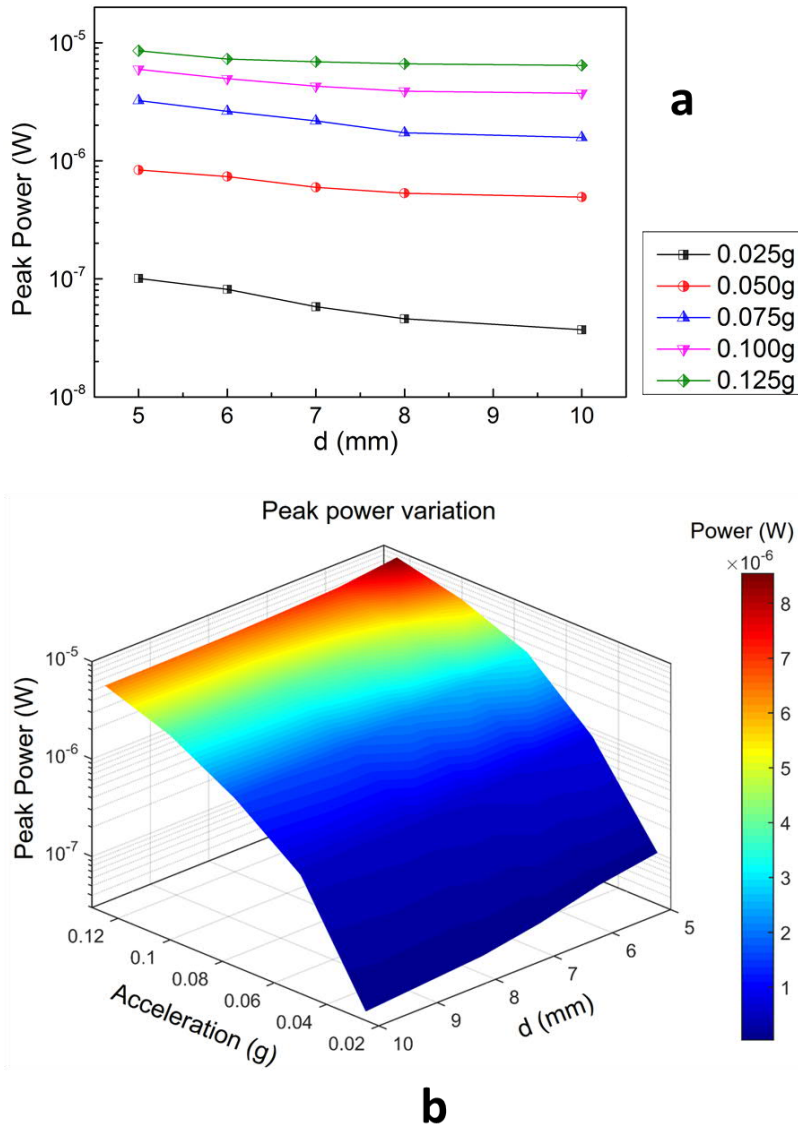
Figure 6.21: (a) Variation of Peak power frequency with *d* for different accelerations. (b) Dependence of forward and reverse sweep jump frequencies on *d* and applied vibrational acceleration.

Width of the hysteresis region in a frequency sweep often indicates the nonlinearity of the oscillator. Figure 6.22 (a) shows that the width of the hysteresis region keeps decreasing with decreasing *d* for a fixed acceleration. This effect can be attributed to the fact that as the spring stiffens due to increased magnetic repulsion at smaller *d*, the linear spring coefficient (k_0') increases significantly, while the nonlinear spring coefficient (k_3) remains unchanged [Figure 6.20].
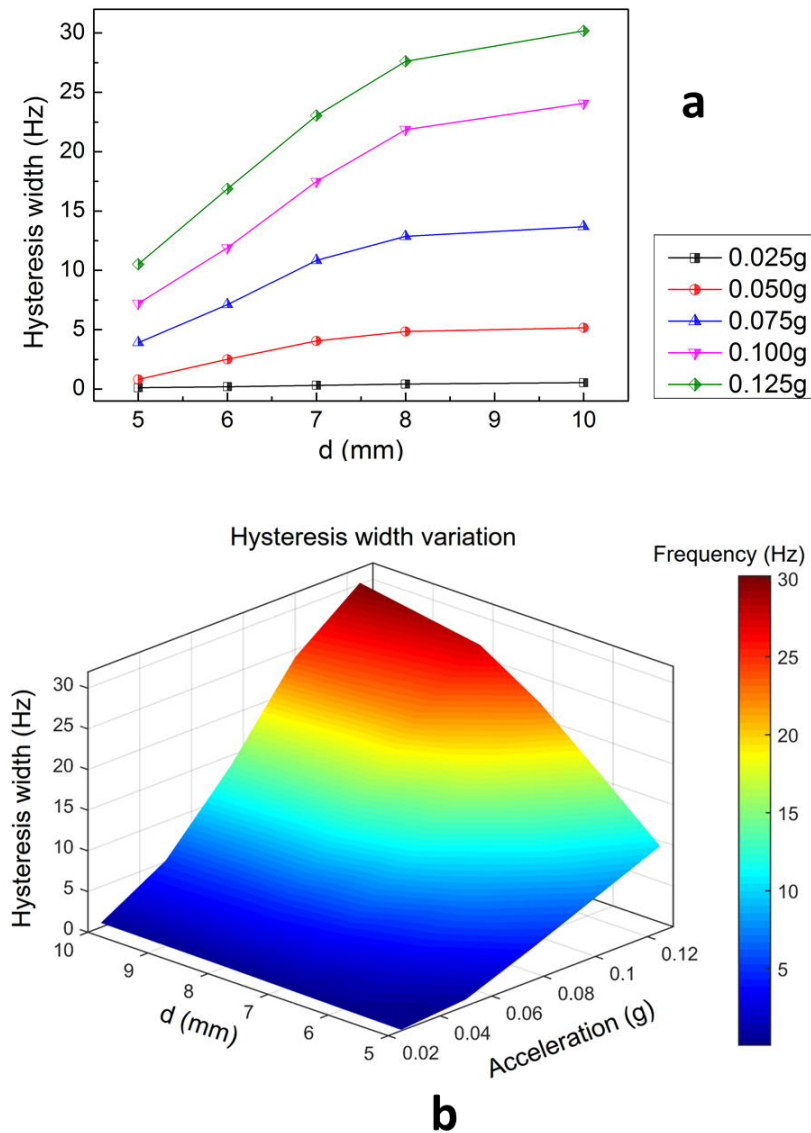
Figure 6.22: (a) Variation of the width of the hysteresis region in the frequency sweep with *d* for different accelerations. (b) Dependence of the width of the hysteresis region on *d* and applied vibrational acceleration.

Therefore, with reduced relative contribution from the dynamical nonlinearity, the resulting frequency response approaches the linear resonant type with gradually decreasing width of the hysteresis region. Figure 6.22 (b) shows that the hysteresis increases with increasing acceleration, due to the increased nonlinearity at larger amplitude of oscillation. The peak load power increases significantly (e.g. 165% at 0.025g, 32.8% at 0.125g) with decreasing *d* even at constant accelerations Figure 6.23 (a). The enhanced peak power level with decreasing *d* is attributable to the increased magnetic flux linkage between the coil and transducing magnet as the equilibrium position of the suspended transducing magnet is shifted proximally to the coil with increasing repulsion force due to the tuning magnet.

Figure 6.23: (a) Variation of peak load power with _d_ for different accelerations. (b) Dependence of peak load power on _d_ and applied vibrational acceleration.

Furthermore, the peak load power level predictably increases with the increasing vibrational accelerations (Figure 6.23 (b)).

The spectral power integral or the total harvested power from the high energy branch (i.e. power integral over the hysteresis region ($\int_{f_1}^{f_2} P \, df$, where f_1 and f_2 are the reverse and forward sweep jump frequencies respectively) is reduced gradually due to the reduction in width of the hysteresis region (Figure 6.24 (a)).
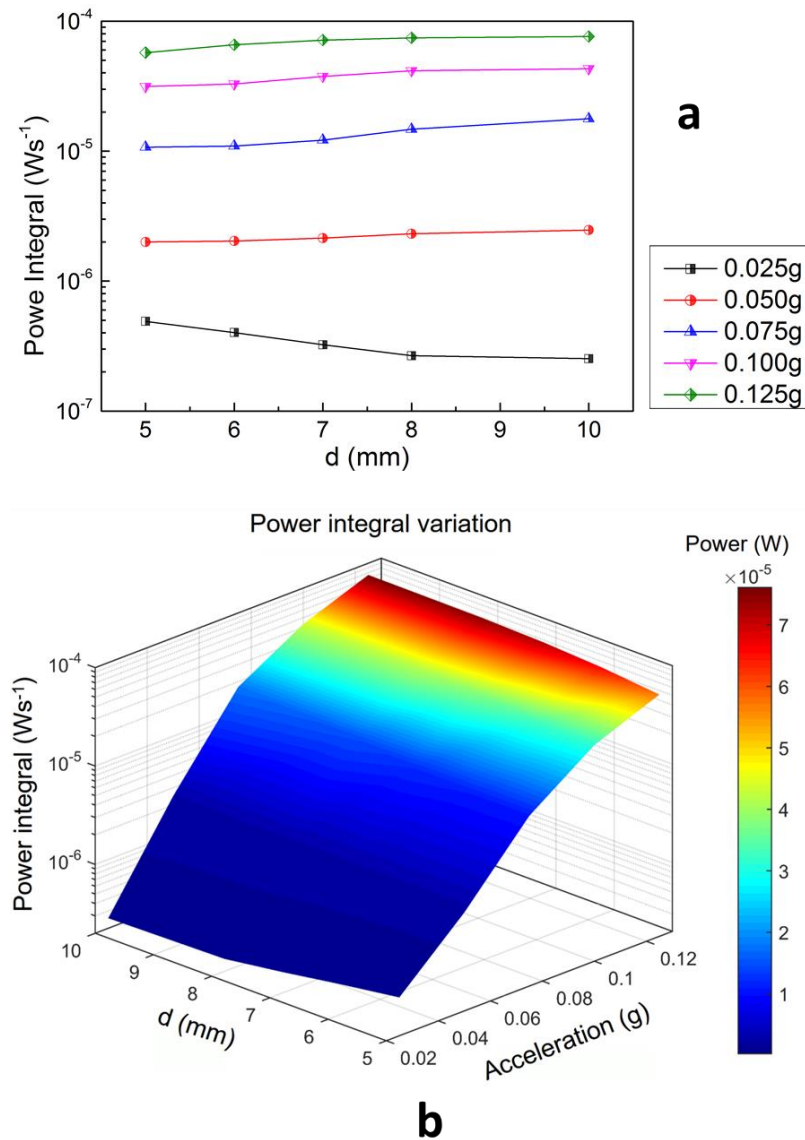
Figure 6.24: (a) Variation of spectral power integral with *d* for different accelerations. (b) Dependence of spectral power integral on *d* and applied vibrational acceleration.

At the maximum applied acceleration of 0.125g, for *d* = 10 mm the maximum power harvested by the VEH device is 6.43 μW, and the half power bandwidth is 11.86 Hz. At the same acceleration for *d* = 5 mm the maximum power is 8.45 μW, while the bandwidth is reduced to 7.49 Hz. Therefore, by varying the distance *d*, the peak power level, hysteresis width and the operational bandwidth of the device can be altered to suit specific application scenarios.

This tuning methodology for micro-scale devices can be exploited for vibrational energy harvesters with other transduction mechanisms (i.e. piezoelectric, electrostatic, triboelectric etc.) and can be deployed for customizable tuning of pre-fabricated micromechanical oscillators. The developed prototype has been subject to moderate level of mechanical

vibrations (<0.2g) for extended periods of time (several weeks), without any observable degradation in performance. However, at higher excitations (>0.3g) the oscillating mass may collide with the bottom coil plane, which can eventually lead to deterioration in both the coil and the spring structure. Therefore, it is advisable not to expose the device to high vibration environment for a prolonged period of time.

A button-cell (SR66) of a size (diameter 6.8 mm, height 2.6 mm) similar to the MEMS energy harvester presented in this chapter contains approximately 24 mAh (129.6 J). At the peak harvested power level (8.45 µW), the proposed MEMS harvester will take approximately 178 days to generate the same amount of energy.

Table 6.2: Comparison of the MEMS energy harvesters. ES: Electrostatic, PZ: Piezoelectric, EM: Electromagnetic

Reference/ Transduction	Equivalent mass [kg]	Acceleration [m/s^2]	Frequency [Hz]	Bandwidth [Hz]	Average Power [W]	FOM$_{VEH}$
Le and Halvorsen [3], P1/ ES	2.8×10^{-3}	55	1220	300	5.1×10^{-8}	1.21×10^{-12}
Le and Halvorsen [3], P2/ ES	1.2×10^{-3}	3.1	670	140	1.05×10^{-8}	2.84×10^{-10}
Basset, et al. [4]/ ES	6.6×10^{-5}	10	162	40	1.6×10^{-6}	3.69×10^{-7}
Jia and Seshia [7]/ PZ	1.2×10^{-5}	0.65	196	1.1	9.4×10^{-7}	5.47×10^{-7}
Marinkovic and Koser [13]/ PZ	9.3×10^{-6}	43	400	240	5.5×10^{-7}	4.8×10^{-8}
Defosseux, et al. [15]/ PZ	3.1×10^{-6}	0.06	214	0.8	1.9×10^{-8}	3.2×10^{-5}
Liu, et al. [14]/ EM	1.2×10^{-5}	30	82	64.5	0.9×10^{-9}	8.6×10^{-10}
Liu, et al. [16]/ EM	1.4×10^{-4}	10	840	16	7.7×10^{-8}	1.2×10^{-10}
Han, et al. [17]/ EM	3.9×10^{-6}	12	48	15	6.4×10^{-8}	7.5×10^{-7}
This work/ EM	6.3×10^{-5}	1.25	188	35	4.2×10^{-6}	4.3×10^{-5}

Table 6.2 presents a list of some of the MEMS energy harvesters reported in literature and compares the harvested power, bandwidth and the non-dimensional figure of merit (FOM$_{VEH}$), as introduced in Chapter 4 (Eq. 4.42). The nonlinear tunable MEMS device exhibits a high FOM$_{VEH}$ primarily due to high power output under relatively low acceleration, and a moderate frequency tuning range. The post-fabrication frequency tuning mechanism incorporated in this device enables the device to operate over a frequency range of 180 − 250 Hz, which is suitable for application in aircraft vibrations, industrial machines and motors, urban infrastructures (e.g. bridge) etc.

6.3 Conclusions

This chapter described the development of a silicon based nonlinear MEMS electromagnetic vibration energy harvester and demonstrated the effect of magnetic repulsion induced frequency tuning on the prototype device. In the first section the device comprising a spiral-shaped suspension spring and the double-layer planar micro-coils is fabricated using standard MEMS fabrication process. An NdFeB permanent magnet is attached to the spring and transduces the mechanical vibration into electric potential induced in the proximally located micro-coil. The spectral response shows moderately nonlinear response at low accelerations, which increases significantly with increasing acceleration. The nonlinear response is combined with mechanical impact due to large amplitude oscillation at higher accelerations, and produced broader bandwidth. The next section demonstrates the magnetically induced spring stiffness tuning effects in the MEMS-scale vibration energy harvester employing electromagnetic transduction. In order to incorporate frequency tunability, a second NdFeB magnet with opposite polarity to the transducing magnet is positioned at an adjustable distance from the transducing magnet. The adjustable repulsive interaction between the transducing and tuning magnets result into substantial transformation in the potential energy and stiffness profiles of the silicon spring, leading to tuning of the frequency response of the VEH device. The spring structure exhibits linear and nonlinear hardening responses at low and high accelerations respectively. It has been demonstrated that both the linear and nonlinear frequency response profiles can be tuned by appropriately adjusting the magnetic repulsion between the transducing and tuning magnets. In addition to tuning the forward sweep jump (peak power) frequency, the frequency range of the hysteretic high energy branch and the peak load power level can also be modified to conform to various applications. The experimental results show that the entire frequency response of the device, including the

peak power frequency, hysteresis region and harvested power level can be adjusted to match any vibration frequency within a certain range (~19% of initial resonance frequency). This effect can be exploited for post-fabrication tuning of the operational frequencies of linear or nonlinear vibration energy harvesters employing different transduction mechanisms and can potentially be extended towards the tuning of any generic micro-mechanical oscillator.

References

[1]   M. S. M. Soliman, E. M. Abdel-Rahman, E. F. El-Saadany, and R. R. Mansour, "A wideband vibration-based energy harvester," *Journal of Micromechanics and Microengineering,* vol. 18, p. 115021, 2008.

[2]   P. Podder, A. Amann, and S. Roy, "Combined Effect of Bistability and Mechanical Impact on the Performance of a Nonlinear Electromagnetic Vibration Energy Harvester," *IEEE/ASME Transactions on Mechatronics,* vol. 21, pp. 727-739, 2016.

[3]   C. P. Le and E. Halvorsen, "MEMS electrostatic energy harvesters with end-stop effects," *Journal of Micromechanics and Microengineering,* vol. 22, p. 074013, 2012.

[4]   P. Basset, D. Galayko, F. Cottone, R. Guillemet, E. Blokhina, F. Marty*, et al.*, "Electrostatic vibration energy harvester with combined effect of electrical nonlinearities and mechanical impact," *Journal of Micromechanics and Microengineering,* vol. 24, p. 035001, 2014.

[5]   J. F. Gieras, J. H. Oh, M. Huzmezan, and H. S. Sane, "Electromechanical energy harvesting system," ed: Google Patents, 2011.

[6]   X. Wu, J. Lin, S. Kato, K. Zhang, T. Ren, and L. Liu, "A frequency adjustable vibration energy harvester," *Proceedings of PowerMEMS,* pp. 245-248, 2008.

[7]   Y. Jia and A. A. Seshia, "Power Optimization by Mass Tuning for MEMS Piezoelectric Cantilever Vibration Energy Harvesting," *Journal of Microelectromechanical Systems,* vol. 25, pp. 108-117, 2016.

[8]   D. Zhu, S. Roberts, M. J. Tudor, and S. P. Beeby, "Design and experimental characterization of a tunable vibration-based electromagnetic micro-generator," *Sensors and Actuators A: Physical,* vol. 158, pp. 284-293, 2010.

[9]   A.-A. Waleed, H. Matthias, H. Tobias, and S. Walter, "Frequency tuning of piezoelectric energy harvesters by magnetic force," *Smart Materials and Structures,* vol. 21, p. 035019, 2012.

[10] P. Constantinou, P. H. Mellor, and P. D. Wilcox, "A Magnetically Sprung Generator for Energy Harvesting Applications," *IEEE/ASME Transactions on Mechatronics,* vol. 17, pp. 415-424, 2012.

[11] E. P. Furlani, *Permanent Magnet and Electromechanical Devices: Materials, Analysis, and Applications*: Elsevier Science, 2001.

[12] D. Mallick, A. Amann, and S. Roy, "A nonlinear stretching based electromagnetic energy harvester on FR4 for wideband operation," *Smart Materials and Structures,* vol. 24, p. 015013, 2015.

[13] B. Marinkovic and H. Koser, "Smart Sand—a wide bandwidth vibration energy harvesting platform," *Applied Physics Letters,* vol. 94, p. 103505, 2009.

[14] H. Liu, Y. Qian, N. Wang, and C. Lee, "An In-Plane Approximated Nonlinear MEMS Electromagnetic Energy Harvester," *Journal of Microelectromechanical Systems,* vol. 23, pp. 740-749, 2014.

[15] M. Defosseux, M. Allain, E. Defay, and S. Basrour, "Highly efficient piezoelectric micro harvester for low level of acceleration fabricated with a CMOS compatible process," *Sensors and Actuators A: Physical,* vol. 188, pp. 489 - 494, 2012.

[16] H. Liu, Y. Qian, and C. Lee, "A multi-frequency vibration-based MEMS electromagnetic energy harvesting device," *Sensors and Actuators A: Physical,* vol. 204, pp. 37-43, 2013.

[17] M. Han, Z. Li, X. Sun, and H. Zhang, "Analysis of an in-plane electromagnetic energy harvester with integrated magnet array," *Sensors and Actuators A: Physical,* vol. 219, pp. 38 - 46, 2014.

7 ULTRA-DENSE MICRO-COIL FOR ELECTROMAGNETIC ENERGY HARVESTER

High performance micro-electromagnetic systems often require micro-coils with very high packing ratio to generate maximum magnetic flux linkage (in energy harvester, sensor, and actuator applications) or large inductance (in micro-inductor and transformer applications). High packing ratio in a micro-coil translates into large number of turns in the same volume, which is critical to achieve very high magnetic flux linkage between the coil and magnet assembly in vibration energy harvesting applications. This chapter describes the motivation, design, and fabrication of an ultra-dense micro-coil, where the number of turns is doubled within the same volume as a regular planar spiral coil. One of the most important aspects of such ultra-dense coil architecture is the electrical insulation between the adjacent coil layers. This requirement has been investigated in this chapter by incorporation of four different insulating dielectric materials and subsequent characterization.

7.1 Motivation for ultra-dense micro-coil

In electromagnetic transduction systems it is of critical importance to achieve maximum flux linkage gradient between the magnet and coil. According to Faraday's law, high flux linkage gradient translates into high induced voltage in the coil, which contributes to even higher power for a given source impedance. High flux linkage gradient can be achieved either by using magnet assembly with high remnant flux density, or by using coils with high packing ratio. In a cross-section of a generic coil winding, packing ratio or packing factor (P_f) is defined as the ratio of the total area of the conductors in the cross-section and the total area of the coil cross-section (Eq. 7.1).

$$P_f = \frac{N A_C}{A_W} \qquad 7.1$$

where N is the total number of turns in the coil winding, A_C denotes the cross sectional area of a single conductor, and A_W denotes the total cross-sectional area of a coil winding. For conventional wire-wound coils, the most important parameters to have a direct effect on the packing factor are the thickness of the insulating enamel (for enamelled wire-wound coils) and the nature of the winding (e.g. square packing, hexagonal packing etc.). For conventional circular wire with enamel insulation, the packing factor in square packing condition is given by,

$$P_{f(Sq)} = \frac{\pi}{4}\left(\frac{D_C}{D_O}\right)^2 \qquad 7.2$$

where D_C denotes the diameter of the conducting material (metals such as copper, aluminium etc.) and D_O is the outer diameter of the wire including the insulating enamel layer (Figure 7.1). In the ideal case when the insulation is very thin, the diameter of the conductor approaches the total diameter of the wire, and the $P_{f(Sq)}$ reaches a theoretical maximum value of 0.7855. However, in most practical cases the packing factor achievable for square fitted windings are in the range of $0.4 - 0.6$.
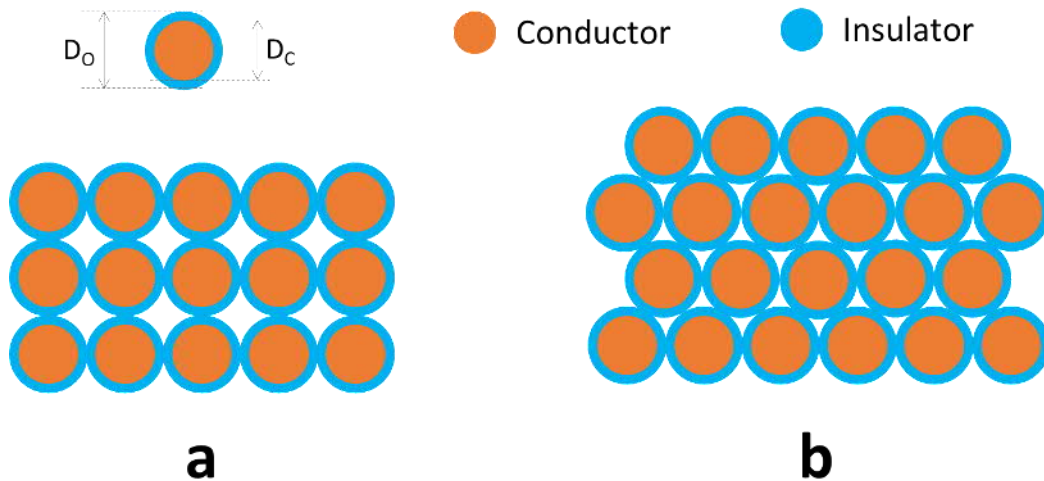
Figure 7.1: Different fitting of wire in conventional coil windings (a) square fitting, (b) hexagonal fitting.

The packing factor for hexagonally fitted winding is given by,

$$P_{f(Hx)} = \frac{\pi}{2\sqrt{3}}\left(\frac{D_C}{D_O}\right)^2 \qquad 7.3$$

In the ideal case when the insulation is very thin, the $P_{f(Hx)}$ reaches a theoretical maximum value of 0.907. However, in most practical scenarios the packing factor achievable for hexagonally fitted coil windings are in the range of $0.5 - 0.7$.

MEMS or micro-electromechanical systems often require coils with very high packing factor, especially in high current devices, electromagnetic actuators and energy harvesting applications. Micro-fabrication technologies offer the feasibility of stacking the coil turns in such a way that very high packing ratio can be achievable. The micro-fabricated copper coils are usually developed by electrodeposition on a seed layer through a photoresist mould, which result in a square or rectangular cross-sectional geometry of the copper conductor. In such configurations, the packing factor is limited by the gap between the coil turns, which is generally dependent on the maximum aspect ratio achievable by the photoresist mould.
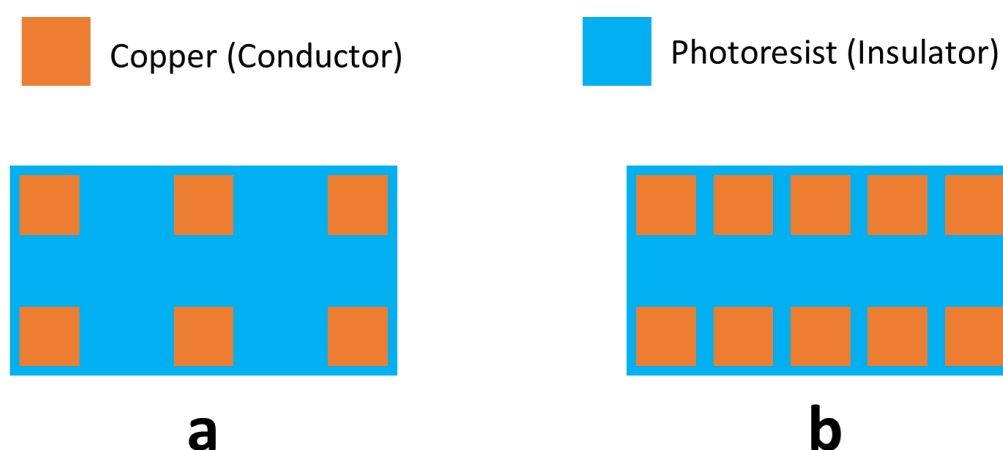
Figure 7.2: MEMS micro-coils fabricated by electrodeposiotion, (a) Regular multilayer micro-coil, (b) proposed ultra-dense micro-coil.

One of the critical factors in the performance of MEMS electromagnetic energy harvesters and high performance inductors is the number of turns in the planar micro-coils, which must be maximized in order to achieve high magnetic flux linkage and inductance. This is often achieved by stacking multiple layers of micro-fabricated coil layers separated by an insulating photoresist (such as SU-8) layer (Figure 7.2). However, due to lack of planarity of subsequent layers and limitations in the photolithography process, the stacking of multiple coil layers is usually limited to 2 or 3 layers. In this work an ultra-dense micro-fabricated coil has been attempted, where the packing factor is not limited by the maximum achievable aspect ratio of the photoresist, but by the thickness of a sidewall insulating material deposited on top of the first copper coil layer [Herrault, et al. [1]]. This

approach exploits the inter-track gap in electrodeposited planar micro-coils to incorporate another coil layer of similar geometry and number of turns, and effectively improves the packing ratio by almost a factor of 2.

7.2 Design of the proposed ultra-dense micro-coil

This section discuss the different aspects of the ultra-dense micro-coil design. A theoretical approach for estimation of the number of turns and resistance of planar square-shaped spiral micro-coils has been described. Then a detailed description of the proposed ultra-dense coil topology has been included, followed by a discussion to validate the series and parallel inter-connection of the different coil layers.

7.2.1 Calculations for a single layer planar micro-coil

The resistance of a planer micro-coil is determined by several factors such as the inner and outer diameters, width and height (or thickness) of the spiral conductor track (copper, gold, aluminium etc.) and the inter-track gap. The schematic diagram of a simple single layer coil is shown in Figure 7.3. If the total number of turns in the coil is assumed to be N, then the total length of the N turns of the conductor track needs to be determined in order to estimate the resistance of the coil.

d_I = Inner dimension

d_O = Outer dimension

t_W = Width of conductor track

t_H = Height of conductor track

g_W = Gap between conductor tracks
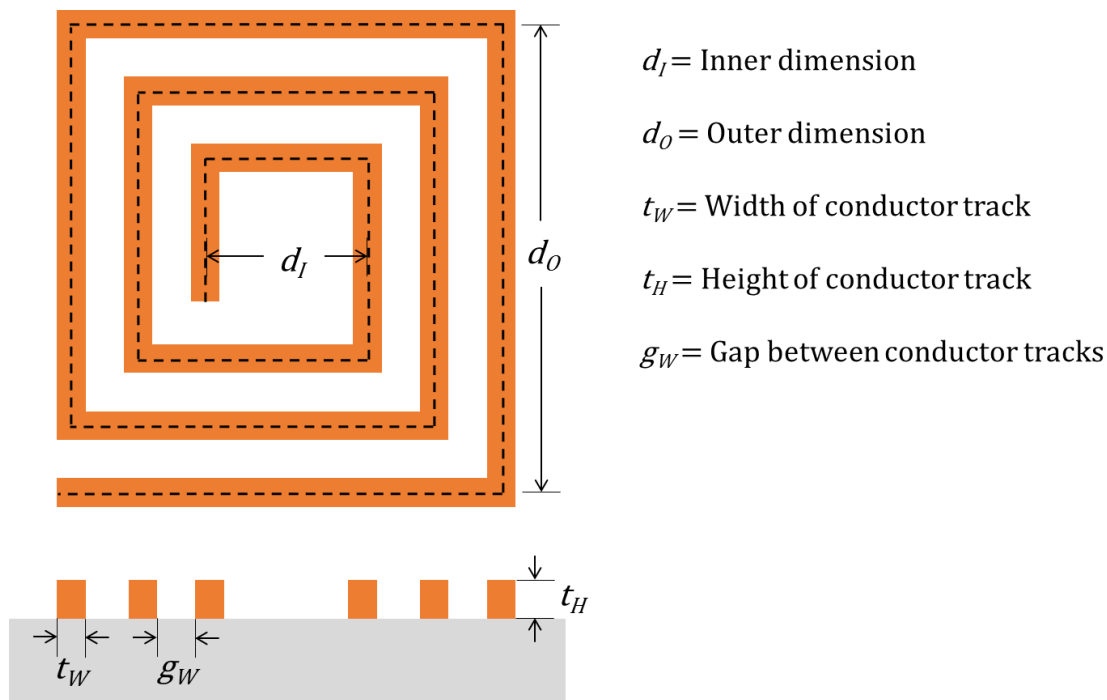
Figure 7.3: Schematic representation of planar square-shaped spiral micro-coil.

The total number of turns in a square-shaped spiral coil can be estimated as,

$$N = \left| \frac{d_O - d_I}{2(t_W + g_W)} \right| + 1 \tag{7.4}$$

where d_I and d_O are the inner and outer diameters respectively; t_W and g_W are the width of the conductor track and the inter-track gap. Assuming a square shaped spiral coil and starting with the inner-most turn in the coil, the length of the first turn is given by,

$$T_1 = 2d_I + 2[d_I + (t_W + g_W)] = 2[2d_I + (t_W + g_W)] \tag{7.5}$$

The length of the second turn can be determined as,

$$T_2 = 2[d_I + 2(t_W + g_W)] + 2[d_I + 3(t_W + g_W)] = 2[2d_I + 5(t_W + g_W)] \tag{7.6}$$

Similarly, the length of the third and fourth turns are given by,

$$T_3 = 2[d_I + 4(t_W + g_W)] + 2[d_I + 5(t_W + g_W)] = 2[2d_I + 9(t_W + g_W)] \tag{7.7}$$

and,

$$T_4 = 2[d_I + 6(t_W + g_W)] + 2[d_I + 7(t_W + g_W)] = 2[2d_I + 13(t_W + g_W)] \tag{7.8}$$

respectively. Extrapolating the equations 7.5 - 7.8, the length of the n-th turn can be estimated as,

$$T_n = 2[d_I + 2(n - 1)(t_W + g_W)] + 2[d_I + (2n - 1)(t_W + g_W)] \tag{7.9}$$
$$= 2[2d_I + (4n - 3)(t_W + g_W)] = 4d_I + 2(4n - 3)(t_W + g_W)$$

The total length of the coil can be determined as the sum of all N turns, as given below:

$$T_N = \sum_{n=1}^{N} T_n = \sum_{n=1}^{N} [4d_I + 2(4n - 3)(t_W + g_W)] \tag{7.10}$$

$$= 4\sum_{n=1}^{N} d_I + \left[8(t_W + g_W) \sum_{n=1}^{N} n \right] - \left[6\sum_{n=1}^{N} (t_W + g_W) \right]$$

Therefore the total length of the conductor track of the square spiral coil is given by,

$$T_N = 4Nd_I + \left[8(t_W + g_W)\frac{N}{2}(N + 1) \right] - [6N(t_W + g_W)] \tag{7.11}$$

$$= 4Nd_I + 2N(2N - 1)(t_W + g_W)$$

Furthermore, in case of low frequency (<10 kHz) operation, it can be assumed that the lengths included at the corners do not contribute to the resistance of the coil, since the current follows the shortest path.
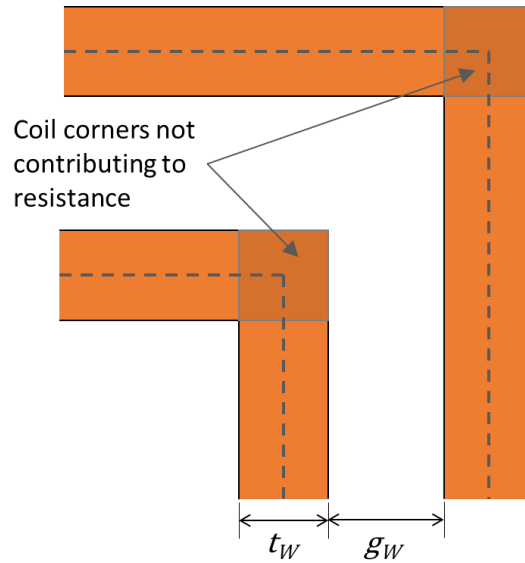
Figure 7.4: Schematic representation of corners of the square micro-coil turns.

Therefore, subtracting the corner lengths from the total length of the coil, the effective length becomes,

$$T_N = 4Nd_I + 2N(2N - 1)(t_W + g_W) - 4Nt_W \qquad \text{7.12}$$

The resistance of the coil can be determined as,

$$R_N = \frac{\rho T_N}{t_W \times t_H} \qquad \text{7.13}$$

where ρ represents the resistivity of the conductor material. Considering spiral copper (resistivity $\rho_{Cu} = 1.69 \times 10^{-8}$ Ω-m) tracks of variable track width (t_W) and inter-track gap width (g_W) and fixed track height ($t_H = 10$ µm), within fixed outer ($d_O = 2.8$ mm) and inner ($d_I = 0.4$ mm) dimensions, the variation of number of turns and resistance has been plotted in Figure 7.5. The number of turns and correspondingly, the resistance of the coil is observed to be increasing with decreasing width of conductor track and the inter-track gap. The equations developed in this section can be extrapolated to coils with multiple levels connected through via or bond pads. Furthermore, these results can also be used to estimate the number of turns and resistances of planar ultra-dense coils, where the inter-track gaps are utilized to electrodeposit a second layer of parallel coil tracks.
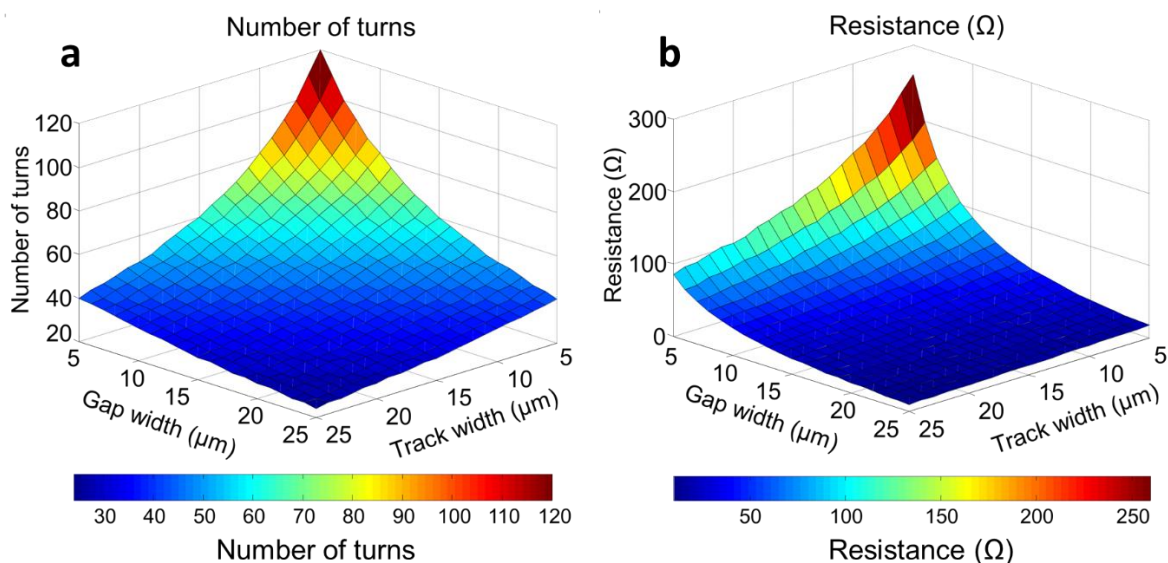
Figure 7.5: Variation of the (a) number of turns and (b) resistance of single layer planar micro-coils with copper track width inter-track gap.

7.2.2 Topology of the proposed ultra-dense micro-coil

The proposed ultra-dense micro-coil consists of two levels of spiral conductor, separated by insulating SU-8 photoresist (Figure 7.6 (a)). Each of the conductor levels accommodate two layers of spiral conductor, insulated from each other by conformally deposited insulation materials (e.g. silicon dioxide, Parylene, aluminium nitride etc.). The ultra-dense (UD) coil is to be fabricated on silicon substrate using electrodeposition process. In the Level 1 of the ultra-dense coil, the first layer Coil 1 is electrodeposited with a connecting pad P1 and via pad V1 at the centre. The Coil 1 is then coated with a conformal deposition of a thin insulation layer.

Then the second layer Coil 2 is deposited within the inter-track gap of the Coil 1, with a connecting pad P2 and via pad V2 at the centre. In the next step both Coil 1 and Coil 2 are coated with an insulating layer and the via pads V1 and V2 are opened for connecting to the Level 2 of the coil.
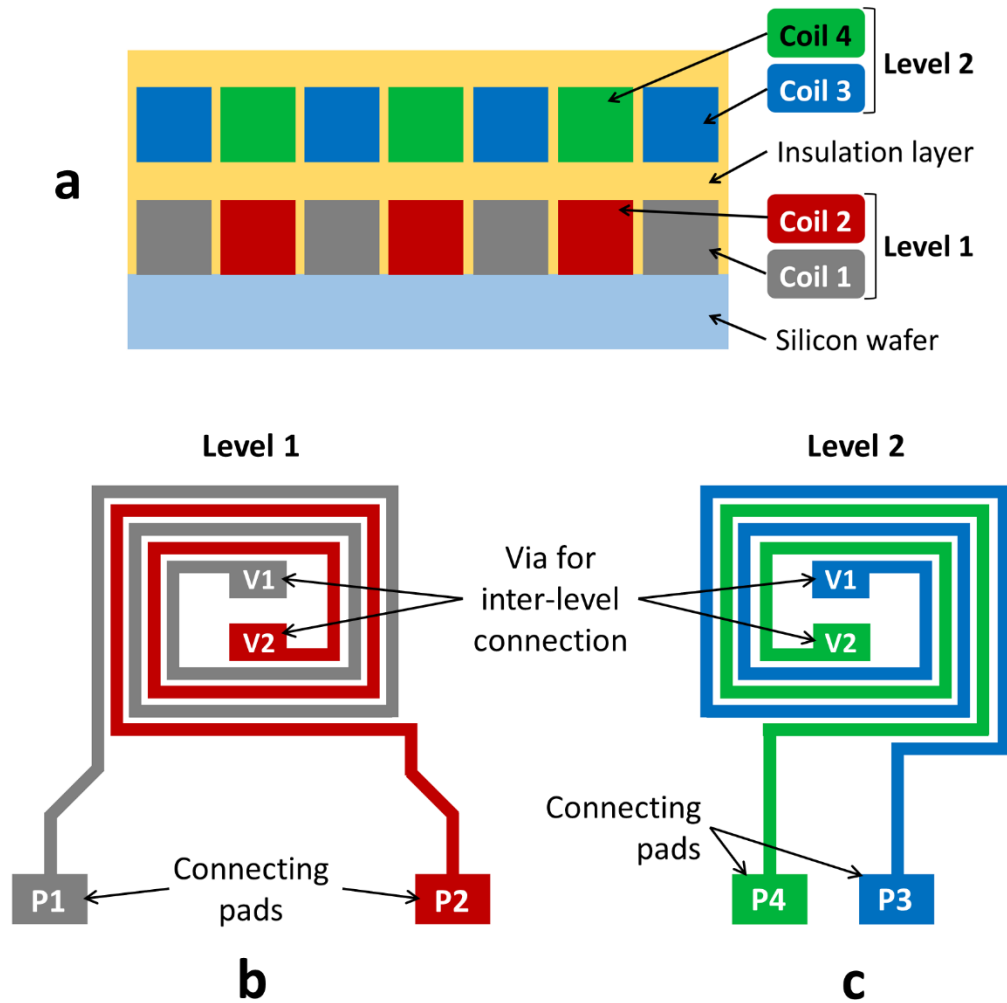
Figure 7.6: (a) Schematic cross-sectional representation of four-layer ultra-dense micro-coil. (b) Coil layers 1 and 2 in level 1. (c) Coil layers 3 and 4 in level 2.

In the Level 2, the third layer Coil 3 is then electrodeposited with a connecting pad P3 and via pad V1, connecting to Coil 1 of Level 1. The Coil 3 is conformally coated with a thin layer of insulating material. In the next step the fourth layer Coil 4 is electrodeposited in the inter-track gap of the Coil 3, with a connecting pad P4 and via pad V2, connecting to the Coil 2 of Level 1. Therefore, the ultra-dense coil constitutes of two layers of spiral coils with metal tracks running parallel to each other.

A schematic diagram of the proposed ultra-dense coils with the dimensions are illustrated in Figure 7.7. The inner and outer dimensions of the proposed square-shaped coil are 0.4 mm and 2.8 mm respectively. Each of the central vias are 0.2 mm × 0.15 mm, while the external bond-pads are 0.6 mm × 1 mm in dimension. Two more external bond-pads are included on both sides of the coils to provide for connectivity with the vias through wire-

bonding. The entire coil and the pads can be included within a die area of 5 mm × 5 mm, however, some space has been provided above the coil device for identification marks.
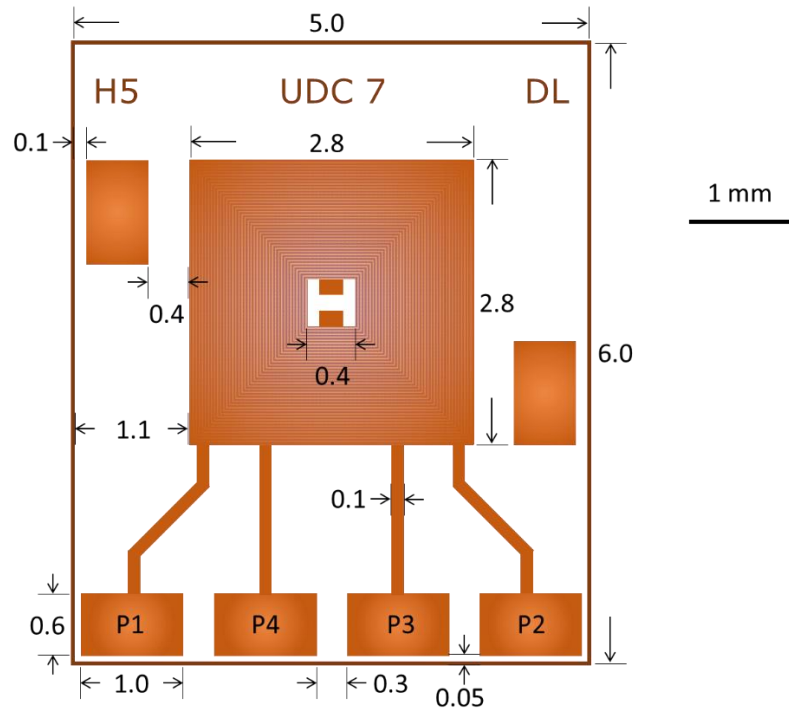
Figure 7.7: The proposed ultra-dense micro-coil topology. All dimensions are in the unit of mm.

The parameters of the proposed double-layer micro-coils has been listed in Table 7.1.

Table 7.1: List of ultra-dense micro-coil parameters

Coil parameters	Values
Inner dimension	400 µm
Outer dimension	2800 µm
Track width	10 µm, 15 µm, 20 µm
Inter-track gap width	10 µm, 15 µm, 20 µm
Number of turns in a single coil layer	60, 40, 30
Total number of turns in 4 coil layers	240, 160, 120
Size of inter-level via pads	200 µm × 150 µm
Size of bond-pads	1000 µm × 600 µm

7.2.3 Validation of series and parallel connection

In order for proper operation in a micro-energy harvester, it is crucial to ensure that the coil architecture is consistent with the path of current flow, such that current induced by the magnetic flux linkage flow in the same direction throughout all the coil layers in each level. Furthermore, by appropriate interconnection between the connecting pads, the ultra-dense coils can be connected in series (Figure 7.8) or parallel (Figure 7.9) arrangement.
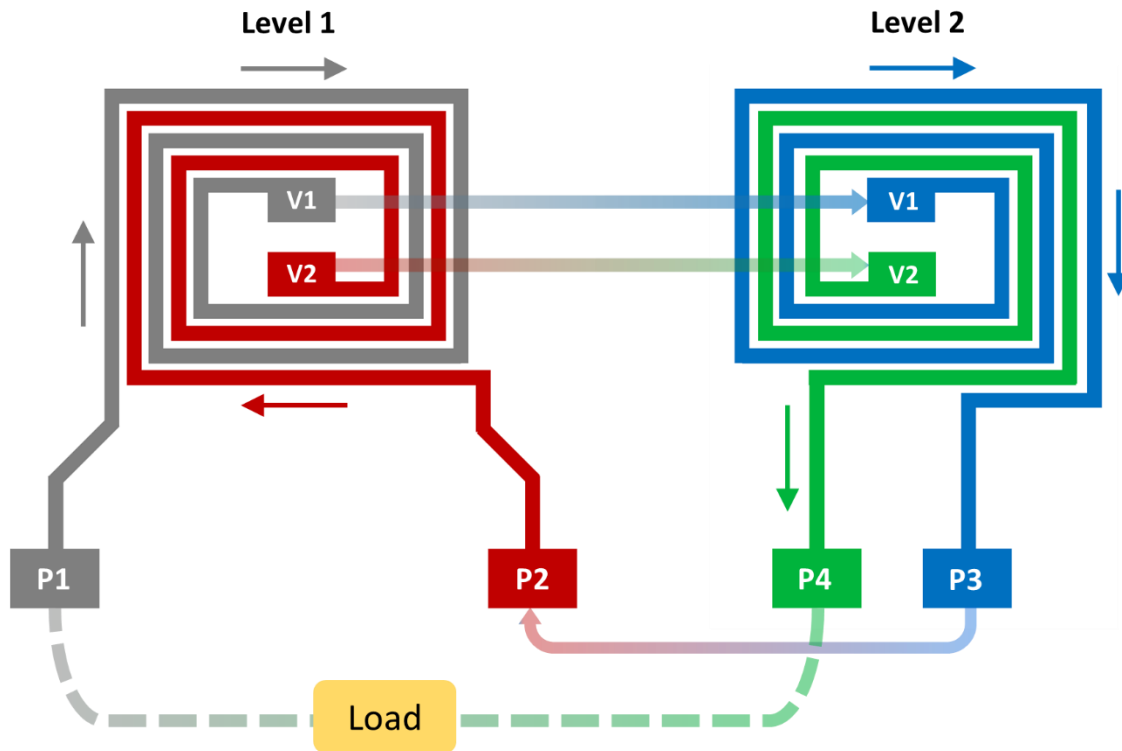
Figure 7.8: Series connected ultra-dense spiral coils. The current flows in the clockwise direction in all the layers in both levels.

The current flow path for a series connected ultra-dense coils has been shown in Figure 7.8, where the coils has been interconnected such that the current flows in the clockwise direction through all the layers. Starting from connecting pad P1 in Coil 1, the path of the current can be traced spirally in the clockwise direction up to the central via V1. The current enters the Level 2 into Coil 3 through via V1 and travels spirally in the clockwise direction up to the connecting pad P3. The connecting pads P3 and P2 are connected by bonded wire and the current enters from Level 2 to Level 1 through P2. Again, the current spirally traces a clockwise path from P2 to the central via V2. Through V2 the current exits Level 1 and enters Level 2, which then travels down a clockwise path through Coil 4 up to connecting pad P4. Therefore, while connected in series, the current flow through each coil

layer in the same clockwise pattern. An external load can be connected between pads P1 and P4 to close the circuit.
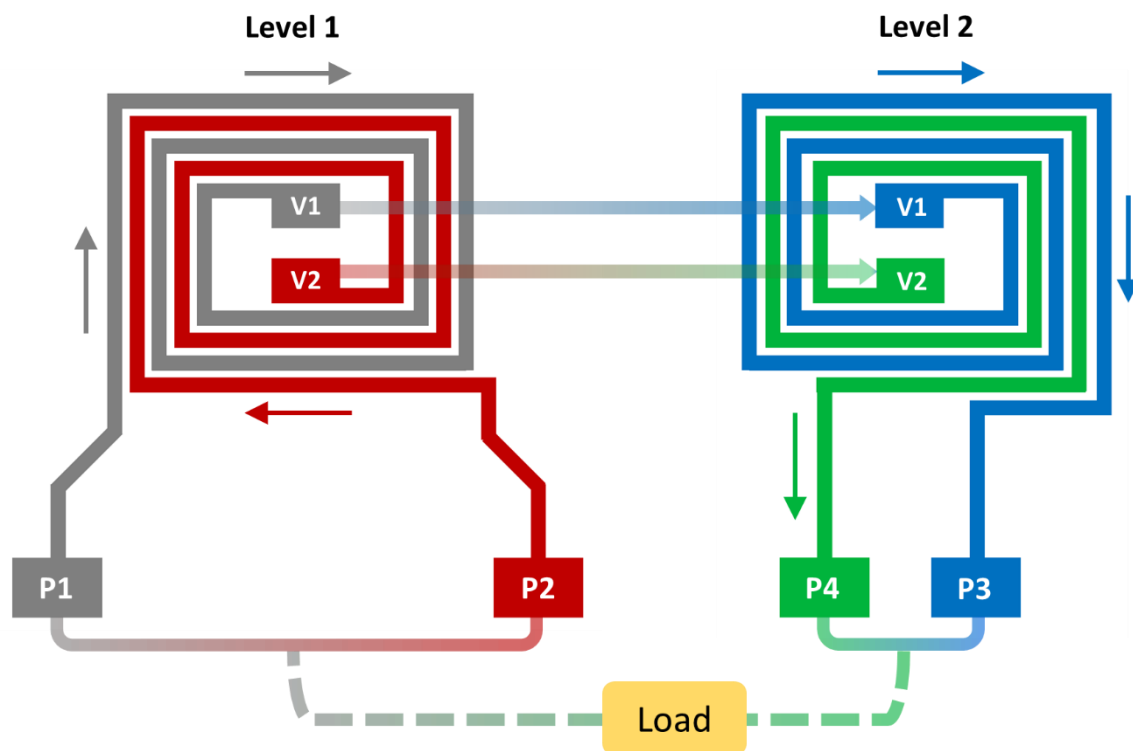
Figure 7.9: Parallel connected ultra-dense spiral coils. The current flows in the clockwise direction in all the layers in both levels.

Alternatively, the coils can be connected in parallel such that the direction of current flow is in the same direction (e.g. clockwise) through all the coil layers (Figure 7.9). In this arrangement, the pads P1 and P2 are connected together, and a current originating in the Level 1 at P1 and P2 can follow two parallel spiral paths through Coil 1 and Coil 2 in a clockwise fashion up to the central via V1 and V2. The current exits Level 1 through vias V1 and V2 and enters Level 2 into Coil 3 and Coil 4 to follow two parallel spiral paths in a clockwise direction. Finally, the current emerges from connecting pads P3 and P4, which are connected together. An external load can be connected between P1, P2 and P3, P4 to complete the circuit. Therefore by simple manipulation of the interconnection between the connecting pads P1, P2, P3 and P4, the four individual coils can be connected either in series or in parallel, and the current flow can be maintained to be in the same direction through all coil layers.

7.3 Simulation results and discussion

It has been demonstrated in the previous section that in comparison to conventional double-layer micro-coils, the proposed ultra-dense double-layer micro coil provides double number of turns within the same volume and footprint. Furthermore, the coil-resistance in the ultra-dense coils can be altered by connecting the coil-layers in series or parallel through external bond-pads. This section demonstrates the impact of the proposed ultra-dense coil on the performance of energy harvesters, and compares that with conventional double-layer coils.
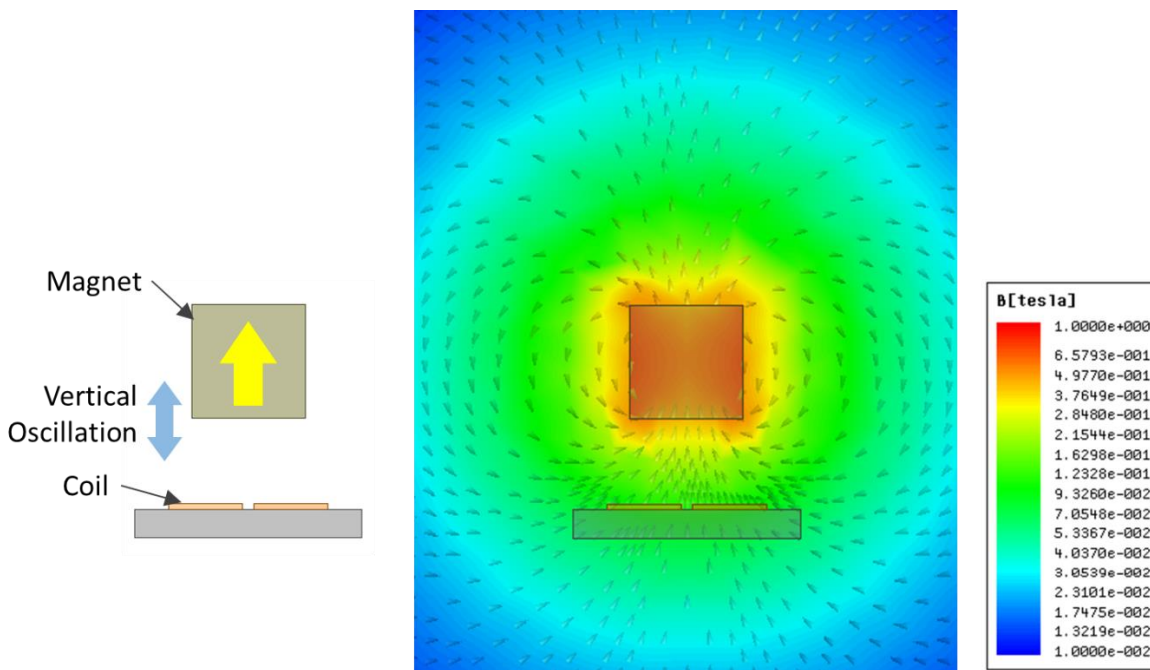
Figure 7.10: Electromagnetic simulation to estimate power harvested by different planar micro-coil topologies.

Considering a conventional double-layer micro-coil with track width and gap width of 10 µm each, the total number of turns are calculated to be 120 [Eq. 7.4] within a footprint of 2.8 mm × 2.8 mm. The resistance of the conventional double-layer micro-coil is estimated to be 130 Ω [Eq. 7.11]. In comparison, the ultra-dense micro-coils are calculated to have double the number of turns (240) of the conventional micro-coil [Figure 7.11 (a)] of the same size. The resistance of the ultra-dense coils may vary depending upon the inter-connection through the bond-pads. For example, the series connected ultra-dense coil shows a resistance twice as large (260 Ω) as that of a conventional coil, while the resistance for the parallel connected ultra-dense coil is the same as that of a conventional coil. For a parallel connection of the conventional double-layer micro-coil, the calculated resistance is 65 Ω, the smallest of all configurations. The parameters of the coils are

incorporated in the Ansoft Maxwell model of a MEMS electromagnetic vibration energy harvester [Figure 7.10], which in principle is similar to that outlined in Chapter 6. In this model an NdFeB magnet (2 mm × 2mm × 2 mm) is considered to be oscillating above a fixed planar spiral coil at a frequency of 200 Hz.

The magnetic flux linkage gradient for the ultra-dense micro coils estimated from the simulation results show a two-fold increase over that for the conventional coil [Figure 7.11 (c)], since the flux linkage is proportional to the number of turns.
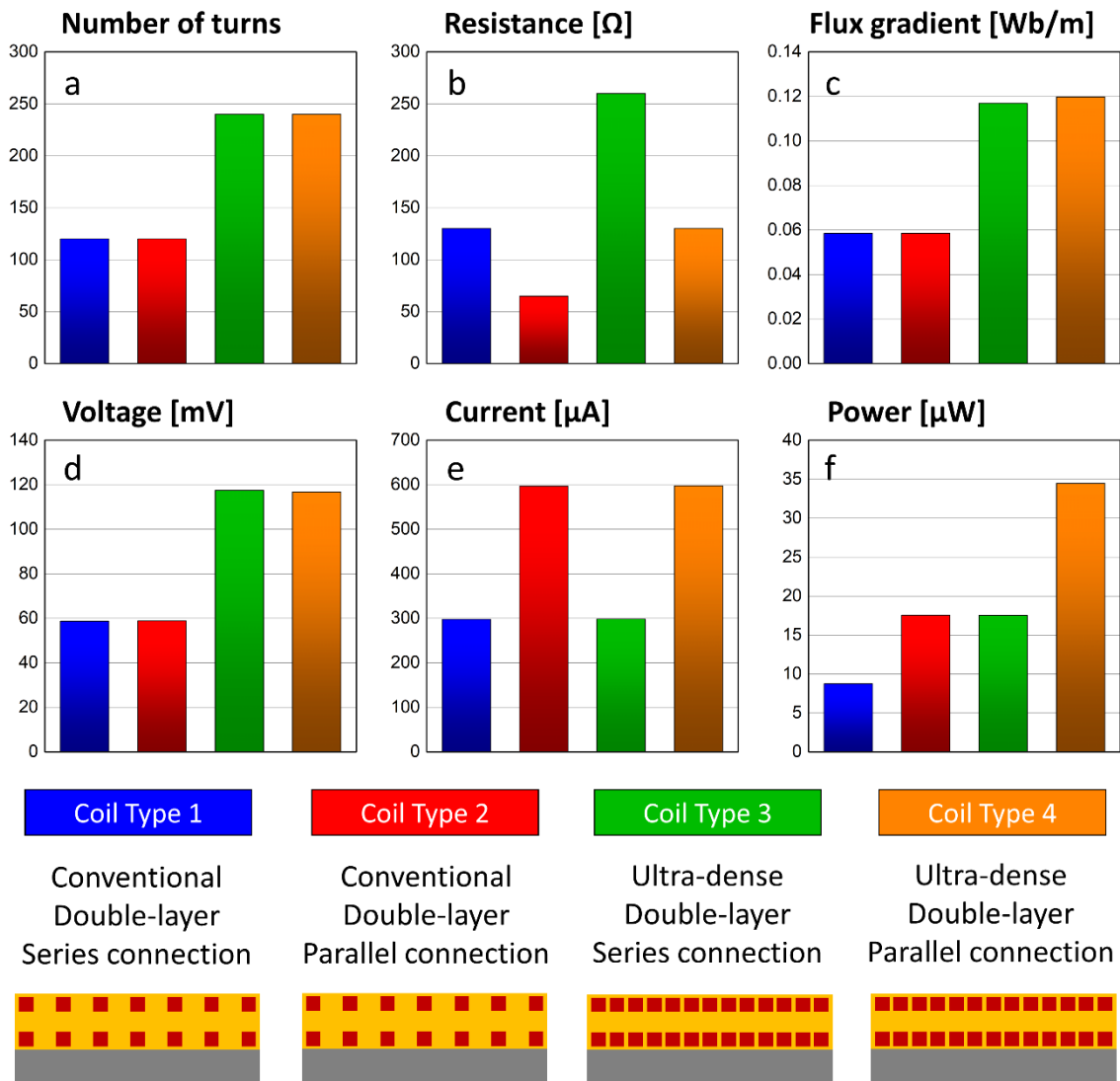
Figure 7.11: Variation of (a) number of turns, (b) resistance, (c) flux gradient, (d) induced voltage, (e) induced current, and (f) generated power for different planar micro-coil topologies and connections.

Similarly, the voltage induced in the ultra-dense coils are almost twice as high as that induced in the conventional coil [Figure 7.11 (d)], since the induced voltage is proportional

to the number of turns, as well as the flux linkage gradient. On the other hand, the induced current is the same in the conventional as well as the series connected ultra-dense coil. However, since the effective resistance of the parallel connected ultra-dense coil is half of that of the series connected ultra-dense coil, the parallel connected coil carries twice as much current as that of the series connected ultra-dense and conventional coils [Figure 7.11(e)]. Similarly, the parallel configuration of the conventional coil carries twice as much current as the series connected conventional coil. The generated power obtained from the induced voltage and current has been compared in Figure 7.11 (f), where the parallel connected conventional coil and the series connected ultra-dense coil shows a two-fold improvement in power output over the series connected conventional coil. Furthermore, the parallel connected ultra-dense coil exhibits a power output twice as high as that of the series connected ultra-dense coil, which can be attributed to the higher induced current in the parallel connected coil. Therefore, the energy harvested by micro-power generators can be significantly enhanced by utilization of the proposed ultra-dense coil in MEMS-scale electromagnetic vibration energy harvesting devices.

7.4 Ultra-dense micro-coil fabrication process flow

This section discuss the various aspects of fabrication of the proposed ultra-dense microcoil. The micro-fabrication process flow is first developed (jointly by Elias Laforge, Peter Constantinou and Joe O'Brien within the team) and failure modes and effects analysis (FMEA) is carried out (by Peter Constantinou within the team) to minimize the risk of potential failure of devices. Then a set of multiple photomasks were designed for use in the photolithography process to fabricate the ultra-dense coils. The proposed fabrication process flow is described in the following paragraphs. In each of the associated figures the left-hand panel shows a schematic cross-section of the wafer at each process step, while the right-hand panel shows a schematic top-view of the permanent layer patterns only. The non-permanent layers and patterns are not shown in the top-view, as it is intended only to illustrate the interleaved nature of the coil layers, spiral turn orientation and bond pad connections.

The proposed fabrication process flow starts with RCA cleaning of the silicon wafer, and thermal oxidation (~ 1 µm thickness) is performed. Then sputter deposition of titanium (20 nm) and copper (200 nm) is performed in vacuum chamber at ambient temperature. This

sputtered Ti/ Cu layer serves as the seed layer for electrodeposition of subsequent metal layers [Figure 7.12].
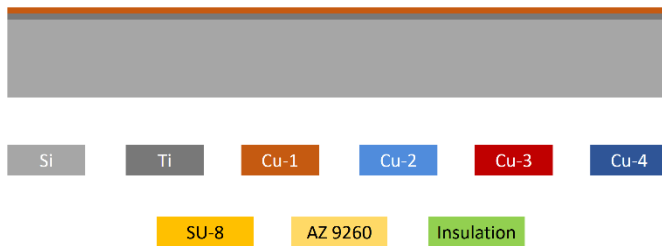
Figure 7.12: Ti/Cu (20/ 200 nm) seed layer sputtered on the silicon wafer.

In the next step AZ9260 photoresist is spin coated (thickness = 15 µm) on top of the sputtered Ti/Cu seed layer. The first layer of the spiral coil pattern is then transferred onto the AZ9260 photoresist by UV-ray photolithography. The wafer is then developed to create the first coil layer pattern in the photoresist layer [Figure 7.13].
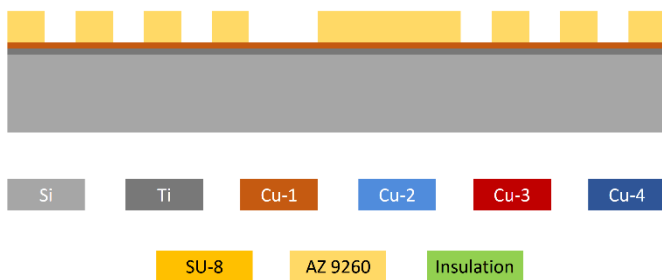
Figure 7.13: AZ 9260 photoresist spin-coated and coil layer 1 pattern transferred.

The first copper coil layer is then electrodeposited (thickness ~ 10 µm) in acidic bath using a commercial electrodeposition system [Figure 7.14].
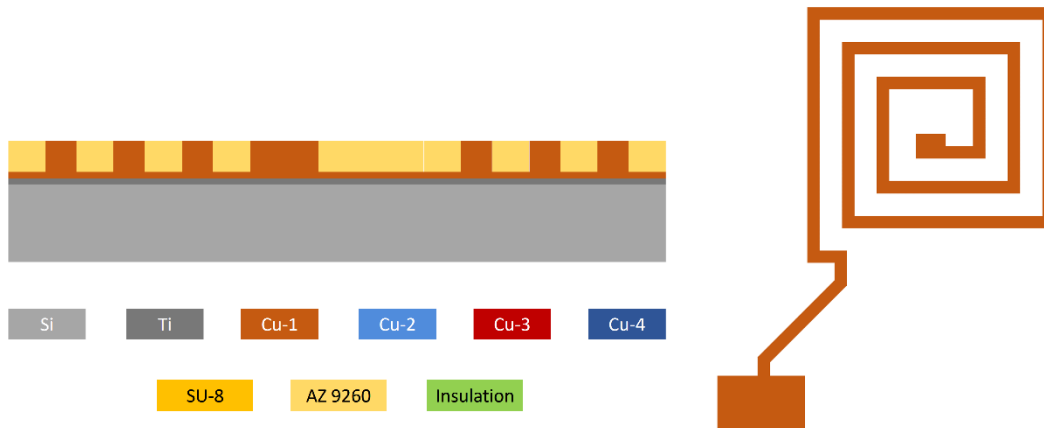
Figure 7.14: Coil layer 1 electrodeposited in the photoresist mould.

In the next step the photoresist is stripped using acetone, and the seed layers are etched. The copper seed is etched using ammonium persulfate solution, while the titanium seed is etched using HF solution [Figure 7.15].
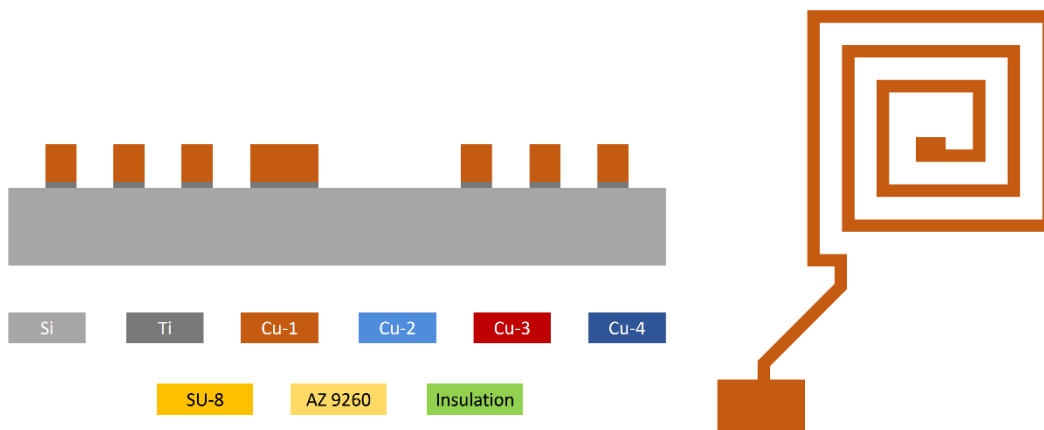
Figure 7.15: Photoresist removed, and Ti/Cu seed layer etched chemically.

In the next step an insulation layer (silicon dioxide, or aluminium nitride, or parylene) is conformally deposited with 500 nm or 1 µm thickness. This layer is intended to provide electrical insulation between the first coil layer, and the second interleaved coil layer which will be electrodeposited within the inter-track gaps of the first layer [Figure 7.16].
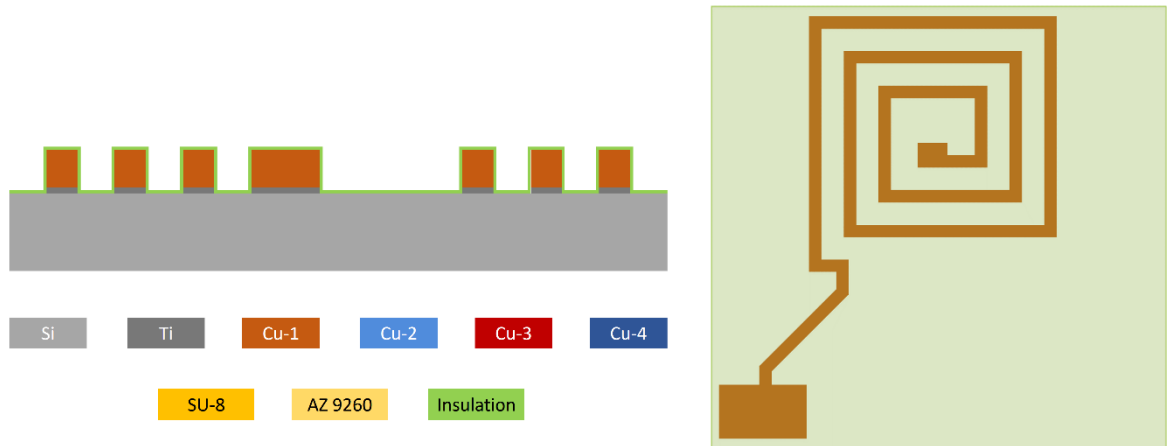
Figure 7.16: Blanket deposition of insulation layer on top of the first coil layer.

The AZ9260 photoresist is then spin coated on the wafer with a thickness of 20 µm. This followed by the photolithographic transfer of the central via and connecting pad area on the photoresist. The photoresist is then developed and the via and pads are exposed by plasma etching of the insulation layer [Figure 7.17]. Following this, the remaining photoresist is stripped using acetone.
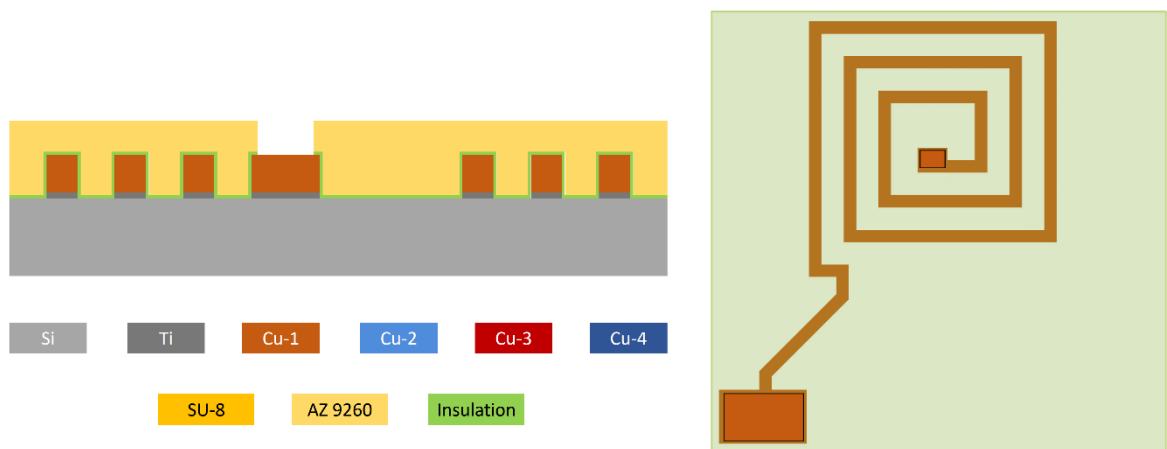
Figure 7.17: Spin-coating of AZ9260 photoresist, patterning of central via and pad, and etching of insulation from the via and pads.

In the next step a second Ti/Cu seed layer is sputter deposited on the wafer. This layer is intended for use as seed layer for electrodeposition of the second interleaved coil layer [Figure 7.18].
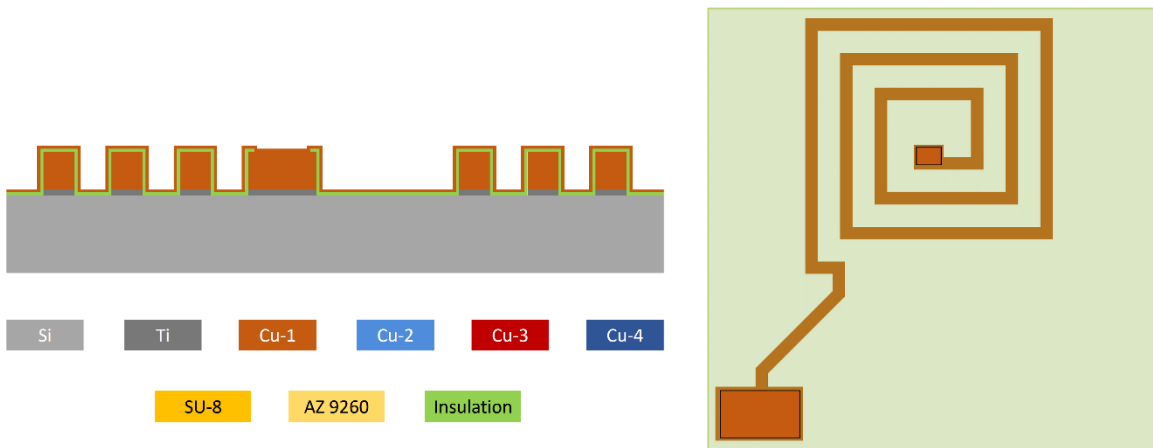
Figure 7.18: Removal of photoresist, and sputter deposition of Ti/ Cu seed layer.

In the next step, the AZ9260 photoresist is spin coated (thickness 20 µm), and the second coil layer pattern is transferred onto the wafer by photolithography. The second interleaved coil pattern is then developed in the photoresist layer [Figure 7.19].
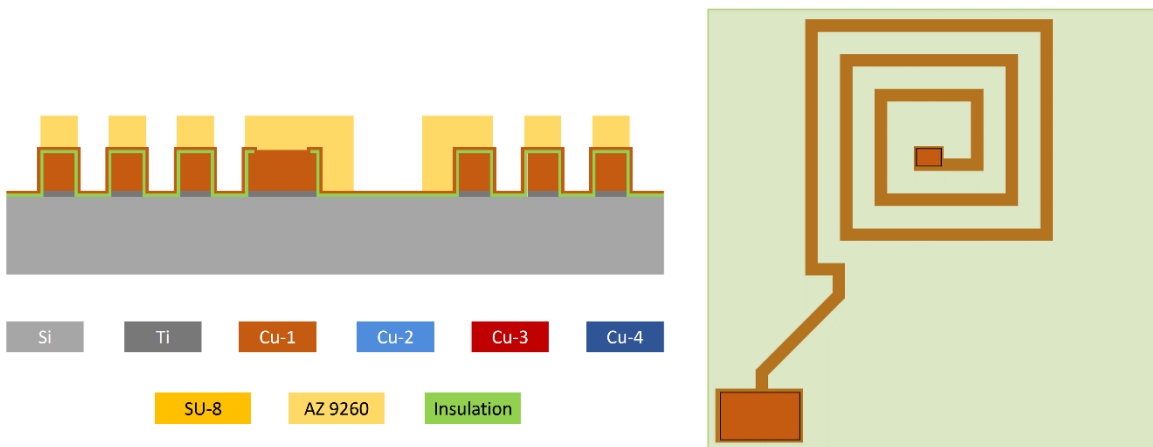
Figure 7.19: Spin-coating of photoresist, and pattering of the second micro-coil layer.

Following the photolithography, the second coil layer is electrodeposited upto a thickness of 10 µm in acidic bath using a commercial plating line [Figure 7.20].
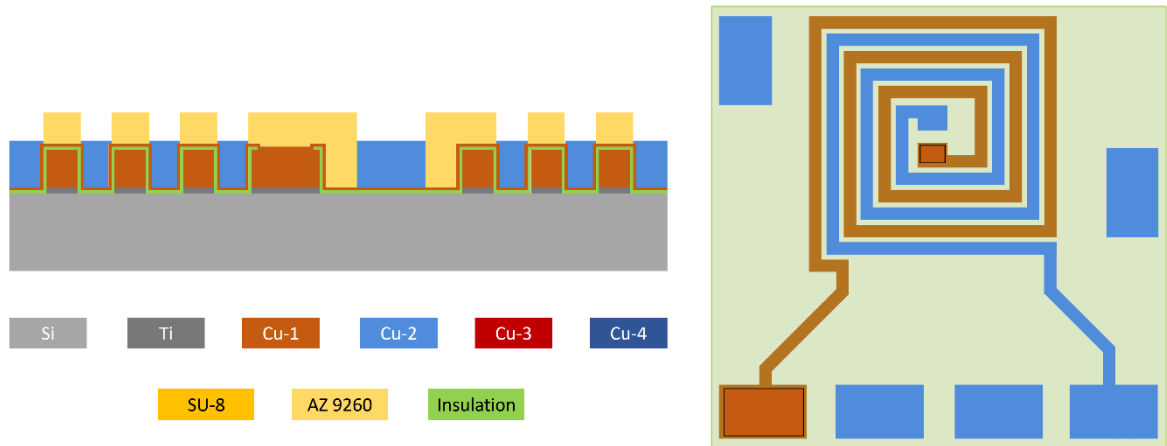
Figure 7.20: Electrodeposition of the interleaved coil layer 2 within the inter-track gap of coil layer 1.

The remaining photoresist layer is stripped by acetone [Figure 7.21].
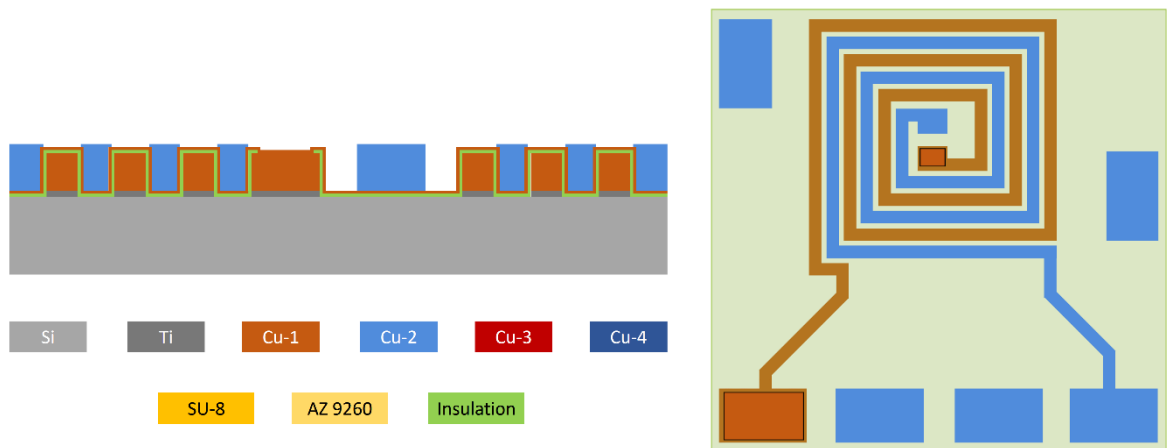
Figure 7.21: Removal of photoresist.

Another layer of AZ9260 photoresist is spin-coated, and the pattern for the central vias and the connecting pads are transferred by photolithography [Figure 7.22].
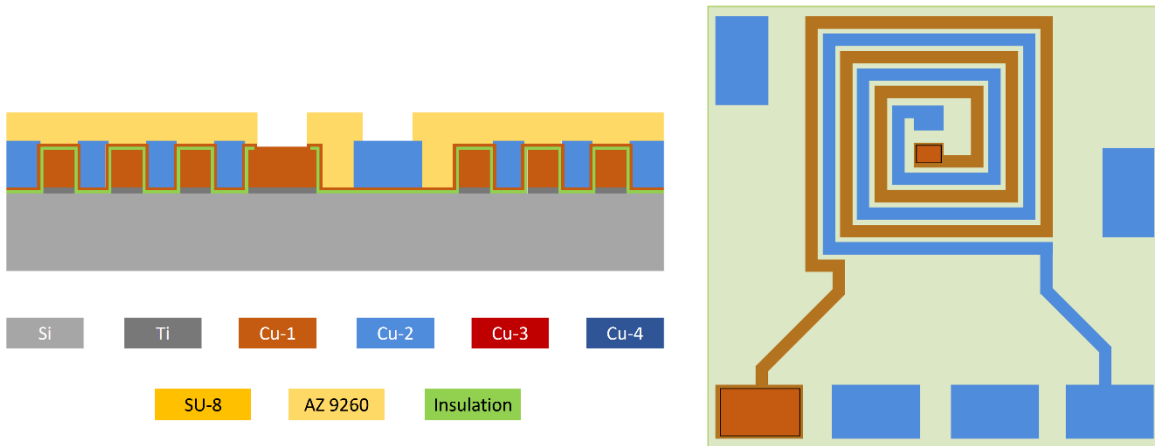
Figure 7.22: Spin-coating AZ9260 photoresist, and patterning of via and pads.

The exposed vias and connecting pad areas are electroplated to a height of 12 µm. This is required for maintaining electrical contact between the level 1 copper coils and the level 2 copper coils through the vias [Figure 7.23].
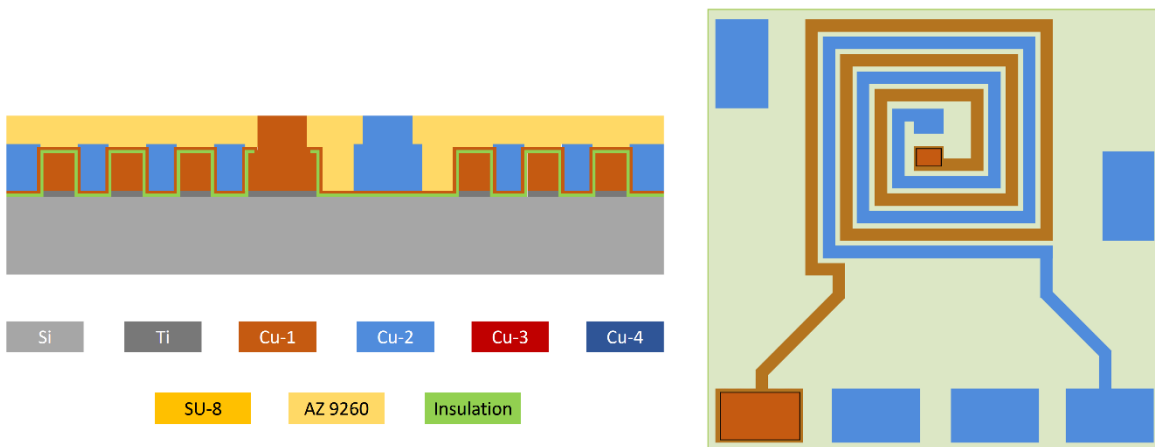
Figure 7.23: Electrodeposition of the vias and pads to connect to level 2.

The remaining photoresist is removed using acetone. The copper seed layer is etched using ammonium persulfate solution, and the titanium layer is etched using HF solution. The coil layers 1 and 2 should be electrically isolated at this point [Figure 7.24].
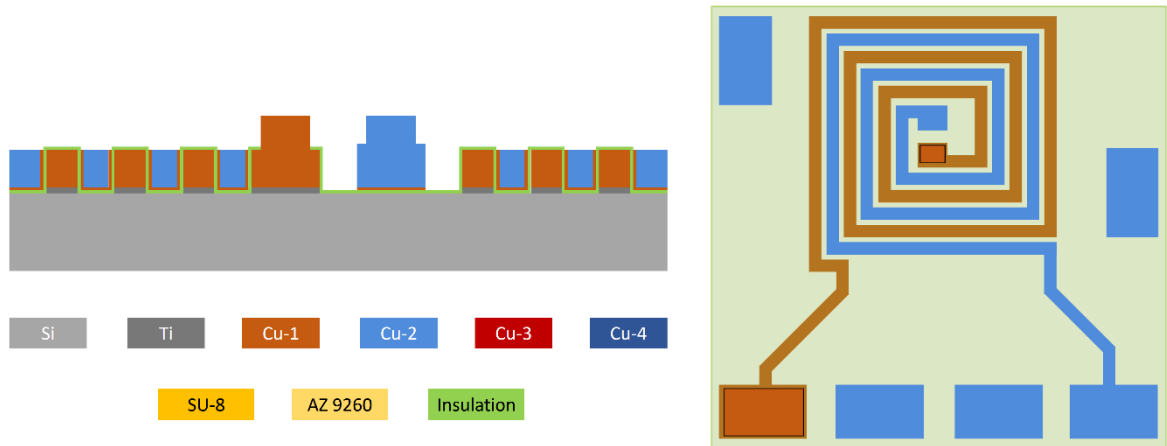
Figure 7.24: Removal of photoresist, and etching of second seed layer.

The top surface of the wafer is spin-coated with SU-8 photoresist upto 12 µm thickness. [Figure 7.25].
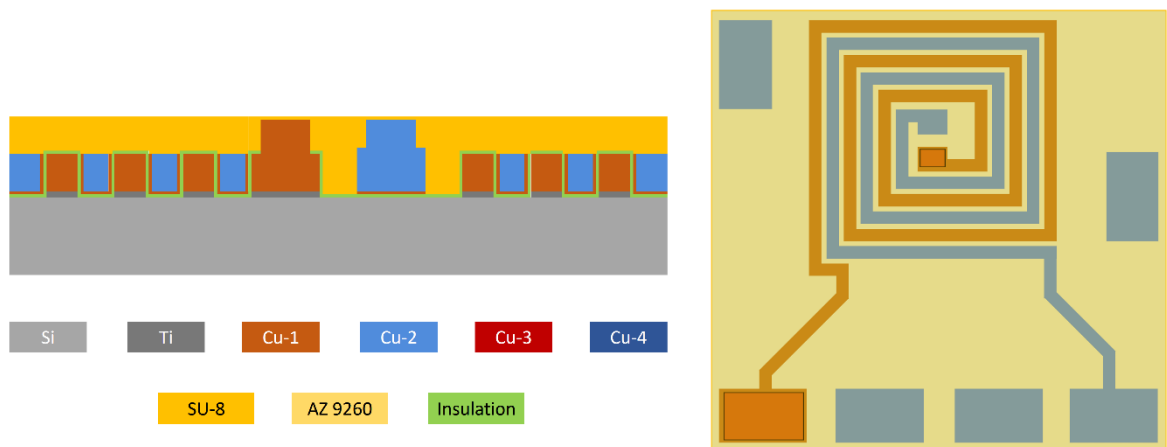
Figure 7.25: Spin-coating of SU-8 photoresist.

The central via and connecting pads are patterned on the SU-8 photoresist using photolithography, and the SU-8 layer is developed to open the vias and pad areas. The SU-8 is a permanent photoresist, and the remaining SU-8 will provide insulation between the coil layers in the level 1 and level 2 of the ultra-dense coil [Figure 7.26].
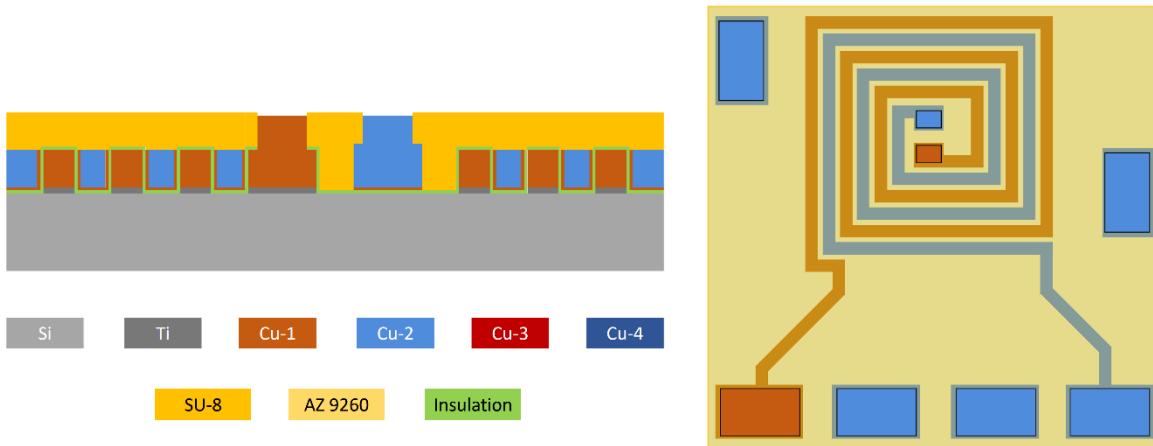
Figure 7.26: Patterning and opening of the vias and the pads.

Copper seed layer (200 nm) is sputter deposited on the SU-8 photoresist layer, which will serve as the seed layer for electrodeposition of the third coil layer on level 2 [Figure 7.27].
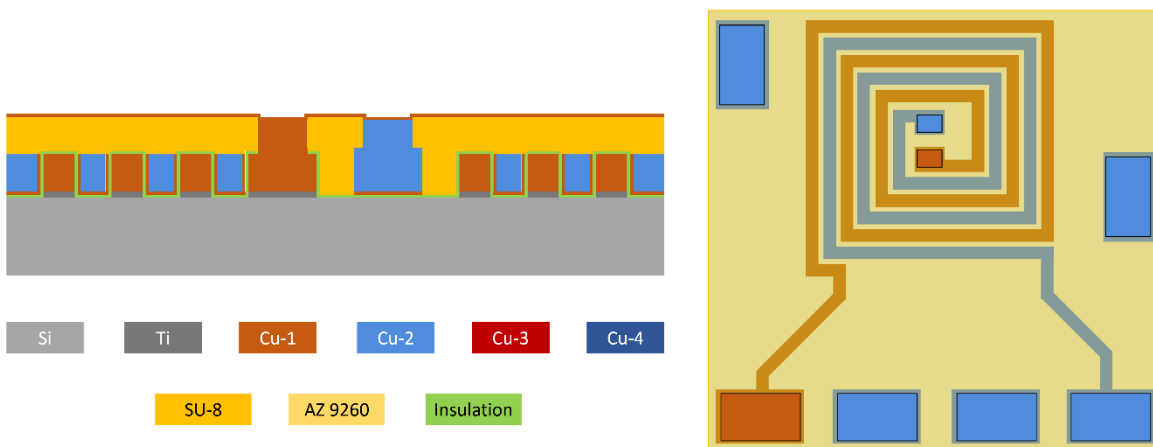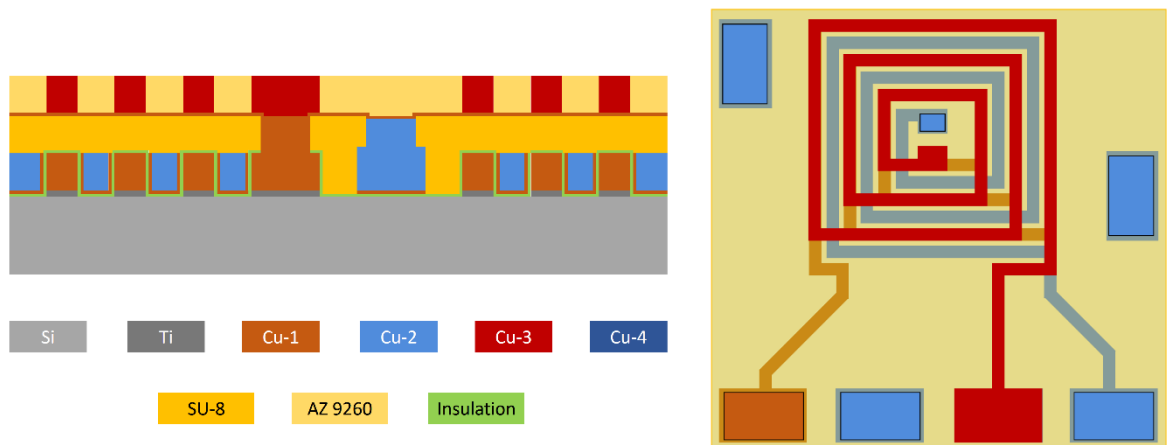

Figure 7.27: Sputter deposition of copper seed layer.

AZ 9260 photoresist is spin-coated in the next step (~ 15 µm thickness), and the third coil layer pattern is transferred onto the photoresist [Figure 7.28]. The coil turns are oriented such that the direction of current flow is the same as in the first coil layer in level 1 [7.2.2].
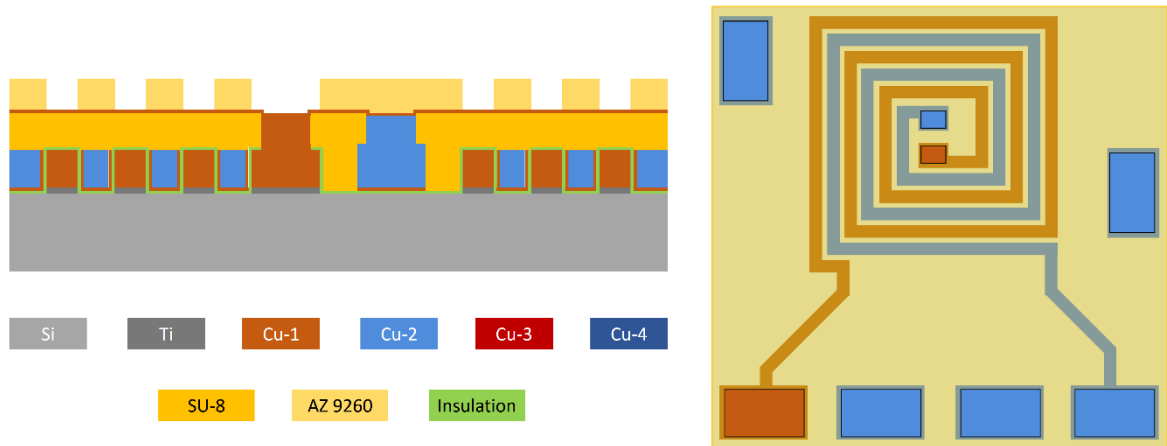
Figure 7.28: Spin-coating of AZ9260 photoresist, and patterning of the coil layer 3.

The third coil layer is electrodeposited to a thickness of 12 µm [Figure 7.29]. The first coil layer in level 1 and the third coil layer in level 2 are connected to each other through the central via. Also, the coil layers 1 and 3 are designed such that the induced current flow in the same direction through both layers.
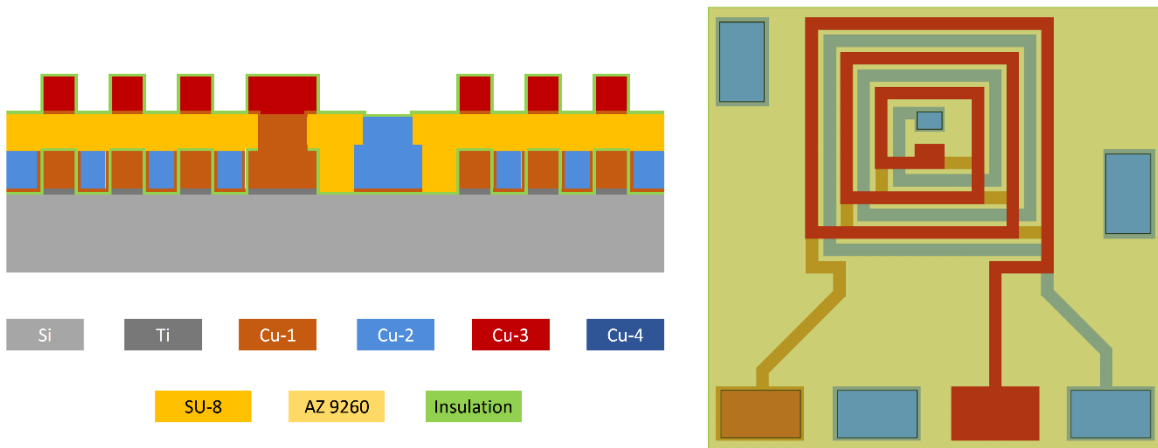

Figure 7.29: Electrodeposition of the coil layer 3, which is connected to coil layer 1 through inter-level via.

The remaining photoresist is removed using acetone, and the underlying copper seed layer is etched using ammonium persulfate solution [Figure 7.30].
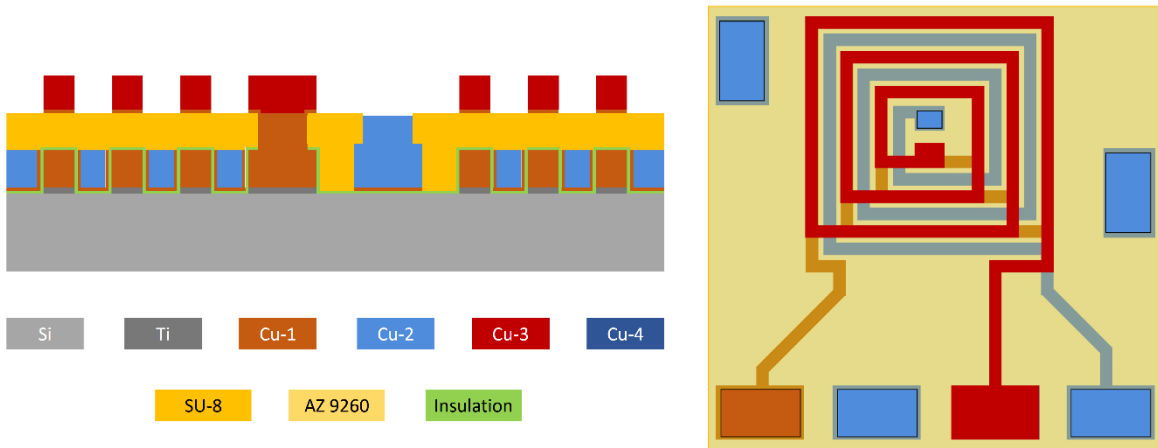
Figure 7.30: AZ9260 is removed, and the seed layer is etched.

The next step is a thin conformal deposition of an insulation layer (silicon dioxide, or aluminium nitride, or parylene) [Figure 7.31]. This layer is intended to serve as electrical insulation between the third coil layer, and the fourth interleaved coil layer which will be electrodeposited within the inter-track gaps of the third coil layer in the level 2.
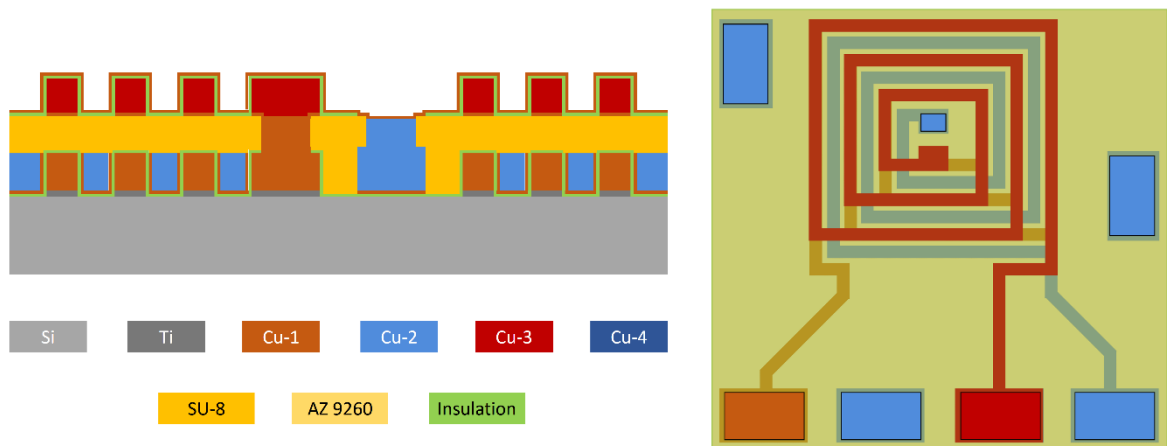

Figure 7.31: Blanket deposition of insulation layer on the coil layer 3.

The AZ 9260 photoresist is spin-coated on top of the conformal insulation layer, and the pattern for the central via and connecting pads are transferred by photolithography. Then the insulation layer material is etched from the via and pad areas [Figure 7.32].
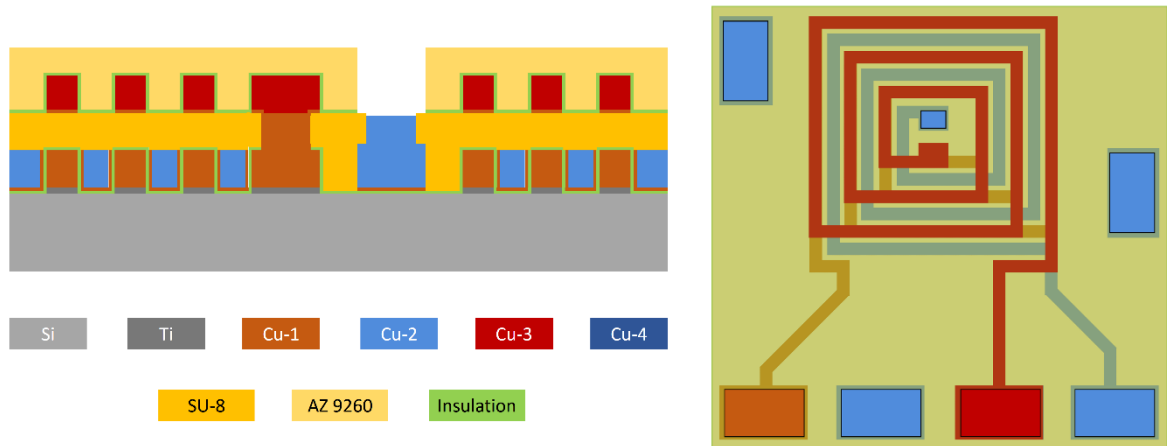
Figure 7.32: Spin-coating AZ9260, and patterning of via and pads. Insulation layer is etched from the via and pads to connect with coil layer 2.

The remaining photoresist is etched, and copper seed layer is sputter deposited on the top of the insulation layer. This is intended to serve as the seed layer for electrodeposition of the fourth interleaved coil layer [Figure 7.33].


Figure 7.33: Sputter deposition of Cu seed layer over the insulation layer.

The AZ 9260 photoresist is spin coated on top of the copper seed layer, and the fourth coil layer pattern, which is interleaved within the inter-track gaps of the third layer, are transferred by photolithography [Figure 7.34].
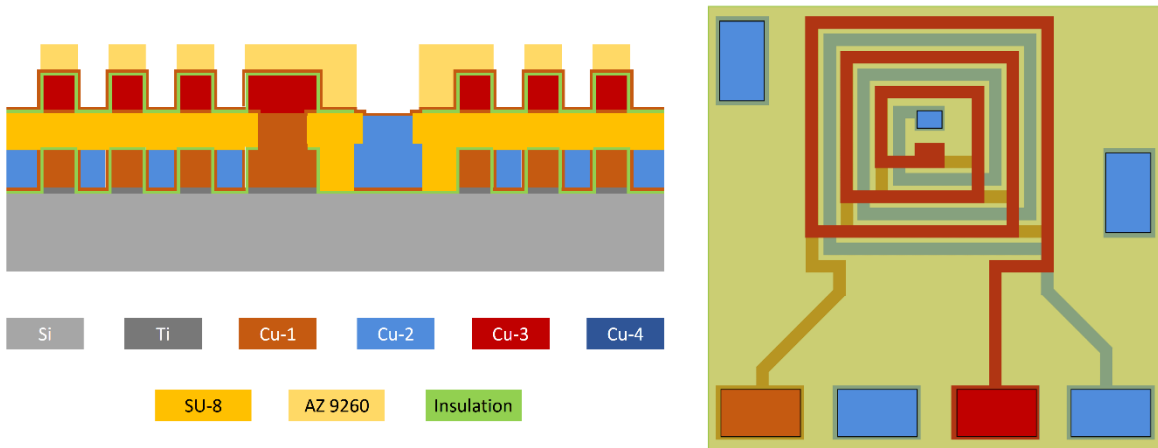
**Figure 7.34: Spin-coating of AZ9260 and photolithoraphy of coil layer 4.**

The fourth coil layer is electrodeposited to a thickness of 12 µm [Figure 7.35]. The fourth coil layer on level 2 is connected to the second coil layer in level 1 through the central via. The spiral turns in the fourth coil layer are oriented such that the current flow path follow the same direction in both the level 1 and 2.
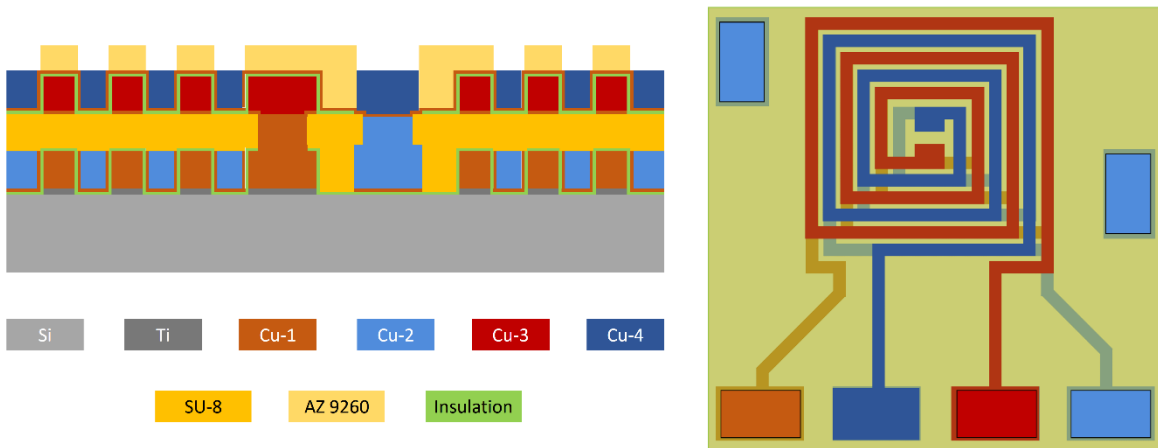
Figure 7.35: Electrodeposition of the interleaved coil layer 4 in the inter-track gap of coil layer 3.

The photoresist mould is removed using acetone, and the copper seed layer is etched using ammonium persulfate [Figure 7.36]. At this point, the coil layer 3 and 4 in level 2 should be electrically isolated. However, the coil layer 4 and 2 should be connected through inter-level via.
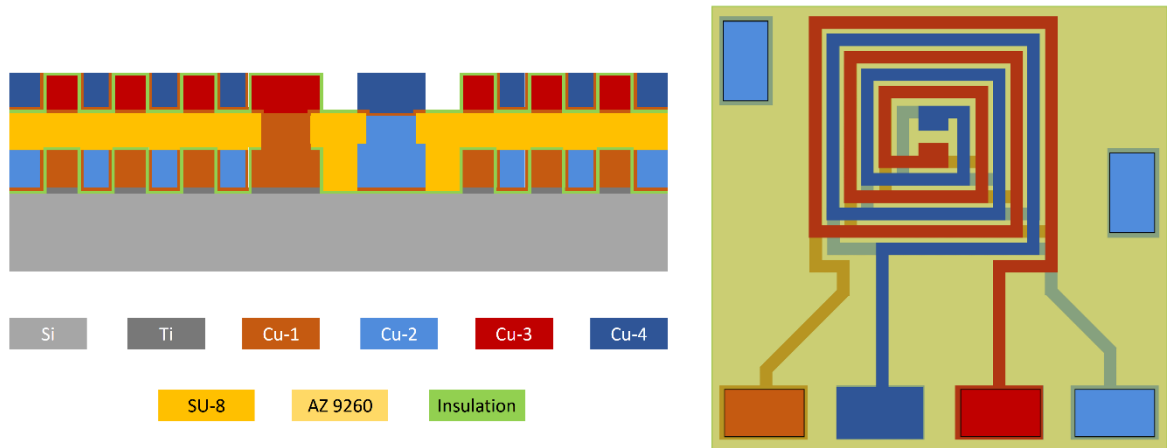
Figure 7.36: Removal of photoresist, and etching of seed layer.

As a final and optional step, the SU-8 photoresist is spin-coated as passivation layer, and the central via and connecting pads are opened by photolithography using the appropriate photomask [Figure 7.37].
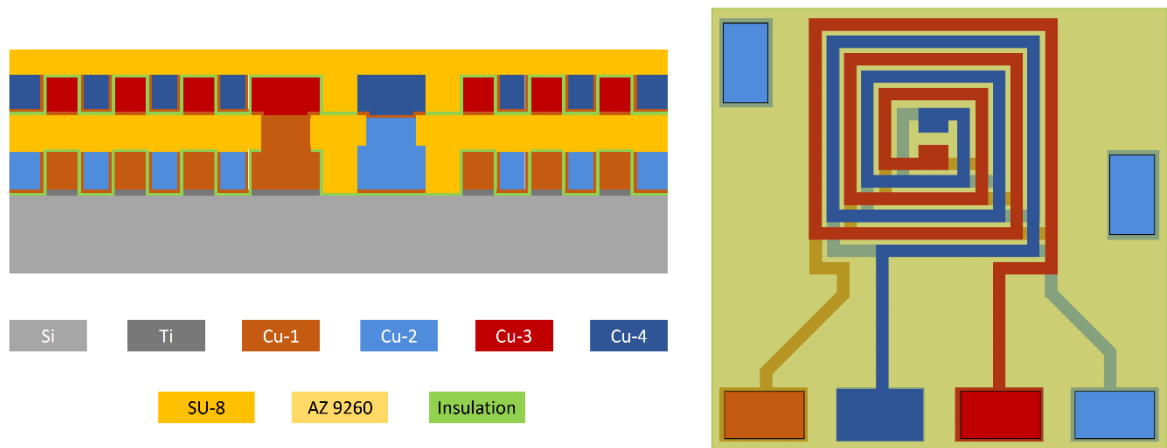
Figure 7.37: SU-8 photoresist spin-coated as passivation layer. Subsequently, the connecting pads are patterned and opened for electrical connection.

The described process flow would yield an ultra-dense multi-layer micro-coil, with two coil layers in each level. The coil layers in each of the levels will be electrodeposited such that one layer is interleaved within the inter-track gap of another layer, and the two layers are designed to be electrically insulated from each other by a thin dielectric layer. Each of the coil layers will be connected to the coil layers of the next level through vias at the centre of the spiral coil topology. The fabrication process can be repeated to develop even more coil layers, which could significantly increase the effective number of turns.

7.5 Fabrication process

The micro-coil fabrication process is discussed in detail in this section, along with the results at each step of the process flow. As an exploratory work, the first two coil layers of level 1 are developed, where several dielectric materials are used as insulation between the layers. The various steps of the fabrication process are carried out by the Tyndall Fab Team lead by Joe O'Brien. The results of the fabrication process and electrical characterization are discussed in the consequent subsections.

7.5.1 Cleaning and preparing the wafer

The ultra-dense micro-coil fabrication process begins with the cleaning and preparation of the substrate silicon wafer (4 inch diameter, 500 µm thick, <100>). The wafer is first dipped in acetone for 1 minute to remove the organic impurities. This is followed by dipping in methanol for 2 minute, which removes the acetone residue. Then running DI water is used to remove the residue of methanol. Finally, the wafer is blow-dried using nitrogen gas.

7.5.2 Sputter deposition of Ti/Cu seed layer

The wafer is then transferred for sputter deposition of titanium and copper seed layer using the Nordico 2500 RF magnetron sputterer. First, the wafers are loaded and the chamber is evacuated down to a pressure of 10^{-5} mbar using a mechanical pump. At a chamber pressure $< 10^{-5}$ mbar, the cryogenic pump is started to create even lower vacuum pressure of 2.4×10^{-7} mbar. Then the chamber is filled up by argon gas until the pressure increases to 7.6×10^{-4} mbar. The radio frequency generator is then turned on, and 20 nm thick Ti is sputter deposited using with 0.3 kW power for 5 minutes. This is followed by the deposition of 200 nm thick Cu at 1 kW power for 5 minutes. The Ti layer serves as the adhesion layer between the silicon wafer and the sputtered copper, while the copper layer serves as the seed layer for the subsequent electrodeposition process. Both deposition steps are performed in inert argon gas environment at 7.6×10^{-4} mbar pressure at room temperature. Finally, the vacuum is disabled and the wafers are retrieved.
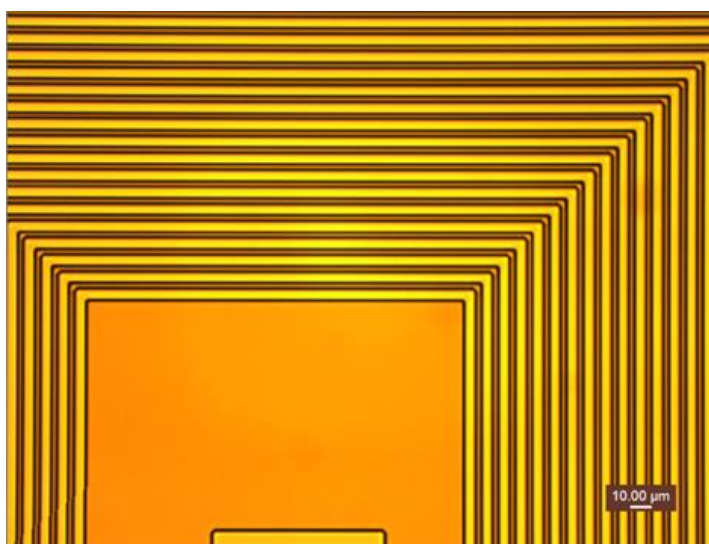
7.5.3 Photolithography of the first coil layer

The wafer with sputtered seed layer is first baked on hotplate at 110º C for 2 minutes to dehydrate. Next, the wafer is spin-coated with AZ-9260 photoresist using WS-650MZ spin coater. First, the photoresist is dispensed on the wafer which is placed on top of the rotating vacuum stage of the spin-coater. Then following spin sequences are performed:

a) Spin at 100 rpm for 10 seconds
b) Spin at 500 rpm for 5 seconds
c) Spin at 3000 rpm for 30 seconds

The spin sequences are followed by hotplate bake at 110º C for 80 seconds, and the wafer is rehydrated for 5 minutes. Then the wafer is mounted in the spin coater, AZ-9260 is dispersed, and the previous spin sequence is repeated, which is followed by hotplate bake at 110º C for 160 seconds. During the photoresist spin coating, edge bead removal (EBR) is applied to eliminate the formation of thick photoresist layer/ beads near the periphery of the wafer. A 20 µm thick AZ-9260 photoresist layer is developed at the end of the spin coating process.

The wafer with AZ-9260 photoresist coating is loaded in Suss MicroTec MA6 mask aligner, and exposed for 55 seconds in UV ray. The wafer is then developed in AZ 400K developer (dilution 1:3) for 3 minutes. The wafer with the first coil layer patterned in photoresist mould is then transferred for electrodeposition.
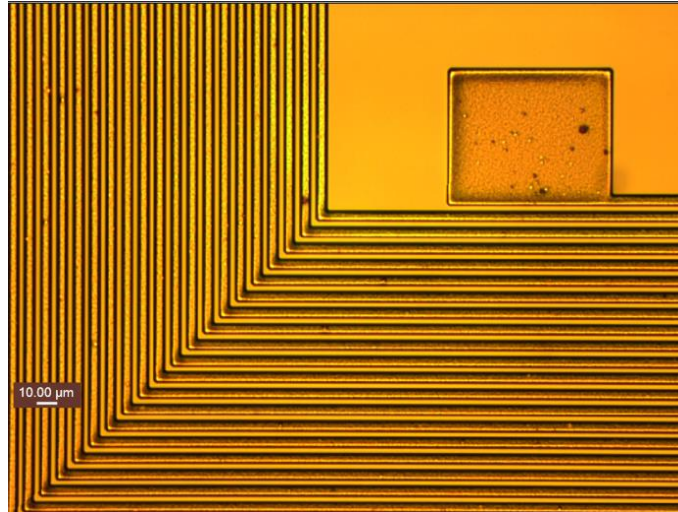

Figure 7.38: First coil layer after photolithography and developing the exposed wafer.

7.5.4 Electrodeposition of the first coil layer

Prior to the electrodeposition process, the wafer is cleaned in S20 etchant (diluted H_2SO_4 and H_2O_2) for 30 seconds to remove copper oxide and other contaminants from the seed layer surface. Then the wafer is treated in oxygen plasma at room temperature and 2×10^{-2} mbar pressure using 300 watt power in the March Plasmod for 30 seconds. This oxygen plasma treatment renders the seed layer surface hydrophilic, which facilitates the electrodeposition process by increasing adhesion. Following the plasma treatment, the electrodeposition of copper coil layers is performed using an acidic copper plating bath ($CuSO_4$ and H_2SO_4 solution with other additives, manufactured by Schlotter Ltd.) in a Digital Matrix electroplating line. The wafer is mounted on the cathode such that the Ti/Cu seed layer is in electrical contact with the electrode. The cathode and the wafer is rotated at 10 rpm during the electrodeposition process to provide stimulation in the solution and promote uniform deposition of copper in the coil track areas.

Parameter	Value	Unit
Ramp Current	0.08	A
Ramp Time	120	s
Ramp Charge	4.8	C
Constant Current	0.08	A
Constant Time	1964	s
Constant charge	157.1	C
Total Time	2084	s
Total Charge	162	C
Amp/hr	0.015	A/hr
Rotational speed	10	rpm
Ep	0.26	V

At the end of the electrodeposition process, the wafer is dismounted from the cathode, and rinsed in DI water.

Figure 7.39: First coil layer after electrodeposition of copper and etching of remaining AZ 9260 photoresist mould.

7.5.5 Etching of Ti/Cu seed layer

After electrodeposition of the first coil layer and removal of the photoresist mould by acetone, the copper seed layer is etched by dipping the wafer in ammonium persulfate solution (20 g $(NH_4)_2S_2O_8$ in 100 ml solution) for 60 seconds. This is followed by etching of the Ti adhesion layer by dipping the wafer in a diluted HF solution (1:1:20 HF: H_2O_2: DI water) for 10 seconds. The wafer is then thoroughly rinsed in DI water and blow dried using pressurized N_2 gas.

After the electrodeposition of the first coil layer and the etching of the photoresist mould, copper seed and titanium adhesion layers, the wafer is transferred for deposition of dielectric insulation material on top of the first coil layer.
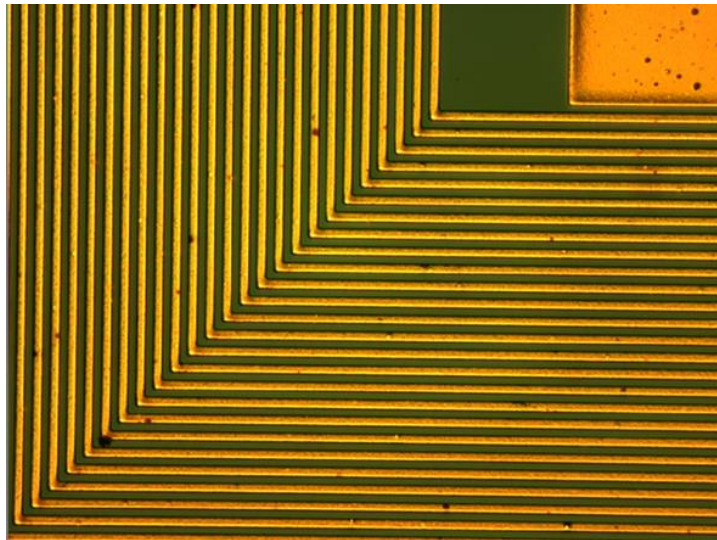
Figure 7.40: First coil layer after etching of the copper seed layer and the titanium adhesion layer.

7.5.6 Deposition of the insulation layer

Following the patterning and electrodeposition of the first coil layer, a thin conformal coating of dielectric material is deposited on the coil to serve as the insulation between the first and second coil layers. In order to identify an appropriate insulating material, four different materials deposited by different processes are investigated. The process for deposition of each of these materials are described here.

a) Silicon dioxide

The silicon dioxide insulation layer was deposited by plasma enhanced chemical vapour deposition (PECVD) process using STS Multiplex instrument. In this process silane (SiH_4) is reacted with N_2O gas at 350 ºC temperature and 650 mT pressure, providing a deposition rate ~ 35 nm/ min. Dielectric oxide films with four different thickness – 100 nm, 200 nm, 500 nm and 1 µm were deposited.

b) Silicon nitride

The silicon nitride insulation layer was deposited by plasma enhanced chemical vapour deposition (PECVD) process using STS Multiplex instrument. In this process silane (SiH_4) is reacted with ammonia (NH_3) gas at 350 ºC temperature and 650 mT pressure, providing a deposition rate ~ 10 nm/ min. The deposited film thickness was 300 nm.

c) Parylene C

The Parylene C insulation layer was deposited using a SCS Labcoter Parylene deposition system. Parylene C is a poly-para-xylylene material with aliphatic carbon bonds and one chlorine group on the main-chain phenyl ring [Jackson, et al. [2]]. The wafer is cleaned prior to Parylene deposition, and the process starts with the vaporization of a Parylene dimer at 175 °C. The dimer then goes through pyrolysis at 690 °C, which breaks up the dimer into monomer. The monomer is then deposited onto the substrate at room temperature (pressure 3.33 Pa) as a polymer with a deposition rate of ~2 µm/ hour. The deposited thickness of the Parylene C coating was 1 µm.

d) Aluminium nitride

The aluminium nitride insulation layer was deposited on the first copper coil layer using DC sputtering process. In this process a 99.99% pure Al target was reacted with N_2 in a nitrogen-rich (100%) environment at 250 °C temperature and 6 mT pressure [Nathan, et al. [3], [4]]. The deposited AlN film thicknesses were 0.5 µm and 1 µm.
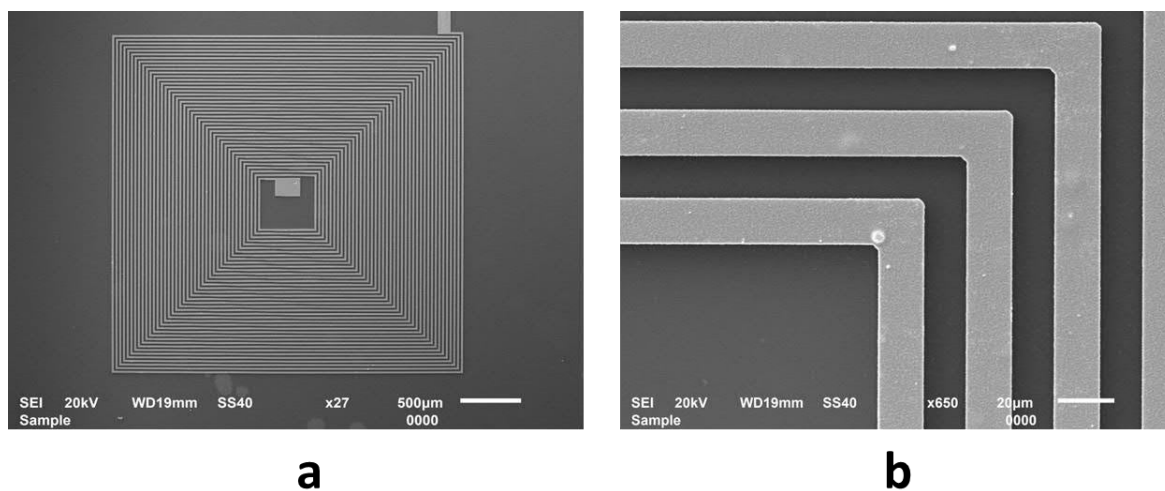
Figure 7.41: (a) and (b) SEM image of the first coil layer following silicon dioxide deposition.

7.5.7 Photolithography and electrodeposition of the second coil layer

After the conformal deposition of the intermediate insulating dielectric layer, the second interleaved copper coil layer is developed by repeating the process steps described in 7.5.2 − 7.5.5. The Ti/Cu seed layer (20 nm/ 200 nm) is sputter deposited using the Nordico 2500 sputterer, and the AZ 9260 photoresist is spin coated on the wafer. At this step, it is

important to ensure proper distribution of the photoresist such that bubble formation within the interleaved gap between the tracks is avoided. This has been achieved by lowering the maximum spin speed from 3000 rpm down to 1000 rpm. During exposure under UV radiation, the alignment of the wafer with the photomask is critical to ensure that the second coil layer tracks are patterned within the inter-track gaps of the first coil layer. In addition, the risk of over exposure is enhanced during this process since the underlying vertical sidewalls of the first coil layer pattern are coated with reflective copper seed layer. Furthermore, care has been taken to avoid over-plating by reducing the electrodeposition time and current. Finally the remaining photoresist is removed, and the Ti/Cu seed layer is etched using the process step described in 7.5.5.

7.5.8 Etching of dielectric from via and connecting pads

In order to make connection to the bond pads and via the dielectric layer was etched from the coil layer 1 bond pads and vias. A photoresist (AZ 9260) layer is spin coated on the wafer and the patterns for the bond pads and via openings were transferred by photolithography. Then the silicon dioxide and silicon nitride were etched using buffered oxide etching (BOE) process. The BOE etchant is a diluted HF solution with a buffering agent, such as ammonium fluoride, which offers slower and controlled etching rate compared HF etch.

7.6 Results and discussions

The results of the coil fabrication process are discussed in this section. The coil resistances are measured after the electrodeposition of the first coil layer, after the dielectric deposition, and after the electrodeposition of the second interleaved coil layer.

7.6.1 Measurement after electrodeposition of coil layer 1

The measurement of resistance between the central via pad and the external bond pad of the first coil layer is performed. Table 7.2 shows the resistance measurement data from the fabricated coils. The resistance measurement results are very well correlated with the calculated resistance values, with < 10% variation. As expected, the coils with thinner track and gap dimensions possess larger number of turns and exhibit higher resistance.

Table 7.2: Measured and calculated number of turns and resistances for different copper track width and inter-track gap width of the coil layer 1

Coil Parameter	Number of turns	Resistance (Ω)	
Track width × Gap width		Measured	Calculated
10 mm × 10 mm	60	62.6	64.6
15 mm × 15 mm	40	27.1	28.2
20 mm × 20 mm	30	15.3	16.5

However, the measured resistance shows marginally lower values in comparison to the calculated resistance. This can be attributed to the fact that the first layer coil tracks are somewhat wider than the designed width, which may result from over-developed sidewalls of the AZ9260 photoresist.

7.6.2 Measurement after electrodeposition of coil layer 2

This measurement is performed between the outer bond pads of the first and second coil layers after the dielectric layers were etched from first coil layer pads in order to confirm electrical insulation between the coil layers. However, the measurement results show that the DC resistance between the two coil layers are very small (0.2 – 10 Ω), which clearly indicate a compromised insulation. Therefore, an extensive analysis of the coil cross-sections and insulation layers is performed to determine the potential causes of the insulation failure.

Insulator	Thickness (nm)	Resistance (Ω)		
		Max.	Min.	Avg.
Silicon dioxide	500	1.6	0.1	0.6
Silicon nitride	1000	1.2	0.1	0.6
Parylene C	1000	10.9	0.8	5.7
AlN	500	2.3	0.2	0.8
AlN	1000	20.6	0.8	1.5

7.6.3 Discussion

The reason for failure of the insulation between the first and second coil layers has been investigated for each of the insulating materials. The investigations included observation

under microscope and SEM, FIB (focused ion beam) cross-sectioning and EDX (energy dispersive X-ray spectroscopy) mapping.

Observation of oxide dielectric deposited on the first coil layer shows that the oxide layer is brittle and prone to developing cracks, which might lead to electrical connection between the top and bottom coil layers.
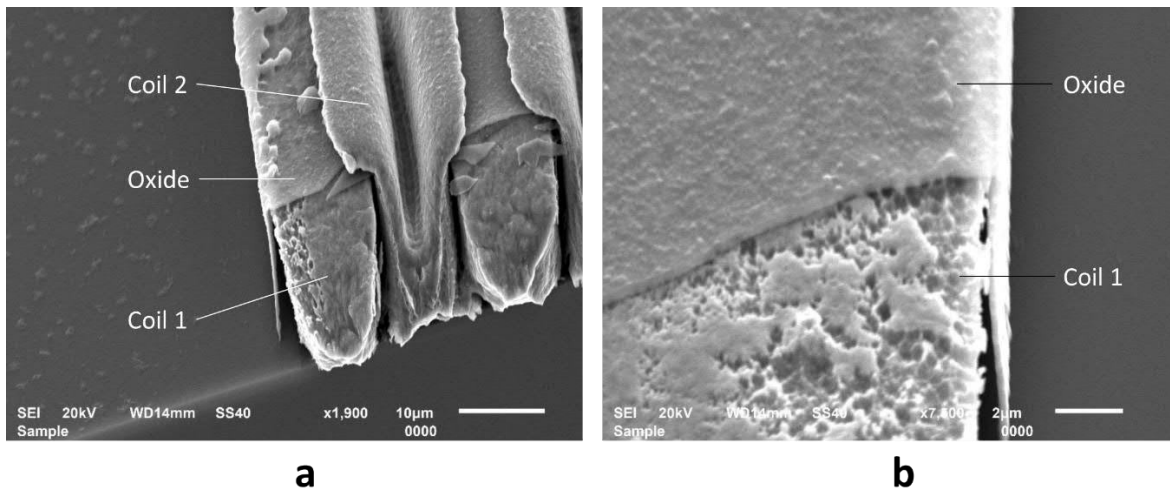
**Figure 7.42: (a) Cross-sectional SEM of coil layers 1 and 2 with oxide insulation layer. (b) Oxide dielectric deposited on top of coil layer 1.**

Another potential reason for lack of insulation could be the diffusion of copper ions through the oxide layers, a phenomenon which prevented the use of copper interconnects in the integrated circuits for several decades [Rosenberg, et al. [5]]. It has been reported that most of the copper ion drift in silicon dioxide occur due to the oxidation of copper at the interface [He and Lu [6]], which can be activated in an oxidising environment such as acid copper electrodeposition bath.
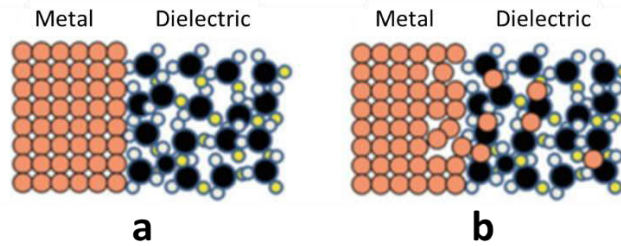
Figure 7.43: A schematic diagram showing the diffusion of metal ions into dielectric materials at the metal-dielectric interface [6]. (a) An ideal sharp interface prior to diffusion. (b) A diffused interface after the penetration of metal ions into the dielectric.

A FIB-milled cross-sectional area of the coil layer 1 with oxide dielectric has been illustrated in Figure 7.44. Although the oxide coating shows good conformal coverage on the top surface and the side-walls in the SEM image, the EDX map of the O-K series [Figure 7.45] shows negligibly small amount of oxygen on the side-walls. Therefore, it can be inferred that there has been substantial diffusion of copper into the oxide layer, which leads to poor insulation.
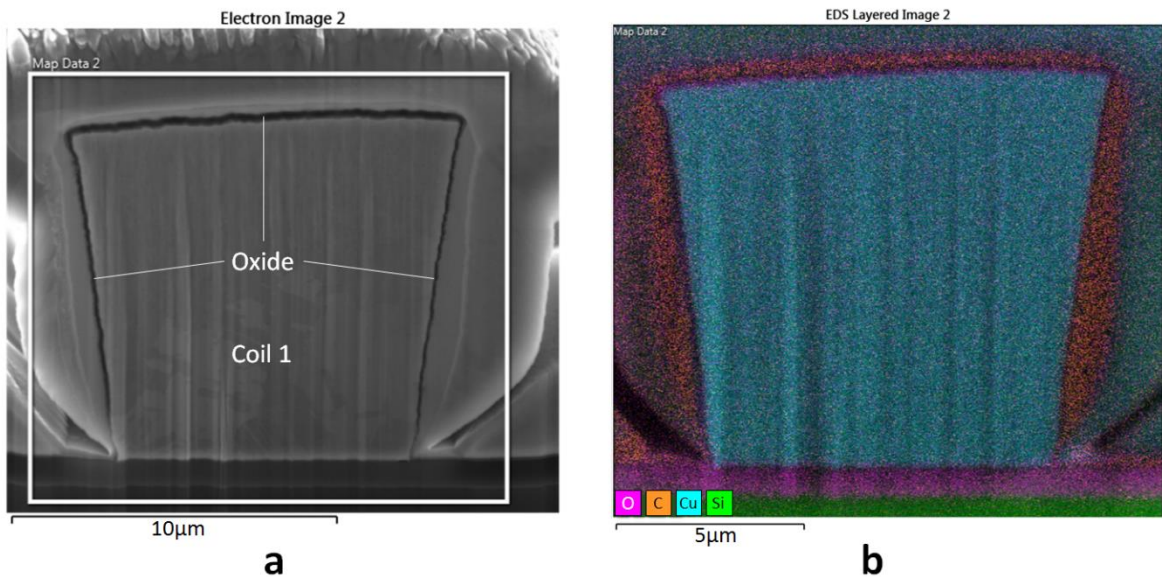

Figure 7.44: (a) SEM image of FIB cross-section of coil layer 1 coated with oxide dielectric. (b) EDX layered imgae of the area within the white square. Carbon was deposited on the oxide layer prior to FIB for protection.
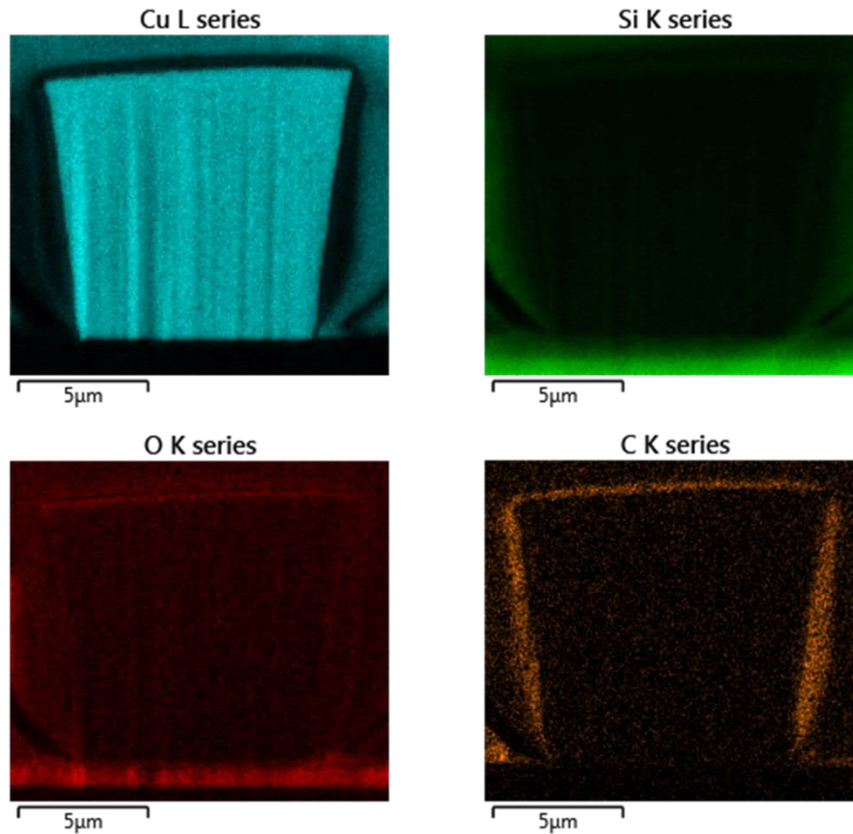
Figure 7.45: EDX maps of FIB cross-sectioned coil layer 1 with oxide dielectric. O-K series shows almost negligible oxide on the top and side-walls, which indicates possibility of diffusion of copper into oxide. Carbon was deposited as protective layer prior to FIB milling.

The observation of PECVD silicon nitride dielectric deposited on the first coil layer shows microscopic cracks in the nitride layer [Figure 7.46]. Silicon nitride is a brittle ceramic material, which is prone to development of cracks under thermal stress. Therefore, sputter deposition of the second copper seed layer and electrodeposition of the coil layer 2 might result into electrical connection between coil layers 1 and 2 through the cracks, and exhibit compromised insulation between the coils.
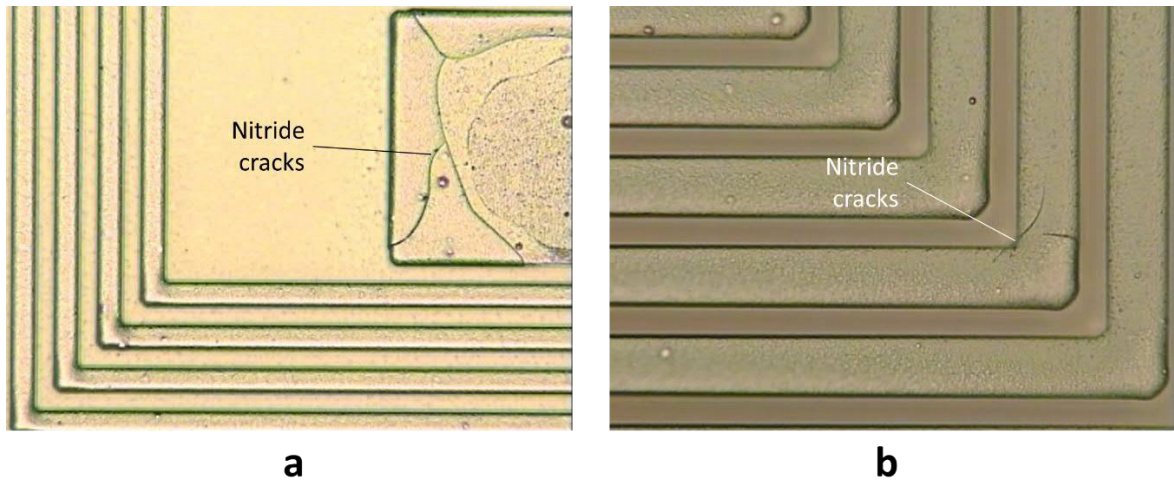
Figure 7.46: Cracks in the silicon nitride insulation layer at (a) the central vias and (b) the coil tracks.

The Parylene C dielectric deposited on the coil layer 1 exhibited formation of micro-bubbles and lack of adhesion to the silicon and copper surfaces. These phenomena can lead to compromise in the insulation and subsequent short circuit between coil layer 1 and 2.
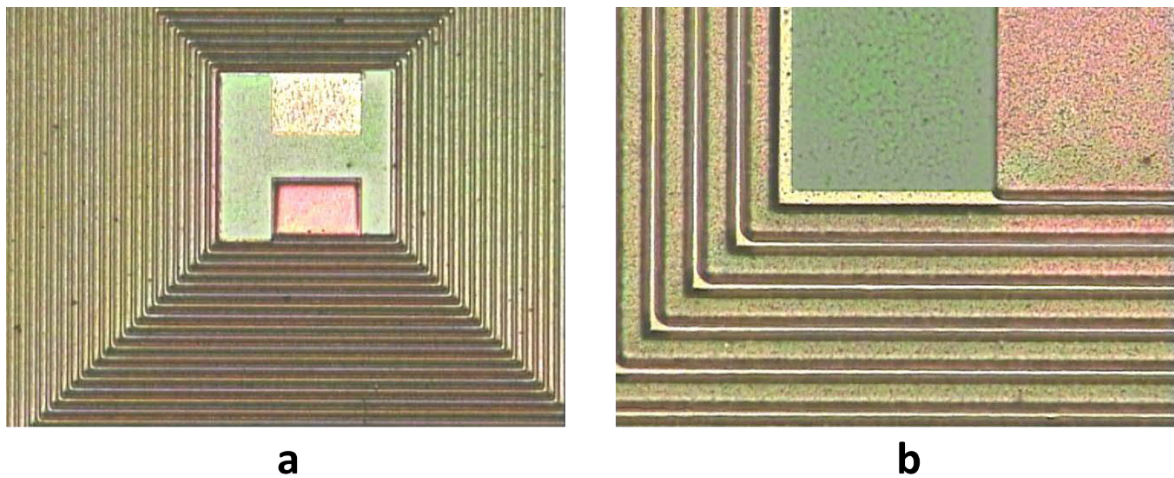
Figure 7.47: (a) Ultra-dense coil with 1 μm thick Parylene C as insulating layer between coil layers 1 and 2. (b) Formation of micro-bubbles in the Parylene C.
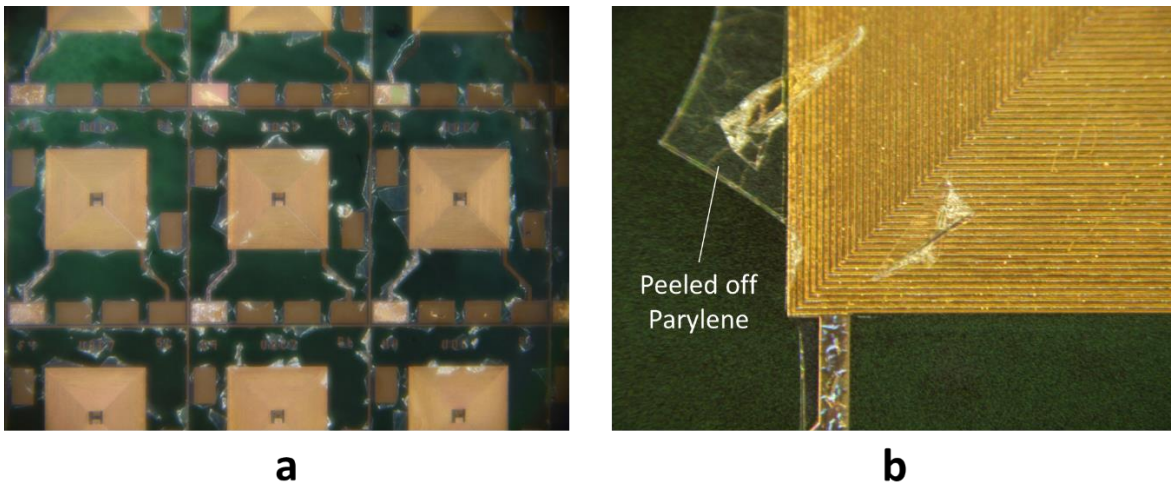
**Figure 7.48: (a) Ultra-dense coil with 1 μm thick Parylene C exhibits lack of adhesion to the copper coil and silicon surfaces. (b) Peeling of Parylene from coil structure.**

The aluminium nitride dielectric shows excellent conformal coverage of the side-walls and initially exhibited very high resistance before electrodeposition of the second coil layer. However, resistance measurements data following the electrodeposition of the second coil layer above the aluminium nitride exhibits very low resistivity between coil layers 1 and 2.
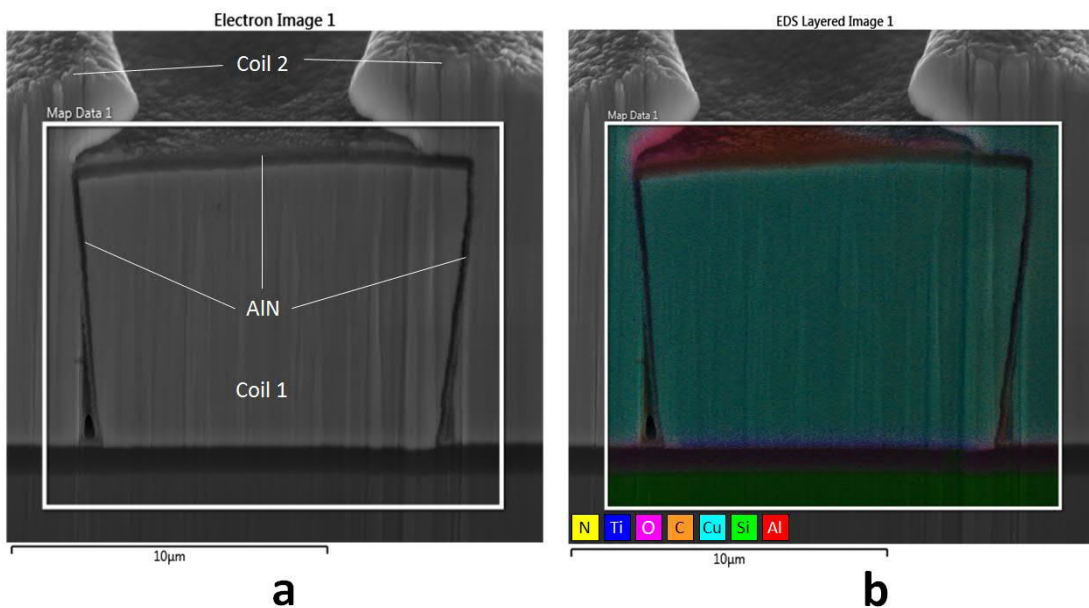
Figure 7.49: (a) SEM image of ultra-dense micro-coil FIB cross-section with AlN insulation. (b) EDX map overlayed on the SEM cross-section.

One of the potential reasons for the low resistance of the AlN dielectric could be the significantly thinner layer, which is as thin as ~100 nm near the top of the sidewalls. This is substantially smaller than the desired AlN thickness of >500 nm. The thin AlN layer could be subject to dielectric breakdown during the electrodeposition of coil layer 2, compromising the resistivity of the insulating layer.

Table 7.3: Variation of AlN dielectric breakdown potential with applied voltage

Thickness (nm)	Dielectric breakdown potential (V)
100	1
200	2
500	5
1000	10

Although the aluminium nitride dielectric coating is conformal [Figure 7.50], the FIB cross-sectioned EDX map shows significant amount of oxygen at the sidewalls and surface. The source of this oxygen could be the atmosphere, or the highly acidic and oxidative copper electrodeposition bath. Regardless of the source, the oxygen could potentially interact with the AlN and form aluminium oxide (Al_2O_3) on the surface of the AlN layer. However, the Al_2O_3 itself is a material with very high resistivity ($2.5 \times 10^6 - 1 \times 10^{14}$ Ω-cm), and therefore unlikely to have any negative impact on the insulation.
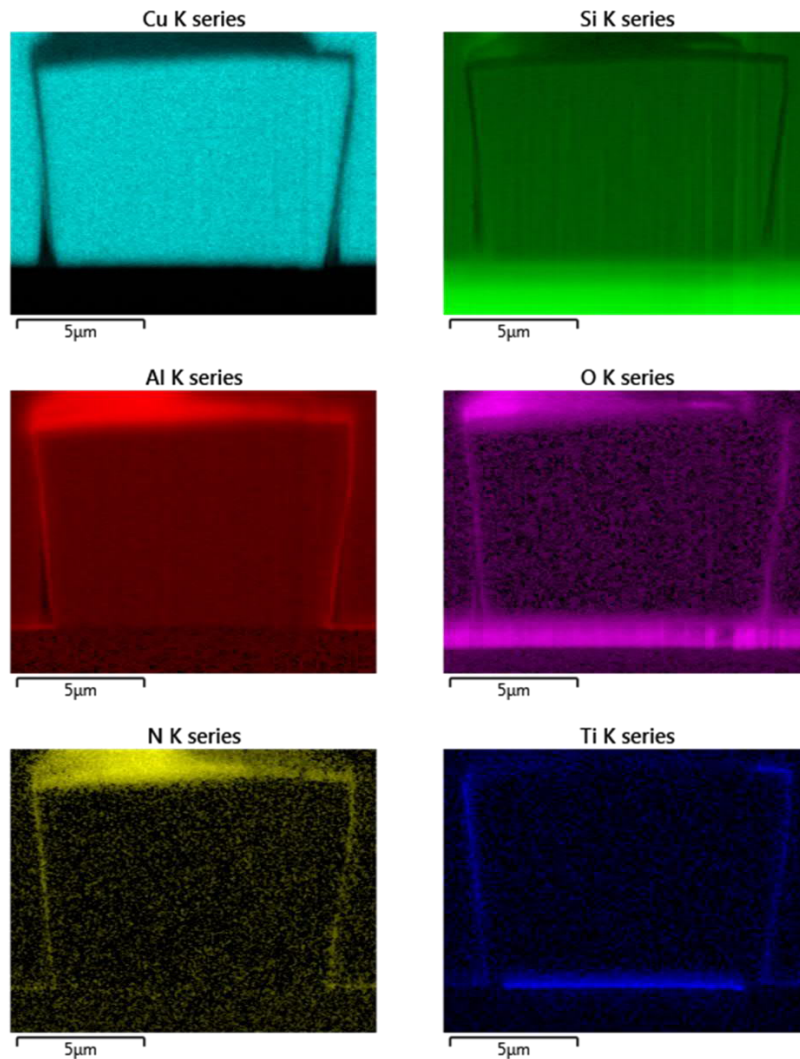
Figure 7.50: EDX maps of FIB cross-sectioned coil layer 1 with aluminim nitride dielectric. Al-K and N-K series shows conformal coverage on top and side-walls. Ti-K series shows the seed layer for electrodeposition of the coil layer 1 and 2.

7.7 Conclusions

This chapter described the development of an ultra-dense planar spiral coil topology for application in MEMS vibration energy harvesters. The ultra-dense micro-coil is designed to substantially increase the packing factor and number of turns, resulting in higher magnetic flux linkage and enhanced harvested power. The proposed design consists of two coil levels with two interleaved planar micro-coils in each level. Within each level, the two interleaved coils are designed to be electrically insulated from each other by a thin dielectric layer. Also, the interleaved coils of the first and second level are interconnected through inter-level vias. This arrangement offers the flexibility of the coils being connected in series or parallel through the external connecting pads. The simulation results of the

proposed ultra-dense micro-coil shows significant (factor of ~ 2) increase in harvested power over conventional planar double layer micro-coils. A detailed description of the process flow for fabrication of the proposed ultra-dense micro-coil has been provided. The next section described the fabrication of the first two coil layers, with four different dielectric materials as the insulation between the interleaved coils. However, none of the dielectric materials (silicon dioxide, silicon nitride, Parylene C, and aluminium nitride) were able to achieve electrical insulation between the two coil layers. Investigative analysis of the fabricated coil micro-structures have revealed different potential reasons for failure of the insulation using different dielectrics. These results can be used to derive insight to optimize the design, material and process for fabrication and implementation of ultra-dense micro-coils for energy harvesters and other applications.

References

[1]   F. Herrault, S. Yorish, T. M. Crittenden, C. H. Ji, and M. G. Allen, "Parylene-Insulated Ultradense Microfabricated Coils," *Journal of Microelectromechanical Systems,* vol. 19, pp. 1277-1283, 2010.

[2]   N. Jackson, F. Stam, J. O'Brien, L. Kailas, A. Mathewson, and C. O'Murchu, "Crystallinity and mechanical effects from annealing Parylene thin films," *Thin Solid Films,* vol. 603, pp. 371-376, 2016.

[3]   J. Nathan, O. K. Rosemary, W. Finbarr, O. N. Mike, and M. Alan, "Influence of aluminum nitride crystal orientation on MEMS energy harvesting device performance," *Journal of Micromechanics and Microengineering,* vol. 23, p. 075014, 2013.

[4]   J. Nathan, K. Lynette, and M. Alan, "Flexible-CMOS and biocompatible piezoelectric AlN material for MEMS applications," *Smart Materials and Structures,* vol. 22, p. 115033, 2013.

[5]   R. Rosenberg, D. C. Edelstein, C. K. Hu, and K. P. Rodbell, "Copper Metallization for High Performance Silicon Technology," *Annual Review of Materials Science,* vol. 30, pp. 229 - 262, August 2000.

[6]   M. He and T.-M. Lu, *Metal-Dielectric Interfaces in Gigascale Electronics*, 1 ed. vol. 157. New York: Springer-Verlag New York, 2012.

8 POWER MANAGEMENT FOR ELECTROMAGNETIC ENERGY HARVESTERS

This chapter discuss the development of a power management module for application with electromagnetic vibration energy harvesters. In order to minimize power loss due to diode forward conduction drop, a diode equivalent low voltage drop rectifier circuit has been used. The subsequent rectified output is then conditioned using an off-the-shelf low voltage boost regulator. The power management module has been tested with a linear harvester under harmonic resonant excitation, and with a nonlinear bistable harvester under bandlimited random vibrations, at different accelerations.

8.1 Introduction

The electricity generated by vibration energy harvesters are AC type, which is required to be converted into DC form by a power conditioning circuit for application in conventional electronics. The power conditioning circuit includes a rectifier section to convert the input AC voltage into a DC voltage. The conventional rectifiers are constructed of multiple diodes, which carry current with a voltage drop across them. The ideal diode is expected to behave like a mono-directional switch, which has zero resistance in the forward direction with zero (or, negligibly small) forward voltage drop, and infinite resistance in the reverse direction, with zero (or, negligibly small) reverse current. However, the commercially available diodes exhibit non-ideal behaviour, where significant forward voltage drop (0.3 – 0.7 V), and reverse leakage current (0.2 – 2 µA) generally occur. The forward bias voltage drop often results in loss of a significant amount of the harvested power, [Chandrakasan, et al. [1], Ramadass and Chandrakasan [2]], ranging from 20 – 200 µW depending on the current. This loss is even more critical for electromagnetic vibration energy harvesters than

the piezoelectric ones, since the output voltage is substantially low in case of EM harvesters than a comparable piezoelectric device. Therefore, by minimizing the diode voltage drops, the efficiency of power conversion circuits for low voltage micro-power generators can be improved significantly.
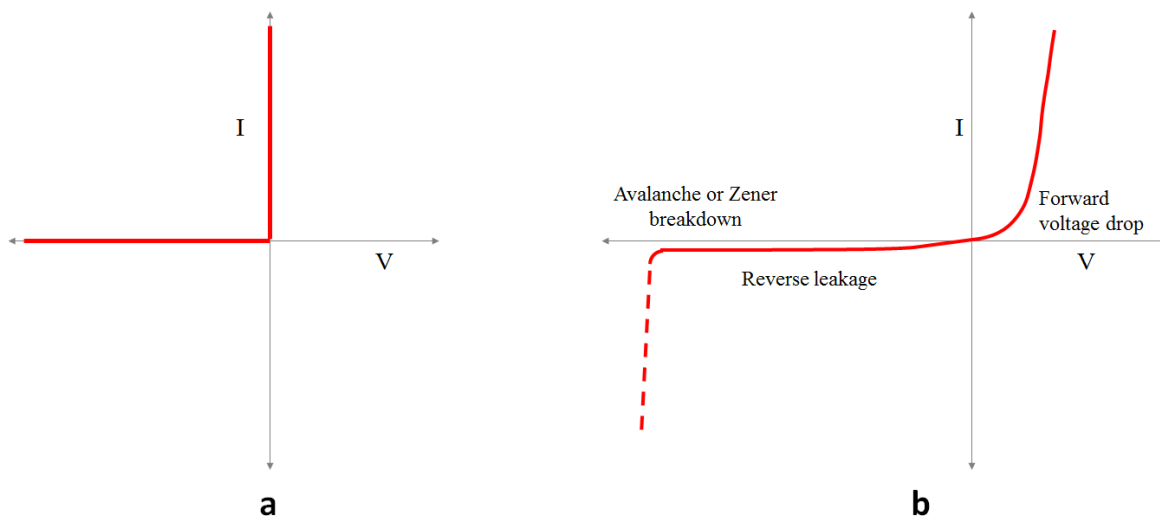
Figure 8.1: (a) Ideal diode and (b) Practical diode characteristics. Contrary to the ideal diode, the practical diode induce voltage drop in forward bias, which result in power loss in rectifier circuits.

8.2 Design of the circuit topology

A low forward voltage drop circuit topology equivalent to a diode [Karthikeyan and Amrutur [3]] is used to construct a full-wave bridge rectifier (FBR) circuit for use with an electromagnetic vibration energy harvester. The requirements of the proposed diode equivalent low voltage drop (DELVD) circuit topology has been broadly outlined as [3],

- Very low forward conduction drop;
- Should be able to block any reverse conduction;
- Should not use an additional external power supply;
- Minimum power consumption in the control circuit, if any.

The proposed DELVD circuit uses MOSFETs operating in the deep triode or linear region to imitate the forward biased condition, and the subthreshold or cut-off region to mimic the reverse biased condition. The circuit to control the DELVD circuit can be configured as a current reversal detection circuit (CRDC) using a combination of diodes and capacitor [3] or resistors and capacitor.

8.2.1 Current reversal detection circuit (CRDC)

The reversal of direction of the output current is required to be detected for switching the MOSFETs in the DELVD circuit. This can be accomplished using a simple circuit as shown in Figure 8.2.
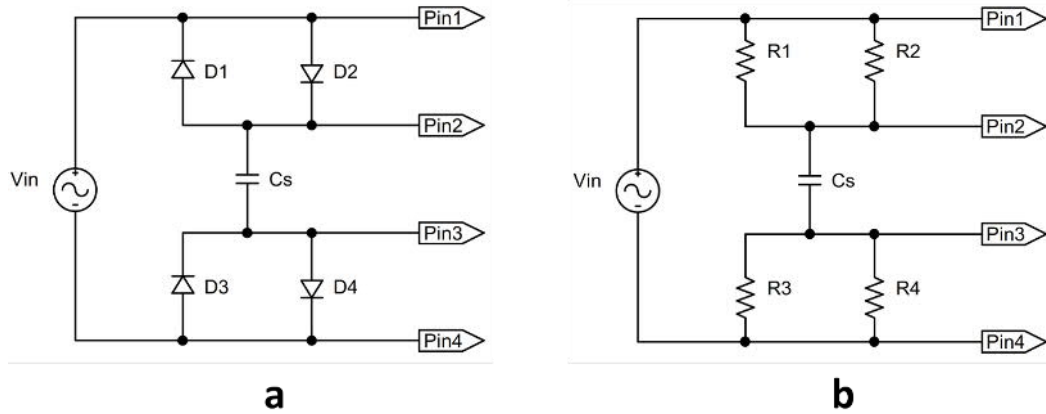
**Figure 8.2: Current reversal detection circuit (CRDC) using (a) diodes, (b) resistors.**

The working of the CRD circuit can be explained by considering a sinusoidal input voltage source (V_{in}). When V_{in} crosses zero from negative to positive, current flows into C_S through the $D2 - C_S - D4$ path and charges up the capacitor. Therefore, the voltage at Pin2 is negative with respect to Pin1, and the voltage at Pin3 is positive w.r.t Pin4. Similarly, when V_{in} crosses zero from positive to negative, the voltage at Pin2 is positive w.r.t. Pin1, and the voltage at Pin3 is negative w.r.t. Pin4. Therefore, the direction of transition of V_{in} is indicated either by the voltage at Pin2 w.r.t Pin1, or the voltage at Pin3 w.r.t. Pin4. The outputs of Pin2 and Pin3 are fed into the DELVD circuit as the control signal.

8.2.2 Diode equivalent low voltage drop (DELVD) circuit

A single DELVD circuit along with the CRD circuit has been illustrated in Figure 8.3. In the DELVD circuit, M1 and M2 are n-channel and p-channel MOSFETs, and Q1 and Q2 represent n-p-n and p-n-p transistors respectively. In the positive half-cycle of the input voltage source V_{in}, the emitter-base junction of Q1 is forward biased, which turns ON Q1. As Q1 turns ON and begins to conduct, it provides the base drive current to Q2, which is then turned ON, and begins to conduct. Therefore, the gate-source capacitor ($C_{GS,M1}$) of M1 gets connected to the sinusoidal voltage source V_{in} through Q2, and $C_{GS,M1}$ begins charging up. As the source-gate voltage of M1 ($V_{SG,M1}$) exceeds the threshold ($V_{Th,M1}$), M1 begins to conduct in the forward direction and current begins to flow into the load resistor

(R_L) and capacitor (C_L). As $V_{SG,M1}$ keeps on increasing, M1 enters into the linear regime from saturation, and the source-drain voltage V_{SD} reduces to a very low value.
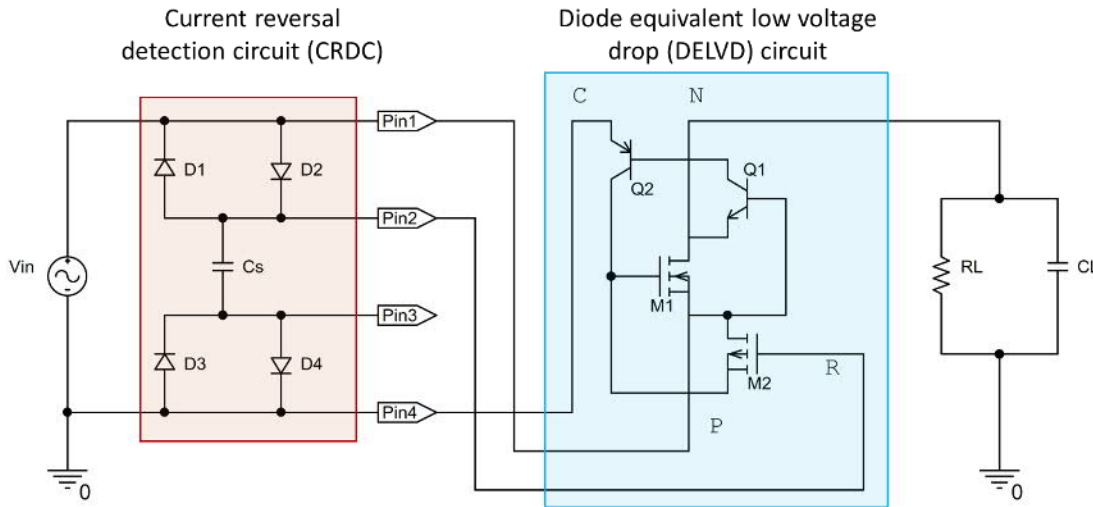
Figure 8.3: A single DELVD circuit connected to the CRD circuit.

In the negative half cycle of the input voltage Pin2 is at a higher potential than the Pin1. Therefore, the gate-source capacitor ($C_{GS,M2}$) of M2 starts charging and M2 is turned ON. This provides a discharge path for $C_{GS,M1}$ and M1 is turned OFF, which prevent any conduction in the reverse direction. Therefore, a single DELVD module can functionally imitate a diode with low forward voltage drop. Figure 8.4(a) shows a load current (I_L) vs. input voltage (V_{In}) characteristics for $R_L = 1$ kΩ, and resembles that of low drop diode. The active components (MOSFETs and BJTs) used to construct the circuit has been listed in Table 8.1.
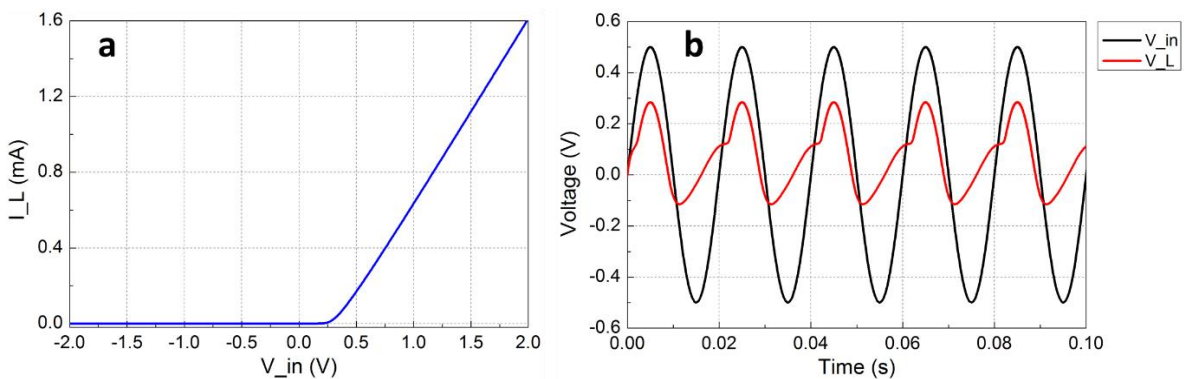
Figure 8.4: (a) DC sweep characteristics of DELVD circuit. (b) Time domain response of DELVD circuit for AC input signal.

Table 8.1: MOSFETs and BJTs used in Fig. 8.3 and 8.5

M1	M2	Q1	Q2
BSG0811NDQ2	SI3445DV	2N2369	2N5771

8.2.3 Full bridge rectifier using CRDC and DELVD circuit

A full bridge rectifier (FBR) circuit can be constructed by using four DELVD modules as shown in Figure 8.5. The electromagnetic vibration energy harvester has been represented by an equivalent electrical circuit. The method of such alternative representation of electromagnetic vibration energy harvesters have been detailed by Zhu, et al. [4]. I_m, R_m, C_m and L_m represent the current source, resistor, capacitor and inductor of the electromagnetic energy harvester equivalent circuit. The following equations associate the electrical parameters with the corresponding mechanical parameters.

$$I_m = \frac{ma}{k_e} \qquad\qquad 8.1$$

$$R_m = \frac{k_e^2}{b} \qquad\qquad 8.2$$

$$C_m = \frac{m}{k_e^2} \qquad\qquad 8.3$$

$$L_m = \frac{k_e^2}{k_s} \qquad\qquad 8.4$$

Where m is the inertial mass, a is the applied vibrational excitation, k_e is the electromagnetic coupling coefficient, which also represents the ratio of the induced voltage and the velocity of the inertial mass. The parameter b represents the damping coefficient, while k_s is the spring coefficient of the oscillator.

The output of the transducer equivalent circuit is supplied to the CRD circuit, which is connected to the DELVD full bridge rectifier module. The output of the DELVD rectifier can be fed into a boost regulator (such as ADP5090) module for further processing.
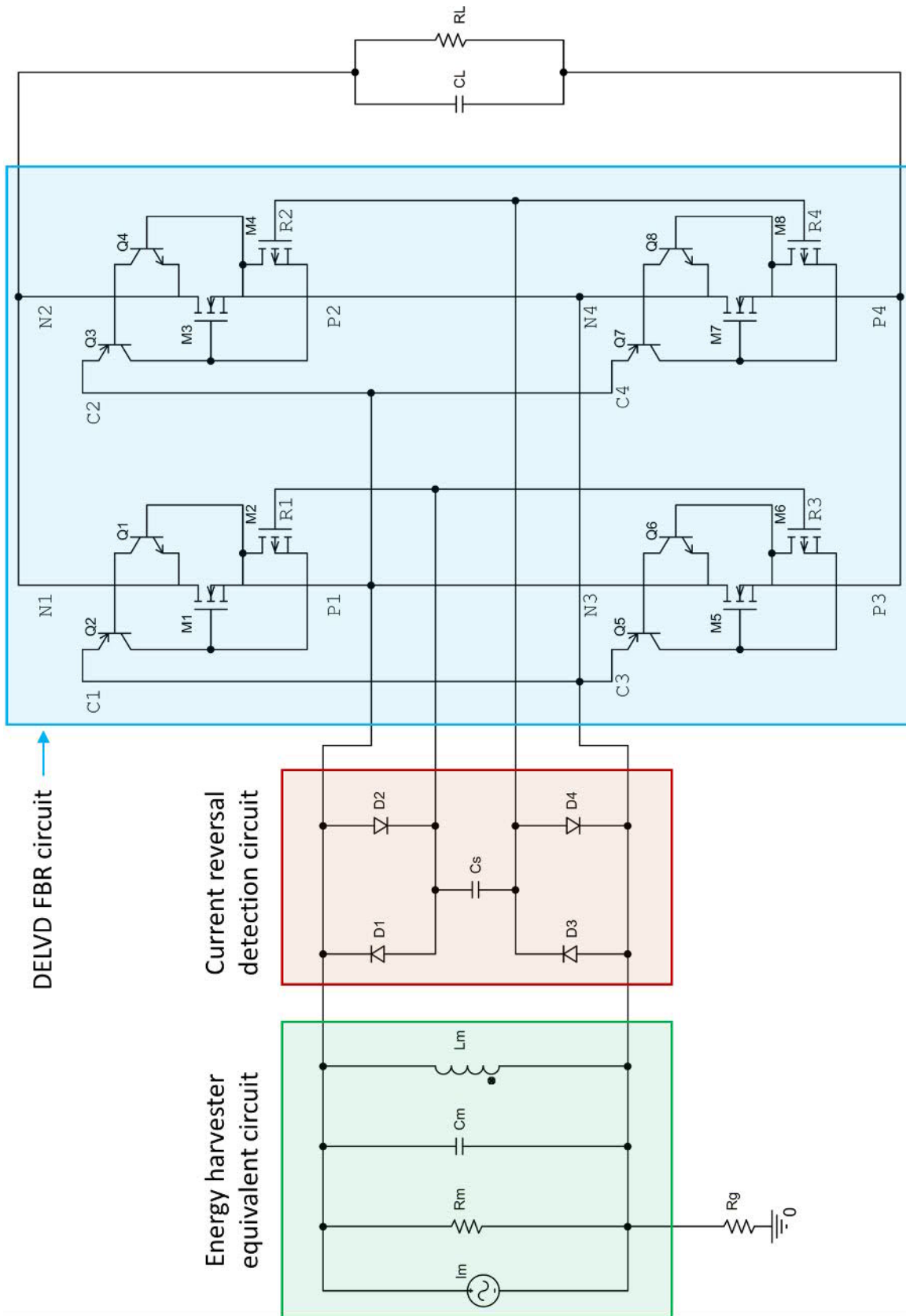
Figure 8.5: Full bridge rectifier (FBR) circuit using the DELVD and CRDC modules.

8.3 ADP5090 boost regulator

The ADP5090 is an integrated boost regulator that includes a cold-start charge pump and a maximum power point tracking (MPPT) module. The input of ADP5090 takes in DC power and delivers upto 3.5 V regulated output, which can be used to charge up super capacitors or rechargeable batteries. The ADP5090 can be started with as little as 380 mV input voltage (minimum 16 µW input power) and after start-up, the regulator functions with input voltages ranging from 80 mV to 3.3 V. Typical applications of the ADP5090 include energy harvester (photovoltaic, thermoelectric, vibrational) power management for self-powered WSNs and portable/ wearable electronics.
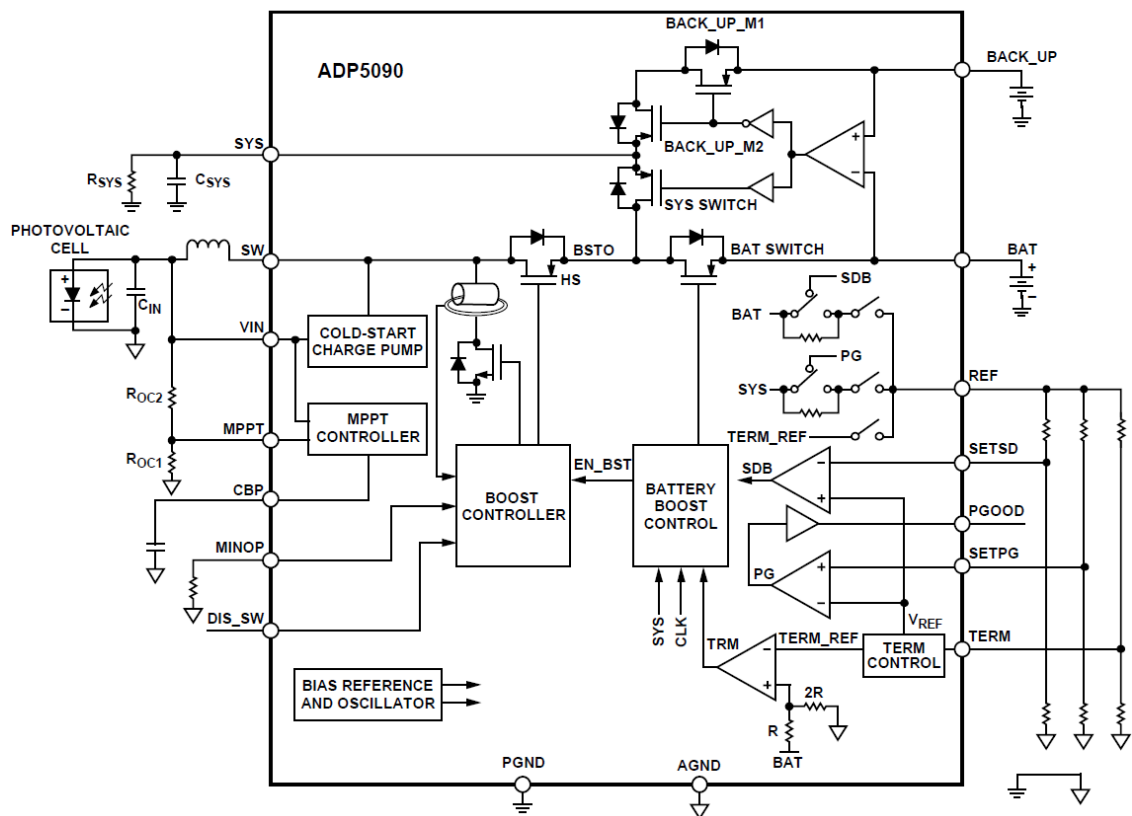

Figure 8.6: Functional block diagram of the ADP5090 boost regulator. (Data sheet).

An evaluation board for ADP5090 provides all of the passive components and connection ports necessary for use in energy harvesting power management [Figure 8.7].
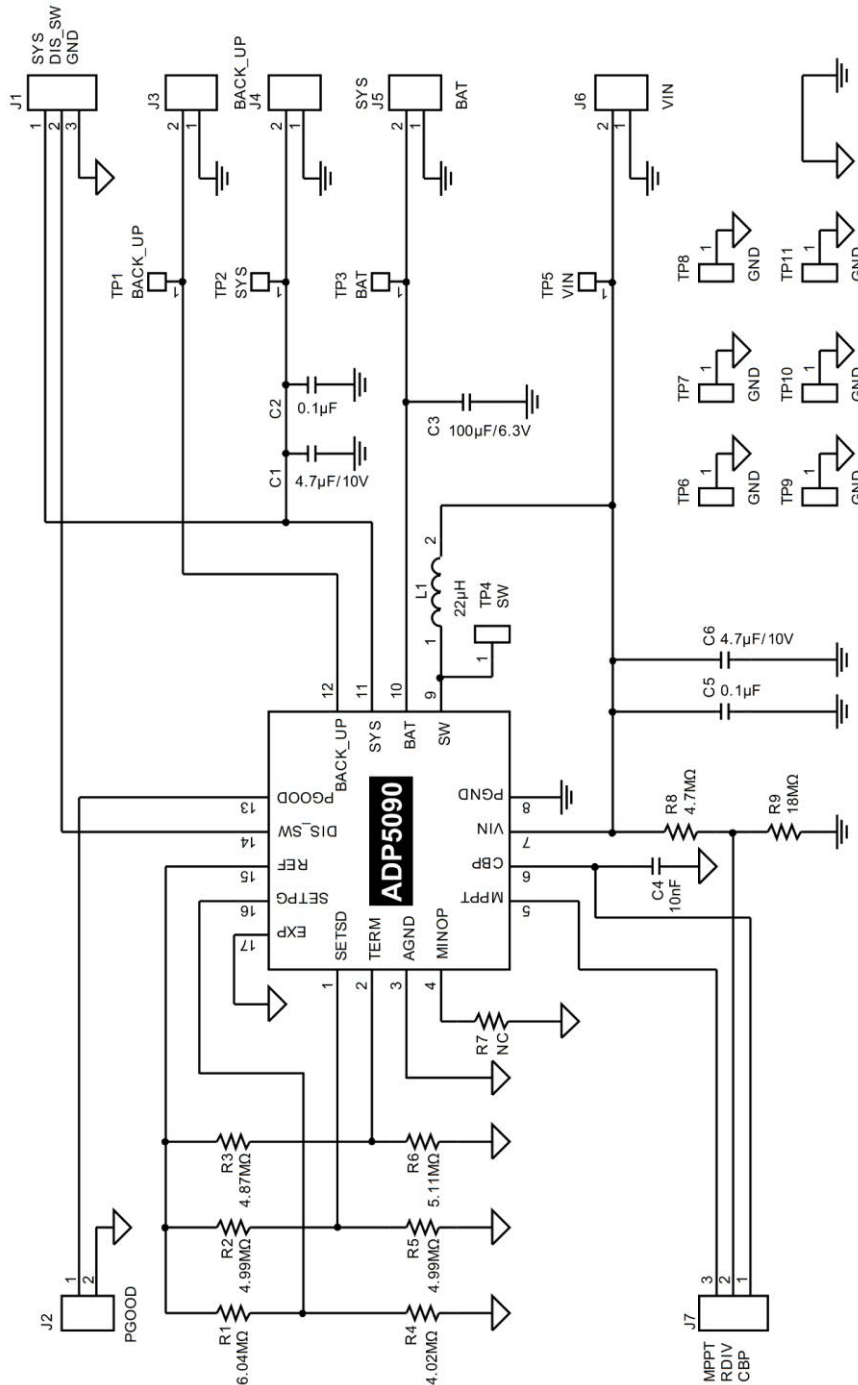
**Figure 8.7: ADP5090 Evaluation board layout.**

8.4 Experimental results and discussion

The power management circuit comprising the vibration energy harvester, CRD circuit, DELVD full bridge rectifier and ADP5090 evaluation board has been shown in Figure 8.8. The output of the DELVD rectifier (V_in) is fed into the input of ADP5090, and V_out denotes the regulated output.
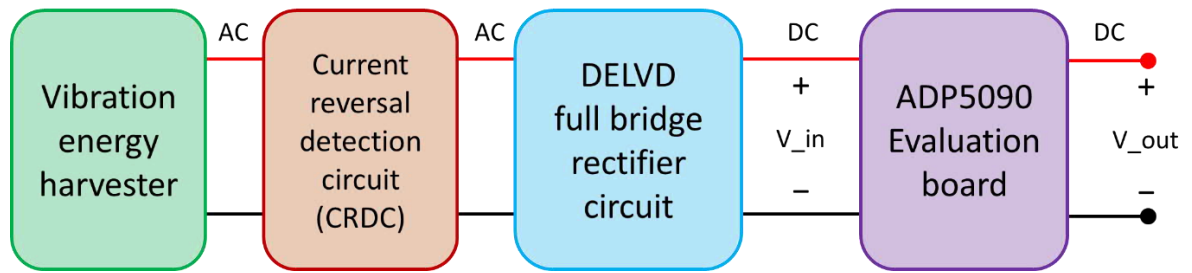
Figure 8.8: Schematic layout of the power management configuration.

The power management circuit has been tested with output from linear resonant harvester under harmonic fixed frequency excitations. Furthermore, it has been tested with output from nonlinear bistable and bistable-monostable combined energy harvester under bandlimited random vibrations. The energy harvesters used in these experiments are the same as described in Chapter 6.
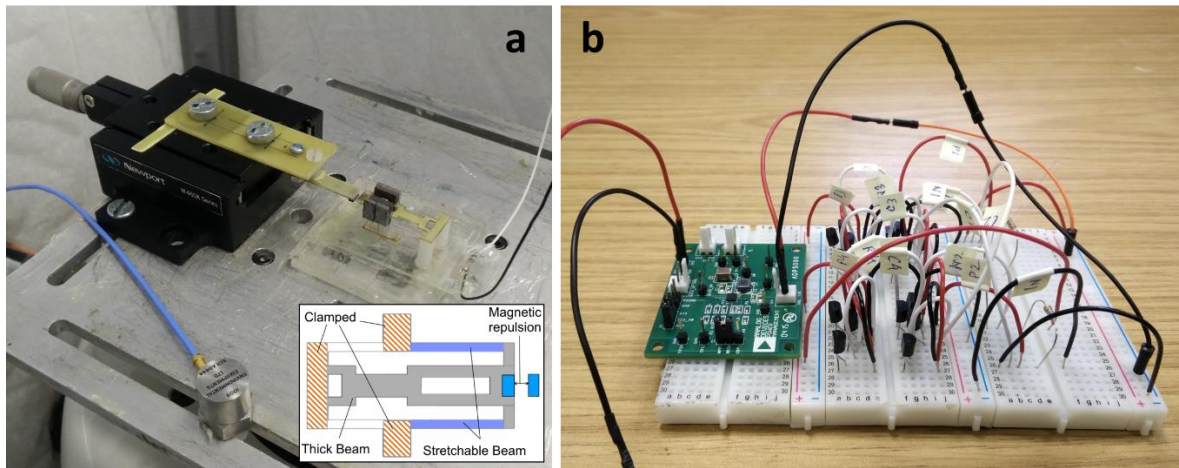
Figure 8.9: (a) Vibration energy harvester mounted on shaker table. Inset shows the device topology. (b) The power management module comprising CRD circuit, DELVD rectifier and ADP5090 board.

8.4.1 Harmonic excitation test

Sinusoidal harmonic vibrational excitation was applied to a linear harvester (resonance frequency 42.5 Hz) at different acceleration levels. Figure 8.10 shows the time traces of the DELVD FBR output (V_in) and the ADP5090 output (V_out) for each input acceleration level. At low acceleration levels (0.1 – 0.2g) the average DC value of V_in is around 0.35 V, while the DC component of V_out increases from 0.38 V (at 0.1g) to 1.7 V (at 0.2g). This can be attributed to the fact that with the fixed input voltage, the input current increased with increasing acceleration, delivering the enhanced regulated output with

increasing acceleration. Also, both V_in and V_out exhibit almost stable voltage outputs without any noticeable ripple.
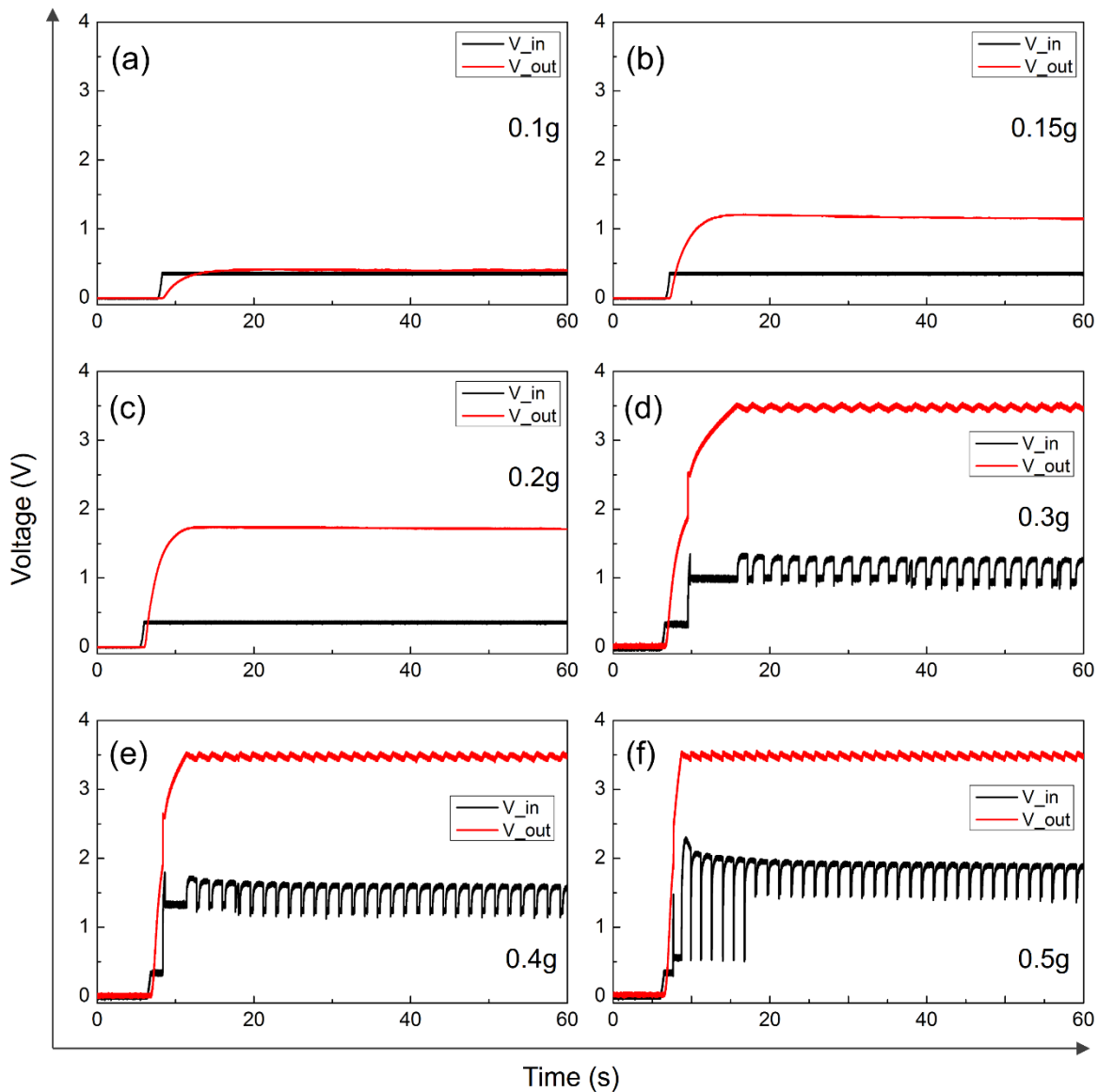
Figure 8.10: The input and output voltage-time traces of the ADP5090 evaluation board at different input vibrational accelerations.

As the vibrational acceleration is increased (0.3 – 0.5g), the DC value of V_in also increases, while DC value of V_out remains almost constant at 3.5 V, which is the rated maximum output of the ADP5090. In addition, significant ripple is introduced in the V_in, which is due to the pulse frequency mode (PFM) operation of the boost regulator. In this mode the boost regulator periodically stores the input energy in a capacitor and discharges the energy to the system load. However, the ripple in V_out is negligibly small at accelerations 0.3g – 0.5g, and V_out reaches the regulated value of 3.5 V at a faster rate

with increasing accelerations. This is due to the higher energy delivered into the ADP5090 with increasing acceleration.
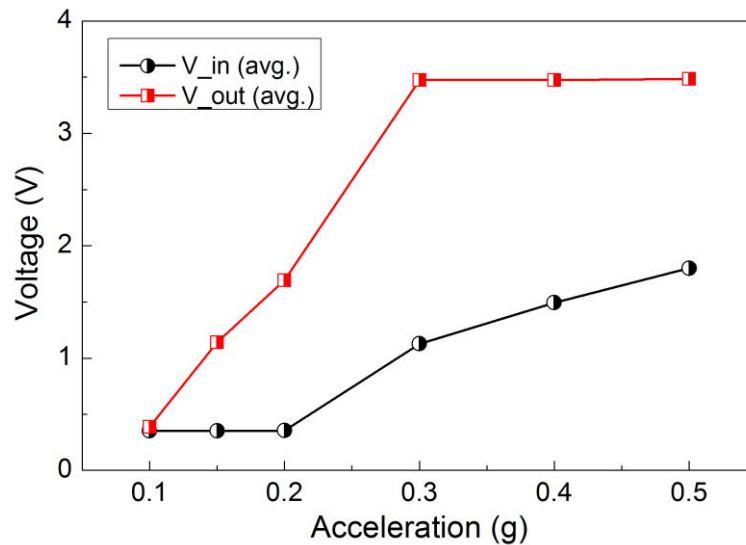

Figure 8.11: Variation of average V_in and V_out with acceleration.

8.4.2 Band-limited random excitation test

Band-limited (10 − 100 Hz) random vibrations with different RMS accelerations were applied to a nonlinear bistable harvester, and a combined nonlinear bistable-monostable harvester, which were described in Chapter 6. The output of the harvesters were processed using the power management configuration illustrated in Figure 8.8. The output of the DELVD full bridge rectifier and the ADP5090 evaluation board at three RMS acceleration levels for the bistable harvester has been shown in Figure 8.12. At the lowest acceleration (0.5g RMS) the DC value of the input is 0.33 V, which is below the rated input threshold voltage. Therefore, the boost regulator module in ADP5090 is not activated, and the resulting output exhibits a randomly varying behaviour with ~1 V DC value. At higher accelerations (1g and 1.5g RMS) the V_in is higher than the input threshold, and the boost regulator is activated, resulting 3.5 V DC regulated output. However, due to the pulse frequency mode (PFM) operation where the boost regulator periodically stores the input energy in capacitor and discharges, V_in exhibits significant random variability. This is due to the unpredictable nature of V_in, which stems from the random vibrational excitation imparted to the energy harvester.
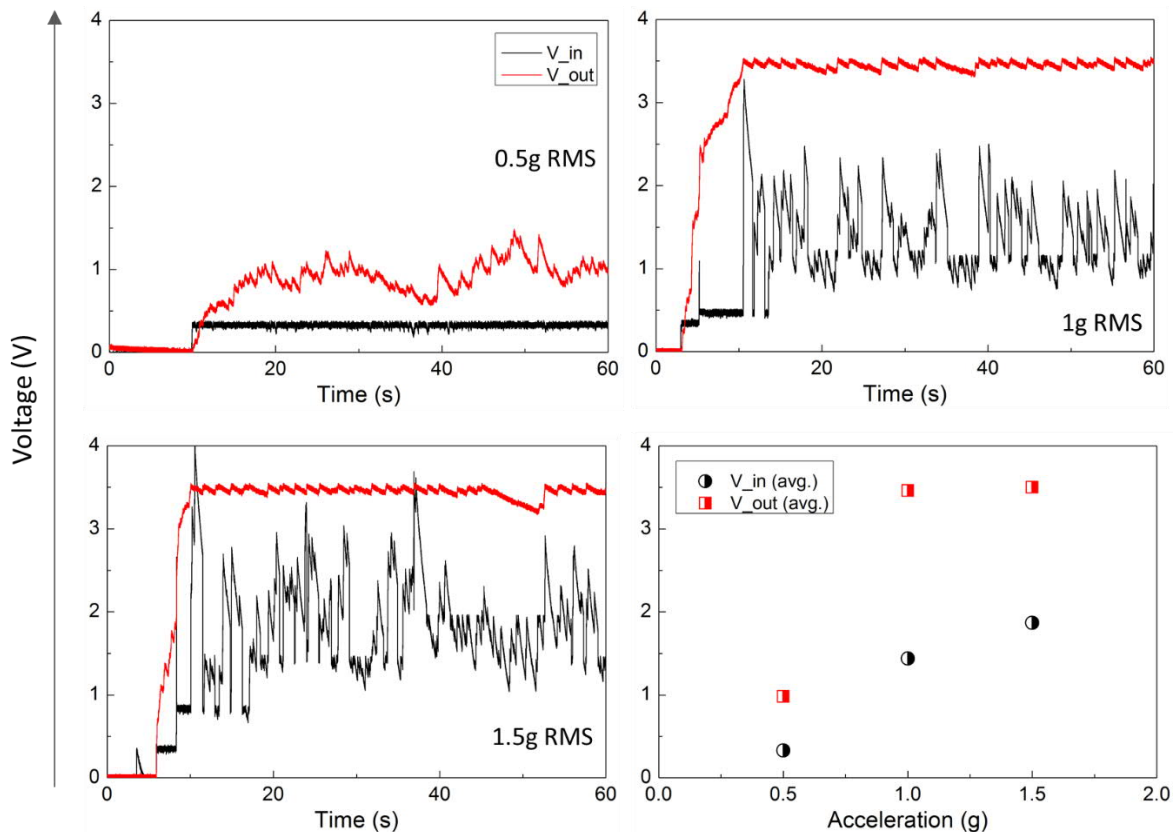
Figure 8.12: The input and output voltage-time traces of the ADP5090 evaluation board for the bistable harvester at different random input vibrational accelerations.

The output of the DELVD full bridge rectifier and the ADP5090 evaluation board at three RMS acceleration levels for the bistable-monostable combined harvester has been shown in Figure 8.13. At the lowest acceleration (0.5g RMS) the DC value of the input increases to a value ~1.2 V after a few seconds, which is well above the rated minimum input of 0.33V. The resulting output of ADP5090 reaches a DC average of 3.1 V with significant ripple in the signal. At higher accelerations (1g RMS and 1.5g RMS) the input DC average increases with random variability due to PFM operation. The output DC average exhibits a stable 3.5 V with less ripple, although the input shows random variation due to the randomness in the input vibrational excitation.
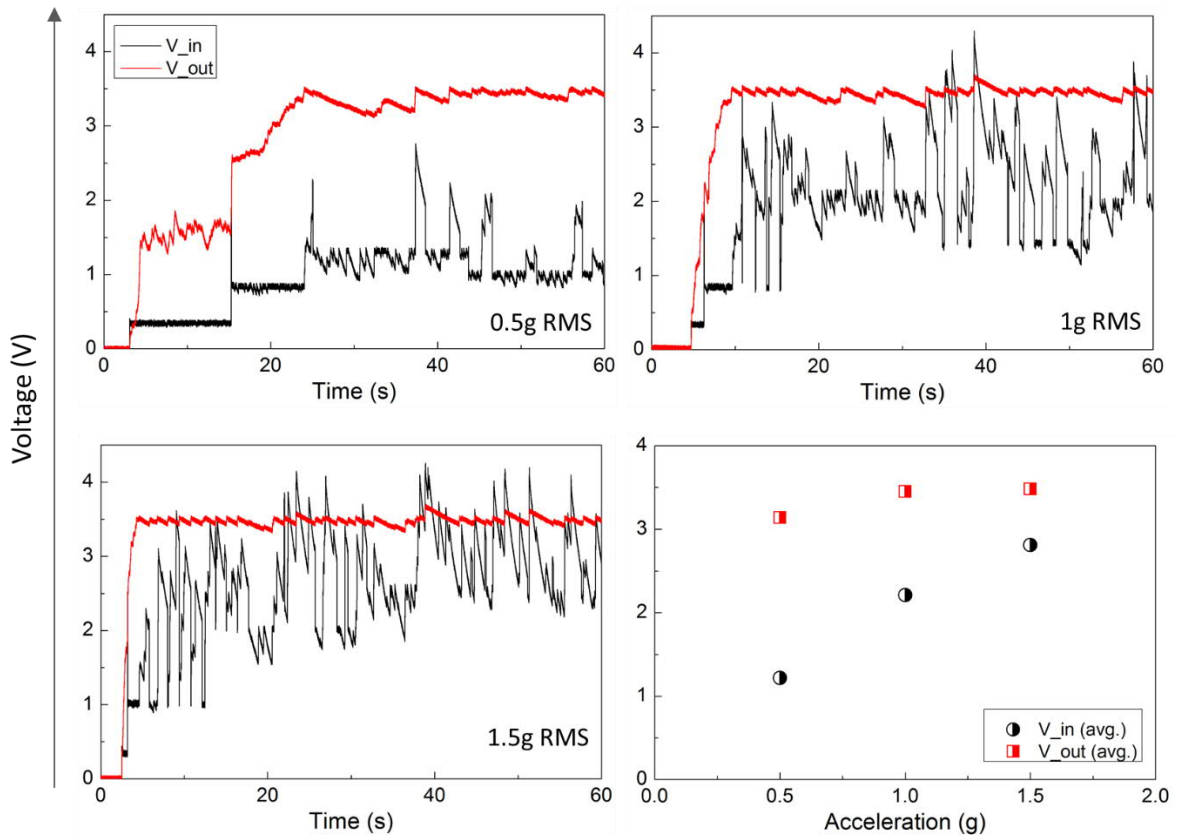
Figure 8.13: The input and output voltage-time traces of the ADP5090 evaluation board for the bistable-monostable combined nonlinear energy harvester at different random input vibrational accelerations.

8.4.3 Efficiency

The efficiency of the power management system can be estimated by taking into account the output load power from the energy harvester into a load resistor, with and without the power management system.
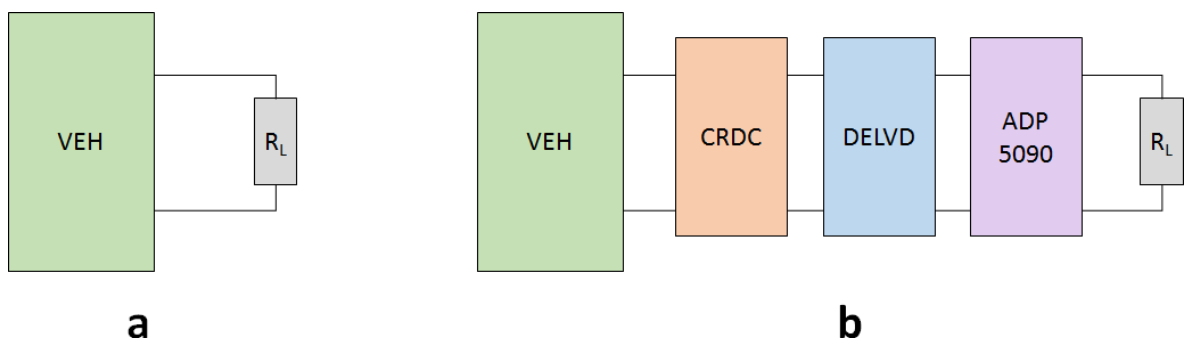
Figure 8.14: Circuit configurations for estimation of PM (power management) efficiency. (a) Without PM. (b) With PM. R_L = 3 kΩ in both configurations.

The PM system was tested in 1g RMS band limited random vibrations with the linear, bistable and bistable-monostable combined energy harvester configurations. The resulting RMS load voltage and load power data are tabulated in Table 8.2.

Table 8.2: Calculation of efficiency

Device Configuration	Without PM		With PM		PM Efficiency (%)
	$V_{L(RMS)}$ (V)	$P_{L(RMS)}$ (mW)	$V_{L(RMS)}$ (V)	$P_{L(RMS)}$ (mW)	
Linear	1.48	0.73	1.18	0.46	63.1
Bistable	1.79	1.07	1.52	0.77	71.9
Combined Bistable-Monostable	2.16	1.56	1.88	1.18	75.6

The efficiency of the PM system tends to increase with increasing input load voltage. This is a result of the combined voltage drop across the DELVD and the ADP5090 modules (datasheet).

8.5 Conclusion

This chapter described the development of a power management topology comprising the diode equivalent low voltage drop (DELVD) circuit and a commercially available low-voltage boost regulator (ADP5090). The construction of the DELVD module using off-the-shelf discrete components (low voltage drop MOSFETs) has been discussed in detail, and overview of the ADP5090 evaluation board has been provided. The developed power management module has been tested with a linear harvester operating in resonant mode under harmonic excitation, and exhibits stable regulated output at accelerations as low as 0.15g. Furthermore, the power management module has been tested with a nonlinear bistable and combined bistable-monostable nonlinear harvester operated under band-limited random vibrational excitation, and exhibits stable regulated DC output when the randomly varying input voltage is above the threshold. Therefore, the power management module has been demonstrated to be effective in both linear and nonlinear devices operated in harmonic or random vibrations.

References

[1]   A. P. Chandrakasan, D. C. Daly, J. Kwong, and Y. K. Ramadass, "Next generation micro-power systems," in *2008 IEEE Symposium on VLSI Circuits*, 2008, pp. 2-5.

[2]   Y. K. Ramadass and A. P. Chandrakasan, "An Efficient Piezoelectric Energy Harvesting Interface Circuit Using a Bias-Flip Rectifier and Shared Inductor," *IEEE Journal of Solid-State Circuits,* vol. 45, pp. 189-204, 2010.

[3]   L. Karthikeyan and B. Amrutur, "Signal-Powered Low-Drop-Diode Equivalent Circuit for Full-Wave Bridge Rectifier," *IEEE Transactions on Power Electronics,* vol. 27, pp. 4192-4201, 2012.

[4]   D. Zhu, S. Roberts, T. Mouille, M. J. Tudor, and S. P. Beeby, "General model with experimental validation of electrical resonant frequency tuning of electromagnetic vibration energy harvesters," *Smart Materials and Structures,* vol. 21, p. 105039, 2012.

9 CONCLUDING REMARKS

This final chapter summarise the works presented in this dissertation, discuss the original contribution of the research, and provides the glimpse of future research work that can be pursued on a thematically similar project. In the first section a summary of the works discussed in the previous chapters are presented, followed by a review of the original contributions of the research work to the energy harvesting community. In the third and final section, future research directions has been discussed which could be aimed at exploiting the opportunities identified in this dissertation, and finding solutions to some of the problems discussed.

9.1 Summary

The dissertation work commenced with the motivation to improve the performance of vibration energy harvesting systems in terms of spectral response, miniaturization and power output. A discussion on the state of the art of vibration energy harvesting using different transduction mechanisms and bandwidth widening mechanism were provided in the second chapter. In addition, some recent developments in power management for energy harvesters and integration were included. The third chapter briefly described the analytical and design techniques, fabrication and characterization tools used in the dissertation work. A nonlinear bistable electromagnetic vibration energy harvesting device was presented in the fourth chapter, where repulsive force between a pair of magnets was used to induce bistability. The prototype exhibited broadband hysteretic frequency response within moderately low frequency range. The bistable nonlinearity was later combined with impact induced nonlinearity when the oscillator collided with the base at higher vibrational accelerations. It was demonstrated that by combining the bistability and the impact induced nonlinearity, the bandwidth could be broadened even further. In the fifth chapter a novel vibrational energy harvesting prototype was introduced which combined magnetic repulsion induced bistable nonlinearity with cantilever stretching induced cubic force nonlinearity. The monostable cubic force nonlinearity was introduced

by a unique combination of thin and thick cantilever structures. In this topology one end of the shorter and thin cantilever beam was fixed, and the other end was constrained to move along the end of a longer and thick cantilever, enforcing the thin beam to be stretched under large bending deflections. At small deflections, the device was subject to magnetic repulsion induced bistable nonlinearity, which could be adjusted by manipulating the distance between the magnets. The prototype combined the beneficial features of both the nonlinearities and demonstrated broadband response. A MEMS-scale nonlinear vibration energy harvesting device is presented in the sixth chapter, comprising a micro-fabricated silicon spring, a double-layer planar spiral micro-coil and an NdFeB micro-magnet. Nonlinearity was incorporated in the system due to stretching of the thin spiral silicon springs at large deflections, resulting hysteretic hardening frequency response. A magnetic repulsion induced frequency tuning mechanism was also incorporated, which could be adjusted by manipulation of screw mechanism. The magnetic tuning mechanism modified the linearized stiffness of the spring, and shifted the entire spectral plot in response to the variable magnetic tuning force. A multi-level ultra-dense micro-coil architecture, aimed at enhancing the magnetic flux linkage gradient and the harvested energy, was introduced in the seventh chapter. The ultra-dense coil topology consisted of interleaved spiral micro-coil layers in each level, which were connected to the next level through inter-level vias. It was demonstrated that such coil topologies could substantially increase the number of turns within the same footprint, and enhance the magnetic flux linkage and harvested power significantly. An elaborate process flow for fabrication of the ultra-dense coils was developed. The primary objective of the initial fabrication runs were the electrodeposition of the interleaved spiral micro-coil layers, and to establish electrical isolation between the interleaved coils by using thin layers of conformably deposited insulating dielectric material. Four different dielectric materials – silicon dioxide, silicon nitride, Parylene C and aluminium nitride were experimentally assessed to achieve insulation between the electrodeposited coil layers. However, the ultra-dense coil prototypes fabricated with different thickness of the dielectric materials were unable to achieve electrical isolation between the interleaved coil layers. The reasons for failure of the first three dielectric materials were traced to diffusion of copper (in silicon dioxide), brittleness and crack formation (silicon nitride), lack of adhesion and bubble formation (Parylene C). However, the reason for failure of the aluminium nitride dielectric could not be determined unambiguously despite extensive inspection through electron microscopy and EDX mapping. The eighth chapter discussed the development of a power management module

comprising a full bridge rectifier using diode equivalent low voltage drop (DELVD) circuits and an off-the-shelf boost regulator evaluation board (ADP5090). The power management module was tested with inputs from a linear harvester under harmonic resonant vibration, and from a nonlinear bistable harvester subject to bandlimited random vibrations. The power management module delivered regulated output power with both types of input electrical energy.

9.2 Contributions of the dissertation

The research work pursued in this dissertation involved development of analytical models for vibration energy harvesting devices, finite element analysis and numerical simulations of the device models, fabrication, characterization and validation. The major contributions of this dissertation are described in the following paragraphs.

- It was demonstrated that the incorporation of mechanical impact in nonlinear bistable vibration energy harvesters could significantly enhance the operational bandwidth beyond that of standalone bistable systems. A new figure of merit was formulated considering the equivalent oscillating mass, average power output, and the half power bandwidth of energy harvesters. With carefully adjusted impact distance, the bistable and impact combined prototype outperformed the equivalent bistable only device.

- A prototype combining magnetic repulsion induced bistable nonlinearity and stretching induced cubic force nonlinearity was introduced, and experimentally validated. The developed bistable quartic prototype combined the bistable potential energy profile with a Duffing quartic potential, and benefitted from both nonlinearities under harmonic and band-limited random excitations. It demonstrated large amplitude chaotic inter-well oscillations in the low frequency large amplitude vibrations, and large amplitude harmonic oscillations at high frequency harmonic excitations. Consequently, the bistable-quartic device exhibited higher overall performance in comparison to equivalent standalone bistable-quadratic and monostable-quartic counterparts. Furthermore, it addressed some of long-standing inconsistencies between the theoretical modelling and practical implementations of bistable Duffing nonlinearities in much of the vibrational energy harvesting literature.

- A MEMS-scale nonlinear energy harvester with variable magnetic force induced frequency tuning mechanism was demonstrated. While the magnetic force induced tuning had previously been reported in literature for macro-scale and meso-scale devices, the prototype developed in this dissertation has miniaturized the mechanism to the MEMS-scale. Furthermore, it demonstrated that this mechanism could be used to effectively tune the linear resonant responses, as well as the hysteretic spectral responses characteristic of nonlinear energy harvesters. In addition, it was demonstrated that with specific device topologies, the negative effect of tuning induced damping forces on the device power output could be averted.

- An ultra-dense planar micro-coil architecture with multiple levels of interleaved spiral coils was proposed, which would substantially increase the flux linkage and power harvesting capabilities of electromagnetic vibration energy harvesters. The process flow for fabrication of the proposed ultra-dense coil was developed, and the initial fabrication runs were focused on determining a suitable dielectric material for electrical isolation between the individual coil layers. Three of the tested dielectric materials (silicon dioxide, silicon nitride, Parylene C) failed to achieve insulation due to various reasons, such as copper diffusion, brittleness and crack formation, and lack of adhesion. However, the failure of the fourth dielectric, aluminium nitride could not be determined through electron microscopy and EDX mapping. Nevertheless, the significant gains in performance as demonstrated in the simulation results underline the substantial advantage of developing such ultra-dense coils for incorporation in future electromagnetic micro-power generators.

9.3 Directions for future research

In an attempt to develop vibration energy harvesters with enhanced performance for powering the wireless sensor nodes in the forthcoming era of IoT, this dissertation investigated some potential solutions to existing challenges. In that process, the research presented in the dissertation came up with some interesting results and further questions, that could be pursued in future research projects.

- The bistable quartic vibration energy harvester prototype combined the magnetically induced bistable nonlinearity and stretching induced cubic force nonlinearity in a single device topology. The prototype combined the beneficial

features of both types of nonlinearity, delivered enhanced spectral performance under harmonic and band-limited random vibrations. The meso-scale prototype was fabricated using FR4 sheets, wire-wound copper coils and discrete NdFeB magnets. The proposed topology could potentially be miniaturized to MEMS-scale in order to facilitate batch fabrication and integration with other WSN components. The miniaturization would require innovation in both design and fabrication of the spring structure in silicon. One of the potential negative consequences of miniaturization is the drop in harvested energy, which needs to be addressed by the novel design, as well as incorporation of high energy density permanent magnets.

- Another consequence of miniaturization in device volume is the inevitable increase in the spring resonance frequency due to smaller oscillating mass and spring dimensions, keeping all other parameters unchanged. On the other hand, most of the naturally occurring vibrations are concentrated at the lower end of the frequency spectrum, which become inaccessible to MEMS-scale silicon (Young's modulus 160×10^9 Pa) springs. Therefore, new spring or suspension materials with much lower Young's modulus (such as PDMS, PVDF, Parylene etc.) need to be incorporated in MEMS-scale micro-power generators for them to be useful in real-life applications. Moreover, many real vibration sources produce multi-directional vibrations, which can be harvested more efficiently by using multi-axis energy harvesters. For these reasons, design of new spring topologies using soft polymer materials for use with miniaturized low frequency vibration energy harvesting devices could be an active area of future research.

- One of the prospective techniques to compensate for the diminished output power of MEMS-scale electromagnetic vibration energy harvesters could be the use of ultra-dense planar micro-coils presented in this dissertation. The simulation results demonstrated that the ultra-dense coil could substantially increase the magnetic flux linkage and the harvested power over conventional micro-coils. However, the individual interleaved coil layers must be electrically insulated from each other in a multi-layer ultra-dense coil. Four different dielectric materials were investigated for application as the insulation between the coil layers, and none of them could provide the required electrical isolation. While the reasons for failure of three of the materials (silicon dioxide, silicon nitride, Parylene) were apparent from the microscopic observation, the reason for failure of aluminium nitride dielectric could not be determined. Therefore, an in-depth review of the ultra-dense coil

design, fabrication process and dielectric material properties are needed to determine the source of failure before future fabrication runs.

- The power management module developed in this dissertation was tested for linear and nonlinear meso-scale energy harvesting devices which produced 100s of µW power and > 400 mV at moderate acceleration ($0.2 - 0.5g$) levels. However, the typical MEMS-scale electromagnetic energy harvesters deliver < 10 µW power and only 10s of mV at similar excitation levels. Besides increasing the energy output of MEMS electromagnetic energy harvesters, research effort should also be directed towards the development of advanced power management modules capable of conditioning the low output power. Such low energy power management modules could potentially be useful with other energy harvesting transducers, such as thermoelectric and photovoltaic cells for powering the WSNs in future.

APPENDIX

This appendix lists the Matlab programs used to numerically simulate the vibration energy harvesting devices, and the photomask files used to fabricate the MEMS devices

A.1 MatLab codes for numerical simulation

Code for simulation of bistable energy harvester

```matlab
% Run_bistable_f_6_power

clear
R_coil = 770;      % Coil resistance
R_load = 1000;     % Load resistance
N_turn = 2500;
COR = 0.5;    % Coefficient of restitution

B1 = -29.13563/2500; B2 = -228585.16441/2500; B3 = 3.50852e6/2500; B4 =
1.01996e10/2500; I1 = 0.76922/2500; % No SOFT Polynomial coefficients

z0 = [0 0 0];
N_step = 2000;
f_start = 1;
f_end = 50;
f_num = 500;
t_max = 5;
tspan = 0:(t_max/N_step):t_max;
f_mat_up = (linspace(f_start,f_end,f_num))';
f_mat_down = (linspace(f_end,f_start,f_num))';
%f = 25;
%w = -10e-3;
w = -3.5e-3;
%w = -3.7e-3;
%w = -2.6e-3;
save_data = 0; % If save_data = 1, data is saved to file_save
file_save = '\\Fileshare1\Docs3\pranay.podder\My
Documents\MATLAB\data_files\bi_new_f_Pload_a_2_d_4.8_w_3.5.mat';
%[t_rk,x_rk] = ode45(@bistable_f_6_power,tspan,x0,[],f);
t = zeros(length(tspan),1);
z = zeros(length(tspan),3);
h = t_max/N_step;
z(1,:) = z0';
t(1) = 0;
amp_max_up = zeros(length(f_mat_up),1);
amp_min_up = zeros(length(f_mat_up),1);
V_rms_up = zeros(length(f_mat_up),1);
P_avg_up = zeros(length(f_mat_up),1);
P_load_up = zeros(length(f_mat_up),1);
```

```matlab
amp_max_down = zeros(length(f_mat_down),1);
amp_min_down = zeros(length(f_mat_down),1);
V_rms_down = zeros(length(f_mat_down),1);
P_avg_down = zeros(length(f_mat_down),1);
P_load_down = zeros(length(f_mat_down),1);

%    Up sweep start

for j = 1:length(f_mat_up)
    f = f_mat_up(j);
for i = 1:(N_step)
    t(i+1) = t(i)+h;
    %x(i+1,:) = x(i,:) + h*bistable_f_6_power(t(i),x(i,:),f)';
    %[t_rk,x_rk] = ode45(@bistable_f_6_power,tspan,x0,[],f);
    k1 = bistable_f_6_power(t(i),z(i,:),f)';
    k2 = bistable_f_6_power(t(i)+h/2,z(i,:)+h/2*k1,f)';
    k3 = bistable_f_6_power(t(i)+h/2,z(i,:)+h/2*k2,f)';
    k4 = bistable_f_6_power(t(i)+h,z(i,:)+h*k3,f)';
    z(i+1,:) = z(i,:) + h/6*(k1+2*k2+2*k3+k4);
    if z(i+1,1) < w
        r = (z(i,1)-w)/(z(i,1)-z(i+1,1));
        t(i+1) = t(i) + r*h;
        z(i+1,1) = (1-r)*z(i)+r*z(i+1);
        z(i+1,2) = -z(i+1,2)*COR;
    end
end
amp_max_up(j) = max(z(1800:end,1));
amp_min_up(j) = min(z(1800:end,1));

    z_1 = z(1800:end,1);
    z_2 = z(1800:end,1).*z(1800:end,1);
    z_3 = z(1800:end,1).*z(1800:end,1).*z(1800:end,1);
    z_4 = z(1800:end,1).*z(1800:end,1).*z(1800:end,1).*z(1800:end,1);
    d_phi_dz = N_turn*(B1*z_1 + B2*z_2 + B3*z_3 + B4*z_4 + I1);
    %d_phi_dz = B1*x(401:501,1) + B2*(x(401:501,1).*x(401:501,1)) + I1;
    D_em = (d_phi_dz.*d_phi_dz)/(R_coil + R_load);     % Electromagnetic
Damping
    P_em = D_em.*(z(1800:end,2).*z(1800:end,2));
    P_avg_up(j) = mean(P_em);
    P_load_up(j) = (P_avg_up(j))*(R_load/(R_coil + R_load));
    V_rms_up(j) = sqrt(mean((d_phi_dz.*z(1800:end,2)).^2));
    %x0 = A(501,2:4);
z(1,:) = z(end,:);
t(1) = 0;
end
%    Up sweep end

clear j i z_1 z_2 z_3 z_4 d_phi_dz D_em P_em

%    Down sweep start

for j = 1:length(f_mat_down)
    f = f_mat_down(j);
for i = 1:(N_step)
    t(i+1) = t(i)+h;
    %x(i+1,:) = x(i,:) + h*bistable_f_6_power(t(i),x(i,:),f)';
    %[t_rk,x_rk] = ode45(@bistable_f_6_power,tspan,x0,[],f);
    k1 = bistable_f_6_power(t(i),z(i,:),f)';
    k2 = bistable_f_6_power(t(i)+h/2,z(i,:)+h/2*k1,f)';
    k3 = bistable_f_6_power(t(i)+h/2,z(i,:)+h/2*k2,f)';
```

```
    k4 = bistable_f_6_power(t(i)+h,z(i,:)+h*k3,f)';
    z(i+1,:) = z(i,:) + h/6*(k1+2*k2+2*k3+k4);
    if z(i+1,1) < w
        r = (z(i,1)-w)/(z(i,1)-z(i+1,1));
        t(i+1) = t(i) + r*h;
        z(i+1,1) = (1-r)*z(i)+r*z(i+1);
        z(i+1,2) = -z(i+1,2)*COR;
    end
end
amp_max_down(j) = max(z(1800:end,1));
amp_min_down(j) = min(z(1800:end,1));

    z_1 = z(1800:end,1);
    z_2 = z(1800:end,1).*z(1800:end,1);
    z_3 = z(1800:end,1).*z(1800:end,1).*z(1800:end,1);
    z_4 = z(1800:end,1).*z(1800:end,1).*z(1800:end,1).*z(1800:end,1);
    d_phi_dz = N_turn*(B1*z_1 + B2*z_2 + B3*z_3 + B4*z_4 + I1);
    %d_phi_dz = B1*x(401:501,1) + B2*(x(401:501,1).*x(401:501,1)) + I1;
    D_em = (d_phi_dz.*d_phi_dz)/(R_coil + R_load);    % Electromagnetic
Damping
    P_em = D_em.*(z(1800:end,2).*z(1800:end,2));
    P_avg_down(j) = mean(P_em);
    P_load_down(j) = (P_avg_down(j))*(R_load/(R_coil + R_load));
    V_rms_down(j) = sqrt(mean((d_phi_dz.*z(1800:end,2)).^2));
    %x0 = A(501,2:4);
z(1,:) = z(end,:);
t(1) = 0;
end

%   Down sweep end

figure
plot(f_mat_up,amp_max_up,'-r','Linewidth',2)
hold on
plot(f_mat_up,amp_min_up,'--r','Linewidth',2)
hold on
plot(f_mat_down,amp_max_down,'-b','Linewidth',2)
hold on
plot(f_mat_down,amp_min_down,'--b','Linewidth',2)
xlabel('Frequency (Hz)'); ylabel('Maximum Amplitude (m)');
grid on

figure
subplot(2,1,1)
plot(f_mat_up,V_rms_up,'-r','Linewidth',2);
hold on
plot(f_mat_down,V_rms_down,'-b','Linewidth',2);
xlabel('Frequency (Hz)');
ylabel('RMS Voltage (V)')
%plot(t,x(:,1),'ob');
grid on
hold on
subplot(2,1,2)
plot(f_mat_up,P_load_up,'-r','Linewidth',2);
hold on
plot(f_mat_down,P_load_down,'-b','Linewidth',2);
xlabel('Frequency (Hz)');
ylabel('Load Power (W)')
grid on
hold on
```

```matlab
figure
semilogy(f_mat_up,P_load_up,'-r','Linewidth',2);
hold on
semilogy(f_mat_down,P_load_down,'-b','Linewidth',2);
xlabel('Frequency (Hz)');
ylabel('Load Power (W)')
grid on
hold on

if save_data == 1
    save(file_save,'f_mat_up','P_load_up','f_mat_down','P_load_down');
end;
```

Bistable device function

```matlab
function dx = bistable_f_6_power(t,x,f)
%global d_phi_dz_global;
m = 2.7e-4;      % mass in Kg
a = 10;          % acceleration
k = 17.5;        % spring constant
D = 5e-3;        % Distance between magnet poles
mu_o = 1.256e-6;     % Air permeability
m_1 = 6.2e-3;    % Magnet dipole moment
m_2 = m_1;   % Magnet dipole moment
C = (mu_o*m_1*m_2/(4*3.142));    % Constant Prefactor
L = 15e-3;   % Length of cantilever
F_ext = m*a;     % External force due to vibration
omega = 2*3.142*f;   % Angular frequency of vibration

zeta = 0.008 + 0.00208*a - 9.94247E-5*a*a;    % Parasitic damping ratio
%zeta = 0.01;
D_p = 2*m*zeta*omega; % Parasitic damping
N_turn = 2500;   % No. of coil turns
B1 = -0.00753; B2 = -100.08737; B3 = 880.39191; B4 = 4.97734e6; I1 =
3.1751e-4; % Polynomial coefficients

NB1 = N_turn*B1; NB2 = N_turn*B2; NB3 = N_turn*B3; NB4 = N_turn*B4; NI1 =
N_turn*I1;

R_coil = 770;    % Coil resistance
R_load = 1000;   % Load resistance

dx(1) = x(2);

dx(2) = (1/m)*F_ext*cos(x(3))-(k/m)*x(1) - ((D_p + ((NI1 + NB1*x(1) +
NB2*x(1)^2 + NB3*x(1)^3 + NB4*x(1)^4)^2)/(R_coil + R_load))/m)*x(2)...
    + (C*L/m)*(2*x(1)*(7*D^2 - 2*x(1)^2)*(D^2 + x(1)^2)^-4); % DIPOLE
magnetic force with angle correction

dx(3) = omega;

dx = dx';
```

Codes for simulation of MEMS device

```
% Run_SOI_7_f_3
clear all;

m = 7e-5;
a = 1;

f_1 = 100;
f_2 = 300;
f_num = 400;
f_up = (linspace(f_1,f_2,f_num))';

rho = 7e-4;        % *

%k3 = 0.1e8;           % *
k3 = 0;

RL = 135;
RC = 130;

A = -6.3e-5;      % *
R0 = -1200;       % *

z0 = [0 0 0];

t_end = 2;
t_num = 5000;
tspan = (linspace(0,t_end,t_num));

V_rms_up = zeros(f_num,1);
V_rms_down = zeros(f_num,1);

P_av_up = zeros(f_num,1);
P_av_down = zeros(f_num,1);

Amp_max_up = zeros(f_num,1);
Amp_min_up = zeros(f_num,1);

Amp_max_down = zeros(f_num,1);
Amp_min_down = zeros(f_num,1);

vel_rms_up = zeros(f_num,1);
vel_rms_down = zeros(f_num,1);

acc_vel_up = zeros(f_num,1);
acc_vel_down = zeros(f_num,1);

for i = 1:length(f_up);
    [t,z] = ode45(@(t,z) SOI_7_f_3(t,z,f_up(i),rho,k3,RL,RC), tspan, z0);
    x = z(:,1);
    xdot = z(:,2);
    xdott = z(:,3);
    n = length(z(:,2));
    V_rms_up(i) = sqrt(mean(((A*R0*exp(R0*x)).*xdot).^2));
    P_av_up(i) = RL*((V_rms_up(i)/(RC + RL))^2);
    Amp_max_up(i) = max(x);
    Amp_min_up(i) = min(x);
    vel_rms_up(i) = sqrt(mean(xdot.^2));
    acc_vel_up(i) = sqrt(mean((xdott.*xdot).^2));
```

```
    z0 = z(n,:);
end

clear x xdot xdott n

f_down = (linspace(f_2,f_1,f_num))';

for j = 1:length(f_down);
    [t,z] = ode45(@(t,z) SOI_7_f_3(t,z,f_down(j),rho,k3,RL,RC), tspan,
z0);
    x = z(:,1);
    xdot = z(:,2);
    xdott = z(:,3);
    n = length(z(:,2));
    V_rms_down(j) = sqrt(mean(((A*R0*exp(R0*x)).*xdot).^2));
    P_av_down(j) = RL*((V_rms_down(j)/(RC + RL))^2);

    Amp_max_down(j) = max(x);
    Amp_min_down(j) = min(x);
    vel_rms_down(j) = sqrt(mean(xdot.^2));
    acc_vel_down(i) = sqrt(mean((xdott.*xdot).^2));
    z0 = z(n,:);
end


figure()
semilogy(f_up,P_av_up,'b','Linewidth',2)
hold on;
semilogy(f_down,P_av_down,'r','Linewidth',2)
xlabel('Frequency (Hz)'), ylabel('Power (W)')
xlim([150 250])

figure()
plot(f_up,V_rms_up,'b','Linewidth',2)
hold on;
plot(f_down,V_rms_down,'r','Linewidth',2)
xlabel('Frequency (Hz)'), ylabel('RMS Voltage (V)')
xlim([150 250])

figure()
plot(f_up,Amp_max_up,'b','Linewidth',2)
hold on;
plot(f_down,Amp_max_down,'r','Linewidth',2)
hold on;
plot(f_up,Amp_min_up,'--b','Linewidth',2)
hold on;
plot(f_down,Amp_min_down,'--r','Linewidth',2)
xlabel('Frequency (Hz)'), ylabel('Deflection (m)')
xlim([150 250])

save_data = 1;

save_power = '\\Fileshare1\Docs3\pranay.podder\My
Documents\MATLAB\data_files\SOI_7\SOI_7_k3_0_a_1_d_6.5_power.mat';
save_volt = '\\Fileshare1\Docs3\pranay.podder\My
Documents\MATLAB\data_files\SOI_7\SOI_7_k3_0_a_1_d_6.5_volt.mat';
save_disp = '\\Fileshare1\Docs3\pranay.podder\My
Documents\MATLAB\data_files\SOI_7\SOI_7_k3_0_a_1_d_6.5_disp.mat';
save_vel = '\\Fileshare1\Docs3\pranay.podder\My
Documents\MATLAB\data_files\SOI_7\SOI_7_k3_0_a_1_d_6.5_vel.mat';
```

```
if save_data == 1
    save(save_power,'f_up','P_av_up','f_down','P_av_down');
    save(save_volt,'f_up','V_rms_up','f_down','V_rms_down');

save(save_disp,'f_up','Amp_max_up','Amp_min_up','f_down','Amp_max_down','Amp_min_down');
end
```

MEMS device function

```
function zdot = SOI_7_f_3(t,z,f,rho,k3,RL,RC)
%m = 6.45e-5;       % Mass in kg
m = 9e-5;        % Mass in kg      *

k = 120;          % *
a = 1;
F = m*a;

%m1 = 5e-3;       % *
m1 = 7.5e-3;
m2 = m1;
mu0 = 1.256e-6;     % Air permeability

C = (mu0*m1*m2)/(2*3.142);      % Constant prefactor

d = 6.5e-3;       % *

%d = 8e-3;        % *


A = -1.1e-5;       % *
R0 = -1490.98961;   % *

w = 2*pi*f;          % Angular freqency

Dp = 2*m*w*rho;     % Parasitic damping

zdot = zeros(3,1);

zdot(1) = z(2);
zdot(2) = -(k*z(1) + k3*z(1)^3 + 3*C*((d-z(1))^-4) + Dp*z(2) +
(z(2)*(A*R0*exp(R0*z(1)))^2)/(RC+RL))*(1/m) + F*sin(z(3))/m;
zdot(3) = w;
```
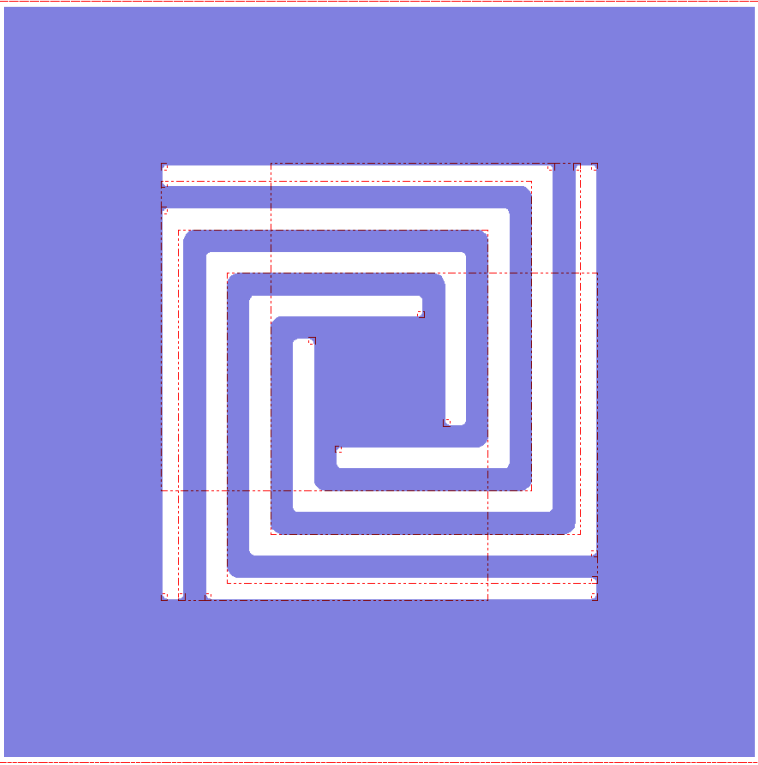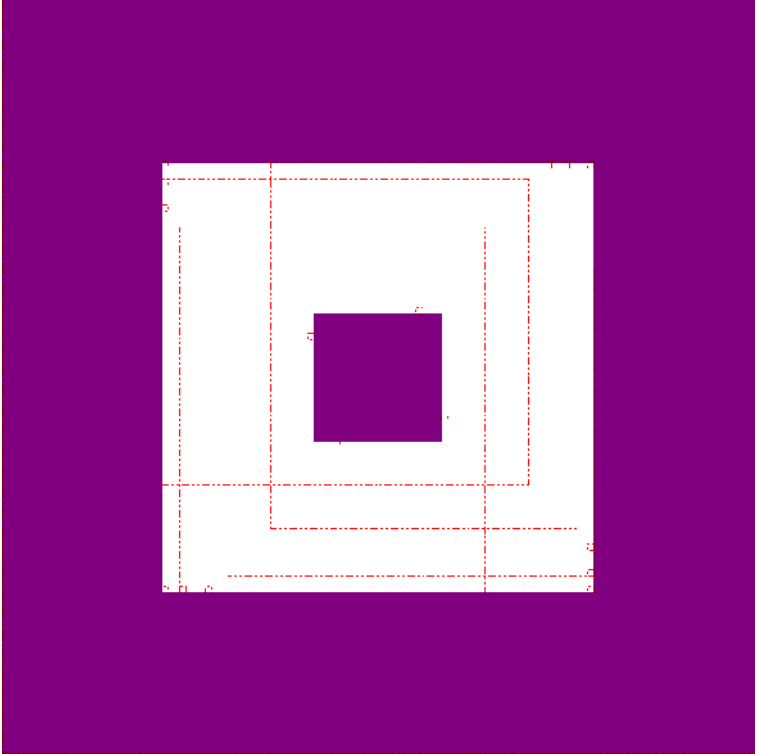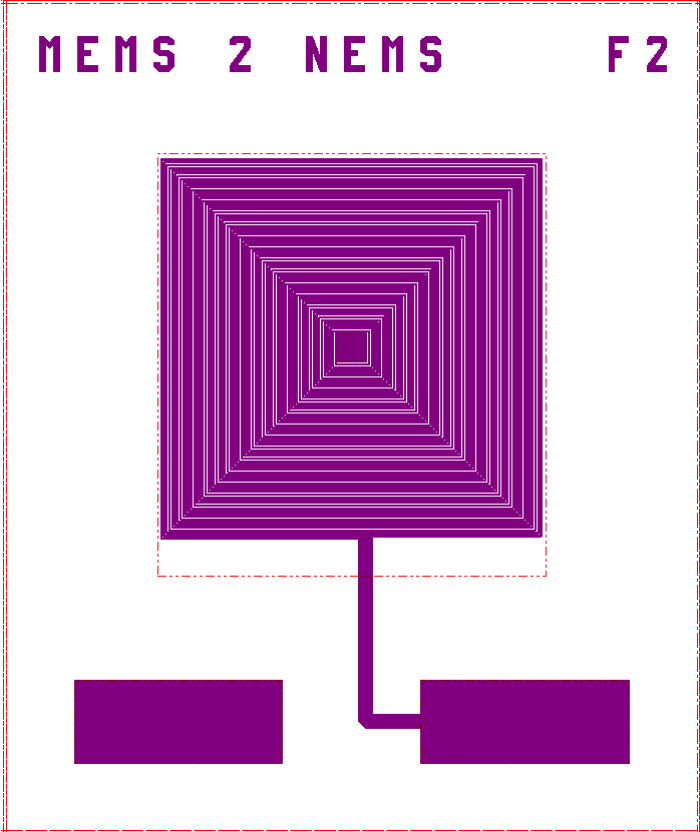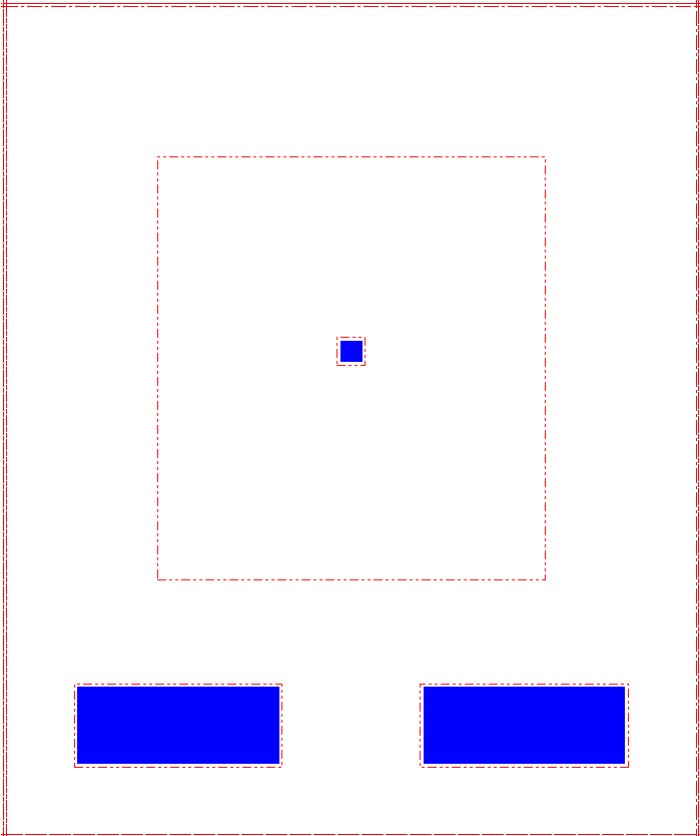
A.2 Photomask layouts used in microfabrication

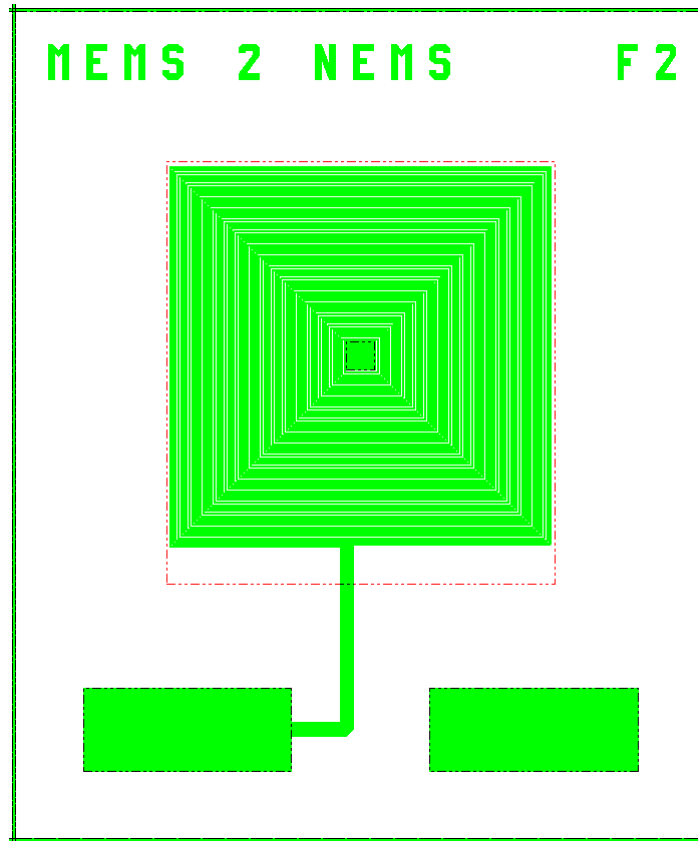Photomask layouts for fabrication of ultra-dense micro-coil.

Mask layer 1 for SOI spring.	
Mask layer 2 for etching handle wafer.	

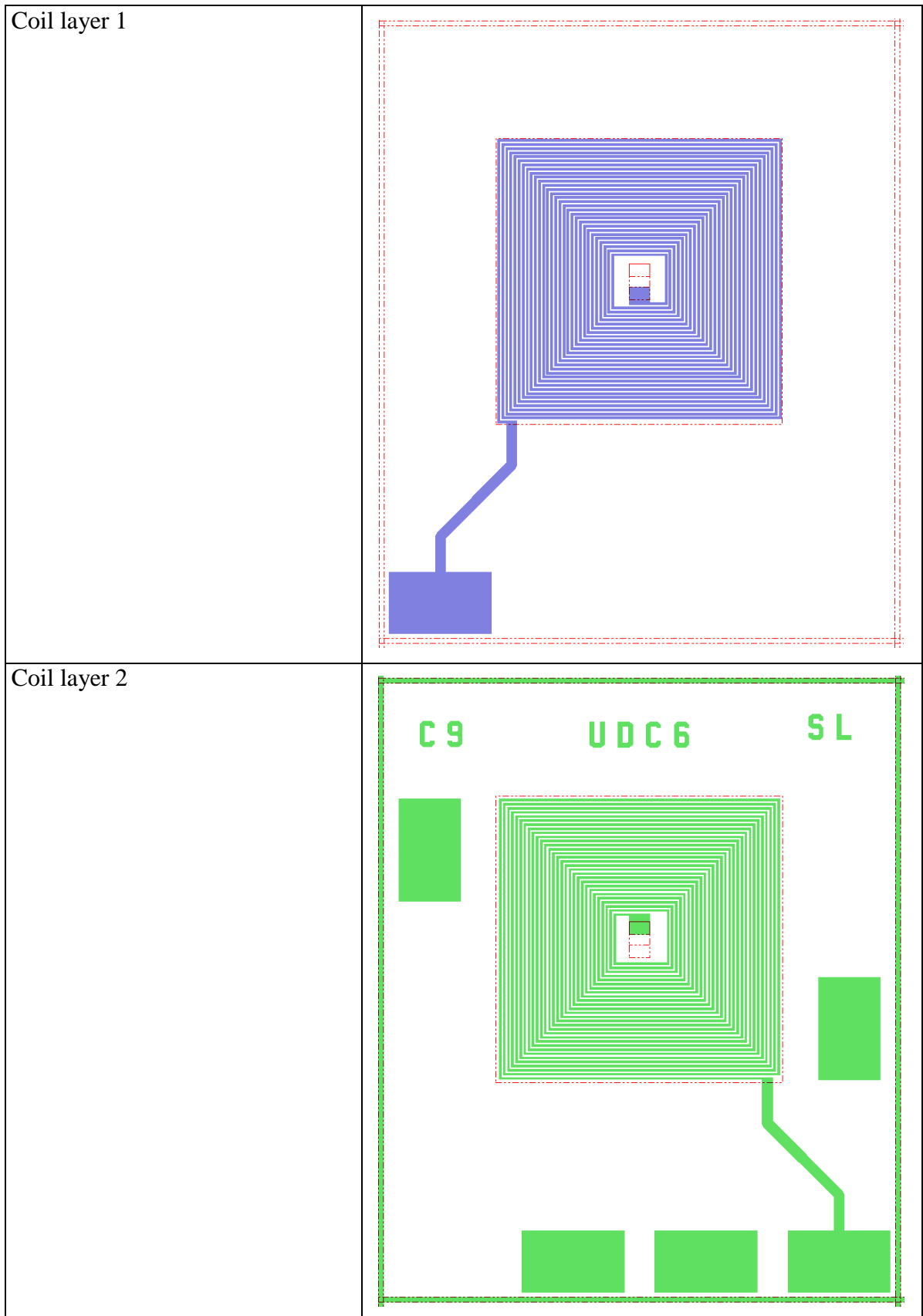Photomask layouts for fabrication of planar double layer micro-coil.

Bottom coil layer and bond-pads	
Central via and bond-pads	

Top coil layer and bond-pads

Photomask layouts for fabrication of ultra-dense micro-coil.

| Coil layer 1 | |
| Coil layer 2 | |

| Vias and bond-pads | |